UNIVERSITÀ
DEGLI STUDI
DI PADOVA

Sede Amministrativa: Università degli Studi di Padova

Dipartimento di Scienze Chimiche

SCUOLA DI DOTTORATO DI RICERCA IN SCIENZA ED INGEGNERIA DEI MATERIALI

CICLO XXVI

PLASMONIC NANOSTRUCTURES FOR THE REALIZATION OF SENSORS BASED ON SURFACE ENHANCED RAMAN SPECTROSCOPY

Direttore della Scuola : Ch.mo Prof. Gaetano Granozzi

Supervisore : Dott.ssa Raffaella Signorini

Dottoranda : Verena Weber

“Researchers should no longer be ashamed to report a SM SERS EF of 10^8 or even 10^6, which are perfectly respectable Figures as long as the experimental approach to estimate them is well detailed and justified.”

(Pablo Etchegoin, 1964-2013)

CONTENTS

ABBREVIATIONS

AFM = Atomic Force Microscopy

Ag NPs = Silver Nanoparticles

Au NPs = Gold Nanoparticles

Au NSs = Gold Nanoshells

Bzt = Benzenethiol

diph = bis(triethoxysilyl)biphenyl polysisesquioxane film

DLS = Dynamic Light Scattering

EF = Enhancement Factor

HABA = 4-hydroxyazobenzene-2 carboxylic acid

HOMO = Highest Occupied Molecular Orbital

LSPP = Localized Surface Plasmon Polaritons

LSPR = Localized Surface Plasmon Resonance

LUMO = Lowest Unoccupied Molecular Orbital

PhAS = Photoacoustic Spectroscopy

PSPP = Propagating Surface Plasmon Polaritons

PSPR = Propagating Surface Plasmon Resonance

RRS = Resonant Raman Scatterer

SEM = Scanning Electron Microscopy

SERRS = Surface Enhanced Resonant Raman Spectroscopy

SERS = Surface Enhanced Raman Spectroscopy

SPP = Surface Plasmon Polariton

SPR = Surface Plasmon Resonance

TBA = Thiobenzoic acid

TEM = Transmission Electron Microscopy

VOC = Volatile Organic Compound

ABSTRACT

La Plasmonica si occupa dell'interazione di una radiazione elettromagnetica di opportuna lunghezza d'onda con gli elettroni di conduzione di un metallo. L'oscillazione collettiva degli elettroni, indotta da questa interazione, è chiamata appunto Risonanza Plasmonica. La risonanza plasmonica di superficie localizzata avviene quando gli elettroni coinvolti sono quelli di superficie di un metallo nanostrutturato con dimensioni minori o comparabili alla lunghezza d'onda di eccitazione. Da questa eccitazione deriva una forte amplificazione del campo elettromagnetico locale, localizzato nelle immediate vicinanze della nanostruttura metallica. Tale amplificazione, unita a una tecnica di rivelazione spettroscopica specifica, quale la spettroscopia Raman, può essere sfruttata per la realizzazione di sensori molecolari. La tecnica Raman è conosciuta come altamente specifica, perché in grado di fornire uno spettro caratteristico della singola molecola, identificandone univocamente la presenza e la costituzione. La sua maggiore limitazione, però, è la bassa sensibilità. Ponendo l'analita in prossimità di un substrato plasmonico, proprio nella regione di forte amplificazione del campo locale, la sensibilità di rivelazione viene fortemente aumentata, dando origine alla spettroscopia Raman amplificata da superfici (*SERS*).

La prima parte del presente lavoro è focalizzata sulla sintesi e sulla caratterizzazione di nanoparticelle d'argento, d'oro e di nano gusci d'oro (chiamati *nanoshell*) e sul loro impiego per la realizzazione di substrati SERS, sia in soluzione colloidale che su substrato solido. L'utilizzo di differenti nanostrutture metalliche, dà la possibilità di sfruttare la risonanza plasmonica localizzata di superficie in un'ampia regione spettrale, che si estende dal visibile al vicino infrarosso. La caratterizzazione ottica e morfologica delle nanostrutture è stata effettuata con tecniche convenzionali, come la spettroscopia di assorbimento UV-visibile, il SERS, la microscopia elettronica a trasmissione e la microscopia a forza atomica. Ad esse è stata affiancata anche una tecnica raramente usata nell'ambito della plasmonica: la spettroscopia fotoacustica. Questa può fornire informazioni riguardanti il contributo di

assorbimento, all'estinzione totale, di una nanostruttura plasmonica. Da una rigorosa misura dei fattori di amplificazione e delle proprietà di fotoacustica al variare della lunghezza d'onda, possono essere fatte alcune considerazioni riguardanti la possibile relazione tra l'estinzione (proprietà di campo lontano) e l' amplificazione SERS (proprietà di campo vicino). Le misure dei profili di eccitazione SERS su substrati plasmonici in liquido e su supporto solido, hanno evidenziato la presenza di *hot spots*, ovvero di zone fortemente amplificate dall'interazione di due o più nanostrutture.

I substrati SERS solidi sono risultati chimicamente stabili, omogenei e riproducibili; essi presentano valori di fattori di amplificazione attorno a 10^4-10^5. In soluzione colloidale, i fattori di amplificazione delle nanostrutture hanno raggiunto valori nell'intervallo 10^3-10^6, dipendentemente dal tipo di nanostruttura metallica investigata. Le misure di fotoacustica effettuate su soluzioni colloidali di nanoshell d'oro si sono rivelate in accordo con le predizioni teoriche di letteratura.

Nella seconda parte del lavoro, i substrati plasmonici, realizzati principalmente con nanoparticelle e nanoshell d'oro, sono stati impiegati per la realizzazione di sensori SERS per la rivelazione di specie chimiche e biologiche.

É stato realizzato un sensore di composti tossici aromatici volatili, accoppiando un substrato plasmonico con un film poroso di sol gel ibrido organico-inorganico. La componente organica della matrice sol gel è stata appositamente scelta per la sua alta affinità a composti aromatici, quali lo Xilene. È stata dimostrata l'amplificazione dei segnali della matrice da parte della componente plasmonica, ma si sono riscontrati alcuni problemi nella rivelazione delle molecole di analita attraverso il SERS. La difficoltà nella rivelazione è probabilmente dovuta al veloce deadsorbimento dello Xilene dalla matrice a causa del forte riscaldamento locale causato dalla radiazione laser. Nonostante questo, si è comunque dimostrata l'aumentata efficienza del sensore progettato, rispetto ai suoi componenti singoli.

La seconda applicazione studiata ha riguardato la realizzazione di un sistema analita-accettore innovativo, che può essere utilizzato per diverse applicazioni bioanalitiche; esso è basato sull'interazione tra un cromoforo diazobenzenico (HABA) e il suo anticorpo specifico. Alla base dell'applicazione si trova una proprietà interessante del suddetto cromoforo, che è quella di cambiare la sua struttura molecolare, passando da una forma azo alla forma idrazo, dopo aver interagito con il suo anticorpo specifico. Questa variazione nella struttura molecolare può essere sfruttata per la rivelazione dell'avvenuta interazione analita-accettore, mediante SERS.

Alcuni derivati di questo cromoforo sono stati sintetizzati e caratterizzati in modo da poter essere adsorbiti su un substrato SERS, che viene successivamente incubato in una soluzione di anticorpo. I segnali SERS della molecola di HABA sono risultati ben visibili sia sui substrati di nanoparticelle che di nanoshell d'oro. Purtroppo non è stato possibile rivelare la variazione strutturale del cromoforo, in quanto gli anticorpi, estratti in vivo da due coniglietti, inducono solo un parziale cambio di struttura, rendendo la rivelazione SERS alquanto difficile.

ABSTRACT

The field of Plasmonics deals with interaction processes between an electromagnetic radiation of appropriate wavelength and the conduction electrons of a metal. The induced collective oscillation of the electrons is called Plasmon Resonance. The Localized Surface Plasmon Resonance (LSPR) occur when the excitation involves surface electrons of nanostructures with dimensions less or comparable to the excitation wavelength. The excitation causes a strong enhancement of the local field around the metal nanostructure, which, combined with Raman Spectroscopy, could be very interesting for molecular sensing. The Raman technique is well known for providing a fingerprint spectrum of a given molecule, but has the great limitation of low sensibility. By adsorbing the analyte of interest on a plasmonic substrate in the region of enhanced local field, high detection sensitivity can be reached through Surface Enhanced Raman Spectroscopy (SERS).

The first part of the present work is focused on the synthesis and characterization of gold and silver nanoparticles (Au and Ag NPs) and gold nanoshells (Au NSs) and their exploitation for the realization of SERS substrates, both in colloidal solutions and on solid supports. Different metal nanostructures give the possibility to exploit the LSPR in a wide spectral range, from the Vis to the near IR. Their optical and morphological characterization is carried out with conventional techniques, like TEM, AFM, UV-Vis absorption and Surface Enhanced Raman Spectroscopy, and with a new characterization technique, rarely used in this research field: the Photoacoustic Spectroscopy. It provides information about the absorption contribution to the total extinction of a plasmonic nanostructure. From a rigorous measurement of the SERS enhancement factor and from Photoacoustic Spectroscopy data at different excitation wavelengths, some considerations could be done concerning the relation of far field extinction and near field SERS properties. SERS EF profile measurements on liquid and solid SERS substrates demonstrated the presence of hot spots. The solid SERS substrates were chemically stable, homogeneous and reproducible and showed EF values of about 10^4-10^5. In colloidal

solution, the EF values were about 10^3-10^6, depending on the metal nanostructure. Photoacoustic measurements performed on Au NSs in solution were in agreement with theoretical predictions found in literature.

In the second part of the work, the plasmonic substrates, realized with Au NPs and Au NSs, were used for the realization of label free SERS sensors, to detect toxic aromatic chemical species and biological molecules. A sensor for toxic volatile compounds, based on Au NPs and Au NSs substrates coupled with a porous organic-inorganic hybrid sol-gel matrix, was realized. The matrix was specifically chosen for exhibiting a high-affinity interaction to aromatic hydrocarbons. The enhancement activity of the Au NPs and Au NSs substrates on the sol gel matrix alone was demonstrated. Some problems in the xylene detection process through SERS were probably due to the fast matrix regeneration under the laser radiation. Although, the enhanced SERS efficiency due to the detection design was demonstrated.

Another application was based on the development of a novel label-receptor system, based on the cromophore 4-hydroxyazobenzene-2 carboxylic acid (HABA) and its specific antibody, to be used in bio-analytical applications. The interesting behaviour of the HABA dye relies in changing its tautomeric structure from an azo to a hydrazo form, thanks to the interaction with its antibody. This structural change can be exploited for SERS detection of the label-receptor interaction. Properly synthesized and characterized HABA derivatives were adsorbed onto SERS substrates, further incubated in the antibody solution. The HABA signals were well visible on both Au NSs and Au NPs substrates. No HABA change could be detected through SERS, because the antibodies extracted in vivo from two rabbits, do not cause the quantitative change of the HABA structure.

Chapter 1

INTRODUCTION

1.1 Motivations

The field of nanotechnologies has gained ever rising importance since the early 90s, where high technology and miniaturization became the key growing factor. During the years, new and unknown properties of nanostructured materials has been observed, described and exploited for high technology and innovative applications.

In this context, also the field of *Plasmonics* has developed as an important and challenging research field. It deals with an interesting property of nanostructured metal, properly excited with an electromagnetic radiation: the plasmon resonance [1,2]. This phenomenon results in interesting optical properties of absorption and scattering in the Vis - IR region and can be exploited for many applications, ranging from the energy storage for solar cells [3,4], organic photovoltaic [5,6], catalysis [7] optical limiting [8–10] and sensing [11,12]. The control over geometry, dimensions and morphology of the metallic structures can give the possibility to exploit the unique plasmonic properties in a wide spectral range, from the Vis to the IR [13–15].

The plasmonic properties are particularly interesting for sensing applications, which are, in most cases, based on the exploitation of the surface plasmon polaritons (SPPs), which can be described as coherent electron oscillations at the metallic surface, coupled to an exciting incident radiation. Two basic characteristics of this phenomenon are usually exploited in sensing literature:

- the variation of the plasmonic resonance due to a change in the local chemical environment,

- the strong enhancement of the local electromagnetic field around the metal nanostructure.

In the first case, the refractive index variation around the metal nanostructure, introduced by the presence of the analyte, causes the variation of the plasmonic resonance. This sensing approach is particularly used in the so called Surface Plasmon Resonance (SPR) sensors [11], based on propagating SPPs, i.e. electromagnetic radiation associated to the collective oscillation propagating in x and y direction along the interface between a metal and dielectric. The operator looks usually at variations in the reflectivity dips of extended solid surfaces.

In more recent works, instead, the sensing applications look at the variation of the localized surface plasmon resonance (LSPR) [16], present on metal nanostructures having dimensions smaller or comparable to the incident wavelength. In this case, the refractive index changes, causing the variation of the extinction band of nanostructures in solution or on solid substrates, can be monitored through UV-Vis absorption spectroscopy.

In the second case, the strong enhancement of the local electromagnetic field can be exploited to observe the analyte properties instead of the plasmonic ones. In particular, the sensing sensitivity of common spectroscopic techniques like IR [17], fluorescence [18] and Raman Spectroscopy [19], can be strongly improved.

The Surface Enhanced Raman scattering is, for sure, the most studied phenomenon in the enhanced spectroscopies research field. In fact, the Raman technique is very interesting, because it provides a specific fingerprint vibrational spectrum of molecular species, with narrow and well defined signals, contrary to other spectroscopic techniques. The drawback of the traditional Raman spectroscopy lies in the low detection sensitivity, related to the low Raman cross sections [20]. High amount of analyte is necessary to obtain a well defined Raman spectrum. The strongly enhanced local field, given by metal nanostructures, can help in improving the Raman signal intensities many orders of magnitude, reaching even single molecule detection levels [21]. The enhancement is particularly high in the interparticles space of interacting nanostructures forming so called *hot spots*. Depending on the metal, the morphology, the dimension and the nanostructure geometry, the enhancement of the local field, at different excitation wavelengths, can vary several orders of magnitude. To evaluate the performance of a given metallic nanostructure, it is common use, in literature, to quantify the so called SERS enhancement factor (EF), by measuring the SERS spectrum of a probe molecule adsorbed onto the metal and comparing it to a Raman reference [22–27]. This way of

characterizing the enhancement properties of a SERS substrate became a literature issue, because of the difficulty of finding a unique EF definition, and considering and justifying all the experimental parameters [28]. In fact, excitation wavelength, Raman setup, probe molecule and vibrational mode [29–31] chosen, play key roles in the EF determination. Moreover, it would be very interesting to find a direct relation between the plasmonic resonance extinction properties and the SERS local field ones, in order to develop some kind of expectation of the enhancement quality of a specific SERS nanostructure at a given excitation wavelength [32]. Few wavelength scanned studies were made principally on ordered arrays [33] and on hot spot dominated systems [32,34]. The issue on the connection between far field (extinction) and near field (SERS) properties of many metallic nanostructures, remains still an open question in literature.

The correct determination of the EF, together with the development of an enhancement expectation, observing the plasmonic resonance of a SERS substrate, can help in realizing high specific and sensitive molecular sensors, based on the detection through SERS. The SERS sensing research area is still very active in searching new materials and new methods for high chemical specificity and ultrahigh sensitivity. It is of great importance to be able to detect small amounts of species, ranging from toxic gas molecules for environment sustainability [35] to biomolecules for analytical medicine [36–38].

1.2 Aim of the work

In the present work easy and cheap, stable, reproducible and high performing SERS substrates for sensing applications will be realized, exploiting different metal nanostructures, in order to obtain plasmonic resonances in a wide spectral range. The SERS substrate is meant as metal nanostructure, either in liquid or deposited on a solid substrate. Silver and gold nanoparticles in solution give plasmonic resonances in the Vis region, around 400 and 520 nm, respectively, while with more complex systems the gold nanoshells, with silica core and gold outer shell, the plasmonic band can be tuned in the 600-1000 nm region. The SERS nanostructures, in liquid phase or randomly deposited onto a solid substrate, will be fully characterized: morphologically through TEM and AFM and optically through UV-Vis spectroscopy and SERS.

One of the principal aims of the work is the rigorous characterization of the SERS EF at different wavelengths, investigating also other important parameters in the EF determination,

like nanoparticles stability and aggregation and probe molecule concentration. Furthermore the EF profile will be compared with the extinction properties, in order to discuss a possible relation for the specific investigated SERS substrate. A non conventional spectroscopic technique will be introduced at this point in order to investigate if the absorption or the scattering contribution to the total extinction will influence the local field properties of the SERS substrates: the Photoacoustic Spectroscopy. In fact, it gives the possibility to separate the absorption contribution to the total extinction. This characterization is performed for the first time on gold nanoshells.

Finally, the well characterized SERS substrates will be exploited for two different sensing applications:

the realization of a toxic volatile compound (VOC) sensor, based on the interaction of the analyte with a high affinity sol gel matrix coupled to a plasmonic substrate, and the analyte detection through SERS,

the realization of a novel label-receptor system, based on a cromophore and its specific antibody, to be exploited as bio-analytical tool using SERS for the detection of the label-receptor interaction event.

1.3 Thesis overview

The thesis is divided into three main parts: the first concerning a theoretical introduction to Plasmonics and SERS, the second describing the synthesis and the characterization of different plasmonic nanostructures for the realization of SERS substrates, and the third reporting two different SERS sensing applications.

In Chapter 2 a brief introduction to the phenomenon of Surface Plasmon Resonance of metallic nanostructures is given, with the attention focused on the Localized Surface Plasmon Resonance phenomenon, which is the only one exploited in the experimental part of the work. The mathematical models for metal nanoparticles and nanoshells are explained.

In Chapter 3 theoretical aspects of Raman and Surface Enhanced Raman Scattering are described, in order to discuss the critical issues in literature concerning the determination of the SERS enhancement factor. At the end of the Chapter, the state of the art of SERS as sensing technique is reported, highlighting the challenging issues in this research area.

Chapter 4 introduces the experimental part of the thesis, describing the synthesis and morphological (TEM and AFM) and optical (UV-Vis absorption and SERS) characterization of different metal nanostructures in solution. These nanostructures are then used for the realization and characterization of SERS substrates, described in Chapter 5. In this Chapter a detailed EF characterization is performed for different structures in solution and on solid substrates. Furthermore the Photoacoustic characterization, performed on gold nanoshells in solution, is described.

Finally, in the application section, two different SERS sensing applications are shown (Chapter 6 and 7). Chapter 6 reports results on the realization of the VOCs sensor, while in Chapter 7 the realization of the novel label-receptor system for SERS detection of the label-receptor interaction is discussed.

At the end a brief overview of the thesis work will be given in the Conclusions (Chapter 8).

Chapter 2

SURFACE PLASMON RESONANCE OF METALLIC NANOSTRUCTURES

2.1 Introduction to the phenomenon of surface plasmon resonance

The basic physical phenomenon underlying all the results and discussion of the present work is the beautiful topic of plasmonic resonance. The discovery of new interesting aspects and the finding of some answers to issues which had been left unresolved, encouraged new groups to join the ever-growing field of plasmonics, which had his beginnings in the early 20th century. First observations of anomalous reflected light from a mirror with a diffraction grating on its surface by Wood in 1902 [39] followed a physical interpretation by Rayleigh in 1907 [40]. At the same time Gustav Mie published his famous paper on the scattering of light by small spherical particles using Maxwell's electromagnetic theory [41]. These phenomena were interpreted only later in terms of plasmons, which were firstly introduced by Pines in 1956 [42] to describe the quantum of elementary excitation associated with high-frequency collective electronic motion in a plasma. Surface plasmons were explained briefly after the introduction of plasmons in 1957 by Ritchie [43] as plasma modes in thin films corresponding to longitudinal charge density waves propagating at a metal/dielectric interface. Further, more detailed explanations were given after 1968 by Otto[44], Kretchmann and Raether [45].

Plasmonics became, since then, a major part of the field of nanophotonics, which describes how the electromagnetic field can be confined over dimensions on the order of or smaller than the wavelength of light. It deals, in general, with the interaction processes between electromagnetic radiation and conduction electrons in a metal. In fact, metallic structures can be seen as a plasma of free electrons in the conduction band whose charge is neutralized by positive ions, i.e. the nuclei and the core-electrons.

When an electromagnetic radiation with defined wavelength λ_L interacts with the metallic system, provided certain boundary conditions (to be specified later) are fulfilled, the free electron cloud in the conduction band will oscillate with respect to the fixed positive ions. The phenomenon of collective oscillation of the conduction electrons of a metal at the interface with a dielectric is called Surface Plasmon Resonance (SPR). These charge density waves cannot exist without being associated with a transverse electromagnetic wave (a photon). This then corresponds to a mixed mode where the energy is shared between the charge density wave (plasmon) and the electromagnetic wave (photon), and they should therefore be called surface plasmon polaritons (SPPs).

The SPPs can be of two different types, according to the metallic substrate and the resonance conditions:

- Propagating Surface Plasmon Polaritons (PSPPs)
- Localized Surface Plasmon Polaritons (LSPPs)

The difference between these two resonances is represented in Figure 2.1 [16], and lies substantially in the nature of the surface plasmon oscillation.

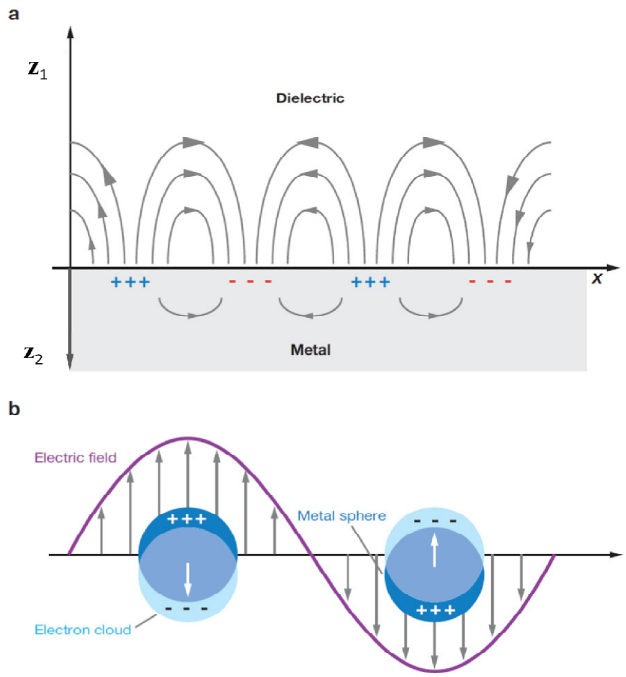

Figure 2.1: Schematic representation of (a) Propagating Surface Plasmon Polaritons and (b) Localized Surface Plasmon Polariton [16]

In the case of PSPPs, the electromagnetic radiation associated to the collective oscillation of the conduction electron, is propagating in *x* and *y* direction along the interface between a metal and a dielectric. This propagation runs for distances on the order of tens to hundreds micrometers in *x* an *y* direction and decays exponentially in the z-direction (z_1 through the dielectric and z_2 through the metal) with 1/*e* decay lengths on the order of hundreds of nanometers.
In the case of LSPPs, instead, light interacts with structures much smaller than the incident wavelength, which leads to the generation of a local plasmon oscillation within the nanoparticle.

In this chapter we will explain briefly the common physical explanation of the two SPRs phenomena with the final aim to better understand how the plasmonic resonance changes with material type, dimension and morphology and with the environment. The SPR mechanisms will then be treated separately, in much more detail. Nevertheless, the chapter content will principally focus on the LSPR phenomenon, which is the only one treated in the experimental part of the work.

2.1.1 Dielectric function of metals

A great role in the understanding of the surface plasmon resonance phenomenon is played by the dielectric function of the investigated system, as will be demonstrated in the later paragraphs. In fact, the optical properties of bulk materials are characterized by this physical quantity. Let us, therefore, begin with the definition of the dielectric function of a free electron gas by Drude, which represents a good model for describing the conduction electrons of metals [46,47]:

$$\varepsilon_D(\omega) = 1 - \frac{\omega_p^2}{\omega^2 + i\gamma\omega} \tag{2.1}$$

where γ is the characteristic collision rate responsible for damping of electron oscillations and ω_p is the plasma frequency of the free electron system defined as:

$$\omega_p = \sqrt{\frac{ne^2}{\varepsilon_0 m}} \tag{2.2}$$

where n is the conduction electron density, e is the elementary charge, ε_0 is the permittivity of free space and m is the electron mass. The plasma frequency is the characteristic frequency

of electron oscillation and plays a central role in the description of the optical properties of metals. Light of frequency above the plasma frequency is transmitted, because the electrons cannot respond fast enough to screen it. Light of frequency below the plasma frequency ($\omega < \omega_p$) is reflected, because the electrons in the metal screen the electric field of light.

The complex dielectric function can be split into real and imaginary components, which describe respectively the refracting and absorbing properties of the material. The total dielectric function can be written as

$$\varepsilon(\omega) = \varepsilon_1(\omega) + i\varepsilon_2(\omega) \tag{2.3}$$

and the different parts described as follow:

$$\varepsilon_1(\omega) = Re(\varepsilon(\omega)) = 1 - \frac{\omega_p^2}{\omega^2 + \gamma^2} \tag{2.4}$$

$$\varepsilon_2(\omega) = Im\big(\varepsilon(\omega)\big) = \frac{\omega_p^2 \gamma}{\omega(\omega^2 + \gamma^2)} \tag{2.5}$$

γ is very small compared to ω, therefore, for frequencies close to ω_p, the real part of the dielectric function becomes zero (no refractive behavior), while the imaginary part tends to diverge (total absorbing behavior). In most metals, the plasma frequency is in the ultraviolet, making them reflective in the visible range. It is the region with $\omega < \omega_p$, i.e. where $Re\big(\varepsilon(\omega)\big) < 0$ and $Im\big(\varepsilon(\omega)\big)$ is relatively small, which is responsible for the interesting optical effects of metal, including the plasmon resonance phenomenon.

Figure 2.2 shows the real and imaginary parts of the dielectric functions in the UV to near IR region of silver and gold, which are the most common metals used in plasmonic research. The dielectric function is reported versus wavelength λ, where $\lambda = 2\pi c/\omega$, in the $\omega < \omega_p$ spectral region.

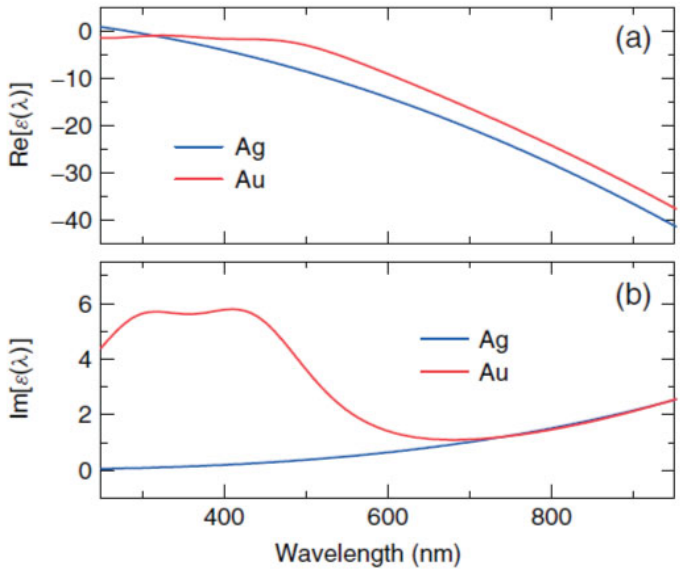

Figure 2.2: (a) Real and (b) imaginary part of the dielectric function of silver (blu line) and gold (red line) [48]

The Drude model of the dielectric function has some limitations in case of gold. In the short wavelengths Vis range the behavior of gold is completely altered by interband transitions, which lead to an increase in $\varepsilon_2(\omega)$, i.e. bound electrons optically excited to a higher energy band. Their contribution, described as $\varepsilon_b(\omega)$ should therefore be added to the free electron contribution of the Drude model. In case of silver, instead, the interband transitions occur at energies in the UV region, much higher than the plasma frequency. Their contribution, in this case, is simply constant and real in the visible region and the expression reduces to the Drude model.

The difference between the imaginary part of the dielectric function of the two metals in the short wavelength Vis region is the principal reason for the higher SERS efficiency of Ag, compared to Au, as will be demonstrated later.

The dielectric function description is the starting point for explaining the two different SPR mechanisms, mentioned above. In the next paragraph the dispersion relation of different plasmon modes are described in order to introduce surface plasmon polariton modes.

2.1.2 Dispersion relations of plasmon modes

Elementary excitations or modes in infinite systems with translational invariance can be described as propagating plane waves, where the electric field has a oscillatory dependence of the form (complex notation) [47]:

$$\boldsymbol{E}(t) = \boldsymbol{E}_0 \exp(i\boldsymbol{k}\boldsymbol{r} - i\omega t) \tag{2.6}$$

Such solutions exist only for specific values (eigenvalues) of ω and $\boldsymbol{k}$. These solutions can usually be described by one or more dispersion relations ω ($\boldsymbol{k}$).

One can distinguish two situations in isotropic and homogeneous media:

- $\boldsymbol{E} \parallel \boldsymbol{k}$ everywhere ($\boldsymbol{k} \times \boldsymbol{E} = 0$). This is called a longitudinal mode or wave.
- $\boldsymbol{E} \perp \boldsymbol{k}$ everywhere ($\boldsymbol{k} \cdot \boldsymbol{E} = 0$). This is called a transverse mode or wave.

The name of the modes refer to the orientation of $\boldsymbol{E}$ with respect to the direction of propagation $\boldsymbol{k}$.

In case of an infinite physical system in vacuum the electromagnetic modes are derived easily from Maxwell's equations and are then transverse propagating plane waves characterized by a wavevector $\boldsymbol{k}$ and frequency ω, related by the dispersion relation: $\omega = c|\boldsymbol{k}|$.

Similar as for a transverse electromagnetic wave in a medium with dielectric function $\varepsilon(\omega)$ and refractive index, the dispersion relation is modified to give:

$$\omega^2 = \omega_p + \frac{c^2}{\varepsilon_\infty} k^2 \tag{2.7}$$

where ε_∞ is the constant real background dielectric function ($\varepsilon_\infty > 1$).

Such an electromagnetic wave creates in the medium an internal polarization wave:

$$\boldsymbol{P} = \varepsilon_0(\varepsilon(\omega) - 1)\boldsymbol{E} \tag{2.8}$$

These transverse modes are called polaritons because they couple transverse electromagnetic excitations (photons) with an internal polarization $\boldsymbol{P}$, which originates physically from internal excitations of the medium, such as plasmons. For metals, in the region where the optical response is dominated by the free-electron plasma, these modes are usually called bulk plasmon polaritons and are quasi-particles. There are no macroscopic charge density oscillations. The corresponding waves are evanescent. From Figure 2.3 one sees that bulk plasmon polariton modes occur only for energies larger than the plasmon frequency (solid black curve). For most metals, these modes are therefore in the UV, or even deep UV.

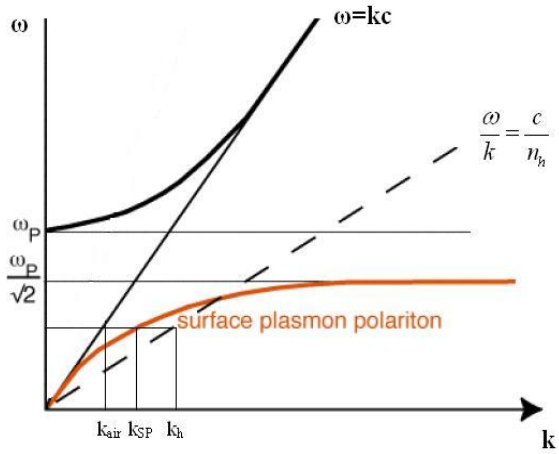

Figure 2.3: Dispersion relation curves of an electromagnetic mode of the incident radiation in vacuum (black straight line), for the bulk plasmon polariton (black curve), for surface plasmon polaritons (red curve) and modified dispersion relation of the incident excitation radiation (dashed black line)

As can be observed in Figure 2.3 the excitation of the bulk plasmon polariton is not permitted in vacuum, because the dispersion curve of the incident light (black straight line) does not intersect the dispersion curve of the bulk plasmon polariton (black curve).

The presence of an interface (typically metal/dielectric) gives rise to a new family of electromagnetic modes, which are much more interesting for SERS and plasmonics. These additional modes are called bound modes or surface modes. In the case of metals, they are called surface plasmon polaritons (SPPs). These electromagnetic surface modes are transverse inside and outside the metal (because $\varepsilon(\omega) \neq 0$). They present, however, also a longitudinal component because of the discontinuities at the interface, and are in this sense also partly longitudinal surface plasmon waves. The characteristics of these modes depend not only on the optical properties of the metal, but also on that of the dielectric forming the interface.

Also in this case the dispersion curve of the light in vacuum does not cross the surface plasmon polariton modes: for a given excitation radiation energy, the wavevector of the surface plasmon polariton (k_{SP}) is always higher than the wavevector of the incident light (k_{air}). The conservation condition of the ***k*** momentum cannot be fulfilled [49].

For the excitation of such surface plasmon polariton modes the only possibility is to change the boundary conditions for solving the Maxwell's equation for this problem, changing the dispersion curve for the incident radiation (black dashed line). This mechanism can give rise to the so called Propagating Surface Plasmon Polaritons, which are described in the following section.

2.3 SPR of massive materials: Propagating Surface Plasmon Polaritons

The exact nature of each plasmon mode will depend on whether the wave-vector components k_x, k_{z1}, k_{z2} are real or complex.

As said berfore the SPPs at a massive metal/dielectric interface can be excited only under particular conditions. The most common methodologies for achieving this conditions are the Kretchmann and the grating configurations [46], which will be shortly discussed and are shown in Figure 2.4.

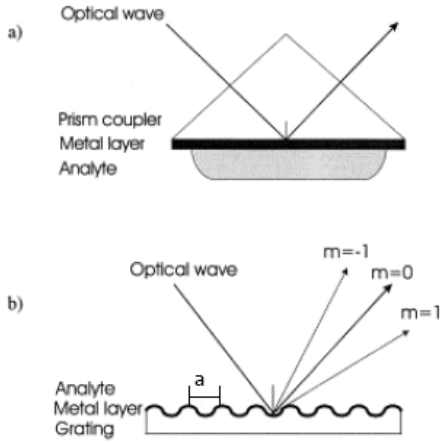

Figure 2.4: Kretschmann (a) and grating configuration (b) for the excitation of surface plasmon polaritons.

The Kretchmann configuration is used for exciting SPPs on a flat metallic surface. In this case a material with refractive index greater than the air is placed on the flat surface in order to change the above mentioned boundary conditions. Commonly, a prism is used on a thin metallic film: the SPP can be excited on the thin metallic surface generating an evanescent wave.

The momentum conditions which have to be verified can be described through the following equation:

$$k_x = \frac{\omega}{c}\left(\frac{\varepsilon_m \varepsilon_d}{\varepsilon_m + \varepsilon_d}\right)^{1/2} = \frac{\omega}{c}\sqrt{\varepsilon_d}\,\mathrm{sen}\vartheta \qquad (2.9)$$

where ε_m and ε_d are the dielectric function of the metal and the environment, respectively and ϑ is the incident angle with respect to the normal of the interface.

In Figure 2.4 (b) another configuration is depicted, which describes the exitation of SPPs through the realization of a metallic greating. For this case the momentum conservation conditions are verified when

$$k_x = k_{SP} \pm m\left(\frac{2\pi}{a}\right) \quad (2.10)$$

with m=0,1,2…

A mode will correspond to a propagating wave along a given direction if its wave-vector k_x along this direction is real. k_{z1}, k_{z2} are, instead, imaginary and therefore correspond to evanescent waves perpendicular to the surface (with an exponential decay of the intensity). In general, the propagating SPPs are excited for $Re[\varepsilon_m(\omega)] < -\varepsilon_d$. The frequency of the SPPs modes approaches for large k_x the limiting frequency $\omega_{SP} < \omega_p$ corresponding to the conditions $\varepsilon_m(\omega_{SP}) = -\varepsilon_d$. These are non-radiative surface modes that are fully trapped at the surface and propagate along the interface. The propagating surface charge density wave at the surface corresponds to a longitudinal surface plasmon wave, where energy is shared between photon and surface plasmon oscillations.

The main parameters that can be varied in a typical experiment are the wavelength λ, the angle of incidence ϑ and the dielectric constant of the outside medium ε_d. For PSPPs modes, the resonances can be extremely sharp and therefore sensitive to the parameters under study. For this reason such SPRs were often exploited for sensing applications.

2.4 SPR of metal nanoparticles: Localized Surface Plasmon Polaritons

The description of surface plamon polaritons in the planar approximation is no longer valid for small metallic objects, when the size becomes comparable or smaller than the excitation wavelength. The description of the electromagnetic modes of the system in terms of k vector becomes irrelevant, according to the relation $|k| = 2\pi/\lambda$, when λ becomes smaller than the physical dimensions of the nanoparticle. The electromagnetic modes then exist for discrete values of ω instead of continuous modes described by a dispersion relation $\omega(k_x)$ and do not propagate at all. These modes are then called localized surface plasmon polaritons (LSPPs) and arise when $-\varepsilon_d < Re[\varepsilon_m(\omega)] < 0$.

2.4.1 Spherical nanoparticles: Mie model

To better understand the nature of this kind of electromagnetic modes in simple terms, it is useful to consider briefly the problem of a small metallic sphere interacting with an electromagnetic field, already described by Mie in 1908 [41]. The simplest treatment of this problem is to consider a sphere much smaller than the wavelength of the incident beam,

immersed in a medium with dielectric constant ε_d. Mie solved the Maxwell equations for the extinction and scattering of an electromagnetic radiation interacting with a small metallic sphere. With appropriate boundary conditions the solutions of the problem could be described as multipolar oscillations. One can distinguish two different situations depending on the particle dimensions: the dynamic ($2r \sim \lambda$) and the quasistatic regime ($2r << \lambda$)[1,46,47], as depicted in Figure 2.5.

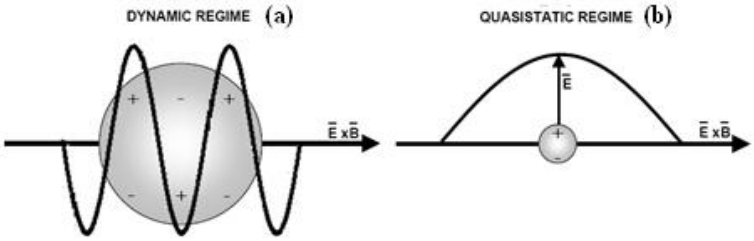

Figure. 2.5: Interaction **s**cheme of an electromagnetic radiation with (a) metal nanoparticles with dimensions comparable and (b) dimensions less than the excitation wavelength.

The most important surface mode in most cases is the lowest frequency one, whose scattered field is that of an electric dipole and it is, therefore, a radiative mode. For larger nanoparticles other surface modes can exist at increasing frequencies, with quadrupolar, octupolar, etc. nature, but they are usually less relevant. They are also radiative modes, but with a larger absorptive character than the dipolar modes (i.e. the proportion of losses through absorption, as opposed to radiation, is larger).

For the quasistatic regime, the complex electric field inside the sphere is constant and proportional to the incident field E_0:

$$E_{\mathrm{sph}} = \frac{3\varepsilon_d}{\varepsilon(\omega) + 2\varepsilon_d} E_0 \qquad (2.11)$$

The resonance conditions can be understood by looking at the denominator of this expression. When it approaches the value zero for $\varepsilon(\omega) = -2\varepsilon_d$, the whole expression becomes very large. This condition is possible for metals if the absorption is small ($Im\left(\varepsilon(\omega)\right) \approx 0$) and $Re\left(\varepsilon(\omega)\right) \approx -2\varepsilon_d$. The optical response (absorption and scattering) at this particular frequency is then very large and is called Localized Surface Plasmon Resonance (LSPR). As can be observed, this resonance conditions are strongly linked to the metal, the geometry and the dielectric environment.

The same resonance conditions can be observed looking at the expressions for the extinction and scattering cross section described by Mie [1]:

$$\sigma_{sca}(\omega) = 2\left(\frac{2\pi}{\lambda}\right)^4 V \left(\frac{\varepsilon_1(\omega) - \varepsilon_d}{\varepsilon_1(\omega) + 2\varepsilon_d}\right)^2 \quad (2.12)$$

$$\sigma_{ext}(\omega) = 9\frac{2\pi}{\lambda}\varepsilon_d^{3/2} V \frac{\varepsilon_2(\omega)}{[\varepsilon_1(\omega) + 2\varepsilon_d]^2 + \varepsilon_2(\omega)^2} \quad (2.13)$$

From the relation $\sigma_{abs} = \sigma_{ext} - \sigma_{sca}$, using Equation 2.12 and Equation 2.13, the absorption cross section can be calculated. V is the particles volume, ω the frequency of the excitation wavelength, ε_d and $\varepsilon(\omega) = \varepsilon_1(\omega) + i\varepsilon_2(\omega)$ the dielectric constant of the environment and the complex dielectric function of the metal, respectively.

Some experiments in literature showed that, for metallic spheres below the diameter of about 9 nm, the plasmonic extinction band is damped and broadened and even disappears for dimensions less than 2 nm, as can be observed from Figure 2.6 [50].

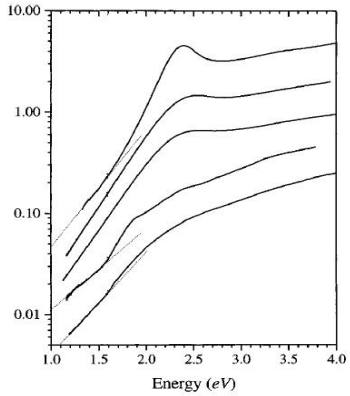

Figure. 2.6: Extinction spectra of colloidal gold nanoparticles with different diameters. From top to bottom: 9, 3.2, 2.5, 1.7, 1.4 nm [50]

This behavior is related to the mean free path of the electrons in the metallic particle. For bulk gold and silver this value is around 40-50 nm and therefore much bigger than the nanoparticle itself. In this case the electron-surface scattering becomes important: the electrons at the metallic surface scatter in an elastic and completely random way inducing a fast loss of the plasmonic oscillation coherence. The smaller the metal sphere the faster the coherence loss and the bigger the band broadening. This phenomenon is called intrinsic size effect. The Mie theory can be slightly modified by assuming the dielectric function of the metal now dependent on the dimensions of the system $[\varepsilon(\omega, r)]$, which has to be considered for a better

understanding of the behavior of small metallic particle. The dielectric function can be rewritten as:

$$\varepsilon(\omega) = \varepsilon_{IB}(\omega) + \varepsilon_D(\omega) \tag{2.14}$$

where $\varepsilon_{IB}(\omega)$ accounts for the core electrons and $\varepsilon_D(\omega)$ for the conduction electrons:

$$\varepsilon_D(\omega) = 1 - \frac{\omega_p^2}{\omega^2 + i\gamma\omega} \tag{2.15}$$

where ω_p is the plasma frequency described by Equation 2.2 and γ is a damping parameter. For a small nanoparticle this damping parameter can be written as:

$$\gamma(r) = \gamma_0 + \frac{Av_F}{r} \tag{2.16}$$

where

$$\gamma_0 = \frac{1}{\tau_{e-e}} + \frac{1}{\tau_{e-ph}} + \frac{1}{\tau_{e-d}} \tag{2.17}$$

is the damping parameter for a bulk material described in terms of lifetimes for the different electron scattering processes (electron-electron, electron-phonon and electron-defect). In fact one has to add another electron-surface contribution to the bulk damping parameter, which depends on a scattering parameter A and on the Fermi velocity v_F. For a perfect gas of free electrons one can approximate $\gamma \ll \omega$ and $\gamma(r)$ represents the width of the plasmonic band with a dimension dependence of $1/r$ for the intrinsic regime.

For particles with dimensions comparable with the excitation wavelength, the dipolar approximation is no longer valid. The plasmonic resonance phenomenon becomes explicitly dependent on the particle dimensions. This is called *extrinsic size effect*. Higher order modes exist at higher frequencies and therefore appear at wavelengths which are blue shifted with respect to the dipolar band (particularly for silver). On the other hand, at even higher particle dimensions the dipolar band red shifts and broadens because of radiation/retardation effects: at higher dimensions, scattering, begins to dominate over absorption, causing an energy loss and therefore a damping. This size dependent optical response is illustrated in Figure 2.7 for Ag and Au spheres in water.

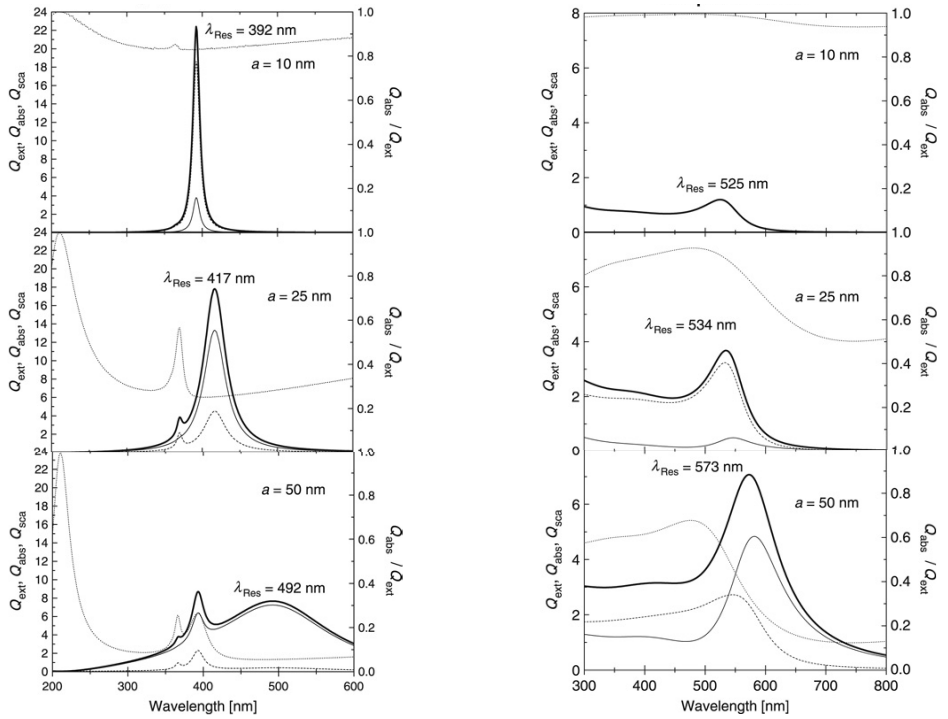

Figure 2.7: Calculated far field properties of silver (left) and gold (right) spheres of varying radii in water as a function of incident wavelength: extinction coefficient Q_{ext}^{NP} (thick solid lines), absorption coefficient, Q_{abs}^{NP} (dashed lines), scattering coefficient, Q_{sca}^{NP} (thin solid lines). Also shown is the ratio $Q_{abs}^{NP}/Q_{ext}^{NP}$ (dotted lines) [47].

The width of the plasmonic band Γ is related to the total dephasing time T_2 through:

$$\frac{1}{T_2} = \pi c \Gamma = \frac{1}{2T_1} + \frac{1}{T_2^*} \tag{2.18}$$

T_1 describes the population relaxation time and T_2^* is the pure dephasing time which may originate from collisions that change the plasmon wave vector but not its energy.

This type of broadening of the band has not to be confused with the broadening due to the presence of a poly-dispersed distribution of particle dimensions.

Moreover, as said before, the chemical environment plays an important role in the frequency dependence and width of the LSPR band. Persson [51] developed a model known as *chemical interface damping* (CID), where the LUMO of an acceptor molecule on the nanoparticle surface couples with the free electrons of the conduction band of the metal: the smaller the energy difference between donor and acceptor, the stronger the coupling. In the case of LSPPs excitation, electron transfer between the two levels could occur causing a loss of coherence of the electron oscillation, which results in a plasmonic band shift and broadening. For different molecules with different electronic structures the values of band shift and broadening will be different.

2.4.2 Elongated nanoparticles: Gans Model

Another important factor in understanding the LSPR band is the role of geometry, that is the shape of the nanoparticles.

The Gans model is, in fact, an extension of the Mie model for spheroid nanoparticles in dipolar approximation regime. The extinction cross section is described as [1]:

$$\sigma_{ext}(\omega) = \frac{2\pi}{3\lambda}\varepsilon_d^{3/2} V \sum_j \frac{(1/P_j^2)\,\varepsilon_2}{\left\{\varepsilon_1 + \left[(1-P_j)/P_j\right]\varepsilon_d\right\}^2 + {\varepsilon_2}^2} \tag{2.19}$$

where $j = A, B, C$ denotes the axes of the spheroid and

$$P_A = \frac{1-e^2}{e^2}\left[\frac{1}{2e}\ln\left(\frac{1+e}{1-e}\right) - 1\right] \tag{2.20}$$

$$P_B = P_C = \frac{1-P_A}{2} \tag{2.21}$$

$$e = \left[1 - \left(\frac{B}{A}\right)^2\right]^{1/2};\ \frac{B}{A} = \frac{1}{R} \tag{2.22}$$

The SPR response is dominated by two bands, one for every electron oscillation mode along the two main axes, one transverse and the other longitudinal, as shown in Figure 2.8.

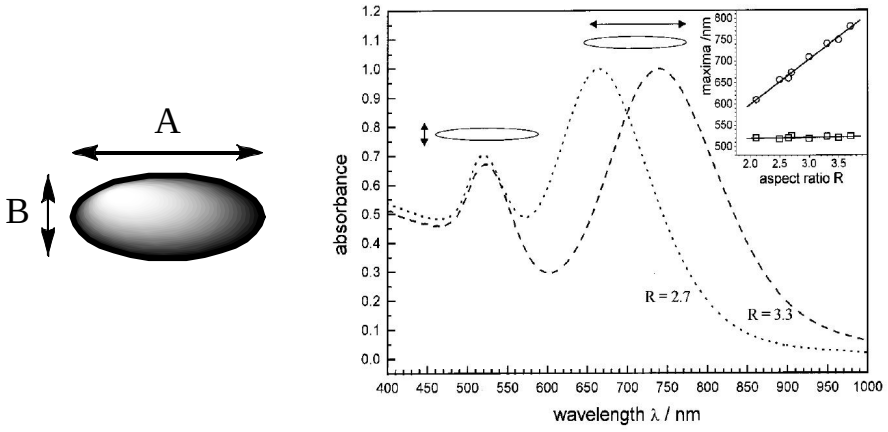

Figure 2.8: Extinction spectra of two different nanorod samples with different R values in solutions. The inset shows the dependence of the peak value on the aspect ratio R [1].

As can be observed in the inset of Figure 2.8, the aspect ratio of the metal nanorods plays an important role in the wavelength position of the SPR bands. At higher R the energy separation between the two bands increases: the band at lower wavelengths remains constant (transverse mode), while the other band (longitudinal mode) red shifts.

2.4.3 Interacting nanoparticles: Maxwell-Garnett model

Mie theory holds for nanoparticles in solution or solid matrix at low particle concentration assuming no interaction between particles. This is no longer valid in case of high particle concentration, when the interparticle distance becomes small. The LSP modes of each object then interact with each other and form hybridized modes, in a similar fashion to atomic orbitals. In the simplest dipolar approximation, we can take linear combinations of the two separate responses, which can be added in phase or out of phase, like for bonding and anti-bonding electronic interactions in molecular systems.

In the simplest case of a nanoparticles dimer, considering the incident radiation perpendicular and the polarization parallel to the dimer axis, we obtain the maximum coupling between the two LSPRs. The resulting resonance is strongly red-shifted and a new band at lower wavelengths appears, like in the nanorod case described through Gans theory. Lower distance between particles causes stronger interaction with a more pronounced red shift. The band at lower wavelengths corresponds to higher order LSPRs. The absence of these secondary resonances in Au compared to Ag is probably due to the much larger intrinsic absorption of Au below 600 nm. The local field in the gap between nanoparticles is strongly enhanced and is called *hot spot*, which is commonly exploited for SERS applications. Small changes in the gap distance (of only 1 nm) can cause differences of several orders of magnitude in the SERS enhancement factor (EF) (Chapter 3).

In case of aggregates of more nanoparticles in a transparent medium, we can introduce the Maxwell-Garnett theory, which is based on the equation of Clausius-Mossotti and describes an effective complex dielectric function ε_C through [1]:

$$\frac{\varepsilon_c - \varepsilon_d}{\varepsilon_c - \kappa\varepsilon_d} = f_m \frac{\varepsilon_m - \varepsilon_d}{\varepsilon_m + \kappa\varepsilon_d} \tag{2.23}$$

ε_d and ε_m are the dielectric functions of the environment and the metal nanoparticles, respectively. f_m is the volume fraction of the metal nanoparticles in the whole sample and κ is a screening parameter describing the geometry of the nanoparticles: it has a value of 2 for spherical nanoparticles and 1 for spheroids oriented with the longitudinal axis parallel to the incident excitation radiation.

2.5 SPR of metal nanoshells: hybridization model

A very interesting metal nanostructure presenting a particular LSPR optical response is the nanoshell, composed by a dielectric core and a metal outer shell [52]. The wavelength position

of the plasmonic band is no longer dependent on the final particle dimension, as for gold nanoparticles, but on the ratio between core and shell dimensions. The LSPR can therefore be tuned from the visible to the near IR by simply changing the synthesis conditions: at fixed core dimension one can change the metal quantity to realize shells with different thicknesses, as can be shown in Figure 2.9 for gold nanoshells.

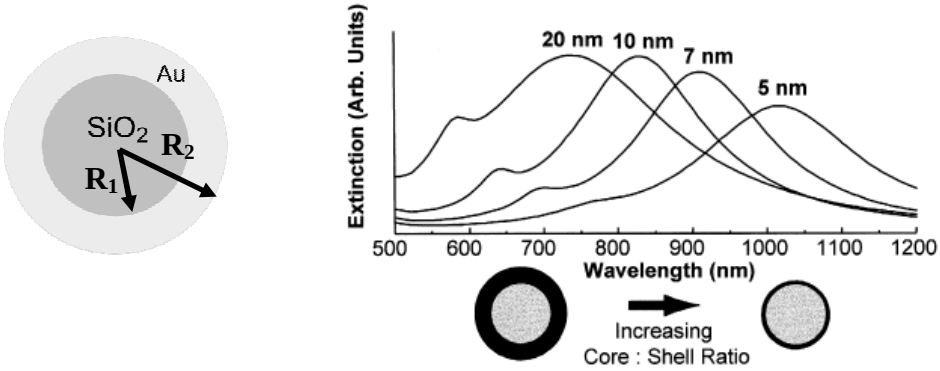

Figure 2.9: Extinction spectra of different nanoshell samples with different core to shell ratio [52].

This surface plasmonic resonance phenomenon was initially described through an extension of the Mie theory in the quasi-static regime considering a combination of two concentric spheres of different materials [53].

In 2003 Prodan et al.[54] developed another mathematical model, known as *hybridization model*, which considers the plasmonic responce of a metal nanoshell as combination of a nanoshpere and a nanocavity, as depicted in Figure 2.10 [55].

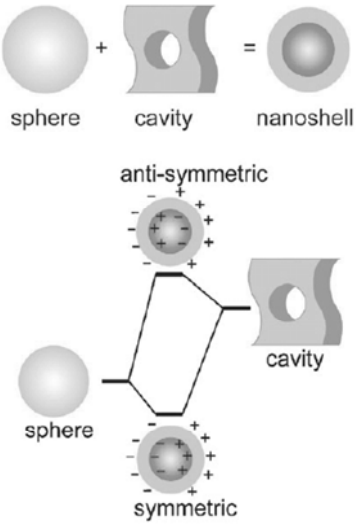

Figure 2.10: Scheme of the hybridization model describing the plasmonic properties of metal nanoshells [55].

The sphere and cavity plasmons are electromagnetic excitations that induce surface charges at the inner and outer interfaces of the metal shell. Because of the finite thickness of the shell layer, the sphere and cavity plasmons interact with each other. The strength of the interaction between the sphere and cavity plasmons is controlled by the thickness of the metal shell layer. The interaction results in the splitting of the plasmon resonances into two new resonances: the lower energy symmetric plasmon and the higher energy antisymmetric plasmon. The inner radius of the shell is described through R1, while the outer radius trough R2. The electron gas deformations can be decomposed as spherical harmonics of order *l*. The plasmon frequencies for the sphere (ω_s) and cavity (ω_c) can be written as:

$$\omega_{c,l} = \omega_B \sqrt{\frac{l+1}{2l+1}} \; ; \; \omega_{s,l} = \omega_B \sqrt{\frac{l}{2l+1}} \tag{2.24}$$

ω_B is the bulk plasmon frequency.

The interaction of the plasmons of the inner and outer surfaces of the shell gives rise to two hybridized plasmon modes $\omega_+\rangle$ and $\omega_-\rangle$ for each l>0. The frequencies of these modes are:

$$\omega_{l\pm}{}^2 = \frac{\omega_B^2}{2}\left\{1 \pm \frac{1}{2l+1}\sqrt{1 + 4l(l+1)\left(\frac{R1}{R2}\right)^{2l+1}}\right\} \tag{2.25}$$

The $\omega_+\rangle$ mode corresponds to antisymmetric coupling between sphere and cavity modes and the $\omega_-\rangle$ mode corresponds to the symmetric coupling. The mode at lower energy $\omega_-\rangle$ interacts strongly with the incident field, while the other mode at higher frequency $\omega_+\rangle$ is damped by interband transitions.

2.6 Plasmonics of complex systems: Discrete Dipole Approximation

For much more complex geometries, it is not possible to solve the Maxwell's equation in an analytical way. For this reason, a numerical method is commonly used, known as discrete dipole approximation (DDA). The sample is seen as a cubic array of N polarizable points, i.e. of N different dipoles. The idea is depicted in Figure 2.11.

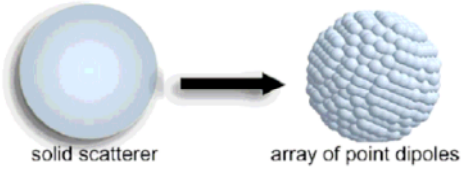

Figure 2.11: Scheme of discrete dipole approximation numerical method.

The polarization induced on every point j at the position $\boldsymbol{r}_j$ with polarizzability α_i is described through [56]

$$\boldsymbol{P}_j = \alpha_i \boldsymbol{E}_{loc}(\boldsymbol{r}_j) \tag{2.26}$$

where the local field is the sum of the electromagnetic incident field with an interaction term with all the nearby dipoles.

This numerical method gives the possibility of calculations with errors within only 10%.

2.6 Summary: PSPPs vs. LSPPs and Gold vs. Silver for SERS applications

At the end of this chapter, based on the description of the optical properties of nanostructured metal and on the theory of the surface plasmon resonance, it is useful to highlight the most important aspects in order to better understand the next chapters, based on SERS applications.

At first we want to make a brief comparison between PSPPs and LSPPs in order to explain why our work is principally based on the last one:

- The PSPR condition requires conservation of both k_x and ω. This is more difficult to fulfill than only ω conservation for LSPR. In particular k_x conservation requires a more complex setup, such as the ATR configuration.
- The PSPR offers more freedom in the implementation, either in terms of angle- or wavelength modulation, whereas only wavelength-modulation can be used for LSPR.
- PSPR are typically much sharper compared to LSPRs ones. It should in principle result in a larger sensitivity but only on a more limited range of parameters. For SERS, resonances must be broad enough to encompass both the exciting laser and the Stokes frequencies (see Chapter 3). PSPRs are typically too sharp to fulfill that condition.
- The active surface for PSPRs is a single planar interface, while for LSPRs it is the nanoparticle surface, which can therefore be spread in a 3D volume.
- There are more degrees of freedom to tailor or engineer the LSPRs (shape, size, etc.) as opposed to the SPRs, which may open more possibilities, but also more problems.
- The local field intensity enhancement factor is the same everywhere on the surface in case of PSPPs. This is no longer the case for NPs, where the LFIEF is expected to be non-uniform on the surface. In addition, LSPPs are usually radiative modes, which therefore introduces an additional mechanism of energy loss.

Beside this discussion, we want to focus our attention on the LSPR phenomenon and compare the optical properties of gold and silver. Firstly, the main (dipolar) LSPR of a small sphere in the quasi-static approximation, described by the condition $\varepsilon(\lambda_{res}) \approx -2\varepsilon_d$, occurs at a longer wavelength for gold (~ 520 nm in water) than for silver (~ 400 nm in water). The dipolar LSPR is much weaker and much broader for gold. Moreover, the radiation/retardation effects (red-shift and broadening of the resonance) are much less evident for gold. The reason for these is that the metal-like optical properties of gold are strongly affected, at shorter wavelengths ($\lambda < 600$ nm), by a large optical absorption, i.e. $\mathrm{Im}(\varepsilon)$ is large for gold in this region, as shown in Figure 2.2. This strong optical absorption damps significantly the LSP resonances that occur in this region. This explains the large discrepancy in the strengths of the dipolar LSPRs between gold and silver. If, instead, the LSPR for gold is sufficiently red-shifted (to over 570 nm) the performance of the two metals becomes comparable. This is, for example, the case of metal aggregates with presence of hot spots.

Gold remains nevertheless the more convenient metal in terms of chemical stability and versatility.

Chapter 3

SURFACE ENHANCED RAMAN SPECTROSCOPY AND MOLECULAR SENSING

3.1 Introduction

Surface Enhanced Raman Spectroscopy is a very interesting technique for sensing applications. Despite the high selectivity, provided by the fingerprint Raman scattering spectrum of the analyte, high sensitivity can be reached by properly matching the LSPR of the SERS substrate with the excitation wavelength used for Raman Spectroscopy. At the beginning of SERS, first predictions assume that the LSPR of the metallic substrate, probed by UV-Vis absorption spectroscopy, should be close to the excitation wavelength, in order to reach the highest local field enhancement and therefore highest SERS sensitivity[57]. Many works, done during the years up to recent literature, show, instead, that a systematic study of the relationship between far field extinction and near field enhancement properties had not been completed. Different plasmonic substrates and a large variety of different analytes opened new questions, which have not find answers yet.

In this Chapter we want to explain the Raman Scattering phenomenon and to extend the description, for introducing the Surface Enhanced Raman Spectroscopy technique in order to lay the foundations for better understanding of interesting experimental results.

3.2 Traditional Raman Spectroscopy

Optical Spectroscopies deal with phenomena that originate from the interaction between the electric field of an electromagnetic radiation with matter. In 1928 the Indian scientists C. V. Raman and K. S. Krishnan observed for the first time the inelastic scattering from a sample

after irradiation with sunlight[58]. This experiment became the starting point for Raman Spectroscopy, which observe the phenomenon of light diffusion by matter either in gaseous, liquid or solid state (amorphous or crystalline).

The Raman Spectroscopy experiments are generally performed by irradiating a sample with an electromagnetic radiation with frequency ν_L (in the UV-VIS-IR wavelength range) and measuring the diffused frequency ν_S at a defined angle ϑ with respect to the incident light direction. The light diffused at the same frequency as the incident radiation is called elastic Rayleigh scattering, while the one at a different frequency is called inelastic, Raman scattering. In Figure 3.1 a molecular energy diagram with illustration of four different scattering processes is shown.

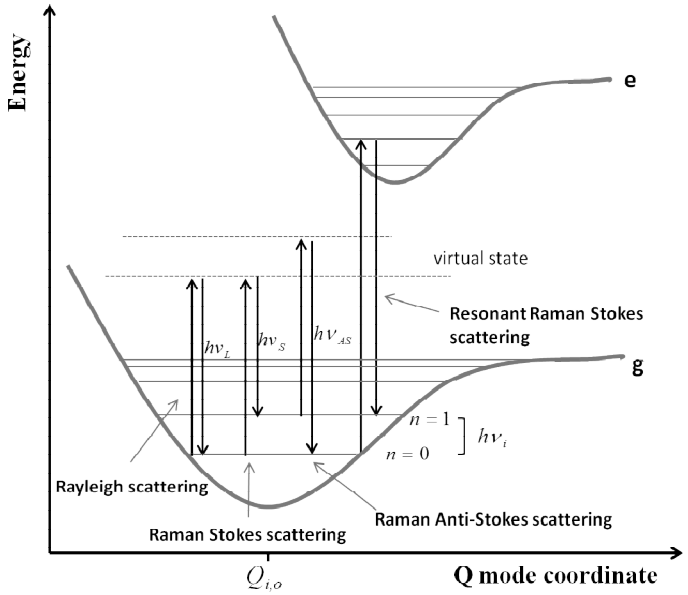

Figure 3.1: Energy level diagram of a generic molecular system with schematic representation of four different scattering processes: Rayleigh scattering with emitted photon energy $h\nu_S = h\nu_L$, Stokes scattering with $h\nu_S=h\nu_L-h\nu_i$, Anti-Stokes scattering with $h\nu_S=h\nu_L + h\nu_i$, and resonant Stokes scattering, where the intermediate transition state is a proper electronic state of the molecule.

From an energetic point of view the Raman scattering phenomenon can be divided into two different events, where in both cases $h\nu_S \neq h\nu_L$ [59]. Depending on whether incident photons cause transition of a molecule to an excited virtual state from its vibrational ground or first-excited state (n = 0 or n = 1), the Raman scattering signal appears shifted to lower or higher energies than the excitation one, respectively. The first case with $h\nu_S=h\nu_L-h\nu_i$, is called Raman Stokes scattering, where $h\nu_i$ is the molecule's vibrational energy. The second one, where $h\nu_S=h\nu_L + h\nu_i$, is called Raman anti-Stokes scattering.

A Raman spectrum consists of scattered intensity plotted versus energy. In order to make the spectrum independent on the excitation frequency, the energy of the scattered photons is reported as Raman shift:

$$\Delta\tilde{\nu} = \tilde{\nu}_L - \tilde{\nu}_S = \frac{1}{\lambda_L} - \frac{1}{\lambda_S} \tag{3.1}$$

The Raman shift clearly corresponds to the energy of the vibrational transition involved into the Raman process. For Stokes spectra the Raman shift is $\Delta\tilde{\nu} > 0$, while for anti-Stokes $\Delta\tilde{\nu} < 0$. As an example, in Figure 3.2 the Raman spectrum of liquid chloroform is shown [20].

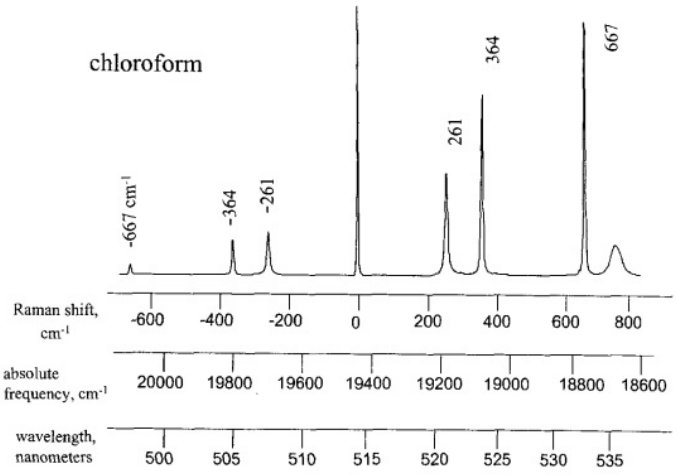

Figure 3.2: Raman spectrum of liquid chloroform at room temperature obtained with 514.5 nm excitation wavelength. The Rayleigh scattering at 0 Raman shift is strongly attenuated by a laser filter and is actually several orders of magnitude much intense than Raman scattering.

It is possible to explain the Raman scattering phenomenon from a physical point of view by a classical approach, which is very simple but give all the basic information[20,60].

We consider a dilute molecular system, where intermolecular interactions are negligible, in a dielectric environment with refractive index n_M. The excitation of this molecular system through an electromagnetic radiation with an oscillating electric field, described in Equation 3.2,

$$\boldsymbol{E}(t) = \boldsymbol{E}_0 \cos(\omega_L t) \tag{3.2}$$

where $\omega_L = 2\pi\nu_L$, gives rise to an induced electric dipole moment, also known as molecular polarization:

$$\boldsymbol{p}(t) = \hat{\alpha}\, \boldsymbol{E}_0 \cos(\omega_L t) \tag{3.3}$$

The molecular polarizability tensor $\hat{\alpha}$ is defined as the tendency of the molecule to be polarized and is strongly dependent on the electron mobility. The polarizability tensor is a function of the instantaneous position of the atomic nuclei in the molecular system. This quantity is not constant in time, but oscillates because of molecular vibrations, which are finally responsible for Raman scattering.

For small displacements from the nuclear equilibrium position, every single element of the $\hat{\alpha}$ tensor ($\alpha_{\sigma\rho}$) can be written through a Taylor series expansion near the equilibrium nuclear position. If we stop the Taylor series at the first term we obtain:

$$\alpha_{\sigma\rho} = \alpha_{\sigma\rho}^{0} + \sum_{i} \left(\frac{\partial \alpha_{\sigma\rho}}{\partial Q_i} \right)_0 Q_i \tag{3.4}$$

where $\alpha_{\sigma\rho}^{0}$ are the elements of the tensor at the equilibrium position and Q_i the vibration mode coordinates with amplitude $Q_{i,0}$ oscillating at the frequency ω_i:

$$Q_i(t) = Q_{i,0} cos\,(\omega_i t) \tag{3.5}$$

If we consider only one vibrational transition, we can rewrite the induced dipole moment as:

$$\boldsymbol{p}(t) = \alpha_0 \boldsymbol{E}_0 \, cos\,(\omega t) + \frac{1}{2}\left(\frac{\partial \alpha_{\sigma\rho}}{\partial Q_i} \right)_0 Q_{i,0} \boldsymbol{E}_0 [cos\,\{(\omega_L + \omega_i)t\} + cos\,\{(\omega_L - \omega_i)t\}] \tag{3.6}$$

This oscillating dipole moment become source of electromagnetic radiation with frequencies ω_L (Rayleigh scattering), $\omega_L + \omega_i$ (anti-Stokes Raman Scattering) and $\omega_L - \omega_i$ (Stokes Raman Scattering). From Equation 3.6, it is clear that a Raman transition occurs only when

$$\left(\frac{\partial \alpha_{\sigma\rho}}{\partial Q_i} \right)_0 \neq 0 \tag{3.7}$$

This relation is the principle selection rule for Raman active modes: the vibrational displacements of atoms corresponding to a particular vibrational mode, should result in a change in polarizability.

3.2.1 Scattering Intensity, Power and Cross section

The power density of the Raman scattering radiation emitted from the molecular dipole can be calculated considering the radiated field and its relation to the second derivative of the oscillating electric dipole. The last describes, in fact, the acceleration of electric charges, which emit electromagnetic radiation. The scattered electric field can be written through the electric dipole approximation as [47]:

$$\boldsymbol{E}_s = -\frac{1}{4\pi\varepsilon_0 c^2}\frac{\ddot{\boldsymbol{p}}(t)}{r} \tag{3.8}$$

The scattered power density (dependent on time) can be related to the scattering field through:

$$\mu\,(t) = n_M\varepsilon_0|\boldsymbol{E}_s(t)|^2 \tag{3.9}$$

where n_M is the refractive index of the molecular environment. The instantaneous power flow, dependent on t, can be written as:

$$S(t) = \mu(t)c \tag{3.10}$$

Substituiting Equation 3.8 into Equation 3.9, the irradiance or intensity can then be written as average of the power flow at t>>T, where T is the oscillation phase of the dipole:

$$I_s \equiv \langle S\rangle_T = \frac{1}{2}cn_M\varepsilon_0 {E_s}^2 = \frac{n_M\omega_s^4}{32\pi^2\varepsilon_0 c^3 r^2}\,|\boldsymbol{p}|^2 \tag{3.11}$$

where ω_S is the scattered frequency, which can correspond to ω_L in case of Rayleigh scattering, or to $\omega_L \pm \omega_i$ in case of Raman (Stokes or Anti-Stokes) scattering.

The differential scattered power, defined as the angular dependence of the scattering power, can either be written in terms of incident radiation intensity or alternatively in terms of scattering intensity. Both definitions are reported here:

$$\frac{dP_s}{d\Omega}(\omega,\Omega) = \frac{d\sigma_s}{d\Omega}(\omega,\Omega)I_0 = r^2\,I_S = \frac{n_M\omega_s^4}{32\pi^2\varepsilon_0 c^3}\,|\boldsymbol{p}|^2 \tag{3.12}$$

where I_0 is the incident radiation intensity and Ω is the solid angle of scattering collection.

As can be observed in Equation 3.12, a new physical quantity known as differential scattering cross section has been defined, in order to relate the intensity of the incident field to the radiation power. This quantity can be used to compare the scattering radiation by different molecules. It is in fact defined as the area which describes the probability of the incident radiation to be scattered by the molecule within a given solid angle.

According to Equation 3.3 and 3.12 we can extract the formal definition of the differential scattering cross section:

$$\frac{d\sigma_s}{d\Omega}(\omega,\Omega) = \frac{\omega_s^4|\hat{\boldsymbol{\alpha}}|^2}{16\pi^2\varepsilon_0^2 c^4}sen\phi \tag{3.13}$$

where ϕ is the angle between the dipole and the detection direction

By integration of the power density over the whole solid angle, the total power [W] of the scattered radiation can then be written as:

$$P(\omega_s) = \frac{\omega_s^4|\hat{\boldsymbol{\alpha}}|^2}{12\pi\varepsilon_0 c^3}|\boldsymbol{E}_0|^2 \tag{3.14}$$

For an ensemble of molecules we can simplify the relation as:

$$P(\omega_s) = N\,\sigma(\omega_s) I_0(\omega_L) \tag{3.15}$$

where N is the number of molecules, σ the Raman scattering cross section of the irradiated species [cm^2] and I_0 the incident radiation intensity [W/cm^2].

Highlighting the three different scattering contributions we find the following proportionalities:

$$\alpha_0{}^2 \omega_L{}^4 \qquad \text{Rayleigh} \tag{3.16}$$

$$P(\omega_s) \propto \begin{cases} \frac{1}{4}\left(\frac{\delta\alpha}{\delta Q_i}\right)_0^2 Q_{i,0}{}^2 (\omega_L + \omega_i)^4 & anti-Stokes \quad (3.17) \\ \frac{1}{4}\left(\frac{\delta\alpha}{\delta Q_i}\right)_0^2 Q_{i,0}{}^2 (\omega_L - \omega_i)^4 & Stokes \quad (3.18) \end{cases}$$

The anti-Stokes process is generally less intense than the Stokes one, because at room temperature only a small fraction of molecules, determined by the Boltzmann population distribution, are in an excited vibrational state. According to the Fermi golden rule we can therefore write the ratio between anti-Stokes and Stokes scattering intensity as:

$$\frac{I_{aSto}}{I_{Sto}} = \left(\frac{\omega_L - \omega_i}{\omega_L + \omega_i}\right)^4 e^{-\frac{\hbar\omega_i}{k_B T}} \tag{3.19}$$

3.2.2 Polarizability and Frequency dependence of Scattering Power

Observing Equation 3.16-3.18 we can extract some interesting information regarding the dependence of the scattered power on the polarizability of the molecule and on the excitation and the scattered frequency.

If we look firstly at the polarizability dependency, it is clear that the Raman scattering phenomenon is a very weak process, because the Raman cross section does not depend on $\alpha_0{}^2$, like in the case of Rayleigh scattering, but on.

$$\left(\frac{\delta\alpha_{\sigma\rho}}{\delta Q_i}\right)_0^2 \tag{3.20}$$

For traditional Raman scattering, generally, the ratio between the scattering and exciting photons is only about 10^{-6}.

Instead, we can analyse the Raman scattering cross section, near a molecular electronic transition, on its frequency dependence writing the polarizability (Stokes component) with a quantum mechanically approach. Starting from the initial definition of molecular polarization (Equation 3.3) and considering $\omega_{eg} = 1/\hbar\,(E_e - E_g)$ the resonance frequency of the electronic transition, characterized by a damping factor $i\Gamma_e$, the polarizability can be written as:

$$\alpha_{g_1 g_0}(\omega) = \frac{1}{\hbar}\sum_{n_e}\left(\frac{\langle g_1|\hat{\mu}_{ge}|e_n\rangle\langle e_n|\hat{\mu}_{eg}|g_0\rangle}{\omega_{eg} - \omega - i\Gamma_e}\right) \tag{3.21}$$

$\langle g_1|\hat{\mu}_{ge}|e_n\rangle$ and $\langle e_n|\hat{\mu}_{eg}|g_0\rangle$ describe the dipole momentum of transition from the intermediate state e_n to the final vibrational state g_1, and from the starting ground state g_0 to e_n, respectively.

Substituting Equation 3.21 in 3.13, we obtain the relation

$$\sigma_R(\omega) \propto \omega^4 \frac{\left(\langle g_1|\hat{\mu}_{ge}|e_n\rangle\langle e_n|\hat{\mu}_{eg}|g_0\rangle\right)^2}{\left(\omega_{eg} - \omega\right)^2 + (\Gamma_e)^2} \tag{3.22}$$

plotted in Figure 3.3:

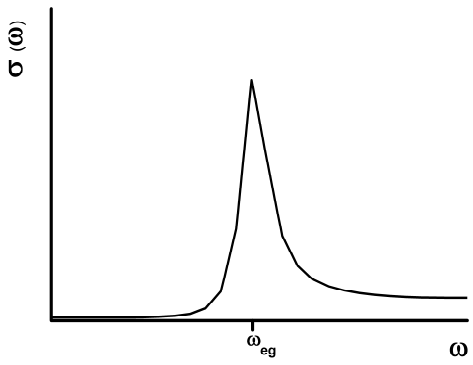

Figure 3.3: Representative plot of Raman cross section dependence on the excitation frequency.

As can be observed from Equation 3.22 and Figure 3.3 the scattering cross section rises dramatically in resonance conditions, i.e. exciting with an electromagnetic radiation with a frequency near to the electronic transition of the molecular system.

In order to make a comparison, the normal Raman cross section values lie around 10^{-32}-10^{-30} cm^2, while resonant ones around 10^{-24}-10^{-23} cm^2. As will be explained later, the cross sections in SERS conditions rises further to values around 10^{-18} cm^2, comparable with fluorescence ones, and can reach 10^{-14} cm^2 for resonant SERS (SERRS) conditions [47].

It is important to point out the fact that when reaching resonant Raman conditions, also fluorescence emission is possible, which can lead to interferences in Raman spectroscopy measurements. The Raman bands are usually very sharp with band widths of only a few cm^{-1}, while fluorescence emission is a very broad process, which can completely cover the Raman spectrum. It is also important to underline that the Raman scattering is a coherent process, where the arrival state for the absorption and the starting state for scattering have the same energy and phase. The fluorescence emission, is instead, an incoherent process.

3.3 Surface Enhanced Raman Spectroscopy

In the early 70s, for the first time, very large enhancements of the Raman scattering signal was observed, induced by the proximity of an analyte molecule to a metal surface. The phenomenon, observed from pyridine adsorbed on an electrochemically roughened silver electrode by Fleischman et al. in 1973 [61], was initially attributed to an increased surface area of the rough substrate. In 1977 the phenomenon was independently discovered by Jeanmarie and Van Duyne [62], which pointed out that a simple increase of the electrodes surface could not give such high signals. In 1978 M. Moskovits finally proposed an increase of the molecular Raman cross section as a result of the excitation of surface plasmons [63]. Many predictions since that are all shown to be true within a few years of discovery: analyte molecules put in proximity of a metal nanostructured surfaces feel a strongly enhanced electromagnetic local field that arise after proper excitation of surface plasmons. The SERS phenomenon should be observable in metal colloids with a hierarchy of intensification that starts from silver, providing the most intense SERS signal, followed by gold and copper and other good conductors such as aluminium, indium and platinum.

The degree of amplification, which will be described in detail later, can be easily understand through the following equation:

$$EF = \frac{P_{SERS}}{P_{Raman}} \tag{3.23}$$

where EF is the so called Enhancement Factor, P_{SERS} and P_{Raman} are the powers of the scattering radiation in SERS and traditional Raman conditions, respectively. It is very important to point out, that the local field intensity strongly decays moving away from the nanostructure surface, with a field intensity dependence of r^{-10}, where r is the distance between the metal and the molecule[64].

In order to have a visual impression of the amplification of a Raman signal in SERS conditions, an example is reported in Figure 3.4.

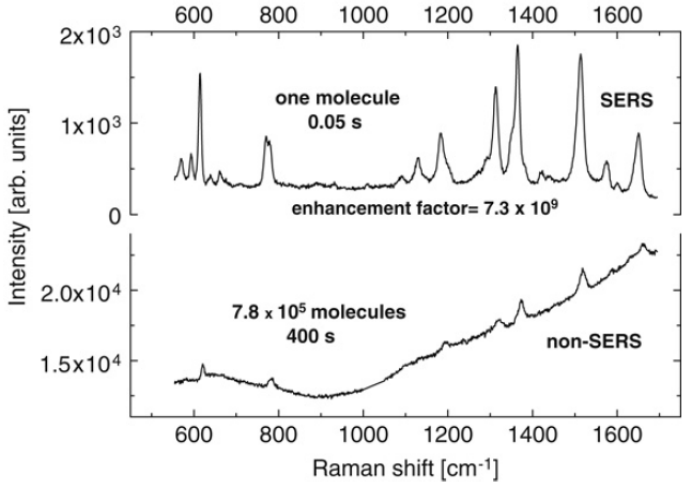

Figure 3.4:.Traditional Raman (non-SERS) and SERS spectra at 633 nm excitation wavelength for rhodamine 6G. In the bottom spectrum the signal rises from 7.8 x 10^5 molecules, while the top signal comes from a single molecule, under same experimental conditions, but different integration times (400 s for the Raman and 0.05 s for the SERS signal.

From the beginning it was also clear, that many parameters have to be controlled for successful SERS, such as:

- the characteristics of the laser excitation radiation (wavelength, polarization, angle of incident for planar substrates);
- the detection setup (scattering configuration, solid angle collection, scattering polarization);
- the characteristics of the SERS-active system (material, structural features, geometry, orientation with respect to incident beam, refractive index of the environment);
- the intrinsic electronic molecular properties of the adsorbed species;
- the adsorption properties over SERS system (adsorption efficiency, concentration, orientation over substrate and distance).

However, as written before, it is not clear in literature yet, how to deal correctly with all these parameters to obtain the highest SERS signals.

In the next paragraphs we try to mix the two basic components of SERS, i.e. Raman Spectroscopy and SPR, to understand the theoretical aspects concerning the critical parameters and finally to point out what are the unanswered questions in literature.

3.3.1 Enhancement Factor definition

The heart of the Surface Enhanced Raman Spectroscopy technique is to understand how much the molecular Raman scattering process can be enhanced by the local electric field around the metal nanostructure. The simplest way to do this is to find a numerical and analytical expression of the EF. This issue is one of the most critical and discussed in SERS research area, because of great difficulties to predict and measure EFs. This uncertainties lead to a non univocal handling of the EF in literature, which make it difficult to compare the merits of different SERS substrates. For introducing some simple mathematical expressions of SERS theory and define the EF, we choose to follow the considerations and models proposed by Etchegoin and Le Ru [47], who, in our opinion, gave a great and important contribution to SERS theory and understanding.

The Raman scattering power, in SERS conditions, can be written with the same expression like for traditional Raman Spectroscopy (Equation 3.15) but multiplied by an additional factor, defined as EF, which is in fact the principal element for SERS technique (according to Equation 3.23):

$$P_{SERS}(\omega_s) = N\ \sigma(\omega_s)\, EF\, S_0(\omega_L) \tag{3.24}$$

Before going into details of different enhancement mechanisms and their expressions, it is important to make a differentiation in EF definition, depending on the application of SERS.

The Surface Enhanced Raman process is a strictly localized effect, where the enhancement of the Raman scattering by the molecule is strongly dependent on the position of the analyte on the metallic surface. According to whether one is interested in knowing the exact enhancement felt by a single molecule in a defined position or in an averaged enhancement value over the whole SERS substrate, the EF definition will fall in one of the two categories:

- Average EFs (average property over the substrate)
- Single-Molecule EFs (SMEFs) (enhancement property in a specific position on the substrate)

The present work is principally interested in finding a good average EF definition and prediction for the detection of randomly oriented molecules. Nevertheless, in order to find some simple mathematical expressions, in the next paragraphs we will begin discussing the formal derivation of SMEF.

3.3.2 Electromagnetic Enhancement mechanism: the $|\boldsymbol{E}|^4$-approximation approach

In general, the SERS EF can be separated into two multiplicative factors:

- the electromagnetic contribution (EF_{em}), given by the coupling of the incident and scattered radiation with the SERS substrate,
- the chemical contribution ($EF_{chem.}$), given by the interaction between a molecule and the excited surface plasmon oscillation, leading to an enhancement in the electronic polarizability of the analyte.

The two mechanisms can coexist and give rise to a cumulative effect. Anyway, the main origin of the SERS enhancement is electromagnetic (up to ~10^{10}), while the chemical one contributes generally with a factor of more or less 10^2. In this paragraph we will principally focus on the EF_{em}, which is also the main component in our experimental section.

Hereafter a very simple approach to mathematically define the EF_{em} is reported. For the further expressions, we will refer to Raman Stokes scattering transitions for a defined vibrational mode. The simplest approach that gives the most insight into SERS effect is the classical electromagnetic theory with the same phenomenological description of a Raman scatterer, already reported in paragraph 3.2. However, the presence of the nanostructured metal surface introduces two significant modifications in the field description:

- the electromagnetic field at the molecule position is modified (*local field enhancement*),
- the radiation properties of the Raman dipole are modified (*radiation enhancement*).

In order to mathematically describe these two enhancement components of the electromagnetic mechanism, we will begin to treat them separately.

For the *local field intensity enhancement*, the macroscopic electric field felt by the molecule has to be analyzed. The local field $\boldsymbol{E}_{loc}$ can be much larger than the incident field $\boldsymbol{E}_0$ and can vary dramatically with position. This local field induces a Raman dipole

$$\boldsymbol{p}_R = \alpha_R \, \boldsymbol{E}_{loc}(\omega_L) \tag{3.25}$$

which radiates in free space with power proportional to $|\boldsymbol{p}_R|^2$ and is enhanced by a local field EF:

$$M_{loc} = \frac{|\boldsymbol{E}_{loc}(\omega_L)|^2}{|\boldsymbol{E_0}|^2} \tag{3.26}$$

The M_{loc} can reach values up to 10^5.

In case of *scattering enhancement*, we have to look to the properties of the modified dipole radiation. Both the scattering pattern, characterized by $dP_s/d\Omega$, and the total scattered power P_s can be modified, compared to the scattered power in free space P_0, by the enhanced local field around the metal surface. This modification arises from the so called self-reaction field, which is the field created by the dipole at its own position through interaction with the environment.

The scattering enhancement factor can be defined as:

$$M_s = \left(\frac{dP_s^P}{d\Omega}(\Omega)\right) \Big/ \left(\frac{dP_s^0}{d\Omega}\right) \tag{3.27}$$

M_s depends on many parameters, like substrate geometry, dipole position and orientation and radiation frequency ω_s. Under best conditions, the collected Raman signal is enhanced by a factor $M_s(\omega_s)$ compared to Raman scattering in free space. These contributions to the EF_{em} can reach values of about 10^5. The estimation and calculation of $M_s(\omega_s)$ is often very difficult, because one have to solve the problem of dipolar emission for each position of the dipole and handle with dipolar singularities. For simplicity the radiation enhancement is often written $M_s(\omega_s) \approx M_{loc}(\omega_s)$. These approximation is very strong but in some cases justified by considering that the coupling with the SPR by the electromagnetic field of the incident beam and the dipole emitted radiation, is qualitative similar.

Considering these two contributions to the electromagnetic enhancement mechanism we can define the EF_{em} for a single molecule:

$$SMEF(\omega_L, \omega_s) \approx M_{loc}(\omega_L)\, M_{loc}(\omega_s) \approx \frac{|\boldsymbol{E}_{loc}(\omega_L)|^2}{|\boldsymbol{E}_0|^2} \frac{|\boldsymbol{E}_{loc}(\omega_s)|^2}{|\boldsymbol{E}_0|^2} \tag{3.28}$$

The Raman shift is small and therefore $\omega_s \approx \omega_L$. This assumption gives rise to the well known $|\boldsymbol{E}|^4$ - approximation:

$$SMEF(\omega_L) \approx \frac{|\boldsymbol{E}_{loc}(\omega_L)|^4}{|\boldsymbol{E}_0|^4} \tag{3.29}$$

This derivation and final expression is of great simplicity and in some cases very useful, as underlined by many SERS works in literature, in which this approximation is commonly used. However, the physics of the SERS process is not well described, mostly because of the strong approximations done for the radiation enhancement contribution.

In the next paragraph a relatively new general description of the SERS electromagnetic enhancement mechanism is given, following the brilliant explanations by Etchegoin and Le Ru [47], which throw in, in a very simple way, all the important parameters, like scattering configuration and field polarization.

3.3.3 Electromagnetic Enhancement contribution: formal derivation

The physical processes involved in the electromagnetic enhancement mechanism (particularly important for polarized detection), are basically two, as written before: the enhancement of the incident exciting field and the enhancement of the emitted scattering radiation by the analyte itself. The two situations can be well understood through the scheme reported in Figure 3.5.

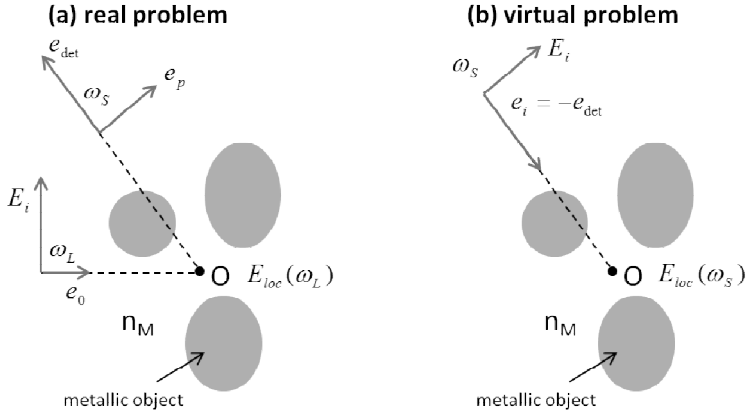

Figure 3.5: Schematic representation of the SERS EM problem (for polarized detection), considering the real excitation problem (a) and the `virtual' plane-wave-excitation problem for re-emission (b).

Let consider a fixed molecule in position O, embedded in a dielectric medium, with refractive index n_M, in the proximity of a metallic nanostructure. The system is excited by an electromagnetic radiation with frequency ω_L, propagation direction $\boldsymbol{e}_0$ and polarization along $\boldsymbol{e}_E \perp \boldsymbol{e}_0$. The incident field induces a dipole $\boldsymbol{p} = p\boldsymbol{e}_p$ generating a local electric field $\boldsymbol{E}_{loc}(\omega_L)$ at the position of the molecule. The Raman scattered signal can be studied in a given direction Ω_{det} along unit vector $\boldsymbol{e}_{det}$ and polarization defined by $\boldsymbol{e}_{pol}$.

In order to account for the so called radiation enhancement, i.e. the modification of the dipole emission, a further, 'virtual' problem has to be solved (Figure 3.5b): a plane-wave excitation with frequency ω_s incoming along $-\boldsymbol{e}_{det}$ and polarized along $\boldsymbol{e}_P$ has to be considered.

The *optical reciprocity theorem* (ORT) allows the calculation of the SERS EF without solving the EM problem of emission from a localized dipole at the molecule position. It can be applied to calculate the time-averaged differential power radiated per unit solid angle along the detection direction, defined by $\boldsymbol{e}_{det}$. The ORT states that the field $\boldsymbol{E}_1$, created at a given point M, by a dipole $\boldsymbol{p}_1$ at point O, is related to the field $\boldsymbol{E}_2$ created in point O by a dipole $\boldsymbol{p}_2$ at point M:

$$\boldsymbol{p}_1(O)\boldsymbol{E}_2(O) = \boldsymbol{p}_2(M)\boldsymbol{E}_1(M) \tag{3.30}$$

Before applying this theorem to our problem, it is important to specify that the ORT has no direct physical meaning related to the interaction energies between two dipoles, but has to be viewed as mathematical method to solve two independent problems with a single dipole in each and not the problem of two dipoles at the same time.

Let's consider a dipole $\boldsymbol{p}_2 = p_2\boldsymbol{e_2}$ at point M with $\boldsymbol{e}_2 \perp \boldsymbol{e}_r$. Before describing the field created in point O $\boldsymbol{E}_2$, we will write an expression for $\boldsymbol{E}_2$ created by $\boldsymbol{p}_2$ at a point r in the absence of any metal nanostructure. Choosing a sufficiently large distance R between O and M, so that the region where molecule and objects are will be r<<R, the field $\boldsymbol{E}_2(\boldsymbol{r})$ can be approximated by expanding the free-space dipole field:

$$\boldsymbol{E}_2(\boldsymbol{r}) \approx E_i e_2\, e^{-ik_M \boldsymbol{e}_r \boldsymbol{r}} \tag{3.31}$$

where

$$E_i = \frac{k_M^2 p_2\, e^{ik_M R}}{4\pi\epsilon_0\epsilon_M R} \tag{3.32}$$

Using ORT, writing $\boldsymbol{E}_2(O)$ as $\boldsymbol{E}_{loc}(O)$ and multiplying nominator and denominator with E_p, we can write:

$$\boldsymbol{e}_2\, \boldsymbol{E_1} = \frac{E_i\, p \boldsymbol{e}_p \boldsymbol{E}_{loc}}{E_i\, p_2} \tag{3.33}$$

According to the paragraph above, we can write

$$\widetilde{\boldsymbol{E}}_{loc}^{P} = \frac{\boldsymbol{E}_{loc}}{E_i} \tag{3.34}$$

and, choosing for $\boldsymbol{e}_2$ one generic polarization direction denoted with $\boldsymbol{e}_{pol}$, the polarization component E_1^{pol} of the radiation field of the dipole $\boldsymbol{p}$ in the direction defined by $\boldsymbol{e}_r$, becomes:

$$E_1^{pol} = \frac{k_M^2\, e^{ik_M R}}{4\pi\epsilon_0\epsilon_M R}\, \boldsymbol{p}\, \widetilde{\boldsymbol{E}}_{loc}^{P} \tag{3.35}$$

It is important to underline here that the expression is independent on the second (*virtual*) dipole p_2, making the mathematical treatment a one molecular dipole problem.

Knowing the expression of the scattered radiation intensity (Eq. 3.11), the time-averaged differential power radiated per unit solid angle in this direction is then:

$$\frac{dP_s^P}{d\Omega}(\Omega) = \frac{n_M \omega^4 |\boldsymbol{p}|^2}{32\pi^2 \epsilon_0 c^3} \left|\boldsymbol{e}_p \cdot \widetilde{\boldsymbol{E}}_{loc}^P\right|^2 \tag{3.36}$$

If we rewrite the radiation enhancement factor definition of Equation 3.27 for polarized detection along $\boldsymbol{e}_P$, as:

$$M_s^P(\Omega) = \left(\frac{dP_s^P}{d\Omega}(\Omega)\right) \Big/ \left[\frac{3}{8\pi} P_s^0\right]^{max} \tag{3.37}$$

the final definition of the directional radiative enhancement factor will be:

$$M_s^P(\Omega) = \left|\boldsymbol{e}_p \cdot \widetilde{\boldsymbol{E}}_{loc}^P\right|^2 \tag{3.38}$$

This expression shows great similarity with the expression obtained within the $|\mathbf{E}|^4$ - approximation approach (Equation 3.28). The denominator of Equation 3.37 has been chosen in order to be a constant value and not a potentially zero value, which would led to an unrealistic infinitive directional radiative enhancement factor. It is in fact the maximum value of $dP_s^0/d\Omega$ for a free space dipole.

It is now possible to define a general differential SERS cross section, like in the case of traditional Raman spectroscopy.

$$\frac{dP_{SERS}}{d\Omega}(IP, SC, r, MO, \omega_L, \tilde{\nu}_k, \hat{\alpha}_k, n_M) = \frac{d\sigma_{SERS}}{d\Omega}(IP, SC, r, MO, \omega_L, \tilde{\nu}_k, \hat{\alpha}_k, n_M)\, S_0 \tag{3.39}$$

From this formal treatment it is clear that the absolute differential Raman cross section is dependent on incident frequency, vibrational frequency of the excited Raman mode, associated polarizability tensor, incident polarization, scattering configuration, molecule position and orientation.

The differential SERS cross section for polarized detection can therefore be written as:

$$\frac{d\sigma_{SERS}}{d\Omega} = \frac{\omega_s^4}{16\pi^2 {\epsilon_0}^2 c^4} \left|\widetilde{\boldsymbol{E}}_{loc}(\omega_L) \cdot \hat{\alpha} \cdot \widetilde{\boldsymbol{E}}_{loc}^P(\omega_s)\right|^2 \tag{3.40}$$

where $\boldsymbol{p} = \hat{\alpha}\boldsymbol{E}_{loc}(\omega_L)$ is the Raman dipole induced at the molecule position and $\widetilde{\boldsymbol{E}}_{loc}(\omega_L)$ is defined like in Equation 3.34. Integrating this expression over the whole solid angle results in:

$$\sigma_{SERS} = \frac{\omega_s^4}{6\pi{\epsilon_0}^2 c^4} \left|\widetilde{\boldsymbol{E}}_{loc}(\omega_L) \cdot \hat{\alpha} \cdot \widetilde{\boldsymbol{E}}^P_{loc}(\omega_s)\right|^2 \tag{3.41}$$

The normalized Raman polarizability tensor is defined as $\hat{\alpha}_N = \hat{\alpha}/\tilde{\alpha}$, where $\tilde{\alpha}$ is the magnitude of the tensor. The single molecule enhancement factor for polarized detection is defined as the ratio of the SERS and non-SERS differential cross section, giving:

$$SMEF^P = \frac{d\sigma_{SERS}}{d\Omega} / \frac{d\sigma_R}{d\Omega} = \left|\widetilde{\boldsymbol{E}}_{loc}(\omega_L) \cdot \hat{\alpha}_N \cdot \widetilde{\boldsymbol{E}}^P_{loc}(\omega_R)\right|^2 \tag{3.42}$$

It is important to underline that the SMEF depends on the symmetry of the Raman tensor, not on its magnitude. In the most general case, the local field enhancement and the radiative local enhancement cannot be entirely decoupled, because the last depends on the induced dipole orientation, which is directly related to the local field polarization.

3.3.4 Chemical Enhancement contribution: the charge transfer mechanism

The existence and mathematical treatment of the chemical enhancement has been the subject of much debate in literature, because it is often very difficult to measure, predict and distinguish from the electromagnetic mechanism.

One of the first definitions of chemical enhancement was given by Moskovits in 1985 [57], which stated that "…it arise from the modification of the Raman polarizability tensor of the adsorbate, resulting from a formation of a complex between the adsorbate and the metal". In fact, this is not really an enhancement mechanism, but a modification of the intrinsic properties of the adsorbate. The most influencing condition for a Raman scattering increase, arises when the modified polarizability is more resonant with the excitation than the original one. This could, for example, happen in case of a charge transfer mechanism in the metal-adsorbate complex, which is the most common chemical enhancement phenomenon. There are principally two different chemical enhancement scenarios, which have been proposed and discussed in literature and are schematically shown in Figure 3.4 [19,47] [mechanism (a) and (b+c)].

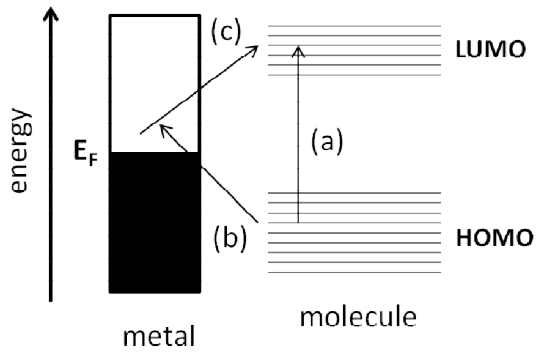

Figure 3.4: Schematic representation of the most common charge-transfer mechanisms

(a) The molecule is not bound covalently to the metal: the metal acts like a perturbation to the electronic structure of the adsorbate and therefore on the polarizability and resonance Raman cross section. An example for this chemical mechanism are some vibrational modes of pyridine (1010 and 1035 cm^{-1}), for which old and new literature[31,65] proposes phenomenological and mathematical treatments.

(b)+(c) A surface metal-molecule complex is present with direct covalent binding or indirect binding through the environment (for example an electrolyte ion, like chloride). This complex creates new electronic states which serve as resonant intermediate states. This transition causes a change in the intrinsic polarizability of the molecule, which depends on the optical transition involved in the excitation process. In some cases the highest occupied molecular orbital (HOMO) and the lowest unoccupied molecular orbital (LUMO) of the molecule are symmetrically disposed in energy with respect to the Fermi level (E_F) of the metal. In this case charge-transfer excitations (from metal to molecule or vice versa) can occur at about half the energy of the electronic transition of the adsorbate.

It is clear that the chemical contribution can difficultly be separated to the total enhancement mechanism by mathematical models and predictions. The most effective way to do it, is the experimental approach, by comparing the SERS signal of a given Raman mode of different analytes in the same conditions, like done by Orendorff et al. [66]. The differences in signal intensity can be attributed to chemical enhacement contribution, because the electromagnetic one should be the same for identical SERS substrate and experimental conditions, independent on analyte.

3.3.5 Enhancement factor measurements: experimental approach

Independently on the experimental application of SERS, the first thing to do in order to evaluate the quality of the used SERS substrate, is to measure his enhancement factor. The knowledge of this value can help in optimizing the final application.

In this paragraph a brief overview of some important experimental EF definitions [28], which will be discussed and used later in the experimental ones, are given.

One of the simplest definitions is given by the Analytical Enhancement Factor (AEF)

$$AEF = \frac{I_{SERS}/c_{SERS}}{I_R/c_R} \tag{3.43}$$

expressed as the ratio between the SERS intensity I_{SERS}, of a given analyte concentration c_{SERS} on a SERS active nanostructure (from now on called generically SERS substrate) and the Raman intensity I_R of the same analyte with possibly different concentration c_R, under non-SERS but identical experimental conditions.

The most important assumption in this definition is that both I_{SERS} and I_R are linearly dependent on the incident power density and molecule concentration c_{SERS} and c_R, respectively. The AEF depends strongly on the adsorption properties of analyte molecules, in particular on the SERS substrate surface coverage. The c_{SERS} is, in fact, not a precise estimation of the number of adsorbed molecules, and therefore not a good characterization of the SERS substrate itself. Nevertheless it is a good measurement of average SERS EF in liquid samples and is easily implemented and reproducible. The *volumetric* nature of the molecular concentration expression for the AEF, makes this definition particularly suited to the case of SERS active liquids.

The expression above ignores that in fact only the adsorbed molecules contribute to the SERS signal. Therefore a SERS substrate enhancement factor (SSEF) can be defined:

$$SSEF = \frac{I_{SERS}/N_{surf}}{I_R/N_{vol}} \tag{3.44}$$

where $N_{vol} = c_R V$ is the average number of molecules in the irradiated volume in non-SERS conditions and N_{surf} is the average number of adsorbed molecules in the same volume for the SERS experiment. The assumption in this case is that the surface coverage should be less than one monolayer.

The greatest difficulty in experimental measurements of SSEF lies in the determination of N_{surf}. Setting $N_{vol} = c_R H_{eff} A_{eff}$ and $N_{surf} = (\delta_{surf}\delta_{ns}A_m A_{eff})$, Equation 3.43 can be rewritten as:

$$SSEF = \frac{I_{SERS}/(\delta_{surf}\delta_{ns}A_m)}{I_R/(c_R H_{eff})} \tag{3.45}$$

c_R is the analyte concentration expressed as molecules/cm^3 in non-SERS conditions, δ_{surf} is the surface density of molecules/cm^2 over the SERS substrate, δ_{ns} is the surface density of individual nanostructures and A_m is the metallic surface area of each nanostructure. $H_{eff}A_{eff}$ is the effective scattering volume. The effective high of scattering volume H_{eff} is the key parameter for comparing 2D with 3D measurements and can be easily calculated experimentally (see experimental section, Chapter 5).

The two definitions above are spatially-averaged EFs, which don't consider the high non-uniformity of local field enhancement over the whole substrate. As said before it could be useful to define a single molecule enhancement factor (SMEF), felt by a single molecule in a specific point of the surface. It is dependent on the symmetry of the Raman tensor of the mode and on the probe and SERS substrate orientation with respect to the polarization of the incident light. The requirement of the difficult exact knowledge of substrate geometry and molecules orientation make this definition a more theoretical than experimental expression.
The SMEF can be written as

$$SMEF = \frac{I_{SERS}^{SM}}{\langle I_R^{SM}\rangle} = \frac{\frac{d\sigma_{SERS}}{d\Omega}}{\frac{d\sigma_R}{d\Omega}} \tag{3.46}$$

where I_{SERS}^{SM} is the SERS intensity of the single molecule under consideration, whereas $\langle I_R^{SM}\rangle$ is the average Raman intensity over all orientations per molecule for the same probe. The relation can also be described as the ratio of SERS over non-SERS differential cross-sections.
It is very difficult to know the exact molecule orientation and probably it does not remain fix during measurement. It is therefore reasonable to define an orientation averaged SMEF

$$OASMEF = \frac{[I_{SERS}^{SM}]}{\langle I_R^{SM}\rangle} \tag{3.47}$$

The average in the nominator is taken over all allowed orientations, while the one in the denominator is taken over all real molecules orientations.

The use of these two definitions can be reasonable in case of spatial restricted enhancements, like in the case of *hot spots*. For SERS substrate comparison, the SMEF could be calculated or measured with probes showing no chemical enhancement and with a representative Raman tensor and/or adsorption orientation. In case of an isotropic Raman tensor, in fact, the the SMEF is no longer dependent on the analyte properties and therefore reflects directly the electromagnetic SERS properties of the surface.

Combining the SMEF with the concept of EF average over the whole substrate, we can write a new, rigorous definition of the SSEF as the spatially-averaged OASMEF on the surface:

$$SSEF = \frac{1}{A}\int_S OASMEF\,(r)dS \tag{3.48}$$

where A represents the total surface area of the metallic substrate.

Applying for SSEF the same assumption as for SMEF, for an isotropic mode subjected only to *em*-enhancement, the SSEF definition is the best one to compare the average EF of different SERS substrates.

3.4 Realization of a biological or chemical sensor: challenges of SERS detection

The EF definitions described above are commonly used in literature to define the enhancement quality of a given plasmonic substrate, through SERS measurements. Usually, SERS EF measurements are performed with little molecules presenting good Raman cross sections, like benzenethiol [33] or Raman dyes like rhodamine [34], and are called SERS labels. The quantification of the enhancement efficiency is then used as indication for the sensing potentiality. In most cases, the SERS sensing works are focused on the presentation of new, high performing SERS substrates, with explanation of theoretical aspects, characterization and improvement of substrates efficiency. The SERS spectra of the Raman labels are sometimes collected at different analyte concentrations, underlining the impressive enhancement of the Raman signal[27,67,68]. EFs in the $10^3 \div 10^9$ range and detection concentration limits in the μM ÷ pM range can be found, as expected when comparing with the mM detection limit of traditional Raman spectroscopy.

Less publications, refer to practical SERS sensing examples, where the molecule of interest is no longer the SERS label but a molecule of real chemical or biological importance. In many of these applied sensing works, the Raman labels are anyway used for indirect determination of the analyte of interest. An example is the work by Fabris et al.[69], where the conjugation of two complementary DNA strands is detected through the SERS signal of the label molecule: this molecule is adsorbed on a gold nanoparticle together with the single stranded DNA. When the DNA interacts with his complementary DNA strand deposited on a solid substrate, the SERS label signal will "switch on" when observing the substrate.
The rare label free sensing examples are usually performed with molecules of biological and genetic interest, like amino acids [70], proteins [71] and DNA [72]. Another part of SERS sensing publications refer to chemical species, like aromatics, or general water [73] and environment [74] pollutants.

Generally, the term "SERS substrate" is used to describe any metallic nanostructure, that produces the SERS enhancement. Within this definition, there can be distinguished two main different types of substrates:

- Metallic particles in solution (generally colloidal solutions)
- Planar metallic structures, such as random deposited metallic particles or ordered arrays of nanostrutctures supported on a planar substrate like glass or silicon.

The presentation of new SERS substrates by measuring the EF and the concentration detection limit of a given test molecule, is for sure the best way to compare the enhancement performances of different nanostructures, but is in some cases misleading. The "real" enhancement efficiency of the Raman signal of a specific analyte, through SERS, is dependent on many factors, some of these are sometimes omitted in the substrates description and not taken into account. Moreover, the spectroscopic results are very sensible to little variations in the experimental setup or even in the nanostructure geometry, which often lead to deviations from the expected, theoretical values.
There are some critical points, in our opinion, which make the definition of a real enhancement efficiency, very difficult. We want to list the main factors here:

1. the intrinsic Raman cross section of the Raman mode chosen for EF measurements
2. the presence of chemical enhancement

3. the analyte affinity to the metallic substrate (surface selection rules, adsorption rate and final coverage)
4. variations in the nanostructure geometry after functionalization or SERS measurement (smoothing, aggregation)
5. the presence of *hot spots* in the nanostructures geometry
6. the detection setup and conditions (wavelength, polarization, objective used etc.)

In the following paragraphs we want to discuss these critical issues in order to point out what are the challenging arguments in literature, which have not find an univocal explanation yet. The first three points can be summarized in one single discussion concerning the analyte role in SERS detection, while point 4 and 5 can be treated from a substrate point of view. The last point describes the influence of the detection setup, but will be included in the two following paragraphs because, in fact, it influences both the analyte and the substrates role.

3.4.1 The analyte role in SERS sensing

Although in paragraph 3.3.5 different EF equations are reported, which shall be chosen carefully for every single sensing application, many authors just use the simplest relation of Equation 3.43 with a random chosen test molecule, making strong approximations in the final discussion of SERS efficiency.

One critical point is the intrinsic Raman cross section of the mode chosen for analyte detection. It is important here to repeat that the Raman cross section is strongly dependent on the specific molecular vibrational mode and on the excitation wavelength. Enhancement factor measurements are commonly performed with little molecules, like benzenethiol [33,75], pyridine [26] and others [34,66,76], which modes present Raman cross sections in the order of $10^{-27} \div 10^{-30}$ cm^2 $molecule^{-1}$ sr^{-1}, dependent on the excitation wavelength [28,77]. It is for sure very useful to exploit the good Raman cross section to perform EF measurements in order to have good signals, but this could often lead to a wrong interpretation of the concentration detection limit. In fact the Raman scattering intensity depends on the Raman cross section, according to Equation 3.15 (or Equation 3.24 for SERS detection) and can vary many orders of magnitude depending on the mode under study and the incident wavelength. It is clear that, in particular near the detection limit, differences of only one order of magnitude can be relevant in the ability of detecting or not a chemical species.

In some works resonant Raman scatterer (RRS) were used (see paragraph 3.2.2), which deserve a separate discussion. In this case the Raman scattering is particularly intense, because the excitation energy is close to the electronic energy of the molecule. RRS intensities can be 10^6 times larger than non resonant Raman scattering. Raman dyes are therefore good SERS probes, often used for imaging applications, but not ideal for SERS sensing "simulations".

This is also the case when a vibrational mode, that lead to a chemical contribution to the total enhancement, is chosen [30,31]. In fact the chemical contribution can reach values of about 10^2 and it is therefore misleading to define a sensing EF for a given substrate with such a SERS probe. This is often the principal reason because different substrates can hardly be compared by their EFs. It is therefore suitable to measure the EF on a molecules vibrational mode which is not affected by chemical enhancement.

Despite the role of the intrinsic electronic properties of the SERS probe, also the absorption orientation gives an important contribution to the enhancement efficiency estimation [78]. In fact, there exist the so called surface selection rules, described for the first time on a flat metallic surface by Moskovits in 1982 [79], which arise from the particular orientation of the molecule on the surface and the specific Raman mode symmetry. This effect can result in different relative intensities of the Raman peaks under SERS conditions. The influence of the surface selection rules on the enhancement efficiency depends also on the local field polarization. At a specific local field polarization, the Raman intensity will be dependent on molecular orientation. In addition, the molecule may change upon adsorption and become a surface complex [29]. This may result in small shifts and/or broadening of the Raman peaks. In some cases, Raman modes that are easily visible in the bare molecule can disappear upon interaction with the surface. Likewise, other modes can be activated and even new modes may arise. One of the first examples of calculated selection rules on a specific analyte was reported by Moskovits in 1984 about phthalazine on silver [80]. Only recently this study has been experimentally proven [81] and rediscussed in a more modern context, extended to more realistic SERS substrates, such as those containing hot spots [82].

Within the formal derivation of the EFs described above, the surface selection rule effects can be contained in the factor T and the SMEF of Equation 3.42 can be rewritten as:

$$SMEF^P = \left|\tilde{\boldsymbol{E}}_{loc}(\omega_L)\cdot\tilde{\boldsymbol{E}}^P_{loc}(\omega_R)\right|^2 \boldsymbol{T}\left(\hat{\alpha}_N, \boldsymbol{e}_{loc}(\omega_L), \boldsymbol{e}^P_{loc}(\omega_R)\right) \tag{3.49}$$

where

$$\boldsymbol{T}\,(\hat{\alpha}_N, \boldsymbol{e}_L, \boldsymbol{e}_R\,) = |\boldsymbol{e}_L \cdot \hat{\alpha}_N \cdot \boldsymbol{e}_R|^2 \tag{3.50}$$

Note that $\boldsymbol{T}$ depends on the local field polarization at the molecule position for both real excitation ($\boldsymbol{e}_L$) and virtual mathematical method ($\boldsymbol{e}_R$) and may be zero for an appropriate combination of $\boldsymbol{e}_L$ and $\boldsymbol{e}_R$. Since these last are unit vectors, it is clear, that for a given tensor $\hat{\alpha}_N$, the maximum possible value of $\boldsymbol{T}$ is $|\mu_{max}|^2$, where μ_{max} is the largest value of $\hat{\alpha}_N$. Considering all possible Raman tensors, one can show that:

$$0 \leq \boldsymbol{T}\,(\hat{\alpha}_N, \boldsymbol{e}_L, \boldsymbol{e}_R\,) \leq {}^{15}/_{4} \tag{3.51}$$

The largest value is obtained for a uni-axial tensor when both $\boldsymbol{e}_L$ and $\boldsymbol{e}_R$ are along the tensor axis. From this equation one can see, that the $\boldsymbol{T}$ factor has not a great influence on the total enhancement factor and is often not added in the enhancement considerations.

Another contribution to a correct EF estimation may be a rigorous definition and measurement of the surface coverage of the analyte molecule on the metallic substrate. This can in some cases change the final EF value of about one order of magnitude. It is therefore very important to know the effective active area available for the analyte molecule, their adsorption rate and the packing density over substrate. For the most common molecules, the last parameter can usually be found in literature, or can be calculated by various techniques, depending on the SERS substrate investigated (AFM measurements for macromolecules, optical ellipsometry, IR Spectroscopy or Electrochemistry on solid substrates [83]).

Despite these possibilities it is very difficult to be really quantitative in SERS sensing applications. Muniz Miranda et al. [76] and Lacy et al. [84] proposed a method for the quantitative determination of the adsorbed molecules on an active surface, based on the difference between functionalization solution concentration and remaining supernatant solution, measured by fluorescence and/or absorption spectroscopy. These procedures can be only effective using fluorescent and/or absorbing molecules in the UV-Vis range and present therefore a limitation on the basis of what written above. More recently, the issue of using SERS as quantitative analytical tool was discussed by Sackmann and Materny, which conclude that the SERS signal could be used as quantitative measurement only in a limited concentration range. This limitation is given by the interaction between analyte and plasmonic sample [85]. Under a given concentration no SERS signal could be obtained, while above a critical one, considerable fluctuations of the SERS intensities is observed, due to the modification of the SERS substrate through the analyte.

3.4.2 The nanostructure role in SERS sensing

The most challenging issue in SERS EF definition is, in our opinion, to understand if there is a direct relation between the wavelength of maximum plasmonic resonance of the used nanostructure and the enhancement efficiency at this specific excitation wavelength. In particular, it can be useful to understand if one of the two contributions to the total plasmonic extinction, i.e. the absorption and scattering cross section, plays the major role in the SERS enhancement mechanism. In a certain way, it would be interesting to create some kind of enhancement expectation on the basis of the plasmonic properties of the metallic nanostructure, by finding a direct spectral relationship between the far-field extinction and the near-field Raman enhancing properties of SERS substrates.

Since early history of SERS up to even some cases of recent literature, it is general assumption to predict highest SERS enhancement at excitation wavelengths equal to the wavelength of maximum plasmonic extinction. The highest local field intensity is expected to occur exactly at this specific condition. This fact found some inconsistencies in some experimental works [24,32,34,86]. In 2006 Le Ru et al. studied the spectral SERS enhancement profile of silver colloids, measured by SERS performed at two different excitation wavelengths (514 and 633 nm). The comparison with the extinction spectrum show a strong red shift of the SERS EF trend with respect to the extinction one. Le Ru et al. supposed that the SERS resonance is sensitive to the local field enhancement which is not always directly visible in the extinction, in particular in presence of coupled plasmon resonances [86]. Similar considerations where made by Joseph et al. [24], which probed the enhancement efficiency of gold nanospheres with different dimensions. Although the extinction spectra of different particle dimensions showed very little changes in the plasmonic resonance maxima (~520 nm), the SERS measurements performed out of plasmonic resonance (633 nm) showed a even better enhancement efficiency at increasing particle dimension.

Except this few examples, not much discussion is spent on finding a relationship between far field (plasmonic resonance through UV-Vis absorption spectroscopy) and near field measurements (SERS). In many works the EF measurements are performed only at one or two excitation wavelengths, near the extinction maximum or even out of the plasmonic range without any specific justification [87]. The enhancement behaviour at other wavelengths is often not proven [75,88]. The resulting conclusion of highest enhancement at the LSPR maximum is therefore sometimes a bit hasty.

A good approach to discuss this issue, is to measure an excitation profile using many different laser wavelengths, like already done by McFarland [33]. In his work, McFarland stated that the maximum SERS enhancement factor for Ag nanoparticle arrays, is shown to occur for excitation wavelengths that are blue-shifted with respect to the LSPR maximum. Moreover, measuring the EF at different vibrational modes of benzenethiol, the smaller Raman shifted peak shows a maximum enhancement closer to the LSPR maximum than that of a larger Raman shifted peak. The last statement may be a general guideline in EF determination, although rarely a discussion about the influence of Raman emitter can be found in other works. For the first statement, instead, one has to be careful because the enhancement behaviour is certainly dependent on the type of substrate under investigation. The results of McFarland did not find many confirmations in other works. Indeed, as described above, in many works a red shifted maximum in SERS efficiency, instead of a blue shift, is reported.

In fact the discrepancy between far field measurements and near field SERS evidences, can often lie in the exact geometry of the nanostructure. One of the most important aspects that for sure is responsible for the above described situation of discrepancy is the presence of hot spots in the nanostructured substrate, already predicted in the works of Le Ru [86] and Joseph [24], where the maximum of SERS efficiency is red-shifted compared to the extinction profile. A very interesting work by Kleinman et al.[34] investigates the simplest form of a hot spot dominated system, a single gold nanoantenna, i.e two gold nanoparticles at a fixed distance. Kleinman demonstrated that SERS efficiency profiles of hot spot dominated systems show little dependence on the far field scattering properties because of differences between near and far field LSPR effects as well as because of excitation of new plasmon modes by the Raman dipole emitter in proximity to the hot spot. These results show the importance of dipole reradiation, with the excitation of “dark” plasmon resonances, typically inaccessible by plane wave excitation. The dipole emitter can couple to plasmonic modes on the nanoantenna that are difficult to excite with a plane wave but dominate the SERS behaviour. Part of this results were suggested before this work by simulation and electromagnetic theory of Litz et al.[89], which propose that interfering plasmonic excitations resulting from scattering of a surface localized emitter, are capable of generating intense local fields at certain excitation energies, without phase coherence of the individual particle plasmons (far field).

Beyond this explanation of no correlation between far field and near field, Zuloaga et al.[90] gave an interpretation of the red shift of the SERS enhancement peak with respect to the

extinction LSPR. The authors explained the phenomenon with a damped harmonic oscillator model for conduction electrons undergoing plasmonic excitation. In this case, the maximum oscillator displacement occurs at a frequency below the fundamental frequency of the oscillator. The difference between the frequencies is related to the damping in the nanostructure. The magnitude of red shift depends directly on whether the damping is intrinsic within the metal of the nanoparticle or is a radiative damping of the localized plasmon.

As can be observed from this discussion, it is already not clear how the SERS near field properties can be related to extinction far field behaviour. It seems that the behaviour is strongly dependent on the SERS substrate under investigation and on the analyte used.

In the next two paragraphs, the state of art of sensing applications in liquid and on solid substrates is treated separately, in order to underline the important differences and critical issues.

3.4.3 Detection in liquid phase

One of the simplest SERS systems, and the most easy to understand, is the metallic colloidal suspension, predominantly made of Ag or Au nanoparticles. The synthesis procedures are usually very simple providing therefore an easy and cheap route for SERS substrate production. First claims of single-molecule SERS detection were made with silver nanoparticles in water by Nie in 1997 [21]. Since then metallic colloidal solutions were used for many SERS applications in liquid phase, but also for deposition on solid substrates (see next paragraph).

The use of Au or Ag colloidal nanoparticles depends strongly on the application. Gold nanoparticles are usually more easy to synthesize and more stable in time than silver ones, particularly in term of resistance to surface oxidation. Also the chemistry of molecular binding to gold is better understood in general. Despite these apparent advantages, Ag colloids were used, especially in the 400-650 nm range, because of larger electromagnetic enhancements. Although the plasmonic resonance for the two nanostructured metals lie in two different spectral ranges (~520 nm for Au and ~400 nm for Ag), the dielectric function of Ag is the most favourite over all the Vis region (see paragraph 2.1.1 of Chapter 2). The better efficiency of Ag nanoparticles is confirmed by literature works, where the EF in liquid phase is measured through Equation 3.43. Muniz Miranda et al.[76] found EF values of about 4×10^5

for phenazine adsorbed on silver nanoparticles in solution with an excitation wavelength of 514.5 nm for the 1408 cm^{-1} Raman mode. A similar investigation was done on gold nanoparticles by Joseph et al.[24], which report a EF for individual gold nanospheres with crystal violet at 633 nm of about 10^2 - 10^3. Despite the analysis of the EF dependence on the gold nanoparticles dimension, they perform also an investigation on the influence of analyte concentration. The last becomes very important in finding the best conditions to measure the EF and to emulate a sensing application, because high analyte concentrations can often induce modifications of the metallic surface and therefore of plasmonic properties. In fact, the work reports an increasing trend in the EF for higher analyte concentration because of formation of hot spots through nanoparticles aggregation.

The use of a sensing device in liquid phase would have some practical advantages, as for example the simplicity of preparation and characterization and, in case of single nanostructures, also a high accuracy in EF determination. On the other hand, one has to take care of the experimental conditions, like analyte concentration, exact nanostructure geometry and sometimes laser power, which can, in turn, induce some surface modifications.

3.4.4 Detection on solid substrates

The term ‘solid’ substrate is generally referred to 2D planar devices, where the plasmonic property is given by metallic nanostructures in a fixed geometry onto a solid support. The realization of these substrates can occur through many different methods, which range from complex lithographic processes to simple deposition of colloidal nanostructures onto a supporting material like glass or silicon. Some recent reviews describe the different preparation methods and last efforts in realizing stable and reproducible SERS substrates [22,91,92]. Wet chemistry synthesis and following deposition techniques allow the fabrication of large quantities of substrates in an easy and cheap way. The synthesis are commonly performed in water solution and the deposition methods can range from simple dip or spin coating over different substrates [23,93] to electrochemical deposition over conductive supports [25,94]. Lithographic ones offer the possibility to fabricate periodic arrays with specific particle shapes, placement and orientation, but are usually more expensive and difficult. The two most common examples are nanosphere lithography [95] and electron beam lithography [96,97].

The basic differences in the characteristics of solid devices, in contrast to nanostructures in liquid phase, are the 2D and fixed geometry, which induces variation in the plasmonic

properties of the nanostructured surface. As was already highlighted in the previous chapter, the dielectric constant of the environment has a great importance in understanding the plasmonic behaviour of the embedded nanostructure. In most cases, however, the environment may not be as simple as a homogeneous and isotropic medium. In case of planar substrates the dielectric constant will be in some way 'half-embedded' in the dielectric environment ϵ_M and 'half-embedded' in the substrate ϵ_S. It was demonstrated [47] that the situation could be approximated by nanoparticles embedded in an effective dielectric constant ϵ_{Eff}, lying somewhere between ϵ_M and ϵ_S. This approach results useful in many cases for qualitative and phenomenological analysis.

To properly characterize the SERS substrate, SSEF (or SMEF) should be measured (Equation 3.45). As was already described in the previous paragraphs, it is necessary for SSEF to be independent on the chosen analyte, in order to compare the enhancement performances of different substrates. It is therefore suitable to use a molecule, or better a Raman mode, for which there is no chemical enhancement. The information of absent *chem*-enhancement can be extracted from literature works [29,30] or experimentally proven by comparing the SSEF of a given Raman mode of different analytes[66]. Another important role is played by the nanostructured geometry. The knowledge of the geometrical parameters, described through $\delta_{ns}A_m$, which can be measured by SEM, TEM or AFM images, significantly improves the accuracy of the SSEF value. The same counts for the molecular packing density δ_{surf}, which is, contrary to the geometrical parameters, hardly measurable. Usually one has to trust in literature values, being aware of making an approximation in the EF measurement. Finally it is also significant to know exactly the setup configuration, in order to measure the high of scattering volume, H_{eff}.

It is again important to point out that *em*-SSEF is dependent on excitation wavelength and vibrational mode energy, which have necessarily to be clearly defined when comparing different *em*-SSEFs. This is an important aspect which, in some literature works, is mishandled.

Chapter 4

SYNTHESIS AND CHARACTERIZATION OF METAL NANOPARTICLES

4.1 Nucleation and stabilization mechanisms of colloidal synthesis

To understand the nucleation and stabilization mechanisms of colloidal nanoparticles, thermodynamic rules have to be introduced. These explain the mechanism of the colloidal synthesis, where the reaction of precursors in solution gives rise to solid nanoparticles.

Two different nucleation processes can be distinguished in thermodynamic theory: the homogeneous nucleation and the heterogeneous one[98]. The homogeneous nucleation occurs in an oversaturated solution through the growing of nucleation sites, while for the heterogeneous one the growing process occurs on defects like dislocations and grain boundaries.

Metal nanoparticles in solution are synthesized through homogeneous nucleation: in an oversaturated solution, the metal precursor is reduced and the metal atoms coalesce forming nucleation sites, which begin to growth.

This mechanism occurs spontaneously when the free Gibbs energy of the system is negative.

$$\Delta G = \Delta G_V + \Delta G_S < 0 \tag{4.1}$$

$$\Delta G_V \propto -\frac{4\pi}{3} R^3 k_B T ln\left(\frac{C}{C_0}\right) \tag{4.2}$$

$$\Delta G_S \propto 4\pi R^2 \gamma_{S-L} \tag{4.3}$$

ΔG_V is the volume free Gibbs energy related to the particle volume and is negative because energy is released in the liquid to solid transformation. ΔG_S is the surface free Gibbs energy. In this case the value is positive because energy is used in the formation of the liquid-solid interface.C and C_0 are the concentrations of precursor before the nucleation and at equilibrium,

respectively. The ratio between these quantities is called oversaturation and is the driving force for the nucleation process. γ_{S-L} is the specific free surface energy. The curves of the different Gibbs free energies as a function of the particle radius are shown in Figure 4.1.

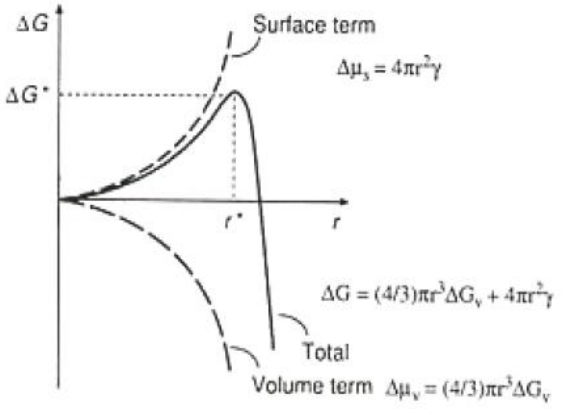

Figure 4.1: Free Gibbs energies as a function of the particle radius [98].

In Figure 4.1 *r** represents the critical radius: above this radius the total free Gibbs energy decreases dramatically and the nuclei become stable. *ΔG** represents the activation energy for this process. Both *r** and *ΔG** could be derived mathematically from the *ΔG* curve.

$$\boldsymbol{r^* \propto \frac{\gamma_{S-L}}{k_B T ln\left(\frac{C}{C_0}\right)}\ ;\ \Delta G^* \propto \frac{{\gamma_{S-L}}^3}{\left\{k_B T ln\left(\frac{C}{C_0}\right)\right\}^2}} \qquad (4.4)$$

Both the equations are inversely proportional to the oversaturation: the smaller the oversaturation value the smaller the critical radius and the lower the activation energy.

In Figure 4.2 a scheme of the concentration of precursor as a function of time is shown: when the solute concentration, during nucleation, decreases to the minimum nucleation concentration, nucleation stops and growth begins.

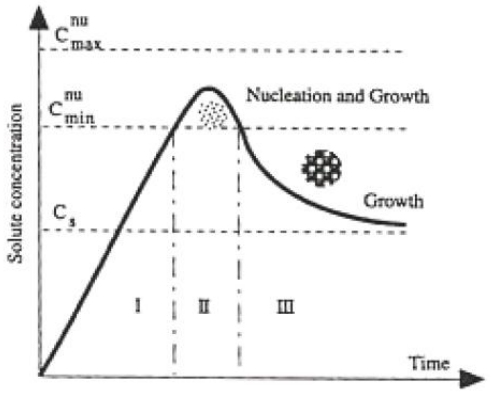

Figure 4.2: Solute concentration as a function of time: nucleation and growth processes [98].

The growth process can be divided in two steps: the diffusion of the solute to the nuclei and the adsorption and incorporation of the solute into the nuclei. The limiting step will determine the dimensional distribution of the nanoparticles in solution. If the growing process is controlled by diffusion, the distribution will be monodisperse. If the diffusion is fast and the limiting process is the adsorption one, the distribution will be much more polydisperse.

Another important aspect is the stabilization of the nanoparticles in solution. The aggregation process in solution through Van der Waals forces is a thermodynamically favored mechanism and has therefore to be controlled for keeping the nanoparticles monodispersed in solution. The stabilization of the colloidal solution can be achieved with two different approaches: the electrostatic or the sterical one.

Derjaguin, Landau, Verwey and Overbeek, from which the term DLVO theory was derived, developed in the early 1940 the theory of electrostatic stabilization of colloidal nanoparticles[99]. This theory states that the stability of the colloidal solution is given by the sum of attractive Van der Waals forces and repulsive ones given by the double electrostatic layer on the nanoparticles surface. The combination of opposite forces gives rise to an energy barrier which avoids particle coalescence. This scheme is depicted in Figure 4.3.

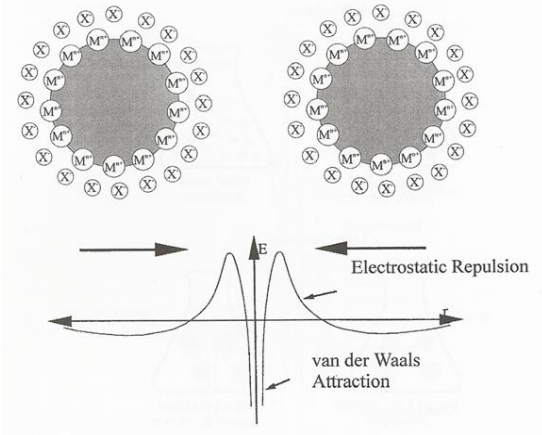

Figure 4.3: Scheme of the DLVO theory [99].

When the energy barrier is exceeded the particles begin to coalesce due to Van der Waals forces. For stable solution the energy barrier has to be high enough, that means that the double electrostatic layer has to be thick enough.

The presence of ions in solution (the ionic force slightly increases) can cause a sort of a secondary minimum, where little nanoparticles aggregates can be stabilized. This situation is very difficult to obtain experimentally.

The charging mechanism of the nanoparticles surface can be achieved through ionization or dissociation of surface species or by adsorption of charged species. The final surface charge is then balanced by counter ions, a part of which is bounded near the nanoparticles surface in the Stern (or Helmholtz) layer, where the surface potential decreases linearly with distance, as shown in Figure 4.4. The remaining counter ions will termically fluctuate near the surface forming the diffuse double electrostatic layer of Gouy, where the surface potential decreases exponentially.

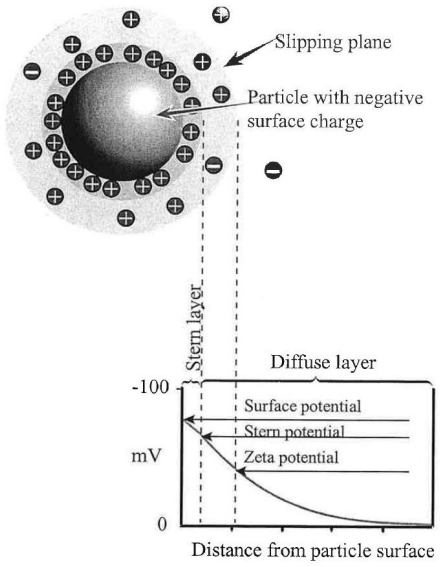

Figure 4.4: Scheme of the electrostatic double layer and potentials in the diffuse layer [99].

The surface potential at the interface between electrostatic double layer and solution is known as Z-potential. The value of this surface potential, which can be measured experimentally, gives an idea of the stability of the colloidal solution. If the value is between 30 and 50 mV, negative or positive, the colloid is stable. For absolute values below 30 mV the nanoparticles in solution tend to aggregate. The Z-potential values depend on different factors, like pH and ionic force: the lower the pH value and the higher the ionic force, the more instable will be the colloidal solutions.

The steric stabilization is, in some cases, more easy to obtain, but can cause other complications. In this case the nanoparticle surface can be functionalized with molecules, like polymers or surfactants. The steric volume of the molecules avoids the nanoparticles to come too close together and therefore to aggregate. Moreover this kind of stabilization avoids the metal oxidation in solution (particularly strong for silver nanoparticles). The presence of

stabilizers on the nanoparticle surface can, nevertheless, be a problem for some sensing applications, where the analyte should be adsorbed on the plasmonic surface.

4.2 Materials and characterization techniques

Gold (III) chloride solution 30% w/w in dilute HCl, silver nitrate, silver acetate, sodium citrate dihydrate, Tetraethyl orthosilicate, Tetrakis(hydroxymethyl)phosphonium 80% in water, (3-Aminopropyl)trimethoxysilane, Tetraoctylammonium bromide, sodium borohydride, formaldehyde solution, potassium carbonate, 1-Dodecanethiol and Polyvinylpyrrolidone (average mol wt 40000), purchased from Sigma-Aldrich, and m-PEG-SH (mol wt 2000), purchased from Laysan Bio Inc., are used without further purification. The synthesis were performed in deionized Milli-Q filtered water or in toluene.

The colloidal samples were optically characterized through UV-Vis absorption spectroscopy and morphologically characterized through dynamic light scattering (DLS), Z-potential, atomic force microscopy (AFM) and transmission electron microscopy (TEM).

4.2.1 UV-Vis Absorption Spectroscopy

The UV-Vis absorption spectroscopy spectra were collected with a Cary5 Varian instrumentation, working in a wavelength region between 175 and 3300 nm. The radiation source for the UV region is a deuterium lamp, while a quartz-iodine halogen lamp is working in the visible and infrared region. Two photomultiplicators for the UV-Vis region and a PbS_2 photocell for the IR are used as detectors. All measurements were performed with quartz cells with optical path of 1 or 10 mm.

4.2.2 Dynamic Light Scattering and Z-potential measurements

The DLS technique is an easy and fast technique to determine the size distribution profile of macromolecules or small particles in suspension in the order of the nano or micrometer.

The experiment is based on the interaction between a laser radiation with the liquid sample, where the scattered light of the particles is collected and analyzed. The DLS instrumentation observes the time-dependent fluctuations of the scattering intensity given by the Brownian motion of the particles in the liquid. The distance between the scatterers in the solution is constantly changing in time and the scattering intensity from a definite volume, collected by the detector, depends on how many particles are inside. The dynamic information of the

particles is derived from an autocorrelation of the intensity trace recorded during the experiments, i.e. the intensity at time t+τ is correlated to the intensity at time t.

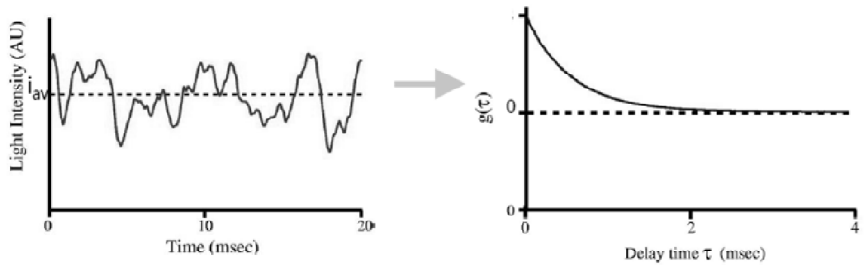

Figure 4.5: Light intensity fluctuation (left) and related correlation function (right).

Within the DLS instrument there is a component called a digital correlator, which measures the degree of similarity between two signals over a period of time and constructs the correlation function $G(\tau)$:

$$G(\tau)^2 = \langle (I(t) - I_{av})(I(t+\tau) - I_{av}) \rangle \quad (4.5)$$

For a large number of monodispersed particles in Brownian motion, the autocorrelation function can be written as:

$$G(\tau)^2 = ce^{-2h^2 D\tau} \quad (4.6)$$

$h = (4\pi n/\lambda) sen(\theta/2)$, c is a constant and D is the diffusion constant, which is related to the hydrodynamic radius through the Stokes-Einstein relation:

$$R_h = \frac{k_B T}{6\pi\eta D} \quad (4.7)$$

where k_B is the Boltzmann constant, T the temperature and η the viscosity of the solvent. By fitting the autocorrelation curve with Equation 4.6, the hydrodynamic radius of the particle can be calculated through Equation 4.7. The knowledge of temperature and viscosity and an adequate sample concentration is needed for optimized measurements.

For Z-potential measurements, an electric field is applied inside the liquid sample: the charged particles will then move with a velocity proportional to the applied field. The particles mobility depends on the dielectric constant, the solution viscosity and the Z-potential. In our work DLS and Z-potential measurements are performed on nanoparticles in solution with a Malvern Zetasizer Nano ZS with a 633 nm laser excitation.

4.2.3 Atomic Force Microscopy

Scanning probe microscopy (SPM) is the general term for describing microscopies that analyze the structure of a surface exploiting the interaction between the sample and a probe tip of the instrumentation. Different interaction forces give rise to different SPMs. In this work we used the atomic force microscopy, which involves Van der Waals forces. The scheme of the instrumentation is depicted in Figure 4.6 [100].

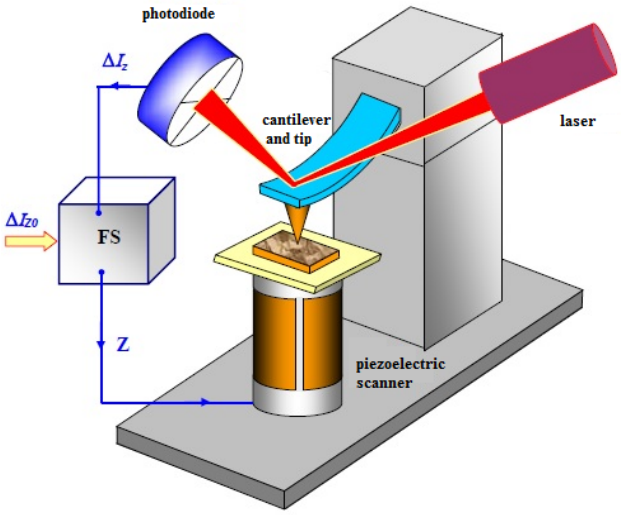

Figure 4.6: Scheme of an atomic force microscopy instrumentation [100].

The general working mechanisms of an AFM is based on a P parameter, which describes the interaction between the tip and the sample. The parameter P depends on the distance between tip and sample and can be written as (P=P(z)). When the distance changes, the P parameter changes and the feedback system (FS) records the differential value $\Delta P=P-P_0$, where P_0 is a starting value, set by the operator. The differential signal is converted in a potential V (x,y), is amplified and then sent to the piezoelectric scanner, which varies the distance tip-sample in order to bring it to the starting value. This mechanism allows screening the surface topography of a solid sample. In case of AFM, the probe tip is anchored on an elastic cantilever which is deflected depending on the interaction force between tip and sample. The cantilever deflections are recorded through a laser: different cantilever deflections induce different laser angle reflections. An appropriate transducer translates the laser reflection angle variations in tip-sample distance variations.

Measurements were performed in tapping mode with a lock-in system in order to increase the signal to noise ratio. The cantilever oscillates at a resonance frequency ω_0. When the tip

approaches the sample, the oscillation amplitude changes due to interaction forces. The resonance frequency curve is shifted and the variation of intensity A is the feedback signal, as shown in Figure 4.7.

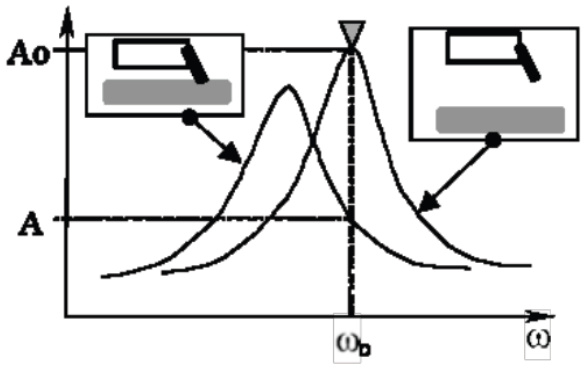

Figure 4.7: Scheme of the variation of the resonance curve of the tip in a tapping mode AFM system [100].

The instrumentation used is a NT-MDT (NT- MDT-Europe B.V., Nuenen, the Netherlands) system, working in air, in tapping mode, with a piezoelectric scanner at 3 μm (in collaboration with Dr. Piero Schiavuta, CIVEN-Nanofab, Marghera). The AFM images were analyzed with appropriate softwares.

4.2.4 Transmission and scanning electron microscopy

The transmission and scanning electron microscopies (TEM and SEM) give the possibility to analyze the morphology of a sample at high resolution.

With TEM the resolution can even reach the crystal lattice dimension (HRTEM with bright field and/or dark field images). Moreover chemical composition information can be achieved through *Dispersive X-ray Spectroscopy* (EDX) and *Electron Energy Loss Spectroscopy* (EELS) [101 102]. In Figure 4.8 the scheme of a TEM instrumentation is shown.

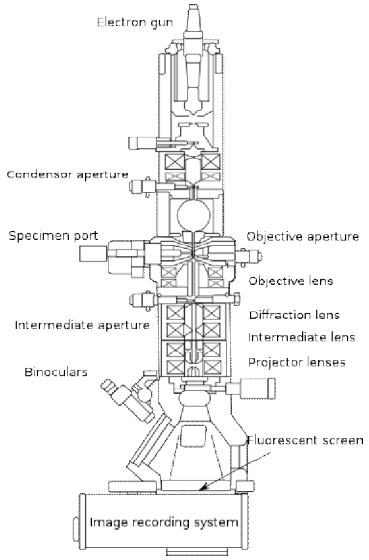

Figure 4.8: Scheme of a transmission electron microscopy instrumentation.

The electron generator is a field emission gun where the electrons are extracted from a tungsten filament. The electron beam is then homogenized by a diaphragm and then focused on the sample by electronic and magnetic lenses (condenser). The interaction between electrons and the sample atoms can generate elastic or inelastic scattered electrons. The elastic scattered electrons were deflected by an objective lens on a focal plane, where the diffraction image is collected. After the focal plane the scattered beams are then focalized through another lenses system on the image plane, where the constructive and destructive interference of the electrons creates the sample image. From bright field images it is possible to construct the dimensional distribution histogram of the observed nano-objects. The inelastic scattering, instead, can be collected and analyzed through EDX or EELS. The energy of the x-rays scattered by the sample and the energy of the transmitted electrons can be analyzed, respectively. From these measurements information about the chemical composition of the sample can be extracted. The resolution of the TEM instrumentation is strongly dependent on the lenses system, but can reach, generally, one million magnifications.

In the present work the samples were prepared by putting some drops of liquid sample on a cupper support mesh grid. To prevent charge build-up at the sample surface, the samples need to be coated with a thin layer of conducting carbon material. The instrumentation used is a Field-Emission Gun (FEG) Tecnai F20 Super-twin (S)TEM operating at 200 keV, equipped with an EDAX (energy-dispersive X-ray spectrometer), a Gatan EELS (Electron energy loss

spectrometer) and a Scanning TEM attachment (measurements done in collaboration with Prof. Giovanni Mattei of the Department of Physics, Padova University).

In case of scanning electron microscopy, the image of the sample is realized observing the scattered secondary electrons from a sample, not the transmitted ones. The scheme of a typical SEM instrument is shown in Figure 4.9.

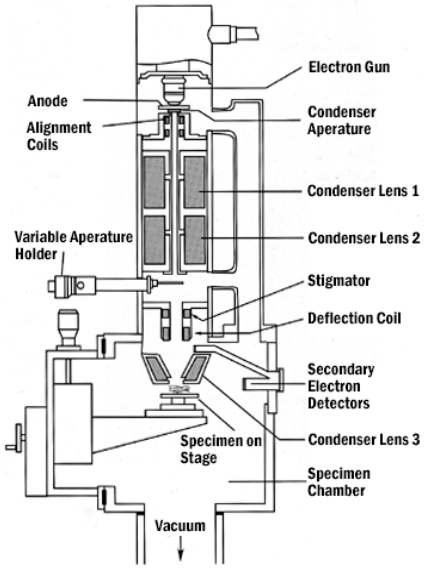

Figure 4.9: Scheme of a scanning electron microscopy instrumentation.

An electron gun emits primary electrons from a tungsten or lanthanum hexaboride filament, which are accelerated towards an anode, condensed by a condenser lens and focused by the objective lens on the sample, with a spot size of about few nm. The electron beam energy ranges typically from a few hundred eV up to 30 keV. The condenser lens system, which is composed of one or more lenses, determines the beam current on the sample. The electron beam passes through pairs of coils or pairs of deflector plates in the electron column which deflect the beam horizontally and vertically in order to scan the sample over a rectangular area of the sample surface. The column and the target chamber are under high vacuum (10^{-6} –10^{-7} mbar).

When primary electrons interact with the target, many different interactions can occur between electrons and sample, within the interaction volume of about 100 nm to 1µm into the surface. The main phenomena which can occur are back-reflection of high-energy electrons by elastic scattering, production of secondary electrons by inelastic scattering and emission of electromagnetic radiation (X-ray). To detect all these signals, different detector must be used.

Scintillator-photomultiplier are commonly used for both secondary and backscattered electrons and solid-state detector for high-energy backscattered electrons and X-rays. The detector converts the radiation leaving the specimen into an electrical signal in order to form an image. The most common imaging technique consists in collecting the low-energy secondary electrons (E < 50 eV). These electrons originate within a few nanometers from the surface. The brightness of the signal depends on the number of secondary electrons reaching the detector: if the beam enters the sample perpendicularly to the surface, the activated region is uniform around the axis of the beam and a certain number of electrons are emitted. As the incidence angle increases, the escape distance of one side of the beam will decrease and more secondary electrons will be emitted. In this way steep surfaces and edges tend to be brighter than flat zones, which results in images with a well defined, three-dimensional appearance. The spatial resolution depends on the size of the electron spot, which is related to the electron energy and the focusing system and it can be also limited by the size of the interaction volume.

4.3 Synthesis and characterization of gold and silver nanospheres

4.3.1 Turkevich method

Since the discovery of the metal nanoparticles importance in the late 19th century, many synthetical procedures were developed. One of the first and most studied synthesis is the Turkevich[103] one, published in 1951. The work reports the study of nucleation and growing processes of gold nanoparticels (Au NPs) through electronic microscopy. Many synthetical methods are listed in Turkevich's work, based on top down and bottom up processes. The most used synthesis in literature is, however, the citrate method, where a solution of sodium citrate is added to a gold precursor solution under reflux conditions. Turkevich demonstrated that the sodium citrate acts both as nucleation and reduction agent: the citrate ion forms a transition compound with the cloroauric ion $AuCl_4^-$ before reduction. Depending on the ratio between precursor and reducing agent, nanoparticles of about 2-25 nm can be synthesized. The dimensional distribution is commonly very sharp and the synthesis is highly reproducible. The particles are electrostatically stabilized by negative citrate ions adsorbed on the external surface. The Au NPs solutions are stable for long time, even for years.

In the Turkevich work also temperature and concentration dependence on the final particle dimensions was investigated: the particle dimension increases at decreasing temperature and decreasing citrate concentration in solution. The reaction is very fast (about 70-80 seconds). Also silver nanoparticles (Ag NPs) could be synthesized with the same method [104].

In this thesis work Ag and Au NPs in aqueous solution were synthesized through the citrate Turkevich method [103].

For the preparation of a Au NPs solution, 1 ml of a 39 mM aqueous solution of sodium citrate were added to 9 ml of a 1 mM solution of Gold (III) chloride 30% w/w in dilute HCl, under reflux conditions. The reaction is kept for 30 min under vigorous stirring. The final NPs concentration, calculated using the mean diameter extracted by TEM analysis, is about $7 \cdot 10^{12}$ NPs/ml for Au NPs dimensions of 14 nm diameter.

For the synthesis of Ag NPs, the same amounts of reagents were used. Two different precursors can be used, silver nitrate and silver acetate. For both precursors the NPs diameter, from TEM images, was about 40-45 nm and the concentration about $2 \cdot 10^{11}$ NPs/ml.

In Figure 4.10, UV-Vis absorption spectra of Au and Ag NPs solution are shown.

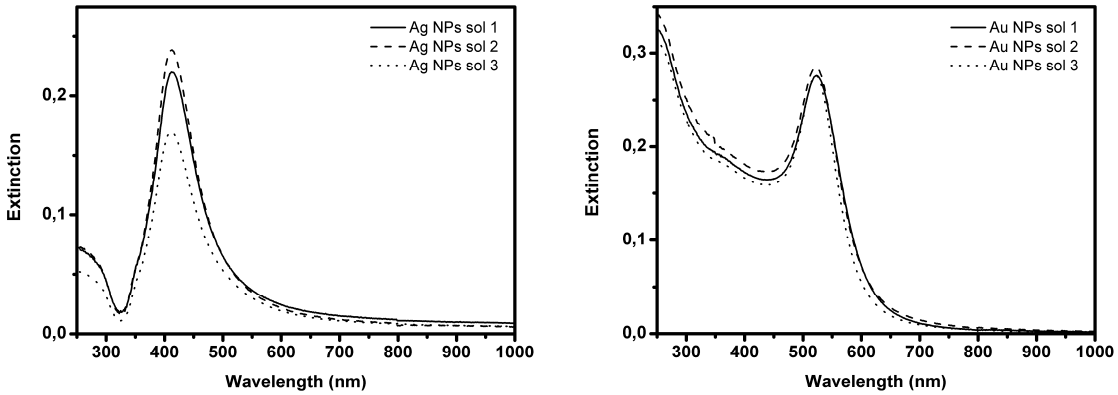

Figure 4.10: Extinction spectra of three different Ag NPs (left) and Au NPs (right) colloidal solutions.

As predicted, the synthesis is very reproducible, particularly with Au NPs. The synthesis of Ag NPs is much more difficult in terms of diameter and morphology reproducibility. In Figure 4.11 a TEM image of Ag NPs is shown, were a great dimensional and morphological polydispersity is visible. Despite spherical nanoparticles of different dimensions, also very long rods and aggregates are visible. In literature there are very less examples of

monodisperse and completely spherical AgNPs samples prepared by Turkevich method [105]. For silver, other more recent synthesis methods seems to be more efficient in obtaining spherical and monodisperse particles [25,106] (ref 25: AgNPs prepared in a collaboration work with Prof. Rizzi and Prof. Granozzi of the Padova University).

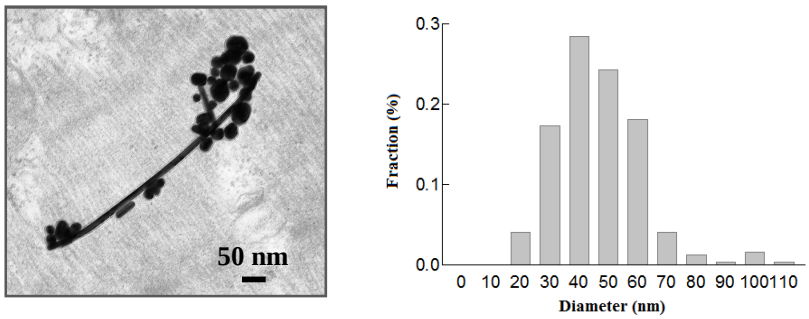

Figure 4.11: TEM image of a silver colloid solution (left) and histogram of the dimensional distribution (right).

Ag NPs are, moreover, less stable than Au NPs, because of surface oxidation in solution with consequent NPs aggregation. Au NPs are, instead, much more stable, and a monodisperse solution with spherical particles is easier to obtain. In Figure 4.12 a TEM image and the histogram of the dimensional distribution of Au NPs sol 3 is reported.

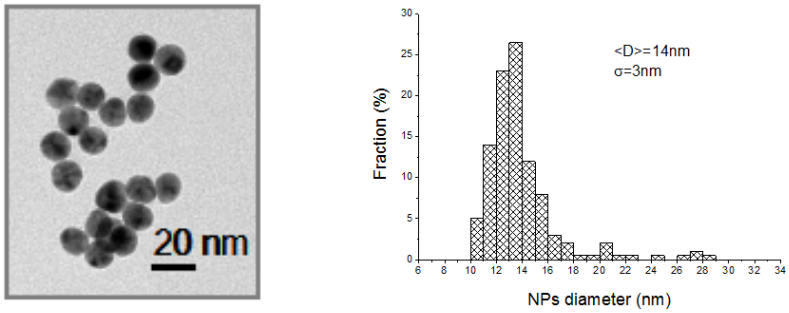

Figure 4.12: TEM image of a gold colloidal solution (left) and histogram of the dimensional distribution (right).

As sad before, the variation of the ratio between gold precursor and reducing agent can vary the nanoparticles dimension. In Figure 4.13 a comparison between two different syntheses is reported, where for Au NPs sol 4 the citrate amount is reduced by 10%. The NPs concentration calculated through the mean value of the TEM analysis for Au NPs sol 4 is about $2 \cdot 10^{12}$ NPs/ml. As can be seen by comparing the dimensional distribution of Au NPs sol 3 and the one of Au NPs sol 4, the dimensions increase from 14 nm to 21 nm diameter, as expected.

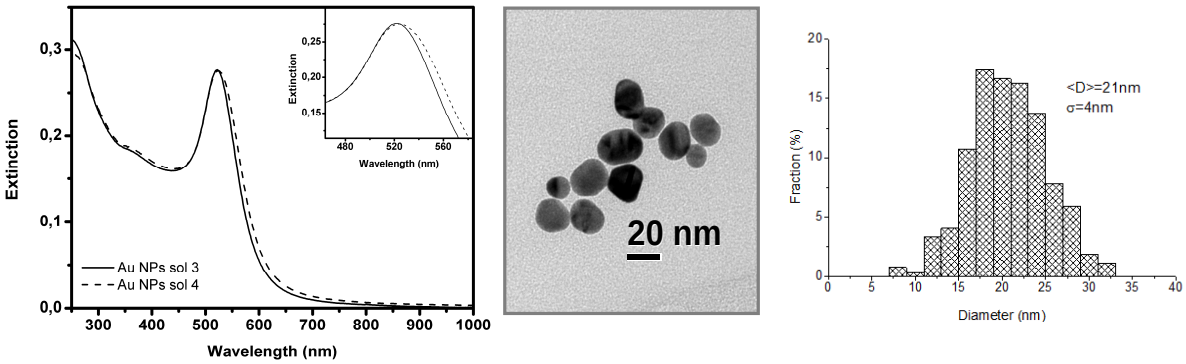

Figure 4.13: UV-Vis spectra of two Au NPs solutions with different ratio between precursor and reducing agent (left), TEM image of Au NPs sol 4 (middle), histogram of the dimensional distribution of Au NPs sol 4 (right).

The UV-Vis spectrum for the Au NPs sol 4 is slightly red shifted (from 519 to 525 nm) and the plasmonic band is broader, as expected (see the discussion of Chapter 2). This is also the demonstration that scattering processes become even more relevant.

The concentrations of Au NPs in solution, expressed as NPs/ml, can be calculated with different methods.

When a TEM analysis is available, one can either calculate a NPs concentration using the mean diameter extracted from the TEM histogram, as calculated above, or use a more precise mathematical method:

$$w(Au) = NPs \cdot \rho(Au) \cdot \frac{4}{3}\pi \sum_n R_n^3 A_n \tag{4.8}$$

$w(Au)$ is the weight of gold calculated from the precursor amount assuming all the gold precursor is reduced by sodium citrate (ICP-AES measurements are performed to demonstrate that more than 99% of gold precursor is reduced). $\rho(Au)$ is the bulk weight density of gold. R_n and A_n are parameters extracted from the TEM histogram: R_n is the mean radius for each n histogram column and A_n is the fraction of Au NPs with the n-th mean radius. By this way, the total number of nanoparticles (NPs) is calculated taking into account the observed distribution of NPs dimension and not only its mean value. The error affecting NPs is then calculated through a series expansion of the errors on R_n, according to the expression:

$$\sigma_{NPs}^2 = \sum_n \left[\left(\frac{\partial NPs}{\partial R_n} \right)^2 \cdot \sigma_{R_n}^2 \right] \tag{4.9}$$

Doing so, the errors on precursor mass and solvent volume are considered negligible, whereas the error of R_n (σ_{R_n}) is equal to the half width of each *n*-th column of the TEM histogram.
Once the total number of NPs is established, the concentration of Au NPs (NP/ml) is calculated as the ratio of NPs with the solution volume.
With this method, Au NPs sol 3 and Au NPs sol 4 have a nanoparticles concentration of (6.1 ± 0.3)×10^{12} NP/ml and (1.3 ± 0.2) ×10^{12} NP/ml, respectively.

A faster method of estimating the NPs dimension and concentration is fitting the UV-Vis spectrum in solution with the Mie-Gans relation and extracting the extinction cross section [107]. The resulting diameter and concentration for Au NPs sol 3 and 4 are 14 nm and 18 nm diameter and concentrations of 6.8 × 10^{12} NP/ml and 3.1 × 10^{12} NP/ml, respectively. The values of the Au NPs sol 3 are similar to that calculated with the above described TEM method (within 11% error) and could be a very interesting alternative when no TEM analysis is available. In case of Au NPs sol 4 the error is about 50%, due to the broader dimensiononal distribution.

The stability of the Au NPs solutions is tested through Z-potential measurements. Values of about -40÷ -45 mV are obtained, confirming the high stability of this nanoparticles in solution.

4.3.2 Brust method

In some applications, were organic solvents are used, metal nanoparticles can either be transferred from aqueous to organic solvents by capping the nanoparticles with appropriate molecules and polymers (see paragraph 4.3.3) or can be directly synthesized in the chosen solvent.
Little Au NPs of about 5-8 nm diameter can be synthesized through Brust method [108]. This strategy is based on the formation of metallic clusters functionalized with self assembled monolayers (SAM) of alcanthiols. The functionalization occurs during nucleation and growing because of the presence of two phases (water-toluene). The $AuCl_4^-$ ion is transferred from the aqueous solution to the organic one through the transfer agent tetraoctylammonium bromide (TOAB) and then reduced through an aqueous solution of sodium borohydride with the presence of dodencanthiol ($C_{12}H_{25}SH$), which acts as stabilizing agent. After the addition

of the reducing agent, the organic phase changes his color from colorless to dark brown in a few seconds. The chemical reactions involved are:

$$AuCl_4^-\,(aq) + N(C_8H_{17})_4^+\,(C_6H_5Me) \longrightarrow N(C_8H_{17})_4^+\,AuCl_4^-\,(C_6H_5Me)$$

$$m AuCl_4^-\,(C_6H_5Me) + n C_{12}H_{25}SH(C_6H_5Me) + 3me^- \longrightarrow 4mCl^-\,(aq) + (Au_m)(C_{12}H_{25}SH)_n(C_6H_5Me)$$

The electron source is the BH_4^- ion.

The nanoparticles are very stable in time and can be precipitated and redispersed in many organic solvents, contrary to the NPs in water.

In this work Au NPs of about 2-3 nm in toluene were synthesized adding 3 ml of a 30 mM aqueous solution of $HAuCl_4$ to 8 ml of a 50 mM solution of TOAB in toluene. Under vigorous stirring 0.1 ml of a 0.21 M solution of dodecanthiol in toluene and 2.5 ml of a 0.4 M aqueous solution of sodium borohydride are added drop wise to the precursor. The reaction is kept under stirring for 3 hours. The colorless aqueous solution is mechanically separated from the organic one and eliminated. The organic remaining is concentrated to 1 ml and brought back to the initial volume with ethanol. The solution is kept at -7 °C for one night. The black precipitate is filtered with cellulose (mesh 0.2 μm) and washed with ethanol in order to remove the dodecanthiol and TOAB excess. The purified black powder is then dissolved in 15 ml toluene. The NPs concentration for Brust Au NPs in toluene is about $5 \cdot 10^{15}$ NPs/ml. As said before the diameter of the nanoparticles is about 2-3 nm and therefore the plasmonic band is strongly damped and hardly visible [1], as shown in Figure 4.14.

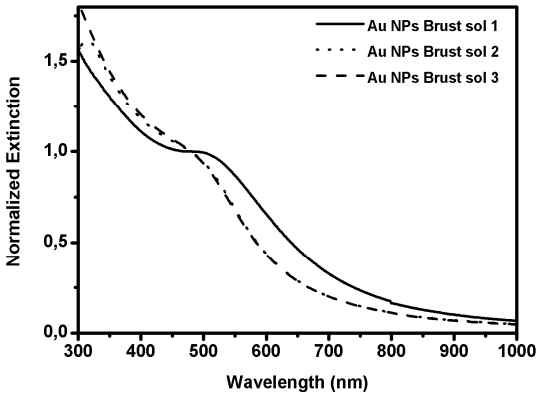

Figure 4.14: UV-Vis spectra of three different Au NPs Brust solutions.

The synthesis is, generally, very reproducible, as can be observed from sol 2 and 3. The spectrum of Brust sol 1, instead, is red shifted and the plasmonic absorption band at about 520 nm is slightly visible. In this case the Au NPs are probably bigger, around 3-4 nm. The syntheses were stable in time up to one year.

These gold nanoparticles are not interesting for plasmonic applications because of small dimensions. Since before 2000 some works reported synthetical strategies to control the size of nanoparticles in organic solvents stabilized by thiols [109 110], but no plasmonic behavior was described. In 2002 Kamat et al.[111] studied the influence of the ratio between reagents and of the solvent, on the properties of Brust Au NPs with little plasmonic behavior.

In the present work, an easy mechanism of growing Brust nanoparticles was developed, capitalizing on a literature work by Maye et al.[112]. The Au NPs were heated in solution in order to cause nanoparticles growing through Oswald ripening processes. The idea was to start from the classic 2-3 nm Au NPs Brust solution and to reach bigger nanoparticles dimension with a plasmonic extinction band.

The evolution of morphology and dimension in solution is a dynamic process induced by the chemical potential of the particles and the chemical environment. The chemical potential of small particles is bigger than that of bigger ones, therefore the growing of small particles is a termodinamically favored process. Moreover, the melting temperature of Au NPs increases with particle radius and the boiling temperature of the solution increases with increasing molar fraction of particles. These are important aspects of the heat treatment processes. In reflux conditions at high nanoparticles concentrations, it is possible to reach high boiling temperatures of the organic solvent. In case of toluene very high temperatures, about 150°C, could be reached. This temperatures are high enough to favor the desorption of the thiol molecules, and contemporary the melting and coalescence of the small nanoparticles to form the bigger ones.

The heat treatment was performed under reflux conditions (about 120-150°C) for 12 h, measuring the UV-Vis spectrum after every hour. After one attempt with the purified Brust solution, which didn´t give any results, the idea was to perform the treatment on the non-purified Brust solution, as described by Maye [112]. In his work, Maye described the role of the TOAB excess for the growing mechanism. The TOA^+ ion is an organic salt at low melting temperature (about 100°C), where the nanoparticles are highly soluble. The hydrophobic

chains stabilize the nanoparticles during the growing process and, at the same time, the charges of the quaternary TOA^+ salt stabilize the polar environment of charged nanoparticles during desorption of the thiol molecules.

The results of the heat treatment are summarized in Figure 4.15.

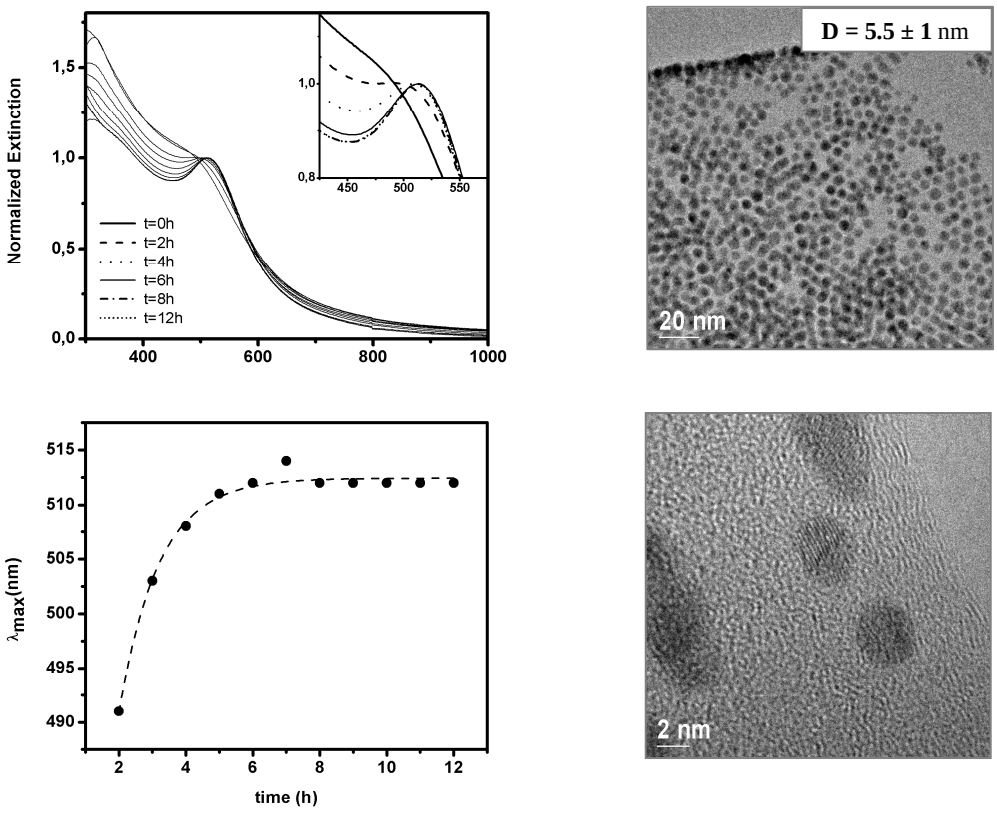

Figure 4.15: UV-Vis spectra recorded during heat treatment of Au NPs Brust solution with zoomed peak in the inset (top left), variation of plasmonic band position during heat treatment (bottom left), TEM images of treated Brust solutions (right).

After 8 h treatment, the gold nanoparticles reached the final thermodynamically most stable dimension, as can be observed from the bottom left spetrum: at that time the variation of the plasmonic band stops and reaches a final wavelength position at 512 nm with a well visible plasmonic absorption behavior. The growing process is fast with increasing exponential trend in the first 8 hours. The TEM images show a final dimension of about 5.5 nm.

4.4 Synthesis and characterization of gold nanoshells

Another very interesting plasmonic structure, in our opinion, are gold nanoshells (Au NSs), because of the easy tunability of the plasmonic band by varying the dimensions ratio between the inner dielectric core and the outer metal shell [52].

In literature there are many nanoshell structures reported, with different dielectric and metal materials, ranging from hollow gold nanoshells [113] to different dielectric cores [114]. The more frequently used dielectric cores are silica and polystyrene, because of their chemical and thermal stability and the transparency to light and solubility in aqueous solvents. All this properties are very interesting for biological and biomedical applications.

In the present work gold nanoshells with a silica core and a gold shell were prepared varying inner and outer radius dimensions. This nanostructure was firstly introduced by Halas in 1998[52], who describes the interesting plasmonic properties at different core and shell dimensions. The band intensity and wavelength position depends strongly on the ratio between core and final radius: at fixed core, a thinner shell should cause the red-shift of the extinction band. The plasmonic behavior can be explained on the basis of the hybridization theory (see Chapter 2, paragraph 2.5). Only a few years later the synthesis procedure was described [115]. The three principal reaction steps are shown in Figure 4.16.

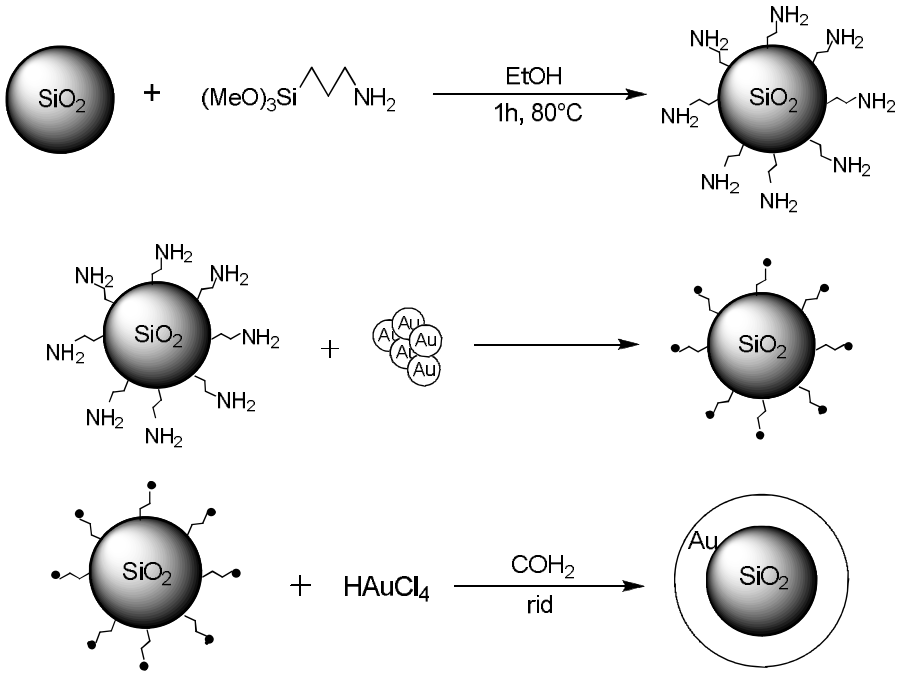

Figure 4.16: Reaction scheme of the three principal steps of gold nanoshell synthesis: functionalization of dielectric core with APTMS (top row), decoration of functionalized dielectric core with small gold nanoparticles (middle row), reduction of a gold precursor with formation of the gold shell (bottom row).

The silica particles are synthesized through Stöber method [116], based on the sol-gel chemistry. The sol gel precursor is the tetraethyl orthosilicate (TEOS) and the catalyst for the hydrolysis and condensation is ammonia. The quantity of the catalyst determines the final dimension of the silica nanoparticles: the less ammonia the smaller the spheres. The obtained nanoparticles present, generally, a monodisperse and sharp dimensional distribution.

The silica core is then functionalized, through sol gel chemistry, with aminopropyltrimetoxy silane (APTMS): the silane groups are covalently attached on the silica surface and expose the amino-groups, which are strongly affine to metals. The functionalized particles were then decorated with gold nuclei, separately prepared. This small gold nanoparticles (about 1 nm) act as nucleation sites for the final reduction of an aged gold/potassium carbonate solution through formaldehyde, with formation of the metal shell.

The kinetics of the reaction process was explained and modelized by Preston and Signorell in their work of 2009 [117]. Initially they suppose the presence of gold drops on the silica surface, which begin to growth during precursor reduction and then coalesce to form the final shell.

The limitation step is often the functionalization of the silica core with APTMS: an inhomogeneous functionalization can lead to a poor or inhomogeneous nuclei presence on the surface, which lead to a slow shell growth kinetics and often to a non uniform and incomplete shell formation. Moreover, a work by Halas in 2008 [118], reports the influence of different reducing agent on the final nanoshell morphology. Despite the much more complicated process, it seems that the use of $CO_{(g)}$ for the reduction of Au^{3+} leads to thinner and more uniform shells.

For simplicity the classical Halas approach was chosen to synthesize nanoshell, but the $CO_{(g)}$ approach could be a very interesting alternative for future work.

In the present work the nanoshell samples are synthetized as follows: To 50 ml of ethanol, different amounts of Ammonium hydroxide solution 30% are added (1.5-3 ml), dependent on the desired final silica particle dimension. Under vigorous stirring, 1.5 ml of TEOS are added slowly and dropwise. The reaction is kept overnight, under stirring. The particles concentration of the opaque solution is dependent on the particle dimension.

For the functionalization of the silica particles with APTMS, 5-15 µl of APTMS (dependent on silica dimension) are added to 10 ml of nanoparticles in ethanol. The reaction is kept overnight under stirring. The covalent bonding between silica nanoparticles and APTMS is

improved by heating the solution to 80°C. The solution (SiO_2@APTMS) is then purified by centrifugation and redispersed in ethanol.

The small gold nanoparticles for silica-APTMS decoration, are synthesized adding to 4.5 ml milli Q water 50 µl of a 1 M NaOH solution and subsequently 0.1 ml of a 68 mM THPC solution. The mixture is kept under vigorous stirring for 5 min and then a 0.2 ml of a 1% aqueos $HAuCl_4$ solution is quickly added. The obtained NPs solution has a concentration of $4 \cdot 10^{14}$ NPs/ml, calculated by estimating the NPs radius of 1 nm.

0.5 ml of SiO_2@APTMS are then added slowly and dropwise to 4.5 ml of nanoparticles solution and kept at room temperature for 5h. The brown solution of SiO_2@APTMS@Au is purified by centrifugation in order to eliminate the non atteched gold nuclei, and finally redispersed in H_2O Milli Q.

The gold/potassium carbonate (K_2CO_3) solution is prepared by dissolving 50 mg of K_2CO_3 in 100 ml H_2O Milli Q. After 10 min vigorous stirring 1.5 ml of a 1% $HAuCl_4$ aqueous solution is added to the salty water. The reaction is kept under stirring for 30 min, until the solution becomes colorless from bright yellow. The solution is aged at least for one night.

The final nanoshell synthesis is then performed by adding a different amount of SiO_2@APTMS@Au solution (50-300 µl) to 8 ml of aged $HAuCl_4$/ K_2CO_3 and finally 50 µl of formaldehyde. The different amount of SiO_2@APTMS@Au influences the final thickness of the gold shell. The NPs concentration depends on the silica core diameter.

Three different silica core diameters were obtained: (75 ± 18) nm, (92 ± 6) nm and (162 ± 10) nm. For each core diameter different gold amounts for the realization of different shell thicknesses are used. The UV-Vis and morphological characterization of the different nanoshell samples are reported in the following paragraphs. Depending on the silica core diameter the sample-sets are named Au NSs (R1=38; R2=x), Au NSs (R1=46; R2=y), and Au NSs (R1=81; R2=z), respectively. R1 and R2 are the inner and final radii of the structures (x, y and z values depend on the shell thickness of each single sample).

4.4.1 Gold nanoshells with silica core of 92 nm diameter: Au NSs (R1=46; R2=y)

The silica core for the first set of gold nanoshells was synthesized using 2 ml of Ammonium hydroxide solution 30% in the Stöber procedure. A first easy and fast measurement of the

particle diameter was performed through dynamic light scattering (DLS). The hydrodynamic diameter of these silica cores was D_{DLS}=(117 ± 16) nm.

As expected, the diameter from TEM analysis gives a smaller diameter of D_{TEM} = (92 ± 6) nm, as can be observed in Figure 4.17. Although the hydrodynamic diameter from DLS is for sure an overestimation of the real particle dimension, TEM images give probably an underestimated value, because the electron beam interacting with the sample causes a densification of the silica core with decreasing of the particle diameter. The error in estimating the diameter through TEM is, nevertheless, much smaller.

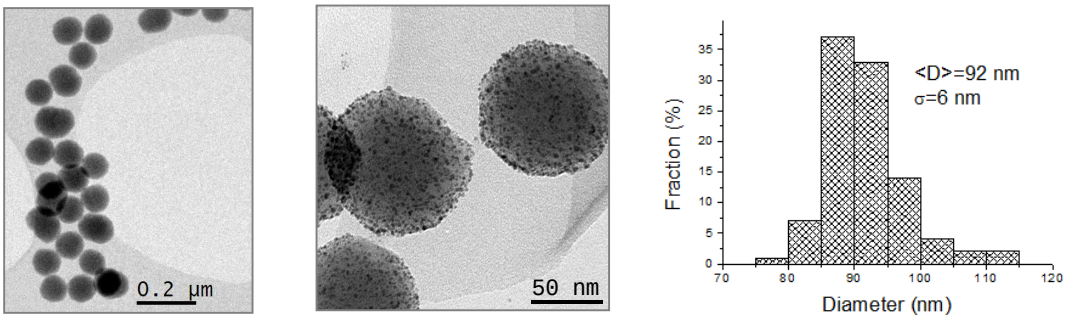

Figure 4.17: TEM analysis on SiO_2 (R1=46) cores: bare SiO_2 nanoparticles (left), SiO_2@APTMS@Au (middle) and histogram of dimensional distribution (right).

The silica cores have a very sharp distribution with a standard deviation of only 6.5 % on the average diameter (left TEM image and histogram distribution in Figure 4.17). EDX measurements on the bare silica particles give 67 % atomic presence of oxygen and 33% of silica, as expected. The decoration of the silica cores with gold nuclei, visible in the middle TEM image of Figure 4.17 seems to be homogeneous.

Using the average diameter value of TEM analysis, the concentration of native silica nanoparticles solution was 1×10^{13} NPs/ml, while the decorated silica solution SiO_2@APTMS@Au had a concentration of 8.2×10^{11} NPs/ml.

The final nanoshell samples were prepared adding a variable amount of SiO_2@APTMS@Au (50-200 µl) to 8 ml of aged $HAuCl_4$ solution and finally adding 50 µl of formaldehyde.

In Figure 4.18 the UV-Vis spectra of all the Au NSs (R1=46; R2=y) samples are reported.

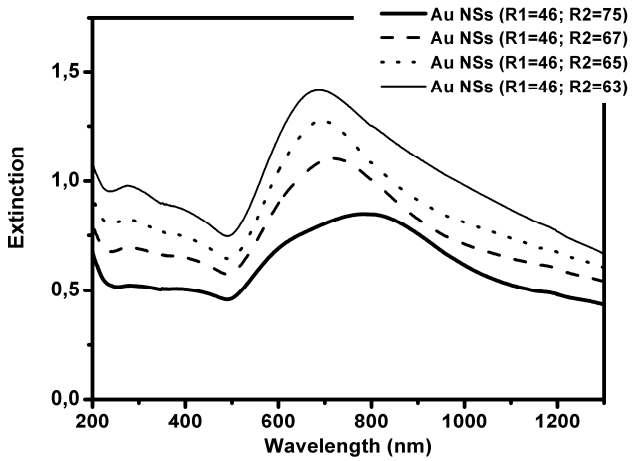

Figure 4.18: UV-Vis spectra of four different Au NSs (R1=46; R2=y) samples.

When TEM analysis of each single nanoshell sample is not possible, the shell thicknesses can be simply obtained through AFM measurements. The sample preparation is fast and easy: a few drops of nanoshell sample can be put on a silicon or soda lime slide. For better adhesion, in order to avoid AFM artifacts through nanoparticles collection from the tip of the AFM instrumentation, the glass slide can be previously functionalized with APTMS (the slide is put 5 min in a 60°C heated 1% APTMS toluene solution). Like for nanoshell synthesis, APTMS acts as binding element between slide and gold nanoshell.

First of all bare SiO_2 nanoparticles, or at least SiO_2@APTMS particles, have to be analyzed by AFM, in order to have a reference measurement when comparing the dimensions of nanoshell samples.

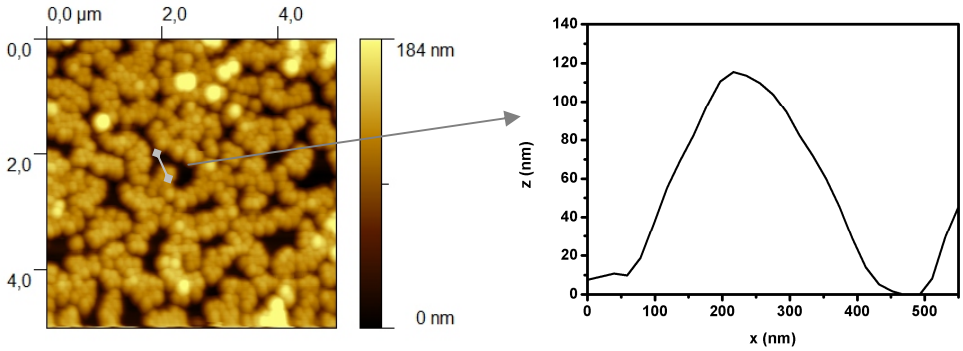

Figure 4.19: AFM image of the SiO_2(R1=46)@APTMS sample: morphology (left) and example of single nanoparticle profile (right). The arrow indicates the particle chosen for profile extraction.

The AFM image show a high particle density and the particles tend to aggregate in hexagonal closed packed conformation. Nonetheless the particles diameter could be measured through

an appropriate software by extracting the nanoparticles profile, like shown in Figure 4.19 (right). From a statistical measurement of 10 profiles extracted from the AFM image, a particle dimension of (122 ± 11) nm could be calculated. The dimension estimated through AFM measurements is bigger than the one measured through TEM. The reason is principally that the AFM images are influenced by the convolution of the AFM tip. In case of nanostructures comparable with the AFM tip (about 20 nm tip curve), the measurements could be affected by a not negligable error. The shell thickness is, however, measured from the difference of diameters extracted from AFM images, and should therefore not be strongly affected by the error given from the tip convolution.

In Figure 4.20, AFM images of all nanoshell samples are reported.

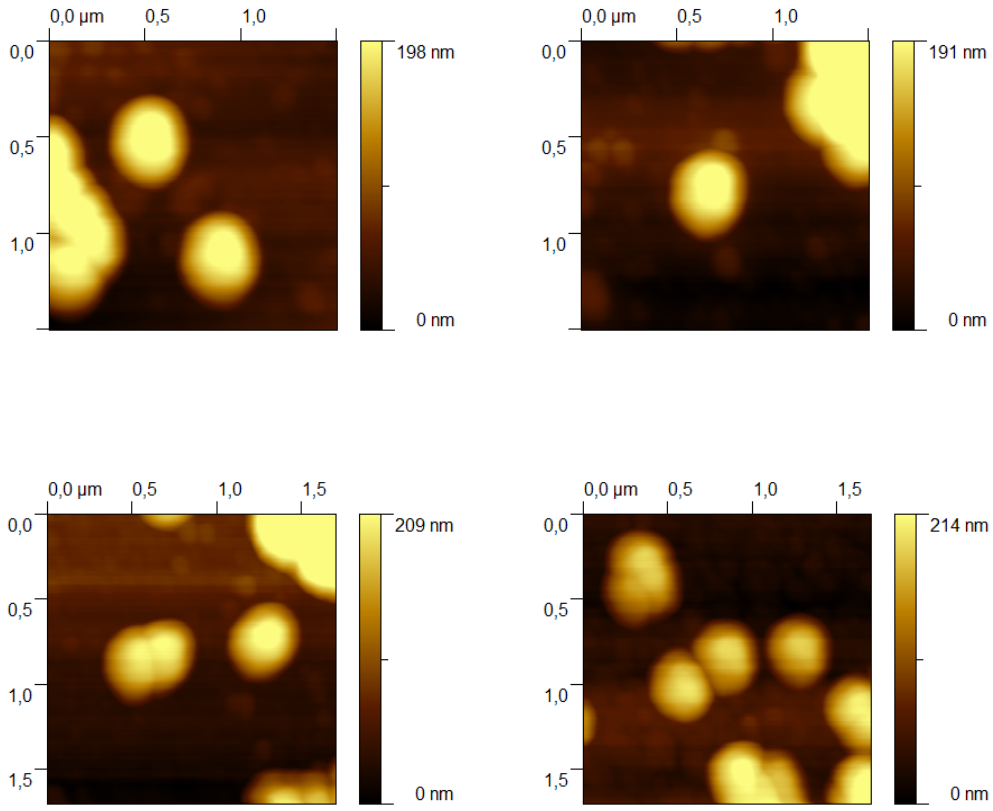

Figure 4.20: AFM images of the Au NSs (R1= 46; R2= 75) (top row left), Au NSs (R1= 46; R2= 67) (top row right), Au NSs (R1= 46; R2= 65) (bottom row left), Au NSs (R1= 46; R2= 63) (bottom row right).

For all nanoshell samples, 10 profiles are extracted and the average diameter with its standard deviation is calculated. From the difference between the measured nanoshell diameter and the SiO_2@APTMS diameter, the shell thickness is calculated. From the average TEM diameter and the average shell thickness, R1 and R2 for every nanoshell could be defined.

In Table 4.1 diameter, shell thickness and R1 and R2 values are reported for all samples.

Table 4.1: Diameter, shell thickness and R1, R2 values of Au NSs (R1=46; R2=y) samples

Sample abbrevation	Diameter AFM (nm)	Shell thickness (nm)	R1; R2 (TEM and AFM)
SiO_2(46)@APTMS	122 ± 11	--	R1= 46 ± 3
Au NSs (R1= 46; R2= 75)	180 ± 4	29 ± 6	R1= 46 ± 3; R2= 75 ± 7
Au NSs (R1= 46; R2= 67)	163 ± 15	21 ± 9	R1= 46 ± 3; R2= 67 ± 9
Au NSs (R1= 46; R2= 65)	160 ± 7	19 ± 7	R1= 46 ± 3; R2= 65 ± 8
Au NSs (R1= 46; R2= 63)	156 ± 5	17 ± 6	R1= 46 ± 3; R2= 63 ± 7

Depending on the amount of SiO_2(R1=46)@APTMS@Au used in the synthesis, the NPs concentration ranges from 0.5 to 1.5 × 10^{10} NPs/ml. Higher particles concentration results in a thinner gold shell.

From the UV-Vis spectra of Figure 4.18, the behavior of the plasmonic band at varying core to shell ratio, described in previous literature for spherical and homogeneous gold nanoshells [52,55,119], is not verified: at fixed core dimension, thinner shells do not result in a red shift of the band. Quite the opposite happens. From the thinner to the thicker shell the plasmonic band shifts form 690 up to 790 nm with the appearance of a second band at 610 nm for the thickest shell.

In order to understand the observed phenomenon, the results were observed on the basis of the literature work of Signorell et al.[117]. As mentioned before, Signorell studies the kinetics of the gold nanoshell formation during precursor reduction. The studies were performed on a silica core of 229 nm and the results are summarized in Figure 4.21.

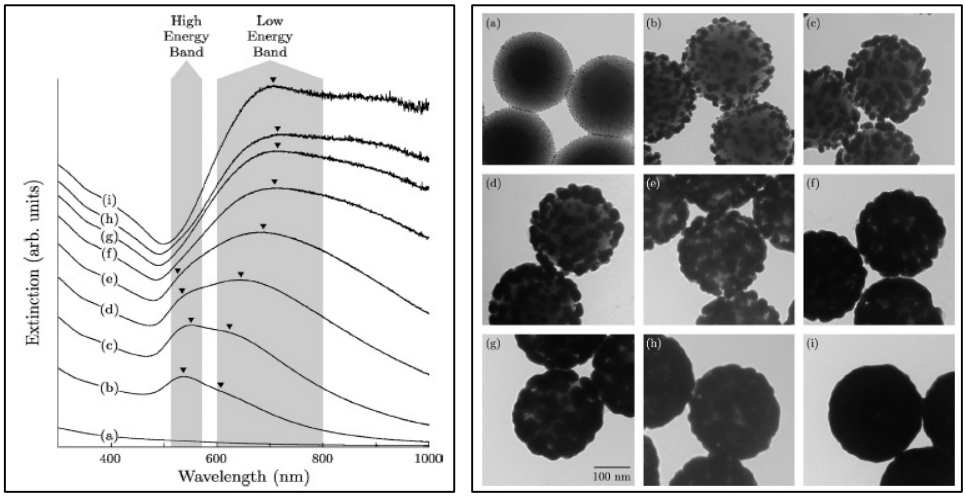

Figure 4.21: UV-Vis spectra at varying silica core coverage (left), relative TEM images (right).

Signorell demonstrates through DDA calculations that the incomplete core-shell system displays two distinct plasmonic bands, one around 500-600 nm (high energy band) and the other around 600-800 nm (low energy band). The calculations and experimental results show that at even higher silica core coverage, the low energy band intensity increases and red shifts. TEM images confirm this assumption. The phenomenon can be understood by supposing drop-like gold nanoparticles on the silica core at the beginning of the shell formation, and therefore the plasmonic behaviour is centered in the high energy region. At increasing gold amount, the gold drops begin to growth with the formation of a second band at lower energies, and finally the particles coalesce in order to form the final gold shell. In the final case the first band at small wavelengths disappears.

On the basis of this study, the experimental results of the present work can be better understood. The principal assumption is that in the most Au NSs (R1=46; R2=y) samples only the high energy band is present. In the Au NSs (R1=46; R2=75) sample, instead, the two distinct bands are well visible. The red shift of the high energy band and the appearance of the second band observing the Au NSs (R1=46; R2=y) samples at even higher shell thickness, indicates the behavior described by Signorell and therefore a not complete core coverage. This statement is confirmed by TEM images of three Au NSs (R1=46; R2=y) samples, shown in Figure 4.22.

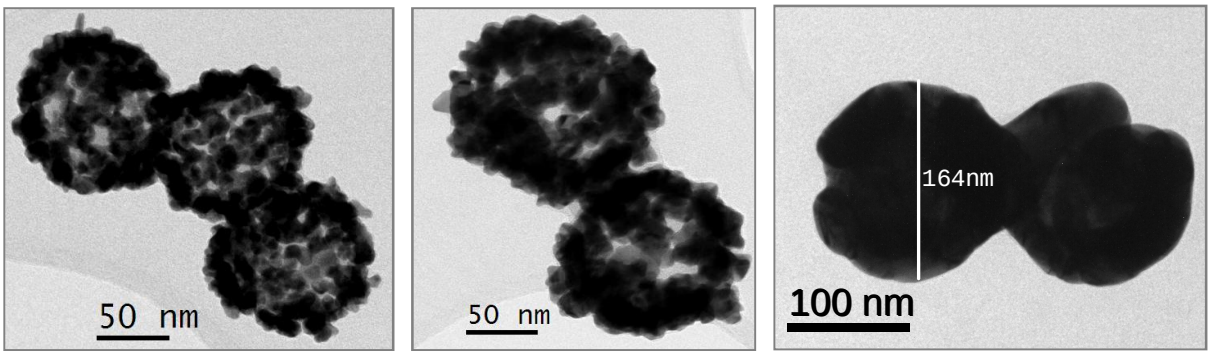

Figure 4.22: TEM images of Au NSs (R1=46; R2=63) (left), Au NSs (R1=46; R2=65) (middle) and Au NSs (R1=46; R2=75) (right).

As can be observed, the TEM images are very similar to the ones reported in Signorell´s work (c and d) in Figure 4.21. For thinner shells, the silica cores are not completely covered, the shell is roughened and inhomogeneous, while thicker shell samples seem to be covered and homogeneous.

The left image in Figure 4.22 shows particles with diameter around 115-120 nm, corresponding to R2 values of 57-60 nm; the middle TEM image shows diameter of 130-135 nm, which corresponds to R2 of about 65-67 nm, and from the right one, diameter values of 155-165 nm, corresponding to R2 of 77-83 nm, can be measured. These values are in agreement with the ones calculated combining TEM and AFM measurements, listed in Table 4.1.

As mentioned in the first paragraph of this chapter, colloidal synthesis is strongly influenced by external factors, like temperature and humidity, which can determine the reaction rate and therefore the final nanoparticle dimension and morphology. This issue is even more important when many steps are involved in the synthesis, like for nanoshells. Since SiO_2 and SiO_2@APTMS solutions are stable for years and can be reused, nanoshell preparation is limited by the gold nuclei decoration and final gold precursor reduction steps, which are the most critical ones. Therefore it happens often, that optical and morphological properties of identical prepared nanoshell solution are no longer the same. Since TEM and AFM analysis is expensive and slow and not always available, UV-Vis spectroscopy becomes the most frequently used technique. It is, anyhow, the principal one that describes the plasmonic properties of the samples, and this is the most important aspect for nanoshell applications.

All following syntheses, with same silica core, were principally characterized through UV-Vis spectroscopy. The dimensions of the nanoshell solutions were estimated from UV-Vis spectra, on the basis of the experience gained in the full characterization described in this paragraph.

After this first nanoshell set, two further syntheses were performed, obtaining gold nanoshells with smaller and bigger silica cores, respectively. The characterization of these samples is described in the following two paragraphs.

4.4.2 Gold nanoshells with silica core of 75 nm diameter: Au NSs (R1=38; R2=x)

Smaller silica cores can be synthetized by lowering the ammonia concentration. Using 1.5 ml Ammonium hydroxide solution 30% in the Stöber procedure, DLS measurements give an average particle diameter of D_{DLS}= (93 ± 27) nm. TEM analysis give a smaller diameter of D_{TEM}= (75 ± 18) nm, as shown in Figure 4.23.

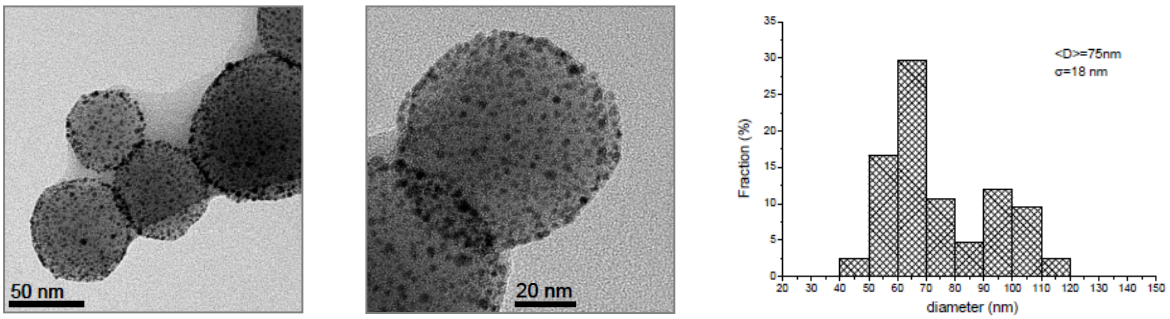

Figure 4.23: TEM analysis on SiO_2 (R1=38) cores: SiO_2@APTMS@Au (left and middle) and histogram of dimensional distribution (right).

Also for this silica cores, the nuclei decoration seems to be homogeneous.

In Figure 4.24 UV-Vis spectra of different shell samples, obtained by adding different amounts of SiO_2 (R1=38)@APTMS@Au to the aged gold precursor solution, are shown.

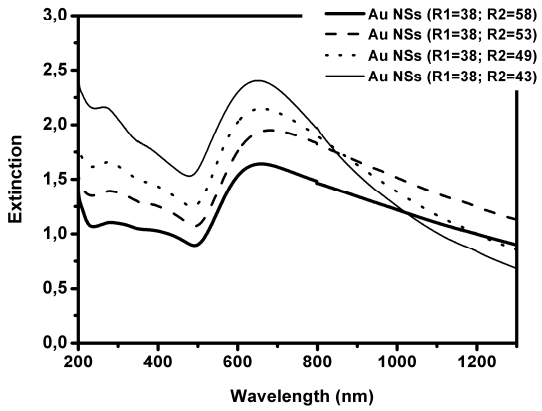

Figure 4.23: UV-Vis spectra of four different Au NSs (R1=38; R2=x) samples.

As can be observed the plasmonic band maximum shift is not that pronounced like in the case of bigger silica cores and no second band is visible. From the thinner shell to the thicker one the plasmonic band maximum shifts from 645-680 nm. This results are difficult to understand using Signorell's work, probably because of the great difference in the silica core dimension used: the Au NSs (R1=38; R2=x) samples are much smaller than that of Signorell. An assumption could be that the low and high energy bands described in literature are very close in the Au NSs (R1=38; R2=x) samples; probably they overlap. Despite the band maximum position, the shape of the UV-Vis spectra are similar to Signorell's. For the thinner shell a sharper peak can be observed with low extinction values at high wavelengths. In case of thicker shells, the extinction in the high wavelength region increases with respect to the band maximum.

From TEM images (Figure 4.25) the silica cores seem, although, more covered than for the Au NSs (R1=46; R2=y) samples.

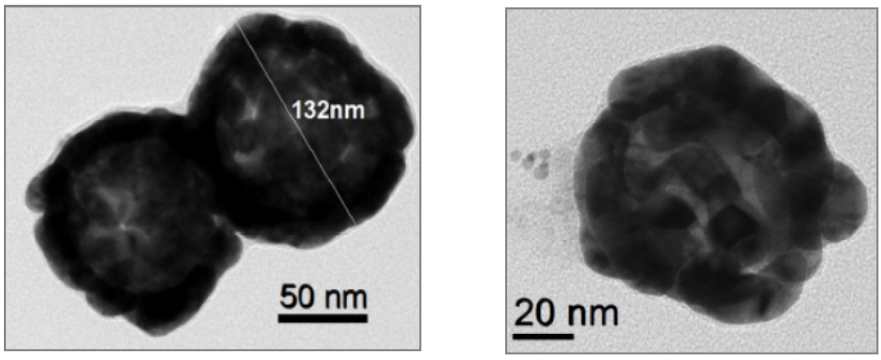

Figure 4.25: TEM analysis on Au NSs (R1=38; R2=x) samples: Au NSs (R1=38; R2=58) (left) and Au NSs (R1=38; R2=49) (right).

The particles diameter were calculated from TEM images (making an average calculation of many nanoshells) only for the two samples shown in Figure 4.25. For the other two, a shell thickness was estimated on the basis of the experience on Au NSs (R1=46; R2=y) samples, observing UV-Vis spectra. The most important quantities are listed in Table 4.2.

Table 4.2: Diameter, shell thickness and R1, R2 values of Au NSs (R1=38; R2=x) samples

Sample abbrevation	Diameter (nm)	Shell thickness (nm)	R1; R2 (nm)
SiO_2(38)@APTMS@Au	75 ± 18	--	R1= 38 ± 9
SiO_2@Au (R1= 38; R2= 58)	115 ± 17	20	R1= 38 ± 9; R2= 58
SiO_2@Au (R1= 38; R2= 53)	--	~15	R1= 38 ± 9; R2= 53
SiO_2@Au (R1= 38; R2= 49)	97 ± 15	11	R1= 38 ± 9; R2= 49
SiO_2@Au (R1= 38; R2= 43)	--	~5	R1= 38 ± 9; R2= 43

As observed in Table 4.2 the errors on the nanoshell dimension through TEM analysis are quite high, probably because the particles are small and differences on the final dimensions become even more relevant. For this reason it was not possible to measure a shell thickness with associated error, because, in some cases, the error was larger than the shell thickness value. Therefore, the values listed in Table 4.2 are estimated and the R2 values are reported without error.

4.4.3 Gold nanoshells with silica core of 162 nm diameter: Au NSs (R1=81; R2=z)

The same characterization was performed on bigger nanoshells, synthesized from a silica core, obtained adding 3 ml of Ammonium hydroxide solution 30% in the Stöber procedure. DLS measurments give an average diameter of D_{DLS}= (193 ± 41) nm, while TEM analysis, reported in Figure 4.26, evidences a bimodal distribution with diameters of D_{TEM}= (104 ± 6) nm and D_{TEM}= (162 ± 10) nm.

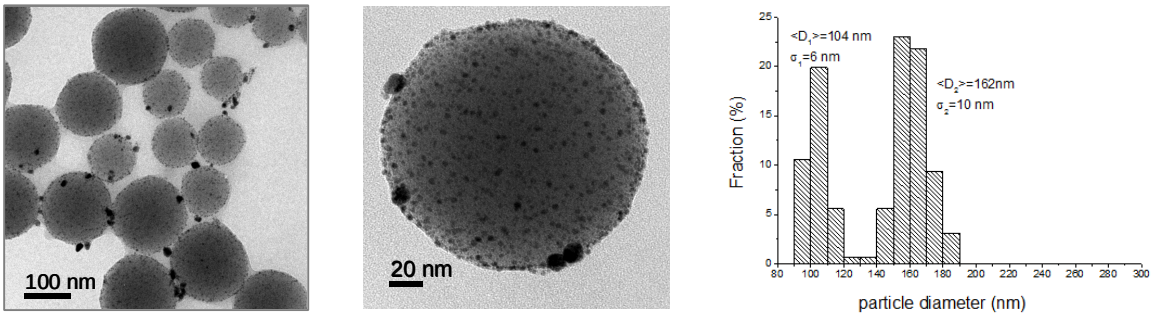

Figure 4.26: TEM analysis on SiO_2 (R1=81) cores: SiO_2@APTMS@Au (left and middle) and histogram of dimensional distribution (right).

The bimodal distribution was probably caused by the synthesis conditions.

In Figure 4.27 UV-Vis spectra of Au NSs (R1=81; R2=z) samples are shown.

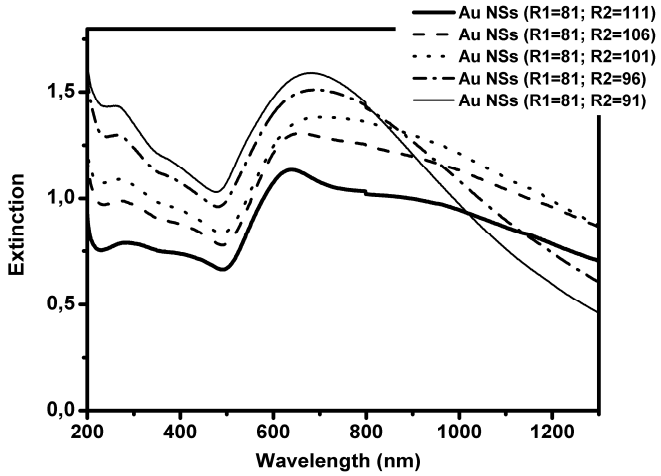

Figure 4.27: UV-Vis spectra of four different Au NSs (R1=81; R2=z) samples.

From the UV-Vis spectra two different bands can be observed for the first three samples with estimated thicker gold shell, while a single band is visible for thinner shells. For thicker shells, the plasmonic band at low wavelengths red shifts from 640 to 680 nm and then disappears.

The broad band at higher wavelengths for the first three samples seems to blue shift from about 940 to 720 nm. For the thinner shells the principal band is centered around 680-700 nm. The slight blue shift of the low energy band in the thicker shell samples is very interesting and follows the behavior described by Signorell for the complete shells (samples g-i of Figure 4.21). TEM images (Figure 4.28) confirm the high silica coverage and homogeneity. The band at lower wavelength, instead, is not usual for covered particles and is probably due to the bimodal particles distribution. The smaller particles will probably be partly responsible for the peak at 640 nm. Since the peak seems to increase at higher gold amount, it could be also a result of quadrupolar plasmonic modes, which can appear with very big nanoshells.

For lower coverage degrees the low wavelength band is no longer visible and the high energy band described by Signorell dominates.

The sample names in Figure 4.27 refer only to nanoshells with core centered around 160 nm, for simplicity. It is clear that the bigger particles are much interesting in the present characterization section, because bigger than the samples shown before. Nevertheless, care must be taken when such particles are used, particularly when a monomodal diameter distribution is needed.The shell thickness for the Au NSs (R1=81; R2=106) sample was calculated through TEM analysis, reported in Figure 4.28, while for the other samples the values (listed in Table 4.3) were estimated from UV-Vis spectra. As sad before, the sample nomination is performed by considering the presence of only particles with bigger silica core.

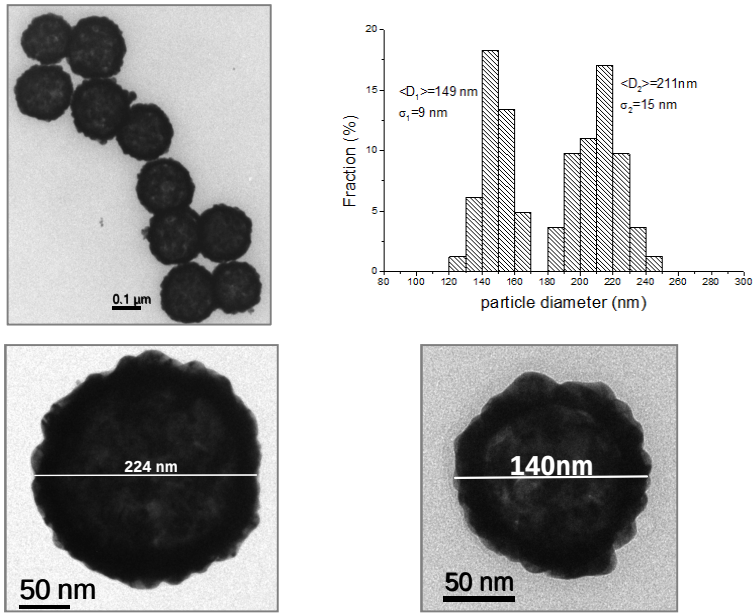

Figure 4.28: TEM analysis on Au NSs (R1=81; R2=106) sample with zoomed images of two particles taken from the two dimensional distributions (bottom row).

Table 4.3: Diameter, shell thickness and R1, R2 values of Au NSs (R1=81; R2=z) samples

Sample abbrevation	Diameter (nm)	Shell thickness (nm)	R1; R2 (nm)
SiO_2(81)@APTMS@Au	162 ± 10	--	R1= 81 ± 5
SiO_2@Au (R1= 81; R2=111)	--	~30	R1= 81 ± 5; R2= 111
SiO_2@Au (R1= 81; R2=106)	211 ± 15	25 ± 9	R1= 81 ± 5; R2= 106
SiO_2@Au (R1= 81; R2=101)	--	~20	R1= 81 ± 5; R2= 101
SiO_2@Au (R1= 81; R2=96)	--	~15	R1= 81 ± 5; R2= 96
SiO_2@Au (R1= 81; R2=91)	--	~10	R1= 81 ± 5; R2= 91

4.5 Other nanostructures

Two further nanostructures are used in the experimental section described in the next chapter, synthesized, within a collaboration, by Dr. Emilia Giorgetti from the CNR-Institute of Complex Systems in Firenze: Au NPs prepared through laser ablation, and gold nanostars (Au NSt) prepared through wet chemistry.

Laser ablated Au NPs are interesting for their surface chemistry[120], because not stabilized by any chemical species. The nanoparticles are "naked" and can therefore be easily functionalized. Au NPs were prepared through laser ablation of a gold target in water employing a mode-locked Nd-YAG laser at 1064 nm and 15 mJ pulse energy. The solution present an average diameter of 8.8 ± 2.6 nm and a concentration of 1.2×10^{13} NPs/ml, measured through TEM analysis, shown in Figure 4.29, togheter with the extinction spectrum.

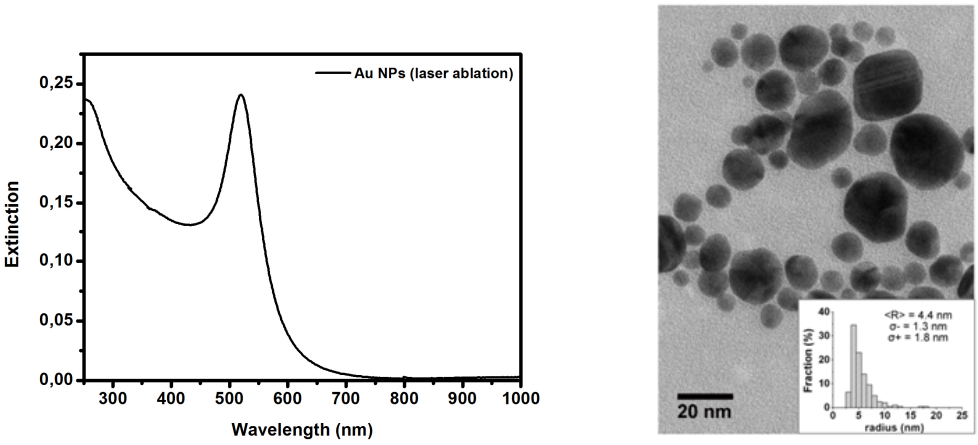

Figure 4.29: Extinction spectrum (left) and TEM image and histogram of dimensional distribution of Au NPs prepared through laser ablation.

The extinction spectrum is very similar to the Au NPs synthesized through Turkevich method. Nevertheless, as can be observed from the TEM image in Figure 4.29, the dimensional

distribution is much broader with the presence of very big nanoparticles. The broad distribution and less control over dimension is the principal drawback of the laser ablation synthesis procedure.

The Au NSt were, instead, prepared through wet chemistry in water and stabilized with Cetyltrimethyl Ammonium Bromide (CTAB). The Au NSt present cores of about 60-70 nm diameter with tips of about 30-40 nm (data not shown). This nanostructure could be very interesting for SERS enhancement at the Au NSt tips[121]. The extinction spectrum of the Au NSt solution used in the further experiments, is shown in Figure 4.30.

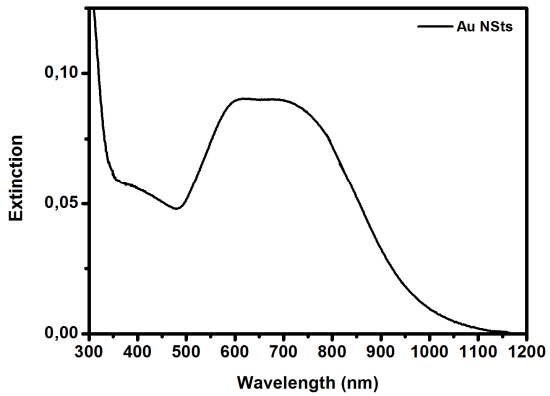

Figure 4.30: Extinction spectrum of gold nanostarts prepared through wet chemistry.

The two componenents visible in the extinction spectrum are due to the presence of the tips around the gold core.

4.6 Transfer into organic solvents

Metal nanoparticles are usually synthesized in aqueous solvents, principally because their application in the biological and biomedical field is increasing from year to year. On the other hand, nanoparticles prepared in organic media, are interesting for many other applications, ranging from catalytic processes to further particles surface modifications with organic functional groups in order to tune their properties and making them useful for sensing applications where organic solvents are required (for examples the sensing of toxic aromatic compounds). Differently sized and shaped metal nanoparticles can be obtained in organic media either by preparing them directly in those media, as we reported in paragraph 4.3.2, or by transferring nanoparticles from aqueous phases to organic ones. Many procedures are

reported in literature, which are principally based on capping the nanoparticles with thiols or amines [122], or on using phase-transfer reagents, such as surfactants, to improve the solubility of nanoparticles in organic media [123]. The efficiency of the latter approach, however, is limited, and for the present work, the first approach was chosen.

4.6.2 Transfer of gold and silver nanoparticles

For the transfer of Au and Ag NPs, a very simple approach was chosen, based on the functionalization of the metal surface with polyethylenglycol-thiol derivatives (PEG-SH). The functionalization of the nanoparticles surface with PEG was already discussed in literature for the stabilization of metal nanostructures in biological media[124,125]; the presence of PEG makes the particles even more inert.

In the present work, the idea was to exploit the simple chemistry of PEG functionalization and the amphiphilic behavior of the molecule, in order to perform the phase transfer.

To Ag or Au NPs solution, a precise amount of 1 mM m-PEG-SH aqueous solution is added, in order to have an excess of about 100 times the ratio between molecules and the available surface of metal nanoparticles. The reaction is kept at room temperature under mild stirring for one night. Few acetone ml are added to the solution, which is then centrifugated two times at high speed for 10 min. The particles are then concentrated, dried under nitrogen flux and dispersed in the chosen organic solvent.

In Figure 4.31 UV-Vis spectra of Au NPs in different organic solvents are shown. In the right spectra of Figure 4.31 an example of the plasmonic band changes during the transfer process are shown for Au NPs in butyl acetate.

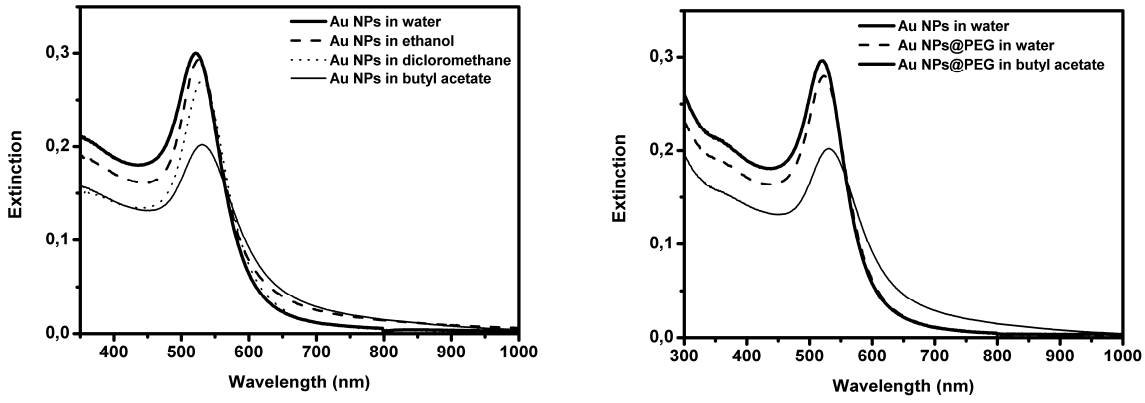

Figure 4.31: UV-Vis spectra of Au NPs in different organic solvents (left) and variation of the plasmonic band during transfer process for Au NPs in butyl acetate (right).

As expected, the plasmonic band maximum slightly red shifts in organic solvent, because the refractive index is changed. Moreover, the intensity decreases: a damping of the plasmonic behavior happens. This effect is even more evident in Figure 4.31 right. The first red shift of about 3 nm occurs due to the presence of PEG molecules, which causes a local chemical environmental change. The presence of an organic solvent causes a further red shift of about 10 nm. Nevertheless the plasmonic shape is preserved. The strong intensity decrease could, partially, be caused by particles loss during the transfer process.

A very similar phase transfer can be performed on Brust particles, changing from toluene to other organic solvents. After centrifugation and concentration, particles are dried and can be dissolved in different organic solvents, as demonstrated in Figure 4.32.

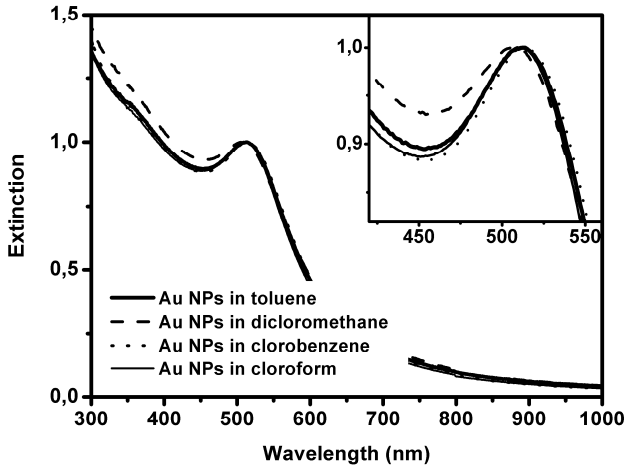

Figure 4.32: UV-Vis spectra of Brust Au NPs in different organic solvents; zoom of plasmonic peak (inset).

4.6.3 Transfer of gold nanoshells

Also Au NSs could be transferred, in a similar way, into organic solvents [115]. In this work three different thiols are tested for the formation of self-assembled monolayers, which should act as stabilizers into different organic solvents.

The three molecules are listed in Figure 4.33.

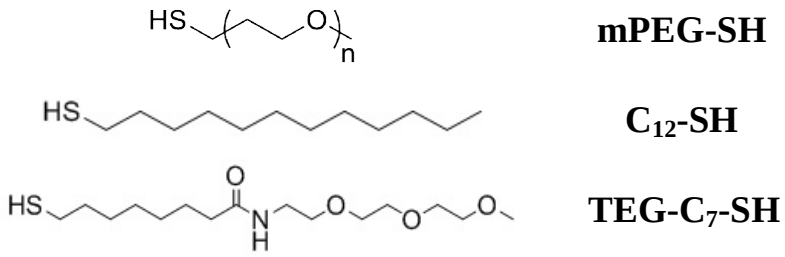

Figure 4.33: Three different alkanthiols used for phase transfer of Au NSs into organic solvents.

The mPEG-SH molecule is used in the same way as for Au NPs transfer. The results for the transfer in butyl acetate are shown in Figure 4.34

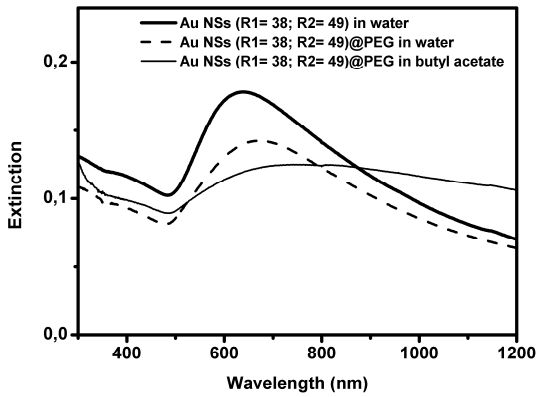

Figure 4.34: UV-Vis spectra of Au NSs (R1=38; R2=49) in water, functionalized with mPEG-SH and transferred into butyl acetate.

Also in this case the red shift due to mPEG-SH and the organic solvent, and the strong damping, is visible.

It is often interesting to use shorter molecules for phase transfer, particularly when the application requires the adsorption of analyte molecules onto the plasmonic surface. mPEG-SH is, in fact, a big molecule with a gyration radius of about 2-3 nm (for PEG mol wt 2000). The other two molecules of Figure 4.33 are therefore tested. The dodecanthiol (C_{12}-SH) was already used by Halas in the work describing the synthesis of gold nanoshells[115]. The functionalization of the NSs surface with this molecule has to be performed in a two phase system, since the dodecanthiol is not soluble in water. The first step is the NSs transfer in ethanol, by simple centrifugation and redispersion in ethanol. No functionalization for this step is needed. To 5 ml NSs in ethanol, a specific volume of 1 mM C_{12}-SH solution in tetrahydrofuran (THF) is added, in order to have a 100 times excess of thiol molecules with respect to the available surface. After one night under slight stirring the solution is centrifugated and the NSs redispersed in different solvents. The results are shown in Figure 4.35.

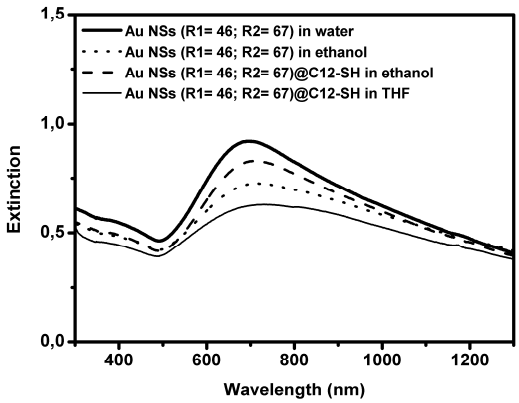

Figure 4.35: UV-Vis spectra of Au NSs (R1=46; R2=67) in water, ethanol and functionalized with C_{12}-SH in ethanol and THF.

As can be observed, the plasmonic band in water and ethanol has the same shape and more or less the same intensity. A slight red shift can be seen. The decrease of intensity is probably due to the loss of NSs during centrifugation. For the functionalized samples, instead, a strong plasmonic damping is visible, in agreement with the CID theory explained in Chapter 2: the plasmonic nanostructure feels a strong change of the dielectric environment due to the organic molecules. The shape of the plasmonic band remains the same in THF. Through the functionalization with C_{12}-SH, the Au NSs could be transferred into hexane, benzene and dicloromethane and remain stable for more than 5 days. Nevertheless, the transfer process with this molecule is difficult, because the intermediate step of transferring the NSs into ethanol causes the loss of much sample.

For this reason, an amphiphilic short molecule is used (the last depicted in Figure 4.33), which has been synthetized from Prof. Mancin of the Padova University. The molecule has a hydrophobic part formed by a short alkyl chain, and a second hydrophilic part composed by a tri-ethylen glycol chain, which makes the molecule soluble in water. With this molecule the functionalization reaction can be performed directly in water, without further steps and therefore less loss of nanoparticles.
The result of the transfer in THF is shown in Figure 4.36.

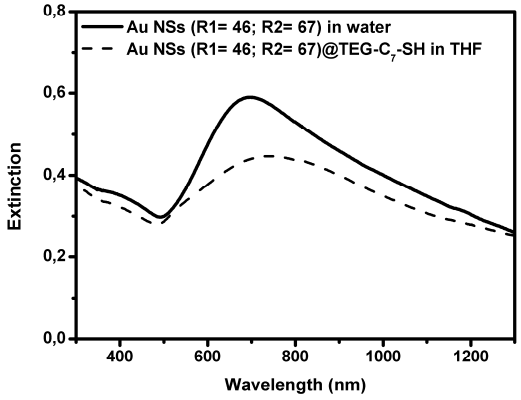

Figure 4.36: UV-Vis spectra of Au NSs (R1=46; R2=67) in water and functionalized with TEG-C_7-SH in THF.

The plasmonic band in THF for functionalization strategies with the last two molecules, is very similar. The only consideration could be of experimental nature: the functionalization with TEG-C_7-SH is much easier and the loss of NSs is less.

The transfer processes where performed on NSs samples of different dimensions and shell thicknesses. The final NSs dimension and the shell thickness (or coverage degree) do not influence the transfer results.

Chapter 5

REALIZATION AND CHARACTERIZATION OF SERS SUBSTRATES

5.1 Introduction

The importance and interest of exploiting plasmonic properties for sensing applications was already highlighted in previous chapters: SERS is an interesting technique to perform sensing measurements, because it combines high detection selectivity with high sensitivity. The most important properties of molecular sensors are the superior chemical specificity, the optimized sensitivity and the easy and fast sensing measurements.

The idea in the present work was to realize easy and cheap SERS substrates, in liquid or in solid phase, and to fully characterize them in order to better understand how to reach the highest detection sensitivity. As extensively described in Chapter 3, the relation between far field plasmonic properties, observed through UV-Vis spectroscopy, and near field enhancement efficiency at specific excitation wavelengths is not immediate and trivial. The SERS excitation at wavelengths similar to the maximum of the plasmonic extinction band does not always led to the highest local field enhancement, as will be shown later. The basic idea lies in the better understanding of the physical phenomenon of the LSPR, particularly when exploited for Surface Enhanced Raman Spectroscopy applications, in order to find some answers to open questions in literature.

The starting point for this study is the possibility to tune the plasmonic extinction band in a wide spectral range, from the UV-Vis to the near IR, by simply varying the metal, the

dimension and the morphology of the nanostructure. This tunability is not only important in order to find the right match with the laser excitation wavelength, but also because different molecules, with particular chemical properties, often require the detection in precise spectral ranges (for example where no fluorescence is present).

With the different nanostructures synthetized in this work and described in Chapter 4, it is possible to exploit the plasmonic resonance phenomenon in a wide spectral range. With Ag and Au NPs the plasmonic band is located at 400 and 520 nm, respectively, while with Au NSs the plasmonic band can be tuned from 600 up to 1000 nm, by varying the core to shell dimensions. The extinction spectra of the most important structures are summarized in Figure 5.1.

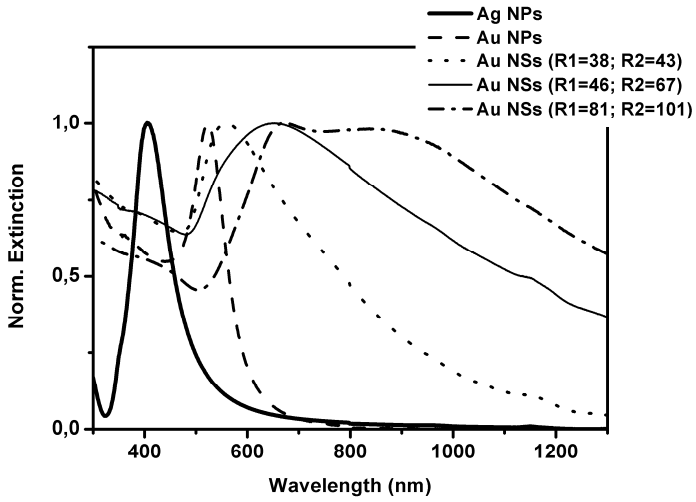

Figure 5.1: Normalized extinction spectra of different metal nanostructures.

Through the exploitation of many laser wavelengths, it is, moreover, possible to probe the SERS efficiency of the single nanostructure over the whole Vis-IR spectral range. This has been performed using diode and gas lasers working in the visible region (at 514.5, 633, 568 and 647 nm) and with a tunable Ti-Sapphire laser working in the near IR (680-950 nm).

Furthermore, Au NSs in solution have been characterized with a non conventional and very interesting technique, the Photoacoustic Spectroscopy (PhAS), rarely used in this research field. PhAS gives the possibility to extract the absorption contribution from the total extinction. Although it deals with optical excitation, it does not reveal an optical signal, like for other conventional spectroscopic techniques, but an acoustic pressure wave, generated by the excitation of a sample with laser light. This acoustic pressure wave is interpreted as

consequence of pure absorption of the sample, as will be described in detail in paragraph 5.2.1. In that way the extinction behavior of a plasmonic sample can be divided into the absorption and scattering contributions. This approach was applied in literature only as simulation and mathematical calculation, but rarely as scientific experiment. The work of Jain et al. [126] describes the Mie theory and DDA calculations made on gold nanospheres, gold nanorods and gold nanoshells, in order to describe their scattering and absorption efficiencies. In the paper the authors demonstrated that by increasing the nanosphere dimension the magnitude of the relative contribution of scattering to the extinction rapidly increases. In case of gold nanoshells, the relative scattering contribution to the extinction can be rapidly increased by increasing the nanoshell size or decreasing the ratio of the core/shell radius. As said before these are calculations, not proven by experimental data. The possibility to experimentally separate the two contributions can provide information about the relation of far field extinction properties and near field enhancement ones in real plasmonic nanostructure solutions, useful for different applications.

5.2 Materials and characterization techniques

Polyvinylpyrrolidone (average mol wt 40000), thiophenol (also known as benzenethiol) and thiobenzoic acid are purchased from Sigma-Aldrich and used without further purification.
Soda lime microscope glasses were purchased from Thermo Scientific.

5.2.1 Surface Enhanced Raman Spectroscopy

Some SERS tests and many of the measurements described in Chapter 6 and 7 are performed on a home-made Micro-Raman setup. A single line argon ion laser, with two principal lines at 488 and 514.5 nm (Spectra Physics Stabilite 2017-output power 1W), a He–Ne laser, working at 633 nm (Melles Griot- output power 35 mW) and a 785 nm diode laser (Xtra-output power 500 mW), were used as excitation light sources. The laser beam was coupled to a microscope (Olympus BX 40) and focused on the sample by a 100x, 50x or 20x objective (Olympus SLMPL). The back-scattered Raman signal was separated from the Rayleigh scattering by an edge filter and analyzed with a 320 mm focal length imaging spectrograph (TRIAX-320 ISA) and a liquid nitrogen cooled CCD camera (Spectrum One, JobinYvon). The typical spot diameter at the focus was between 1 and 3 μm. The laser power on samples could vary from 14 mW for 632.8 nm laser to 80 mW with the 514.5 and 785 nm lasers.

For wavelength scanned enhancement factor measurements, a home-made Macro-Raman setup was used. This system is equipped with a CW Ti:Sapphire Laser tunable in the range 675-1000 nm (Spectra Physics, 3900S) pumped by a CW Optically Pumped Semiconductor Laser (Coherent, Verdi G7) and an Ar^+/Kr^+ gas laser (Coherent, Innova 70) providing the lines at 488, 514.5, 530.8, 568 and 647.1 nm. Laser beams are filtered through a tunable laser plasma line filter (Laserspec III, Spectrolab) and focused on the sample by a cylindrical lens. The Raman scattering diffused by the sample is collected by a camera objective (CANON 50 mm f/1.2) and coupled into the slit of a three stage subtractive spectrograph (Jobin Yvon S3000) by means of a set of achromatic lenses. The spectrograph is made up by a double monochromator (Jobin Yvon, DHR 320), working as a tunable filter rejecting elastic scattering, and a spectrograph (Jobin Yvon, HR 640). The Raman signal is detected by a liquid nitrogen cooled CCD (Jobin Yvon, Symphony 1024x256 pixels front illuminated). A polarization scrambler is mounted right in front of the spectrograph slit. The system is configured in backscattering geometry by placing a tiny mirror in front of the collection objective to steer the beam from the cylindrical lens to the sample. The sample is mounted on a translation stage that allows one to move it parallel and perpendicular with respect to the laser propagation direction.

5.2.2 Photoacoustic Spectroscopy

The photoacoustic spectroscopy (PhAS) is, indeed, a not really new technique. An interesting review of Braslavsky et Heibel in 1992 [127] describes in detail this spectroscopy, which detects the sound waves generated by thermal expansion of samples excited through photons. The review gives a mathematical overview of the phenomena and also explains the experimental aspects, being a useful guideline for new starters in this research field. Other similar works could be found in literature [127–129], but no reference to plasmonic samples is found. Only in recent years some few literature works describe the photoacoustic spectroscopy applied on plasmonic nanostructures [130,131]. Nevertheless no one combines the PhAS with SERS.

In the present work, photoacoustic excitation profiles are performed for the first time on different gold nanoshells in solution. Measurements are performed in collaboration with Dr Alessandro Feis, Dr. Cristina Gellini and Prof. Pier Remigio Salvi from the Chemical Department of the University of Firenze.

Through Photoacoustic Spectroscopy the wavelength dependent laser induced photoacoustic signal of a sample is analyzed. In the simple case of a liquid sample, the absorption of the laser radiation by the solution causes a thermal expansion, which generates a pressure wave with intensity proportional to the absorption. This wave is recorded through a piezoelectric transducer and visualized by an oscilloscope (see Figure 5.2).

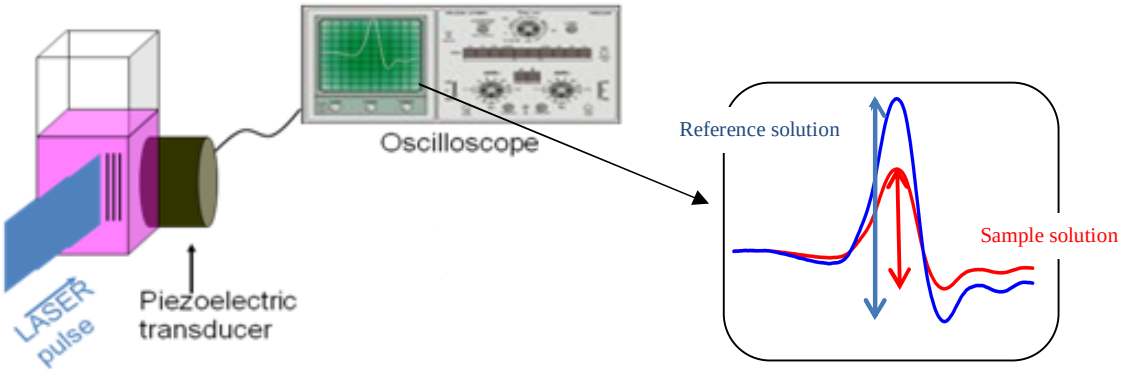

Figure 5.2: Photoacoustic Spectroscopy setup and recorded signal scheme.

The equation which describes the photoacoustic signal can be written as:

$$S = kn_{ph}\left(E_\lambda \beta / C_p \rho\right) \tag{5.1}$$

The signal depends on the instrumental constant k, the number of absorbed photons n_{ph}, the photon energy E_λ, the volumetric thermal expansion coefficient β, the heat capacity at constant pressure C_p and the solvent density ρ.

The signal of the sample has to be correlated to the signal of a calorimetric reference, i.e. a substance which i) releases all the absorbed energy as heat instantaneously and ii) negligibly scatters light. In our case, the reference was a $KMnO_4$-$CuSO_4$ solution, which absorption covers the whole Vis- near IR region (Figure 5.3 left). At every excitation wavelength the photoacoustic signal of reference and sample (depicted in blu and red in Figure 5.2), was recorded at several laser pulse energies. The signal was normalized for small extinction variations between sample and reference.

The ratio between the slope of the reference and the sample straight line can be correlated to the absorption contribution of the sample (Figure 5.3 right). It yields, in fact, the absorption percentage over extinction (or, equivalently, the absorption to extinction cross section ratio σ_A/σ_{Ext} in the results given in paragraph 5.3.2), because a smaller sample slope - when the

extinction of sample and reference is matched - can only be determined by scattering loss, in the absence of other photochemical or photophysical processes in the sample.

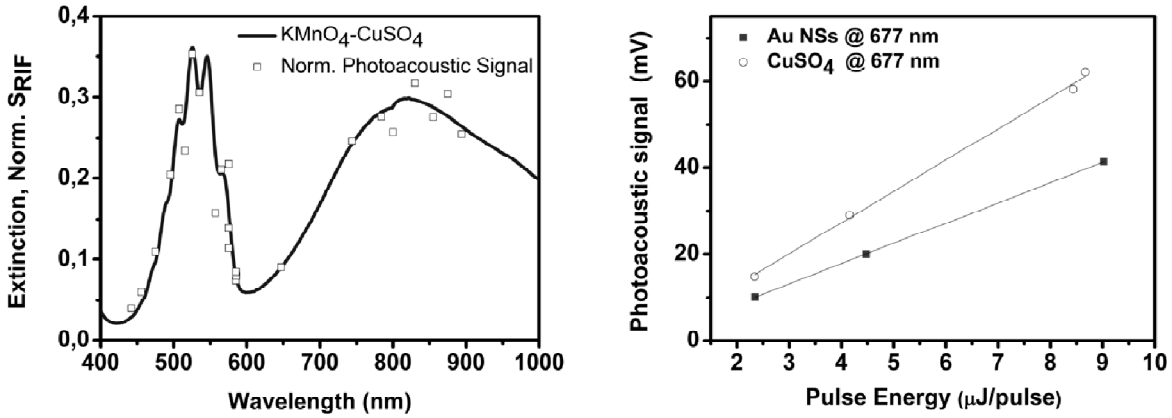

Figure 5.3: Extinction spectrum of reference solution and normalized PhA signal (left), PhA signal at different pulse energies for reference and sample solution (right).

The normalized photoacoustic signal is then obtained by multiplying the σ_A/σ_{Ext} data with the sample extinction to obtain the rescaled photoacoustic profile, which can directly be compared to the extinction spectrum (see Figure 5.3 left for totally absorbing reference). The error bars of the σ_A/σ_{Ext} data are given by propagating the standard error of the regression in the line fitting of the photoacoustic signal to energy pulse data (see Figure 5.3 right).

Photoacoustic signals were detected with a 1 MHz bandpass Panametrics V103-RM piezoelectric transducer clamped to a standard quartz cuvette for absorption spectroscopy. The signals were amplified with a Panametrics 5660 B amplifier and averaged with a Tektronix TDS-3054B digitizing oscilloscope. The minimum number of signals was 512 for each average. The sample temperature was kept constant within 0.1°C with a Lauda Eco RE 415 cryostat and monitored by a thermocouple placed inside the cuvette. The excitation source was a GWU – Lasertechnik GmbH optical parametric oscillator pumped by the third harmonic of a Quanta System Nd:Yag laser. For some measurements, a Quanta System Nd:Yag laser-pumped dye laser, was used. The pulse duration was 10 ns and the repetition rate 10 Hz. The excitation wavelength was measured with a Mut Tristan fiber optic spectrophotometer. The incident laser energy was measured in front of the sample cuvette by a pyroelectric head energy meter before each measurement. The incident laser beam was shaped by a rectangular slit with 1 x 10 mm size without focusing in the sample. The fluence

was therefore on the order of 0.1 mJ/cm^2. Convolution analysis, performed with commercial software (Sound Analysis, Quantum Northwest Inc.), showed that the temporal profile was the same for a calorimetric reference solution and sample, without any detectable delayed component. Therefore, the photoacoustic signal was simply considered as the peak to valley value of the oscillation observed on the oscilloscope (Figure 5.2). Sample integrity was checked by comparing the extinction spectra taken before and after each measurement.

5.3 Colloidal SERS samples

5.3.1 SERS EF measurements on different nanostructures

Nanostructures in solution are very interesting for SERS applications, where liquid samples are required, for example for microfluidic devices [132–134]. For these reason different metal nanostructures are characterized in terms of SERS efficiency in colloidal solutions. The best way to prove their enhancement ability is to perform SERS enhancement factor measurements at different excitation wavelengths. The SERS enhancement factor was also measured at different nanoparticles aggregation degrees. It is well known that colloidal aggregates of metal nanoparticles give best results in term of local field enhancement [21].

Enhancement factor measurements are performed on different nanostructures with the micro-Raman setup at four different excitation wavelengths: 488, 514.5, 632.8 and 785 nm. Thiobenzoic acid (TBA) is used as probe molecule. Very similar to benzenethiol, which is often used for EF measurements on solid substrates [33], thiobenzoic acid is slightly soluble in water, due to the carbonyl group, and therefore suitable for the functionalization in aqueous phase. Moreover, this molecule presents well defined signals with high Raman cross section in the 900-1600 cm^{-1} Raman spectrum range.

The nanostructures tested are Au and Ag NPs, synthesized with chemical Turkevich method (CH), two Au NSs samples with same core but different shell thicknesses (R1=38; R2=58 and R1=43), Au NPs (LA) prepared through laser ablation and gold nanostars (Au NSt).

The functionalization of the solution with TBA is simply performed at room temperature by adding an amount of an aqueous TBA solution, in order to obtain the desired concentration in the plasmonic sample.

The Raman spectrum of pure TBA, recorded with 633 nm excitation wavelength, is shown in Figure 5.4 and the Raman band assignment is listed in Table 5.1.

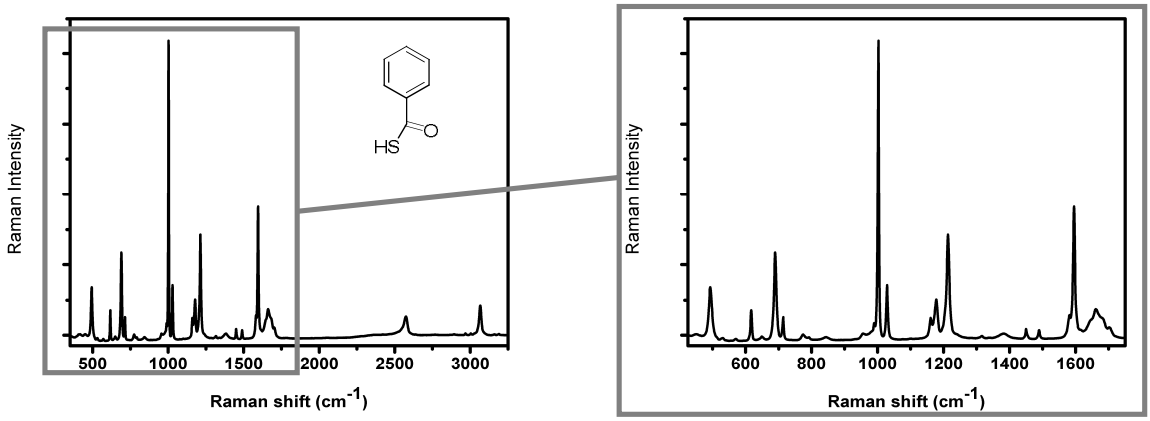

Figure 5.4: Raman spectrum of pure thiobenzoic acid from 350 to 3250 cm^{-1} (left), zoom of the 400-1750 cm^{-1} region (right).

Table 5.1: Raman band position and assignment of pure thiobenzoic acid.

Raman shift (cm^{-1})	**Assignment** [135,136]
492	CO-SH def. vib.
617	S_{6b}
690/713	C-SH in plane def. vib.
775	S_1
845	S-H def. vib.
1002	S_{12}
1028	S_{18a}
1178	S_{9a}
1213	ν_s C-C
1595	S_{8a}
1660	ν_s C=O
2575	ν_s S-H
3065	ν_s =C-H

$S_{ij=}$ ring vibration modes; ν_s= symmetrical stretching.

The benzene ring mode at 1002 cm^{-1} is used for enhancement factor calculations, because it is the strongest Raman mode and less affected by chemical enhancement mechanisms [30].

First of all it is interesting to understand the kinetics of TBA surface functionalization, which can be simply observed through SERS spectra. One possibility is to observe the disappearance of the SH stretching group of the TBA molecule at 2575 cm^{-1}, as a consequence of the functionalization. Another possibility is looking for a Raman band shift. In Figure 5.5 two Raman spectra details are shown.

The spectra of Figure 5.5 left refer to pure TBA and 5×10^{-5} M TBA in Ag NPs solution in the 2400-3500 cm^{-1} region, in order to observe the disappearance of the S-H stretching mode at 2575 cm^{-1}. The right spectra of Figure 5.5, instead, show the zoom of the 1002 cm^{-1} band of 5×10^{-5} M TBA in Ag NPs solution, at different time intervals after the addition of TBA to the NPs solution.

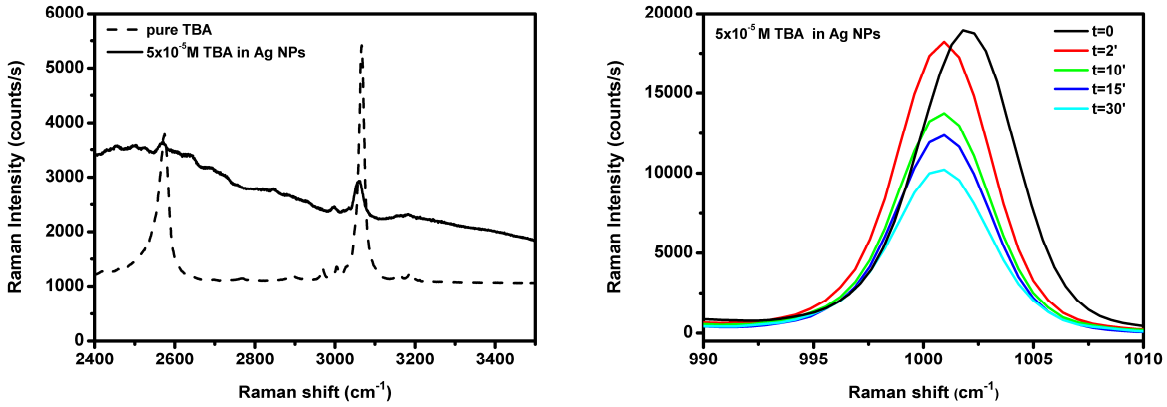

Figure 5.5: Raman spectra of pure TBA and 5×10^{-5} M TBA on Ag NPs in the 2400-3500 cm^{-1} range (left); Zoom of the 1002 cm^{-1} band of TBA at different time intervals after functionalization (right).

As can be observed from the slight shift of the 1002 cm^{-1} Raman band in Figure 5.5 right, the functionalization of the Ag NPs with TBA occurs within the first 2 min after functionalization. Moreover at the same time interval, the S-H stretching mode at 2575 cm^{-1} completely disappears, demonstrating that much of the TBA is bond to the metal surface.

Before carrying out EF measurements, it is also very important to find the best measurement conditions in order to obtain truthful EF values. The most critical issue is the stability of nanostructure and analyte under laser irradiation; therefore some tests are initially performed at constant nanostructure and molecule concentration in solution, at different laser powers. At high powers the analyte spectrum is changing in real time and this can indicate either a nanostructure change or the damage of the analyte on the surface, or both. When the best laser power is chosen, in order to have no spectrum variations in real time and a good signal to noise ratio, SERS spectra are measured at different time intervals, in order to observe the stability of the nanostructure solution.

Since Ag NPs are the less stable and most reactive nanostructures, their SERS results at different time intervals are shown in Figure 5.6, as most significant example.

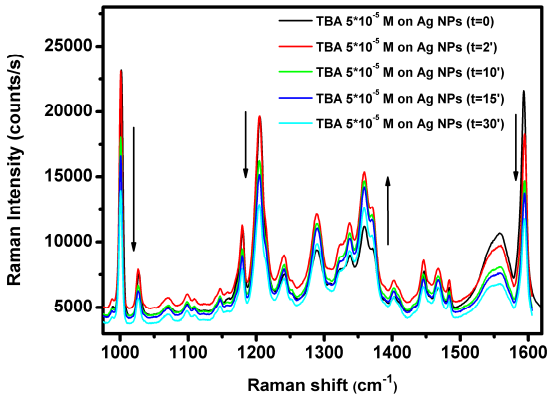

Figure 5.6: SERS spectra of TBA 5×10^{-5} M on Ag NPs in solution, at different time intervals.

After 30 minutes the Raman signal decreases of about 40-50% indicating probably the Ag NPs aggregation due to the presence of a high analyte concentration. Moreover two bands at about 1350-1380 cm^{-1} and 1550 cm^{-1} are present, which can be attributed to amorphous carbon modes. This indicates a still too high laser irradiation power, which causes the analyte degradation.

It is therefore very important to identify the upper limit molecular concentration, in order to avoid nanostructure coalescence, and the correct laser power to prevent molecular degradation.

The EF value in solution was calculated using the following expression, introduced in paragraph 3.3.5 of chapter 3.

$$AEF = \frac{I_{SERS} / c_{SERS}}{I_R / c_R} \tag{3.41}$$

I_{SERS} and I_R are the integrated peak intensities of the 1002 cm^{-1} mode of TBA SERS sample and reference TBA solution, respectively. c_R is the molecular concentration in the reference sample and c_{SERS} is the concentration of the bound molecule in the colloidal sample.

Preliminary data in solution show that the determination of EF is critical and underestimated, due to the difficulties in creating an efficient and stable aggregate system for most of the investigated nanostructures. Nevertheless, the aggregation of nanoparticles, directly caused by the presence of the analyte above a critical molecular concentration, could be a very interesting feature. Without any additional components, like salts generally used to induce aggregation, higher detection sensibility could be reached.

The EF results, measured for the TBA mode at 1002 cm^{-1}, for the different structures, at different molecular concentrations, excited with four excitation wavelengths, are summarized

in Table 5.2. The highest SERS EFs in solution are highlighted for each molecular concentration and excitation wavelength.

Table 5.2: EF results for different nanostructures at different concentrations and Raman excitation wavelengths.

	EF @ 1002 cm^{-1}			
[TBA]= 5×10^{-7} M	λ_L= 488 nm	λ_L= 514.5 nm	λ_L= 633 nm	λ_L= 785 nm
Au NPs (CH)	--	--	--	--
Au NPs (LA)	--	--	--	--
Ag NPs	**2.6×10^3**	**3.4×10^3**	**3.6×10^4**	**3.4×10^4**
Au NSs (R1= 38; R2= 58)	--	--	**7.3×10^2**	**9.2×10^3**
Au NSs (R1= 38; R2= 43)	--	--	**3.2×10^3**	**1.7×10^4**
Au NSts	--	--	--	--
[TBA]= 5×10^{-6} M				
Au NPs (CH)	--	--	**2.0×10^3**	--
Au NPs (LA)	--	--	**3.7×10^2**	--
Ag NPs	**5.8×10^4**	**1.6×10^5**	**5.2×10^5**	**9.1×10^5**
Au NSs (R1= 38; R2= 58)	--	--	**8.5×10^3**	**7.3×10^4**
Au NSs (R1= 38; R2= 43)	--	--	**2.7×10^3**	**2.0×10^4**
Au NSts	--	--	--	--
[TBA]= 10^{-5} M				
Au NPs (CH)	--	**5.5×10^1**	**8.1×10^3**	**2.0×10^3**
Au NPs (LA)	--	--	**5.5×10^2**	**4.5×10^2**
Ag NPs	**5.0×10^4**	**1.0×10^5**	**4.7×10^5**	**1.3×10^6**
Au NSs (R1= 38; R2= 58)	--	--	**3.1×10^3**	**4.1×10^4**
Au NSs (R1= 38; R2= 43)	--	--	**4.2×10^3**	**1.2×10^4**
Au NSts	--	--	**3.7×10^2**	**1.8×10^3**
[TBA]= 5×10^{-5} M				
Au NPs (CH)	--	**5.4×10^1**	**1.5×10^4**	**3.0×10^3**
Au NPs (LA)	--	**6.6×10^1**	**3.9×10^3**	**6.5×10^3**
Ag NPs	--	**5.3×10^4**	**4.9×10^5**	**1.3×10^6**
Au NSs (R1= 38; R2= 58)	--	--	**6.1×10^3**	**2.9×10^4**
Au NSs (R1= 38; R2= 43)	--	--	**3.9×10^3**	**1.2×10^4**
Au NSts	--	--	**1.2×10^2**	**1.7×10^2**

The extinction spectra, for each nanostructure, at different Raman probe concentrations, is reported in Figure 5.7 in order to observe the variations of the plasmonic behavior due to different amounts of probe molecule in solution. The four excitation wavelengths are indicated in the spectra through the vertical lines.

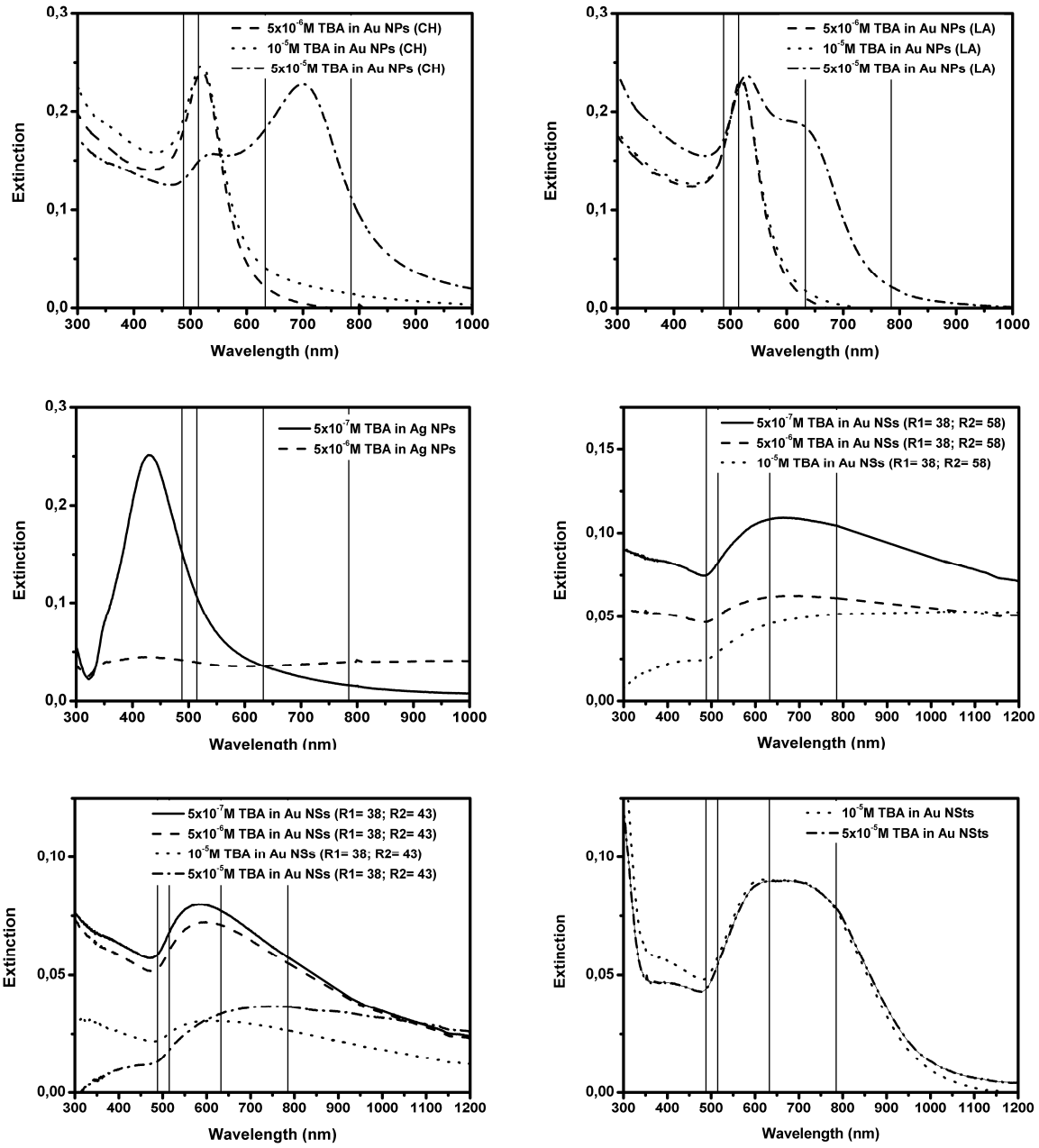

Figure 5.7: Extinction spectra of different nanostructures in solution with different TBA concentrations: Au NPs through wet chemistry and laser ablation (top row), Ag NPs and Au NSs (R1=38; R2=58) (middle row) and Au NSs (R1=38; R2=43) and Au NSt (bottom row). The vertical lines indicate the four excitation wavelengths used.

The estimated EF values are very promising, in particular in the case of Ag NPs with EF of 10^6-10^7. As highlighted in Table 5.2, Ag NPs give the best sensitivity in every condition, both for different TBA concentrations and for different excitation wavelengths. The principal drawback of Ag NPs is the low stability already at low molecular concentrations, as can be

observed from Figure 5.7 at 5 x 10^{-6} M. This problem could be overcome for applications where the measure is taken within few minutes after molecules absorption onto the silver surface: the stability becomes an insignificant problem and the signal, as demonstrated in Figure 5.6 is still very high for SERS spectra accumulations of only few seconds (20000 counts/s).

However, when the stability of the nanostructure is an important part of the SERS application, other nanostructures should be taken into account. With the exception of Au NSs (R1=38; R2=58), all other nanostructures investigated, are stable till with 10^{-5} M TBA in solution. The most interesting structures in term of stability are Au NSt, which are highly stable also at 5 x 10^{-5} M. This is probably due to the presence of CTAB in solution, which stabilizes the particles.

Another interesting aspect is the stable aggregates formation in solution, which causes a further enhancement of the SERS intensities, as demonstrated for Au NPs comparing the EF results with 5 x 10^{-6} M TBA and 5 x 10^{-5} M TBA. The EF increases by an order of magnitude. Observing the extinction spectra in the top row of Figure 5.7, two different stable aggregates are formed for Turkevich and laser ablated Au NPs. In most of the SERS conditions investigated, however, the Au NPs (CH) seems to be more efficient. The aggregates are stable in time up to 2 weeks without coalescence. The picture reported in Figure 5.8 demonstrates the high stability of Au NPs aggregates in solution and the interesting color change attributable to the strong extinction spectra changes during aggregation.

Figure 5.8: Au NPs solution at different probe molecular concentrations, rising from left to right.

Au NSs are a good compromise for SERS applications in solution. They are stable till 10^{-5} M, with good EF values of about 7 x 10^{4} at 785 nm, with a molecular concentration of 5 x 10^{-6} M. With the exception of Ag NPs, only with Au NSs it is possible to measure a EF value for a molecular concentration of 5 x 10^{-7} M.

The EF measurements performed can help to choose the most appropriate nanostructure for the single application. As can be observed from the results listed in Table 5.2, the EF values

are generally higher at increasing excitation wavelength and increases with higher nanoparticle aggregation. Both the considerations can most likely be accounted to the presence of hot spots: interacting nanoparticles give rise to a strong interparticles local field causing a red shift of the plasmonic band. In some cases this red shift is not visible in the extinction spectra, probably because the presence of only few aggregates did not cause strong variations of the far field properties. Contrarily, the local field properties change dramatically causing the increase of the enhancement factor values with the presence of only a few NPs aggregates.

5.3.2 Photoacoustic and SERS characterization on gold nanoshells

In order to better investigate the SERS EF behavior and to find a way to compare far field properties and near field ones, photoacoustic spectroscopy is used for the first time on nanoshell systems. As described above, this spectroscopy can help in separating the absorption and the scattering contributions to the total extinction. The investigation of these two basic optical phenomena, could give some interesting information in order to choose the best nanostructure for the single application. Photothermal cancer therapy, for example, requires nanostructures with high absorption and less scattering [137], while for imaging applications a dominant scattering contribution is needed [138].

It would be interesting to compare this far field properties with the near field behavior, probed by wavelength scanned SERS EF measurements, in order to choose the best nanostructure for SERS applications.

Based on these considerations, photoacoustic measurements were performed on core shell samples; no similar measurements are found in literature before. The approach used follows a literature work done on simple gold nanoparticles, where the photoacoustic technique was demonstrated to be a useful tool for extracting the absorption component to the total extinction[139]. The authors show that the photoacoustic profile performed on gold nanoparticles of about 10 nm can be overlayed to the extinction spectrum, demonstrating the almost absence of scattering contribution.

Larger nanoparticles, instead, show a progressive deviation of the extinction spectrum at longer wavelength, where the photoacousic signal becomes small.

In the present work, four different nanoshell samples, with different core to shell dimension ratio, were tested by performing PhAS and SERS measurements. In Table 5.3 the list of the samples with inner core (R1) and total radius (R2) is reported. For some samples two different syntheses batches are prepared, one was characterized through SERS and the other through photoacoustic spectroscopy.

Table 5.3: List of gold nanoshell samples studied by SERS and photoacoustic spectroscopy.

Sample name	R1	R2	R1/R2	Spectroscopy technique used
Au NSs 38-43	38	43	0.88	batch1: PhAS
				batch2: SERS
Au NSs 38-49	38	49	0.78	batch1: PhAS/SERS
				batch2: SERS
Au NSs 46-67	46	67	0.69	batch1: PhAS
				batch2: SERS
Au NSs 81-106	81	106	0.76	SERS/PhAS

In Figure 5.9 the photoacoustic measurements performed on the first two samples with the same silica core of 38 nm radius, are reported.

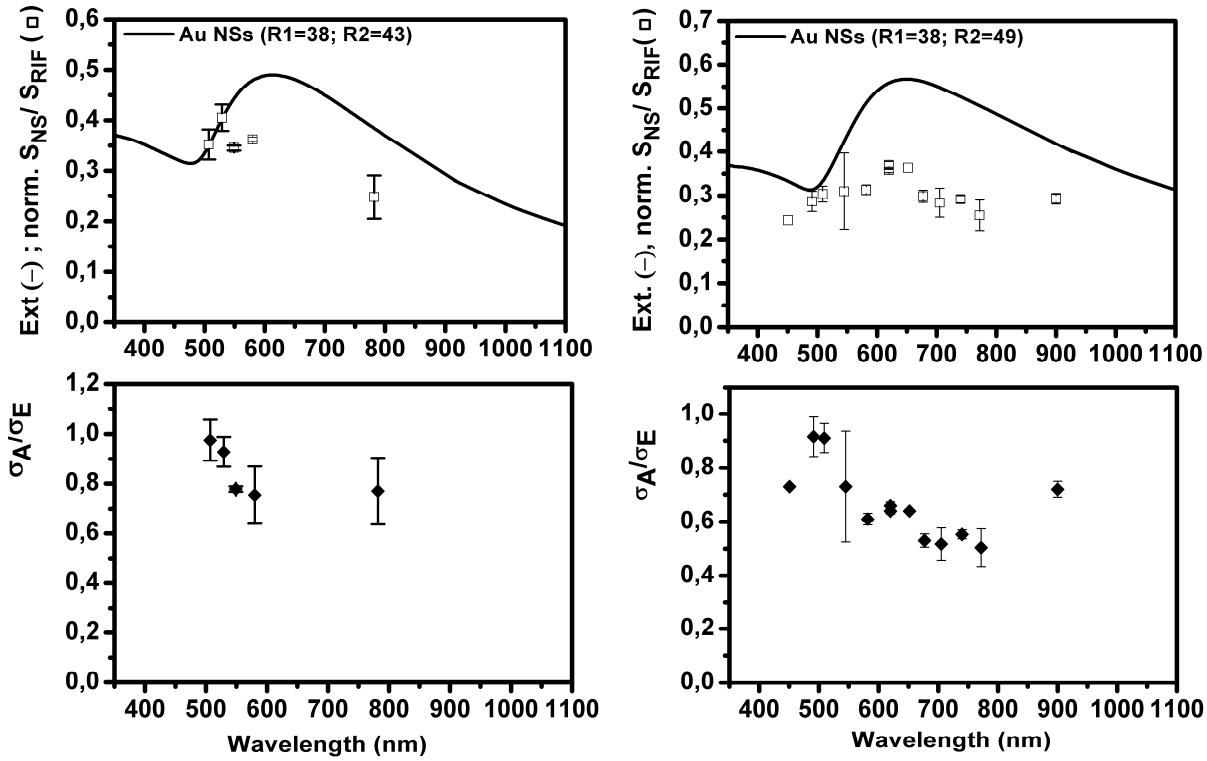

Figure 5.9: Photoacoustic measurements of Au NSs samples: Au NSs (R1=38; R2=43) (left) and Au NSs (R1=38; R2=49) (right). In the top row a superposition of the extinction spectrum and the normalized photoacoustic signal is reported. In the bottom row the ratio between absorption component over the total extinction is shown.

From the photoacoustic measurements on these two samples, it can be observed that the absorption contribution decreases from the Vis to the near IR, for both samples. In case of Au NSs (R1=38; R2=43) the absorption percentage values are about 95% at 500 nm and 75% at 800 nm, while for Au NSs (R1=38; R2=49) values of 90% at 500 nm and 50% at 800 nm are found. The comparison of these data shows an increasing trend of the absorption component with decreasing total radius and increasing R1/R2 ratio. Both statements are in agreement with theoretical predictions made by Jain et al. [126].

Comparing the results in Figure 5.9 with the photoacoustic measurement performed on the Au NSs (R1=46; R2=67) (Figure 5.10 left), similar considerations could be done.

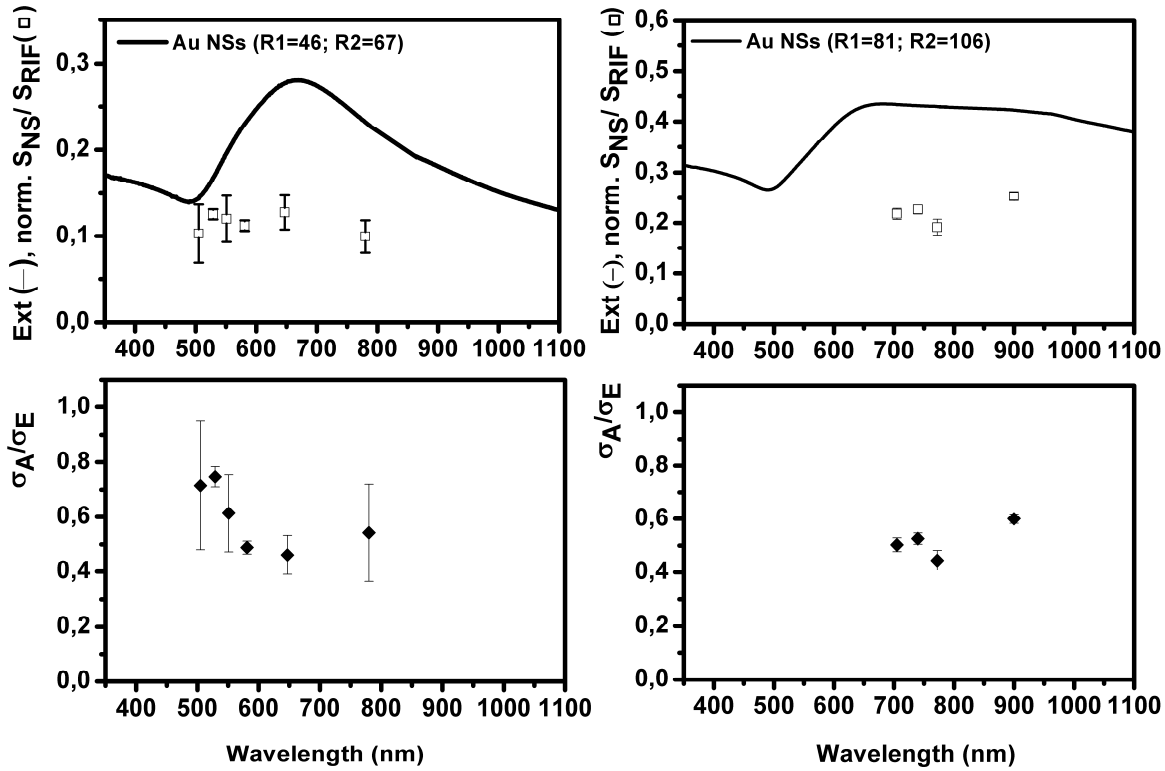

Figure 5.10: Photoacoustic measurements of Au NSs samples: Au NSs (R1=46; R2=67) (left) and Au NSs (R1=81; R2=106) (right). In the top row a superposition of the extinction spectrum and the normalized photoacoustic signal is reported. In the bottom row the ratio between absorption component over the total extinction is shown.

Also for the Au NSs (R1=46; R2=67) sample the absorption percentage trend seems to decrease from Vis to IR with a slightly new increase after 750 nm. The absorption percentage values lie in the range of 75% at 500 nm and 45% at 650 nm. The photoacoustic signal for the Au NSs (R1=81; R2=106) sample could not be measured in the Vis range beneath 700 nm, because of problems at the laser instrumentation. The absorption percentage lies at around 50% at around 700 nm. Comparing the results of these two samples, the absorption contribution to the total extinction seems to be more or less the same at around 700 nm. Some considerations can be done: For the Au NSs (R1=81; R2=106) sample the photoacoustic signal could not be detected in the low wavelength range and, moreover, it is, in fact, composed by a bimodal dimensional distribution, as shown in the TEM images of Chapter 4. Therefore, a correct comparison could be hardly done.

The comparison concerning the first three samples, instead, remains in agreement with theoretical predictions: the absorption component is definitely decreasing with increasing shell dimension and decreasing R1/R2 ratio.

The SERS measurements were performed with the macro Raman setup at different excitation wavelengths, ranging from 568 to 940 nm. Thiobenzoic acid was used as Raman probe and the probe concentration in solution was about $2x10^{-6}$ M. The signal chosen for EF determination was the 1000 cm^{-1} ring breathing mode, because less affected by chemical enhancement contribution. For EF calculations a reference solution of pure TBA was used. The measurements were performed in liquid solution in a 2 ml vial with optical path of 0.8 cm. The maximum absorbance of nanoshell solution was set at about 1 for UV-Vis spectra taken with 1 cm optical path. Since the nanoshell concentration was quite high, it was necessary to introduce an internal standard for controlling the self-absorption of the nanoshells, i.e. the absorption of the incident and the Raman scattered light throughout the optical path of the vial. To this end, the same amount of ethanol (150 µl in 1 ml Au NSs solution) was added to all the samples.

In Figure 5.11 the SERS spectrum of TBA on the Au NSs (R1=46; R2=67) sample at 720 nm excitation wavelength is reported, as example:

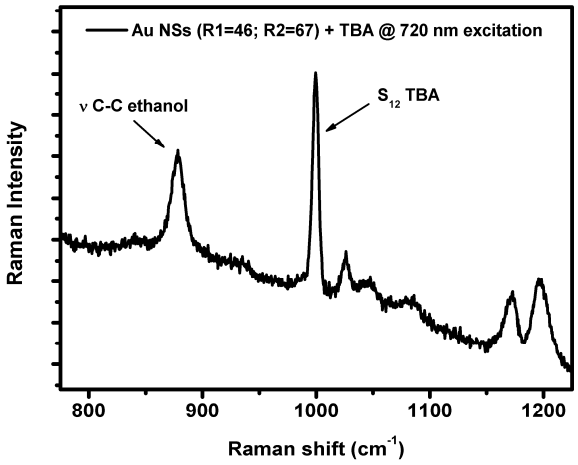

Figure 5.11: SERS spectrum of Au NSs (R1=46; R2=67) with $2x10^{-6}$ M TBA at 720 nm excitation wavelength.

The intensity of the 875 cm^{-1} C-C stretching band of ethanol should act as internal standard for the calculation of the self-absorption factor. Ethanol was chosen because of the intense 875 cm^{-1} signal outside the Raman activity range of TBA and because it doesn't modify the extinction spectra of the nanoshell samples.

The EF definition of Equation 3.43 is then modified to:

$$AEF = \frac{I_{SERS}/c_{SERS}}{I_R/c_R} \cdot \frac{I_{sar}^R}{I_{sar}^{SERS}} \quad (5.1)$$

The self-absorption factor is defined as

$$F_{sa} = \frac{I_{sar}^R}{I_{sar}^{SERS}} \quad (5.2)$$

where I_{sar}^R is the signal intensity of the 875 cm^{-1} Raman band of ethanol in a reference aqueous solution (at the same ethanol concentration than in the SERS samples) and I_{sar}^{SERS} is the intensity of the same signal in the nanoshells solution.

The error on the corrected EF is calculated by measuring the integrated intensity of the TBA signal at 568 nm choosing 5 different baselines; at the mentioned excitation wavelength, the signal is less intense and therefore most affected by mathematical error in the intensity determination. This test is performed on each Au NSs sample and the relative error results about 15% for all the samples. This error was applied (and intended as maximum possible error) for all the excitation wavelengths.

The first SERS characterization was performed on the Au NSs 38-49 sample. Unfortunately, no self-absorption correction was applied for this sample, because the self-absorption observation was done during this measurement and only applied for the subsequent samples. Nevertheless the results are reported in Figure 5.12.

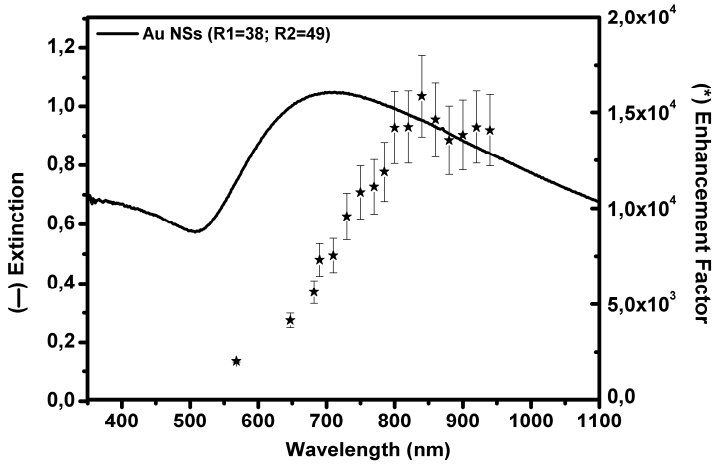

Figure 5.12: Superposition of extinction spectrum (black line) and SERS EF measurements (black stars) for the Au NSs (R1=38; R2=49) sample.

The EF trend is increasing from the UV-Vis to the near IR, with values ranging from 2 x 10^3 to 1.5 x 10^4 and seems to become constant after 800 nm. The behavior is similar to the one reported by Van Duyne for a single gold nanoantenna [34], indicating the possible presence of hot spots in the investigated structure. The red shift of the SERS EF profile with respect to the extinction one was already observed in solution for silver nanoparticles by Von Raben et al. [140] and attributed to the partially aggregation of the particles in solution.

In the sample investigated here, there can be two different sources of hot spots: interparticle and intraparticle ones. In case of interparticle hot spots two or more Au NSs can be close to each other with the formation of dimers and trimers and therefore strongly enhanced local fields in the junctions. In the other case, not completely covered and roughened Au NSs can give rise to intraparticle hot spots on the silica cores.

Since no self-absorption correction was applied for this Au NSs sample, the EF profile is not completely verified: if the self-absorption factor would change strongly at different excitation wavelengths, the EF trend could be modified. In order to verify this, the SERS EF profile was measured at a later time, also on a similar sample, performing the experimental self-absorption correction. The results are reported in Figure 5.13 left, while in Figure 5.13 right a superposition of the uncorrected and corrected data, for the same sample, is shown.

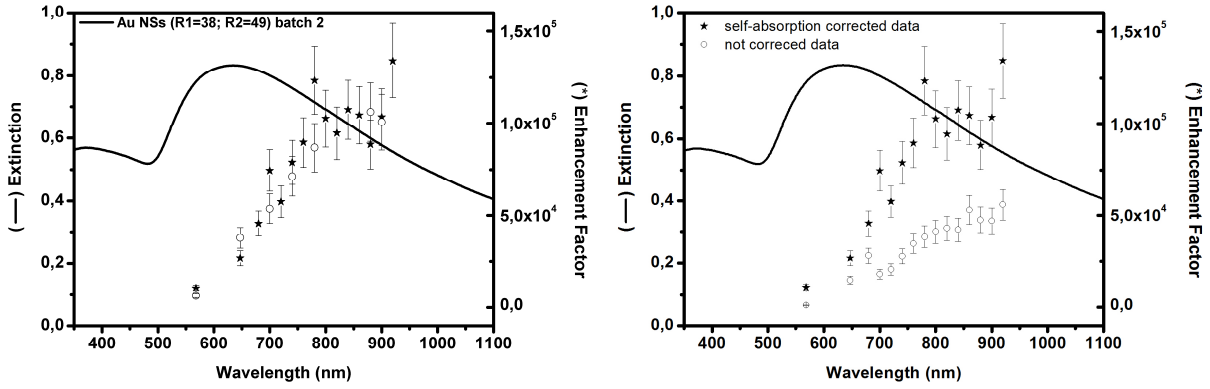

Figure 5.13: Extinction spectrum (black line) and SERS EF measurements [run 1 (black stars), run 2 (white circles)] for the Au NSs (R1=38; R2=49) batch 2 (left); superposition of self-absorption corrected (stars) and uncorrected (white dots) SERS EF values (right).

As can be observed, the corrected EF profile is very similar to the uncorrected one, with the maximum SERS enhancement red shifted with respect to the maximum extinction wavelength. Although, the absolute EF values are about one order of magnitude higher than the uncorrected data, demonstrating that the self-absorption correction is required (the self-

absorption factor data range from 2.3 to 5.9 depending on the excitation wavelength). The empty circles in the left spectrum of Figure 5.13 are data obtained after a few weeks, demonstrating the stability of the SERS sample in time, even with the presence of ethanol, used as internal standard for the self-absorption factor calculation. From these considerations, the trend of the Au NSs (R1=38; R2=49) batch 1 sample reported in Figure 5.12, is convincing, although the self-absorption correction was not applied.

Theoretical calculations, based on simulations, could be also applied to correct the experimental data of Figure 5.12 [28,141,142]. However, since, the simulation is strongly dependent on geometrical factors, which are hardly controllable and can change after setup realignment at every different laser excitation wavelength, the experimental correction is highly preferred.

The SERS results on the other three samples are reported in Figure 5.14.

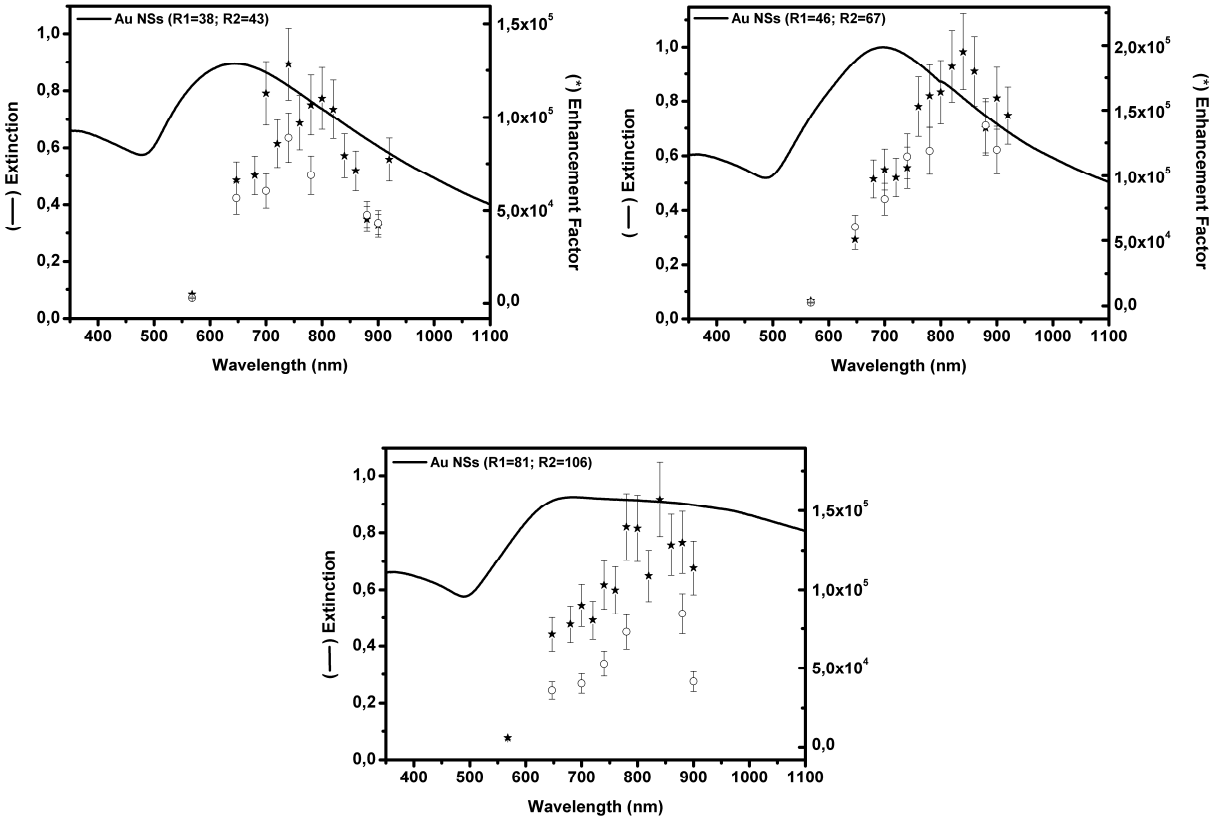

Figure 5.14: Extinction spectrum (black line) and SERS EF measurements [run 1 (black stars), run 2 (white circles)] for Au NSs (R1=38; R2=43) batch 2 (top row left), Au NSs (R1=46; R2=67) batch 2 (top row right) and Au NSs (R1=81; R2=106) (bottom).

As can be observed, in all the samples, the EF profile is very similar: a SERS extinction band is present at excitation wavelengths red shifted with respect to the maximum extinction peak. There seems to be no correlation between the extinction spectrum and the enhancement of the incident (or Raman scattered) radiation, as for some other samples in literature [33]. The strongest assumption remains the present of hot spots in the system.
Future experiments should be done in order to prove if the hot spots are interparticle or intraparticle ones. DLS measurements could not detect the presence of bigger particles indicating dimers or trimers, leading to the assumption that the hot spots are probably present on the single nanoshell surface.

Before changing to the description of solid SERS substrates, in Figure 5.16 the superposition of photoacoustic and SERS data for Au NSs (R1=38; R2=49) sample, investigated with both techniques, is presented. In the left spectra, the extinction spectrum and the photoacoustic data are reported: the data in the bottom spectrum represents the absorption percentage and scattering percentage to the total extinction in white and black, respectively. In the top spectrum the superposition of the extinction spectrum (black line) and the normalized aborption and scattering contributions are shown in white and black, respectively. The data are obtained by multiplying the percentage values with the extinction of the sample. In the right spectra, instead, the absorption and scattering contributions are compared with SERS EF data. In the top right spectrum the comparison with absorption contribution is shown, while in the bottom one, scattering and EF trends are compared.

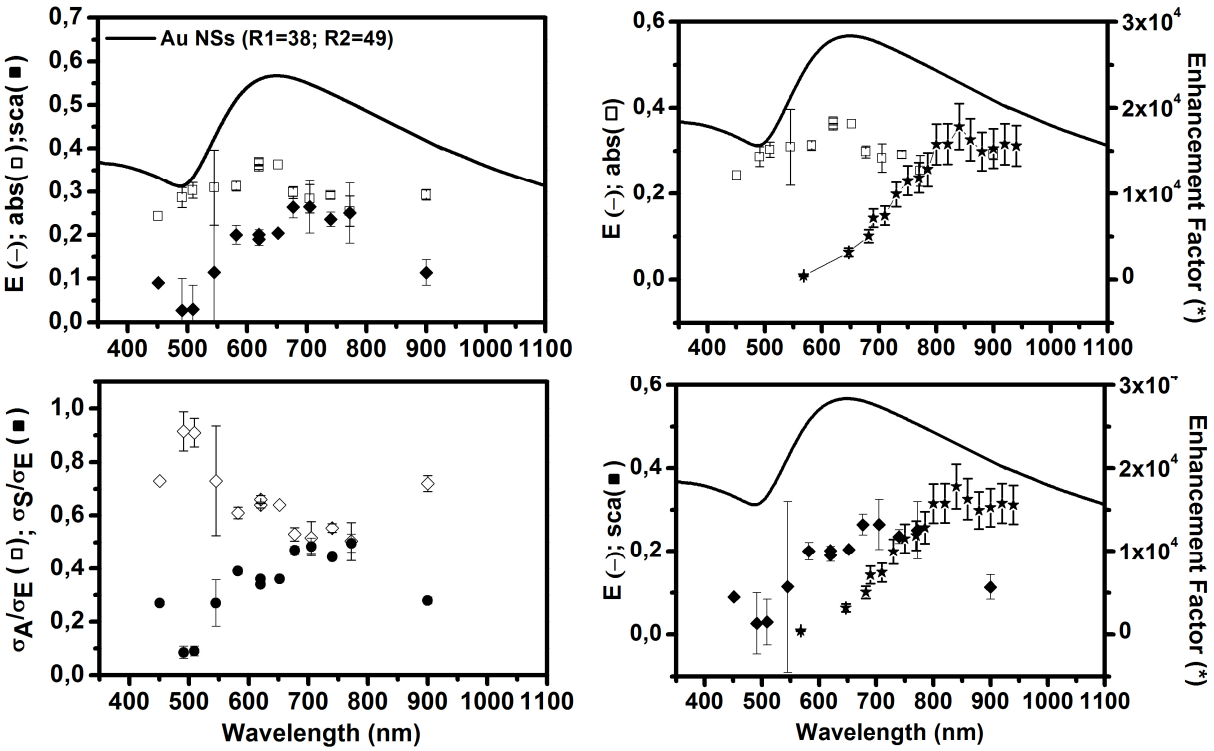

Figure 5.16: Extinction spectrum (black line) of Au NSs (R1=38; R2=49) batch 1 and photoacoustic measurements (left); Extinction spectrum (black line) and comparison between SERS EF measurements (black stars) with absorption contribution (white square) (top spectrum) and scattering contribution (black square) (bottom spectrum).

The purpose of this comparison is the summary of the collected data. For that nanoshell sample in solution, the absorption percentage to the extinction seems to decrease from Vis to the near IR range, while the scattering one is increasing. From the normalized data in the top right spectrum, the absorption contribution seems to reach a maximum value in the 650 nm region, while for the scattering contribution the maximum seems to be red shifted to around 750-800 nm. SERS EF data are clearly increasing toward the IR region. From the bottom right spectrum of Figure 5.16, scattering contribution and SERS EF seem to have the same trend, although in case of SERS EF the profile is even red shifted of about 50-100 nm.

The basic observation done looking to the comparison in Figure 5.16, is that scattering contribution seems to have the same trend than the SERS EF, although blue shifted.

It isvery difficult to find a final solution on the long discussed topic of extinction (absorption + scattering) versus SERS enhancement behavior [32]. In fact, through photoacoustic

measurements the far field properties of the nanostructures are tested and they are not influenced anymore by the presence of hot spots, neither interparticles or intraparticles one. On the other hand, SERS measurements are local field data, and are strongly sensitive to hot spot formation: even few nanoparticles aggregates can cause an enhanced local field of about 1000 times higher than the one around a single nanoparticle.

5.4 Solid SERS substrates

For the realization of sensor devices, it is often more suitable to have solid SERS substrates. They are much more easy to handle and to control with respect to liquid samples and their morphological characterization can be performed with much more detail, through SEM or AFM.

The most important features of high quality SERS substrates are [143]:

- Reproducibility
- Stability in presence of different environments, including solvent and analyte itself
- Homogeneity of the SERS signals over the whole substrate
- Sensibility (high enhancement factors)

In the present work easy and cheap substrates were prepared and tested in order to satisfy the four points listed above and to exploit them for SERS sensing applications.

The solid samples were prepared by simply depositing the different nanostructures, described in Chapter 4, on a glass support, previously functionalized with metal-affine Aminopropyltrimetoxy silane (APTMS) [92]. This molecule can strongly enhance the adhesion of the metal structure onto the support and therefore the stability of the whole sample. The deposition scheme is depicted in Figure 5.16.

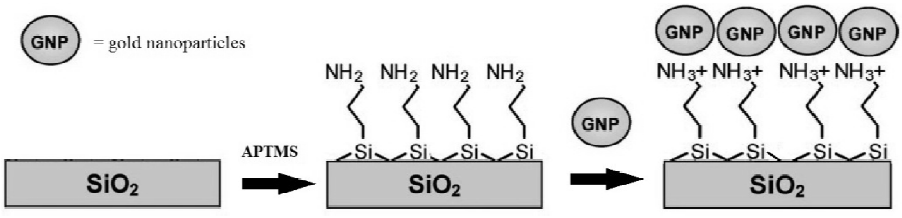

Figure 5.16: Scheme of gold nanostructures deposition onto glass.

Firstly, the glass slides were quickly cleaned with acetone and distillate water and then with acid piranha solution (H_2SO_3:H_2O_2 3:1) at 80°C for 1 h. The slides were then rinsed in distillate water and cleaned one more time with basic piranha (NH_4OH: H_2O_2 5:1) at 80 °C for 20 min. The glass slides were then accurately rinsed in distilled water and can be stored for a few days in water. The glass slides were then functionalized with APTMS at 60°C in a 1% APTMS solution in toluene for 5 min. The dried glass was then immerged into a properly dilute colloidal nanostructure solution, and kept at room temperature for 1 night. Doing so, the nanostructures are deposited onto the glass, gravitationally. The SERS substrates were then cleaned with water in order to eliminate the excess of nanostructures on the substrate and stored in an inert environment.

The reproducibility of the plasmonic substrates was tested by preparing some samples in the same experimental conditions and by checking their plasmonic features through UV-Vis spectroscopy. In Figure 5.17 the UV-Vis spectra of some Au NPs and Au NSs (R1=38; R2=49) are shown.

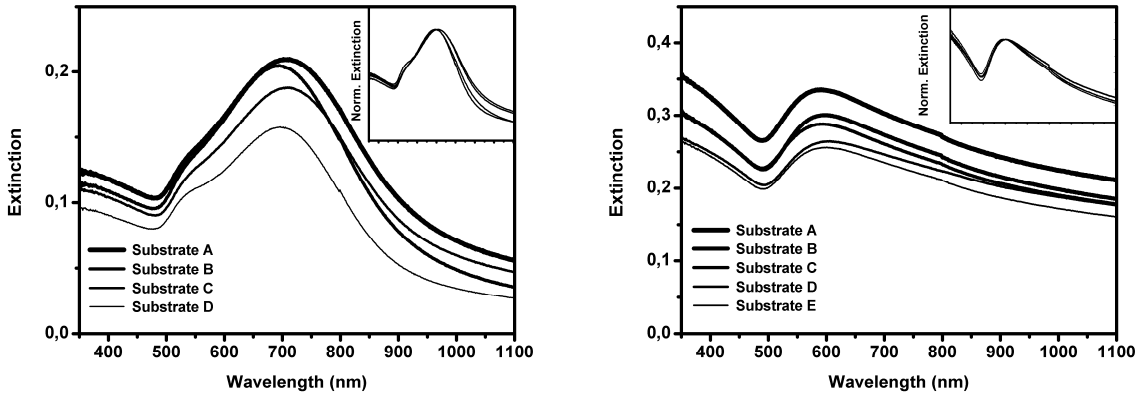

Figure 5.17: Extinction spectra of different Au NPs (left) and Au NSs (R1=38; R2=49) (right) substrates; normalized spectra in the insets.

As can be observed comparing Figure 5.17 left with the colloidal nanoparticle spectrum reported in Chapter 4 (narrow band with maximum at 520 nm), the plasmonic extinction band of colloidal Au NPs is modified after deposition on a solid support. This is due to the formation of aggregates on the glass slide involving the presence of NPs hot spots. Observing the right graph in Figure 5.17, this seems not to be the case for Au NSs (R1=38; R2=49), where the plasmonic band is only damped from the dielectric environment of the glass

support, shifted at lower wavelengths due to the glass and air refractive index around the nanoshell, but not modified in shape. For this sample, probably, more single Au NSs are present on the glass slide. For both samples reported, there is a little change in the concentration of Au NPs and Au NSs on the substrate, but, as demonstrated in the normalized spectra (inset), the plasmonic band shape doesn't change significantly.

Moreover, the NPs concentration on the substrate can be partially controlled, by changing the NPs concentration in the deposition solution. In Figure 5.18 exctintion spectra of Au NPs substrates at different NPs concentration is shown. As can be observed, varying the NPs concentration, also the extinction spectrum changes. In fact, at even higher NPs concentrations (from substrate 5 to 1), the aggregates become predominantly: the band at 700 nm rises with respect to the 520 nm band. This is particularly the case of Au NPs substrates, while for Au NSs the difference, in case of probable aggregate formation, is not visible, as also demonstrated in Figure 5.17 right.

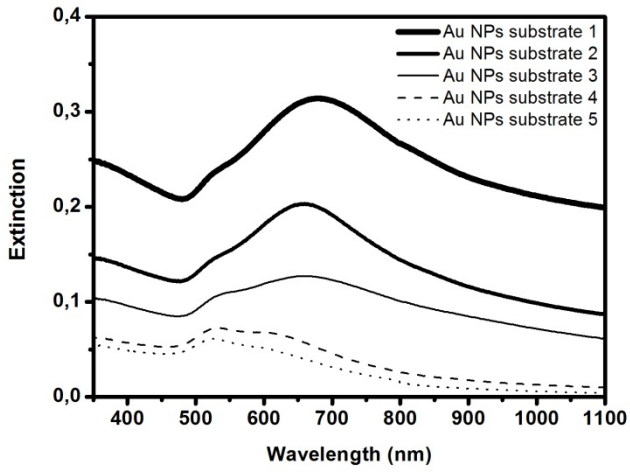

Figure 5.18: Extinction spectra of Au NPs substrates at even lower deposition Au NPs solution concentration (from 1 to 5).

In case of Au NSs substrates, the realization of substrates at varying shell concentrations, was tested through AFM. The same characterization was not performed on the Au NPs substrates reported in Figure 5.17, because the nanoparticle dimension is on the order of the detection limit (the AFM tip dimension is about 10-20 nm) and no significant images could be collected. The AFM images on Au NSs (R1=46; R2=69) substrates, realized with three different Au NSs concentrations, are shown in Figure 5.19.

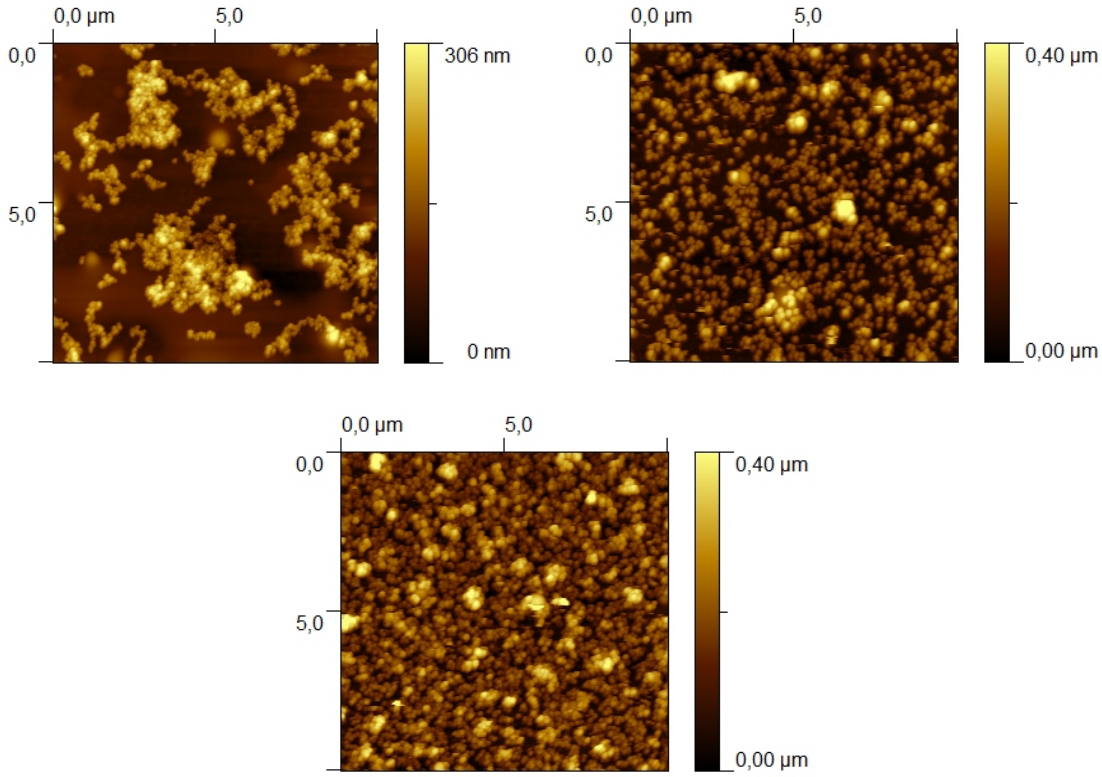

Figure 5.19: AFM images of Au NSs **(**R1=46; R2=69) substrates with about 20% (top row left), 50% (top right) and 70 % (bottom) coverage degree.

As can be observed, at higher coverage degrees, the NSs substrates appear more homogeneous. Therefore, the conditions for obtaining covarege degrees of about 65-70% are usually used for substrates realization.

The stability in presence of different environments was also checked through optical characterization for phosphate buffer solution (used in biological environments) and in neutral and acidic methanol, commonly used for the functionalization of plasmonic substrates with organic species. The final stability test, through UV-Vis spectroscopy, has to be performed after functionalization of the substrate with the analyte of interest in order to check the substrates resistivity. In our study we tested all the chemical environments on the plasmonic substrates before final application.

In Figure 5.20, a stability test in a 1 mM benzenthiol (Bzt) solution in methanol, used for SERS EF determination, on a Au NSs (R1=38; R2=49) is shown.

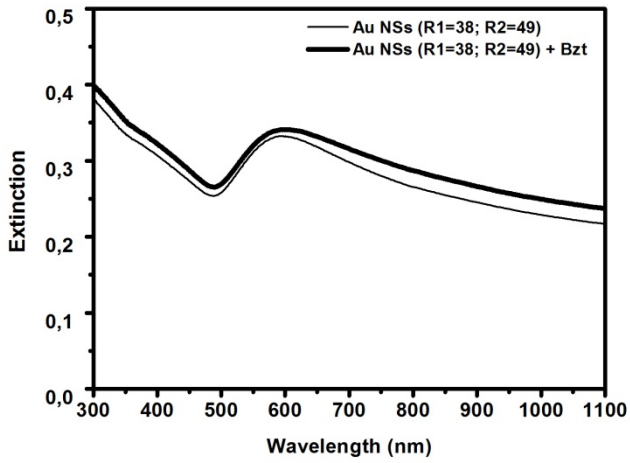

Figure 5.20: Extinction spectrum, of Au NSs (R1=38; R2=49) before and after functionalization with benzenethiol.

As can be observed, the Au NSs substrate is stable and doesn't undergo spectral modifications when immerged into a methanol solution.

Moreover, the substrates present a high homogeneity, already tested with AFM, and a high optical quality, probed by optical microscope images and SERS measurements. With micro-Raman setup, microscopy images of the observed samples can be collected. An example of microscopy images of Au NSs and Au NPs substrates, collected with 50x objective, is reported in Figure 5.21.

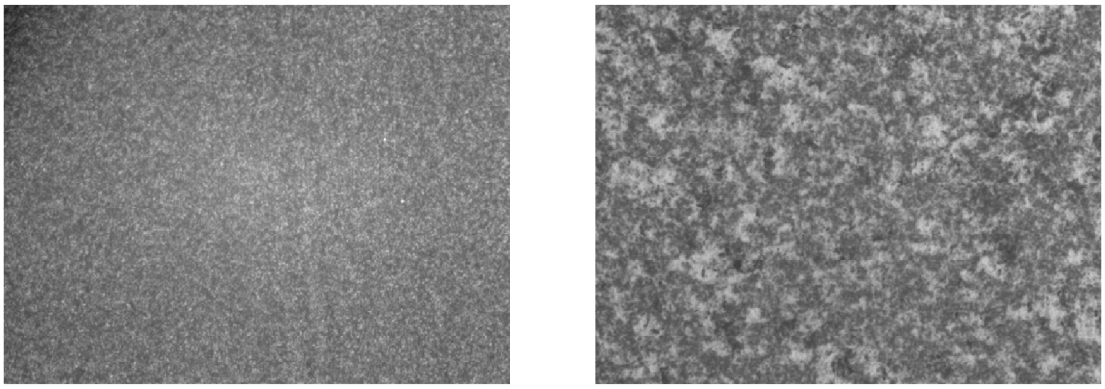

Figure 5.21: Microscopy images, collected with 50 x object on the micro-Raman setup, of Au NSs (left) and Au NPs (right) substrates.

In Figure 5.21 the high presence of Au NPs aggregates is well visible, while the Au NSs substrate seems perfectly homogeneous.

The Raman signal homogeneity and sensitivity (EF) measurements were tested with both micro and macro-Raman detection setups. The optimization of the nanostructure deposition, varying APTMS functionalization procedure and nanoparticles deposition concentrations and times, led to a SERS signal reproducibility on the single substrate of up to 92%, which is very good for substrates with randomly oriented nanoparticles.

For the estimation of the sensibility, EF measurements are performed: for solid SERS substrates, where the not attached molecules are eliminated, it is suitable to use the so called SERS substrate enhancement factor (SSEF) definition, already introduced in Chapter 3:

$$SSEF = \frac{I_{SERS} / (\delta_{surf} \delta_{ns} A_m)}{I_R / (c_R H_{eff})} \quad (3.43)$$

c_R is the analyte concentration expressed as molecules/cm^3 in non-SERS conditions, δ_{surf} is the surface density of molecules/cm^2 over the SERS substrate, δ_{ns} is the surface density of individual nanostructures and A_m is A_m the metallic surface area of each nanostructure. $H_{eff}A_{eff}$ is the effective scattering volume. Benzenethiol is used as probe molecule for EF measurements. Pure Bzt was used as liquid reference. This molecule is often used in literature on solid substrates [33], because it presents a high Raman cross section, few and well defined signals in the 300-1800 cm^{-1} region.

The Raman spectrum of the probe molecule and the list of Raman signals and assignments are reported in Figure 5.22 and Table 5.4.

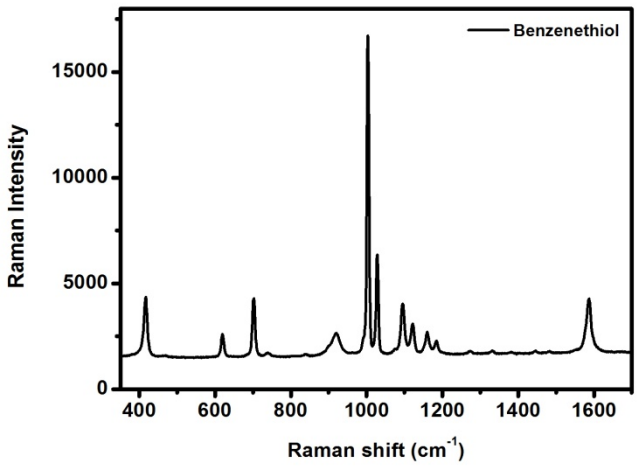

Figure 5.22: Raman spectrum of pure benzenethiol recorded at 647 nm excitation.

Table 5.4: Raman band positions and assignment of pure benzenethiol.

Benzenethiol Raman shift (cm^{-1})	**Assignment** [78,136]
419	ν_s S-C
473	S_{16b}
694	ν_s S-C
998	S_{12}
1021	S_{18a}
1072	S_1
1112	S_{6a} + S_{7a}
1571	S_{8a}

$S_{ij=}$ ring vibration modes; ν_s= symmetrical stretching.

Four different SERS substrates were analysed: Au NPs, Au NSs (R1=38; R2=49), Au NSs (R1=46; R2=67) and Au NSs (R1=81; R2=106) substrates. For SERS EF measurements the ring breathing mode at about 1000 cm^{-1} (evidenced in grey) is used, because less affected on chemical enhancement contribution[30]. The surface density value δ_{surf} for benzenethiol on a planar surface is $6.8 \cdot 10^{14}$ molecole/cm^2, from literature[144]. The A_m value was set to 4, approximating that the surface of a gold nanoparticle deposited onto a solid support is 4 times its projected area. The laser light is probably exciting the molecules adsorbed on only half the nanoparticles, therefore a A_m value of 2 should be more realistic. Setting the value to 4, however, the EF values are underestimated and less error will be done in the results discussion.

The surface density of nanoparticles on the substrate δ_{ns} value, instead, was extracted from the analysis of different zones on the solid substrates, through AFM and SEM. The δ_{ns} was found to be about 0.6 for Au NPs, 0.4 for Au NSs (R1=46; R2=67), 0.65 for Au NSs (R1=38; R2=49) and 0.7 for Au NSs (R1=81; R2=106) substrates.

In Figure 5.23 SEM images for the Au NPs and Au NSs (R1=46; R2=67) (top row) and AFM images for the Au NSs (R1=38; R2=49) and Au NSs (R1=81; R2=106) substrates (bottom row) are shown.

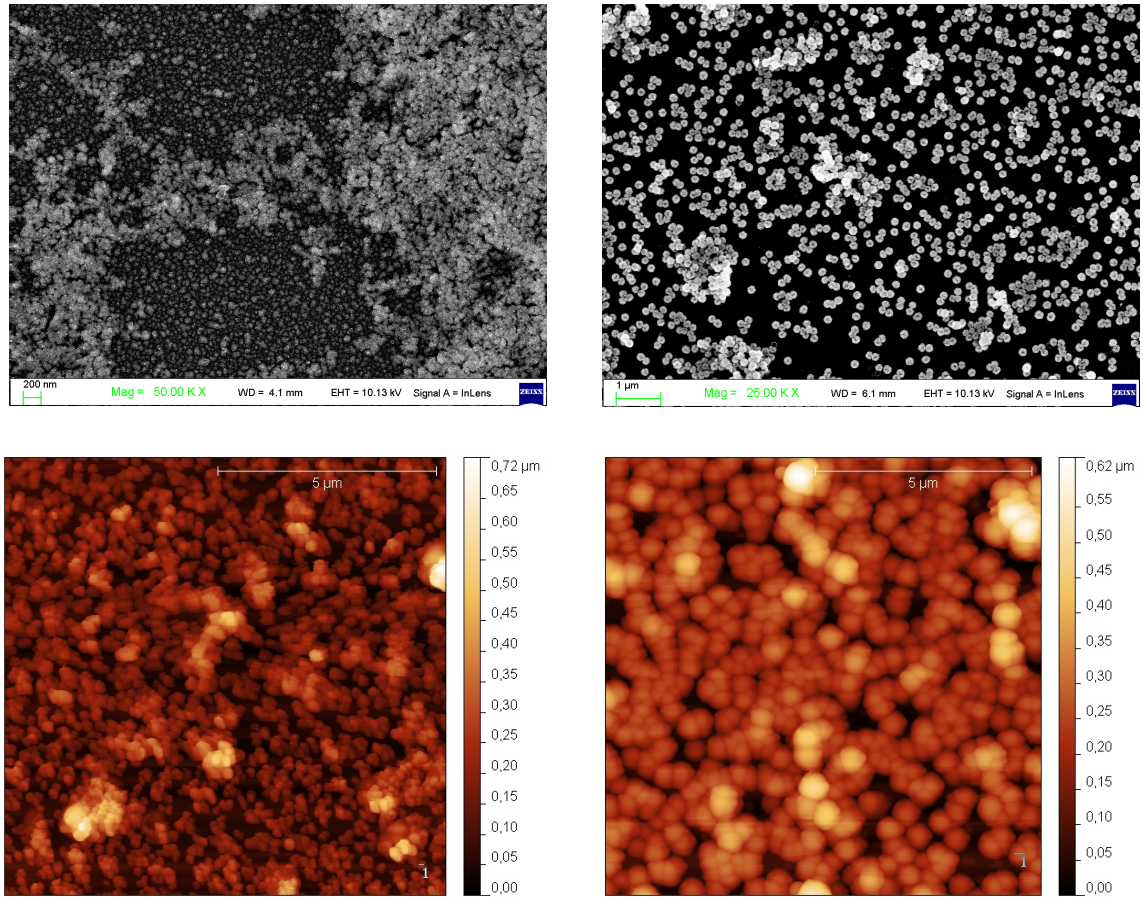

Figure 5.23: SEM images of Au NPs (top left) and Au NSs (R1=46; R2=67) (top right) substrates; AFM images of Au NSs (R1=38; R2=49) (bottom left) and Au NSs (R1=81; R2=106) (bottom right) substrates.

Both micro-Raman and Macro-Raman measurements are performed, at different wavelengths in order to report the enhancement factor profile. The EF results are reported together with the extinction spectrum in Figure 5.24, for all the samples.

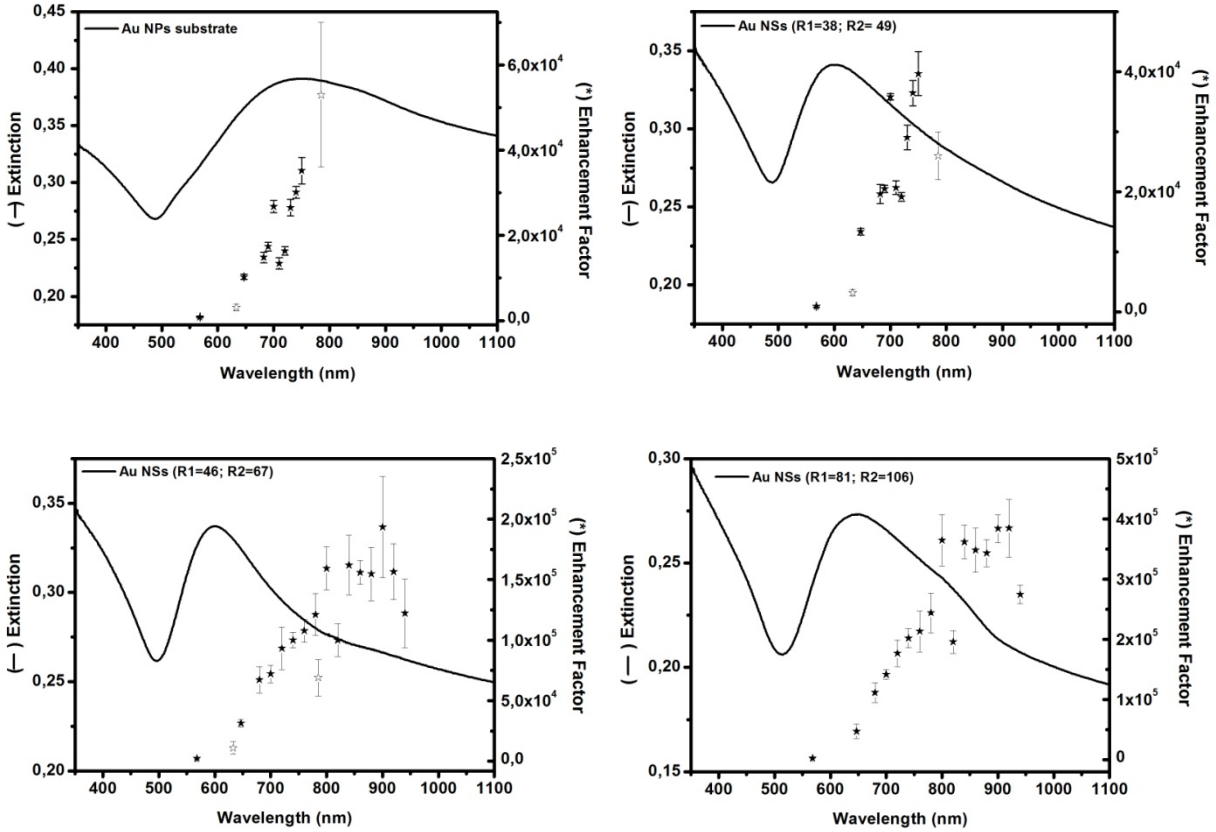

Figure 5.24: Extinction spectrum (black line) and EF values (black stars) for Au NPs (top left), Au NSs (R1=38; R2=49) (top right), Au NSs (R1=46; R2=67) (bottom left) and Au NSs (R1=81; R2=106) (bottom right).

The dark points are recorded with macro-Raman setup, like described in the previous section, by choosing the excitation wavelength through a tunable Ti:Sapphire laser. The white data, instead, are recorded on the micro-Raman setup with a 633 and 785 nm excitation wavelength. The error bars are calculated measuring the SERS signal of Bzt on many zones of the sample. The big error bar for the 785 nm data on the Au NPs substrate is probably given by the less homogeneity of the sample: with micro-Raman setup the laser spot is small, around 1 μm2 with 50 x objective, while in case of macro-Raman conformation, the spot can reach a few mm2. That means that micro-Raman is more sensitive to non homogeneous zones compared to the macro-Raman approach. The H_{eff} value is measured in both the setups, on a reference Si slide, by measuring the intensity of the 520 cm^{-1} signal varying the sample position around the focal plane. The intensity values, versus x position of the sample, give a trend like depicted in an example in Figure 5.25.

The data should be normalized and fitted with a Lorentzian function: the integral of the fit can be attributed to the focal volume high, i.e. the H_{eff} value.

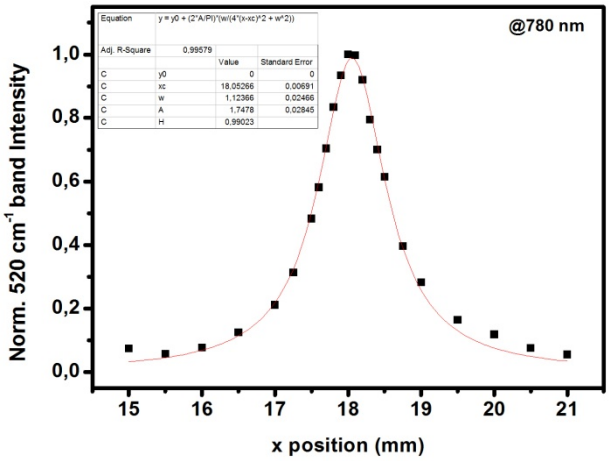

Figure 5.25: Example of H_{eff} measurement for the 780 nm excitation wavelength.

Looking at the data reported in Figure 5.24, the EF profile is very similar to the ones observed in solution. This is in agreement with what expected: particularly for the Au NPs substrates the presence of hot spot is evident even in the extinction spectrum. For this kind of substrate, in fact, the EF profile follows more or less the extinction one, with maximum enhancement at around 800 nm. For the Au NSs substrates, instead, the EF profile reveals the presence of hot spots, which are not clearly visible in the extinction spectrum. The extinction spectra are all blue shifted with respect to the ones in solution, due the refractive index change in air and glass with respect to water. In case of the biggest Au NSs (R1=81; R2=160) a shoulder is present in the red region near the principal extinction band. This shoulder could be given either by aggregation phenomena or also by the presence of the bimodal dimensional distribution. For this sample further considerations are therefore difficult.

As a general rule, the presence of hot spots is very important in order to reach high amplification values on the SERS substrates, but, on the other hand, makes it difficult to find a relation between extinction properties and SERS local field measurements. For substrates dominated by hot spots, the maximum SERS enhancement is always expected at wavelengths red shifted, even hundreds of nanometers.

UV-Vis absorption and SERS characterization was also performed on Ag NPs substrates, which showed high EF values of $(8.9 \pm 1.9) \times 10^4$ and $(3.0 \pm 0.3) \times 10^5$ for 514 and 633 nm excitation, respectively. The stability tests, however, demonstrated that the substrates are hardly stable in different environments, even in the benzenethiol functionalization solution, and the extinction spectrum is changing in time. Due to the strong oxidation and less stability, these structures are therefore not suitable for applications where the control over plasmonic and SERS properties is necessary.

Chapter 6

SERS SUBSTRATES FOR CHEMICAL SENSING

6.1 Introduction

In the previous chapter different SERS substrates have been presented, for applications in liquid and solid phase. The different nanostructures give the possibility to tune the plasmonic properties in a wide spectral range. This overview opens the way to some ideas for the realization of plasmonic sensors based on SERS. Two different applications are described and discussed in the present and in the next chapter.

In the present chapter the realization of a plasmonic sensor for chemical species is reported. In particular, the idea is to realize a device for the detection of toxic volatile organic compounds (VOCs) in traces. The ultrasensitive and selective detection of VOCs is very important for environmental sustainability and human health. The measurement of VOCs, together with the identification of the kind of VOC, either in the gaseous or in the liquid phase, is a challenging task. Many works in literature by Chen et al.[145–147] are based on the detection of organic vapors through the observation of the LSPR band of different nanostructures. This sensor reveals the presence of organic compounds, thanks to the variation of absorbance intensity, wavelength position and band width in the UV-VIS absorption spectrum of the plasmonic nanostructure. Although these works report low concentration detection limits and high detection selectivity, the drawback of exploiting the LSPR band remains the indirect detection of the analyte: the variation of the plasmonic property is observed and not directly a property of the analyte species. In order to overcome this drawback, SERS could be an interesting alternative detection technique.

Only few publications in literature report SERS experiments for organic compounds sensing[148], and still less are about VOCs detection[149]. In this chapter a novel strategy of SERS sensing is proposed, based on the interaction of VOC molecules with a hybrid organic inorganic sol gel matrix. The design of hybrid organic inorganic sol gel membranes for separation and sensing applications was already proposed in 2001 by Guizard et al.[150]. In the same year Shea and Loy described the synthesis of an interesting class of hybrid organic inorganic sol gel precursors, the bridged polysilsesquioxanes[151], interesting for their intrinsic properties of hybrid and functional materials. By changing the bridged compound, one can exploit many different functional groups, ranging from disulfides, aromatics and ureic groups, showing affinity to different analytes. These compounds have been exploited, some years ago, as VOCs adsorbents by Dabrowski et al.[152]. Recently a work by Brigo et al. described the use of polysilsesquioxanes for VOC detection through LSPR observation on solid substrates [153].

6.2 Realization of the VOCs SERS sensor: Xylene detection in high affinity sol gel matrix

The idea to realize a VOCs SERS sensors, based on the interaction of the analyte with a high affinity sol-gel matrix, was developed within a collaboration with the research group of Prof. Guglielmi and Prof. Brusatin of the Department of Industrial Engineering – Materials Section of the Padova University.

The idea was to couple a functional hybrid organic inorganic polysilsesquioxane sol gel matrix with plasmonic nanostructures in order to detect aromatic molecules, in particular p-Xylene, through Surface Enhanced Raman Spectroscopy. The plasmonic substrate should be exploited for enhanced sensitivity and selectivity, while the functional matrix should act as absorber of the aromatic analyte, in order to bring it closer to the plasmonic substrate.

The precursor chosen for the realization of the matrix was the bis(triethoxysilyl)biphenyl polysilsesquioxanes, depicted in Figure 6.1.

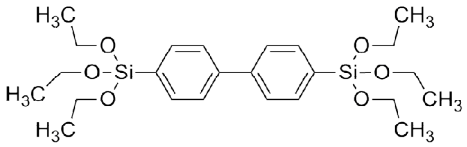

Figure 6.1: Molecular structure of bis(triethoxysilyl)biphenyl polysilsesquioxanes, used as precursor in the sol gel synthesis.

The organic moiety in the hybrid network is specifically chosen for exhibiting a high-affinity interaction to aromatic hydrocarbons. The analyte molecules, penetrating into the porous sol-gel film, interact with the phenyl bridging groups of the organic unit though π- π stacking interaction [154,155].

The basic sol gel synthesis is performed in presence of acid as catalyst and water in a 15-40 g/L dilute sol solution of the precursor, depending on the desired final film thickness. The solution is then spin coated over a soda lime glass (about 2000-6000 rpm for 30-60 s) and subjected to a heat treatment of about 30 min at 60°C. Through this method, already reported in literature[153], films of thicknesses ranging from 50 to 300 nm could be obtained, by simply varying the precursor solution concentration and the spin coating parameters. Higher post application bake temperatures (PAB) can also cause the decrease of film thickness.
The sol gel films present high homogeneity on the optical microscope, a homogeneous pore distribution, probed by AFM images, and a reproducible thickness (Figure 6.2).

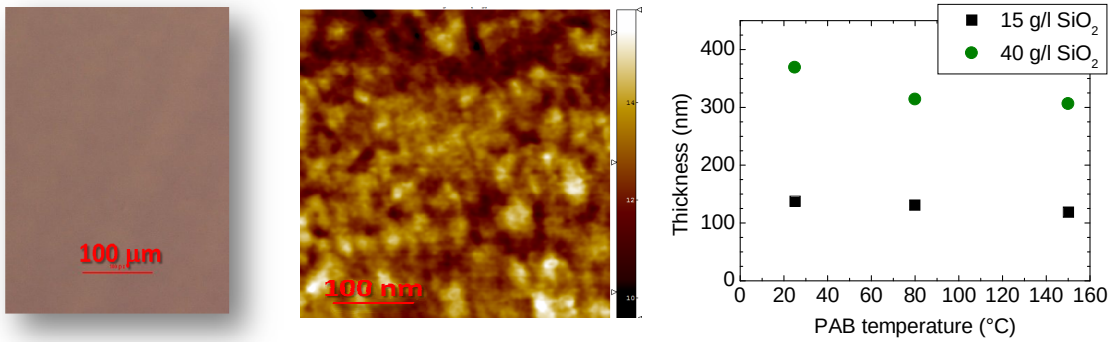

Figure 6.2: Optical and morphological characterization of bis(triethoxysilyl)biphenyl polysilsesquioxane films: optical microscopy image (left), AFM image (middle) and film thickness as a function of heat treatment temperature at different sol dilutions.

Before realizing the SERS sensor, some basic characterization was performed on the matrix and the analyte, in order to identify the best spectral region for Xylene detection. In Figure 6.3 Raman signals of pure Xilene and bis(triethoxysilyl)biphenyl polysilsesquioxane (diph) film are compared. The grey evidenced signals of Xylene lie in spectral regions where the diph-film does not present any Raman activity.

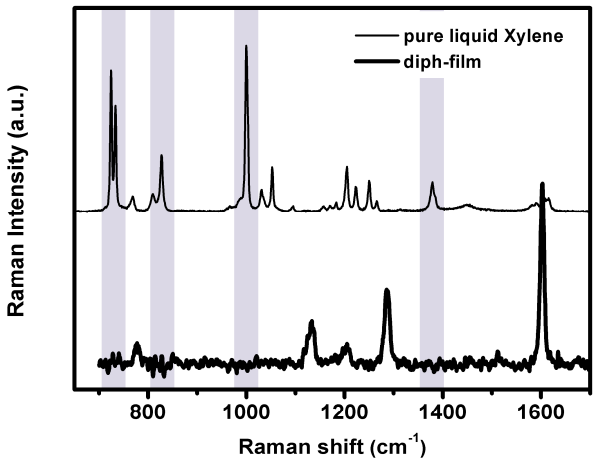

Figure 6.3: Raman spectra of diph-film and pure liquid Xilene in the 650-1700 cm^{-1} Raman shift region.

The Raman band positions and assignments are listed in Table 6.1.

Table 6.1: Raman band position and assignment of pure Xylene and diph-film:

Xylene Raman shift (cm^{-1})	**Assignment** [135,136,156]	**diph-film Raman shift (cm^{-1})**	**Assignment** [135,136]
725/735	ν_1	780	ν_s Si-C
810/827	ν_{10a}	1130	ν_s Si-O
1000	ν_{18b}	1206	=C-H out of plane ring def. vib.
1030	ν_{1a}, ν_{1b}	1290	=C-H in plane ring def. vib.
1050	ν_{1b}	1605	ν_s C=C
1204	=C-H out of plane ring def. vib.		
1223	ν_{1b}		
1250	=C-H in plane ring def. vib.		
1380	ν_s C-H (metyl)		

The most interesting Xylene signals are the ring modes at 810/827 cm^{-1} and the strong signal at 1000 cm^{-1} Raman shift.

6.2.1 First detection scheme: Au NPs embedded into hybrid sol gel matrix

For the SERS detection of Xylene, the first idea was to directly embed gold nanoparticles into the sol gel matrix by adding them to the precursor solution during the sol gel synthesis. The scheme is reported in Figure 6.4.

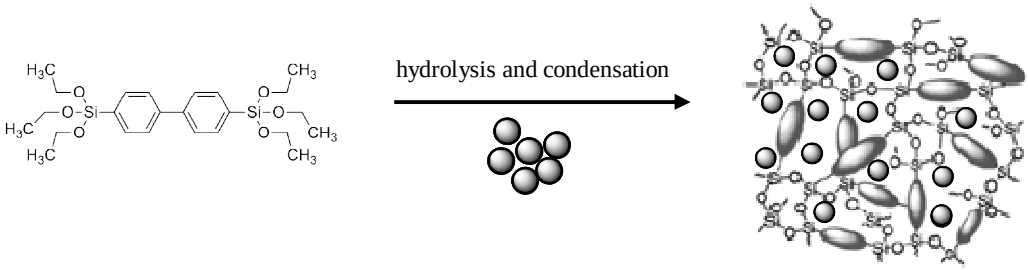

Figure 6.4: First scheme for the realization of the Xylene SERS sensor.

Tests were performed adding grown Brust Au NP, bigger naked Au NPs, synthetized with Turkevich method, and PEG covered Turkevich Au NPs, to the sol gel solution.

Unfortunately, no one of these tests gave good results, principally because of difficulties in the Au NPs addition step. In case of Brust Au NPs the films present a plasmonic band with a very low intensity, strongly damped by the sol gel matrix. Naked Au NPs, instead, aggregate instantly, causing the flocculation of the sol. Some few results, from a synthetical point of view, were obtained using PEG capped Au NPs, previously transferred into ethanol. The films showed a good optical quality, but preliminary SERS tests did not show any analyte signal. Moreover, not even the enhancement of the matrix Raman signals, due to the presence of Au NPs, could be observed. The absence of the Raman signals is probably due to the PEG layer, acting as spacer between the matrix functional group, the analyte and the plasmonic active particles, and to the low particles concentration obtained in the sol gel film. For this reason a further attempt was made, by strongly concentrating the Au NPs solution (20 mM of gold in solution) and adding a higher amount of particles to the sol (18% mol with respect to the precursor). Furthermore after spin coating the films were heat treated at much more higher temperature (about 250-300°C) in order to eliminate the organic PEG layer on the particles surface and to shrink the volume of the sol gel film. Previous studies demonstrated that the high temperatures do not cause the damage of the bridged molecules because of the particular molecular structure bind to the inorganic component. Also in this case, however, the Raman signal of the matrix was not amplified and the analyte could not be detected.

6.2.2 Second detection scheme: hybrid sol gel matrix spin coated over plasmonic substrate

It was necessary to develop a new strategy in order to overcome these synthetical difficulties. The idea was, therefore, to exploit the well characterized and stable SERS solid substrates, described in Chapter 5. In this case the sol gel matrix was spin coated directly over the SERS substrate, forming a two layer system, depicted in Figure 6.5.

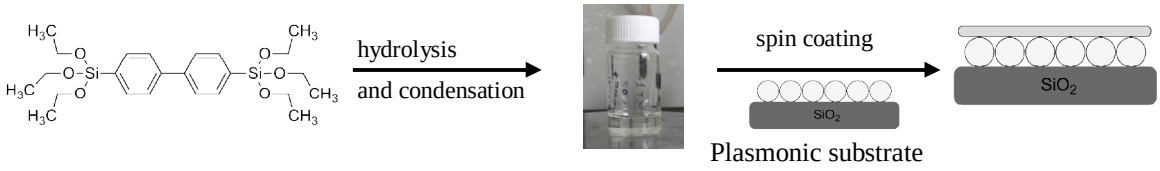

Figure 6.5: Second scheme for the realization of the Xylene SERS sensor.

The hybrid sol was spin coated over Au NPs and Au NSs (R1=46; R2=67) substrates in order to obtain very thin films of about 50 nm thickness. For such a sensor design, the sol gel film could be even thinner, of about 10-20 nm, because only the first 10 nm near to the metal nanostructure feel the local field intensity enhancement. The principal drawback in this detection scheme is, in fact, the low plasmonic active volume generated inside the whole sensor.

Nevertheless preliminary, very promising results were obtained using this strategy. The first important observation was a matrix Raman signal enhancement due to the presence of the plasmonic substrate, reported in Figure 6.6. The best results were obtained using the micro-Raman setup with 633 nm excitation wavelength, exciting the sample with 0.03 mW laser power. The micro-Raman measurements give the possibility to choose the best substrates region in order to obtain the most intense signal.

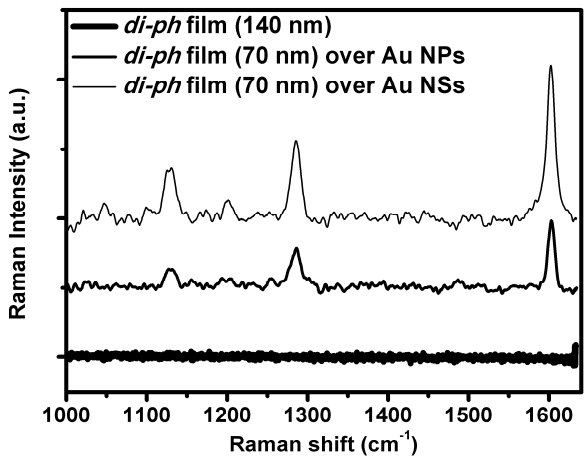

Figure 6.6: Raman/SERS spectra of diph film deposited onto glass, Au NPs and Au NSs (R1=46; R2=67) substrate.

As can be observed from Figure 6.6, the matrix signals are clearly enhanced due to the presence of the plasmonic substrate. A diph film, of about 140 nm thickness deposited onto a glass slide, did not give any Raman signals, while, at the same laser power, even thinner diph films deposited on plasmonic substrates showed relatively strong Raman activity in the 1000-1600 cm^{-1} Raman shift region. From this experiment it is also clear that the Au NSs substrate is more efficient, of about a factor of 2.

SERS experiments were performed also with the analyte in gaseous phase, by connecting a vacuum drier, containing the plasmonic sensor, with a cylinder with liquid xylene. Nitrogen is bubbled into the liquid and the xylene vapor flux, carried by the inert nitrogen, is flowing into the drier. After 30 min, the sample is extracted from the drier and SERS measurements are performed.

Unfortunately no xylene signals were detected, probably because of the fast regeneration of the matrix, i.e. the xylene molecules are desorbed too rapidly from the matrix pores. The principal reason for this phenomenon is probably the high temperature induced from the laser onto the SERS substrate. To support this hypothesis Stokes and Anti-Stokes Raman measurements were performed on a "naked" SERS substrate functionalized with benzenethiol. By recording both the Anti-Stokes and the Stokes signals of a given Raman mode, it is possible to calculate the temperature on the substrate through the Fermi Golden Rule, already described in paragraph 3.2.1:

$$\frac{I_{aSto}}{I_{Sto}} = \left(\frac{\omega_L - \omega_i}{\omega_L + \omega_i}\right)^4 e^{-\frac{\hbar\omega_i}{k_B T}} \tag{3.18}$$

For this measurement a calibration with a liquid reference is needed, in order to perform a relative temperature measurement, independent from instrumental factors. In this case liquid toluene was measured and the $k_B T$ value was set at room temperature. Doing so an instrumental correction factor c could be calculated, which can be then applied to the measurements on the SERS substrates. Measurements were performed at three different incident laser powers, ranging from 80 μW to 0.8 mW. The temperatures on the substrate are found to range from 60 to 110 °C, depending on the laser power used.

Even at the lowest laser power, corresponding therefore to the lowest temperature, xylene sensing measurements could not be performed: the sol gel matrix probably dissipates the high temperature induced on the sample but not enough to avoid xylene desorption. Although the

interactions involved are relatively strong, in the range of 38-140 kJ/mol [153], the temperature seems to be high enough to induce the xylene desorption.

For this reason a home made closed detection setup was realized, which allows to incubate the plasmonic sample with the xylene analyte and to directly perform the detection measurements in the closed cell through an optical window. The picture of the detection device is shown in Figure 6.7. It consists of a round teflon support with inlet and outlet tubes where a plasmonic sample of dimension 2.6 x 1.5 cm could be located. The device can be closed from the top through a Teflon ring with a polymer o-ring resting over a thin glass window. The device can be hermetically closed through little screws.

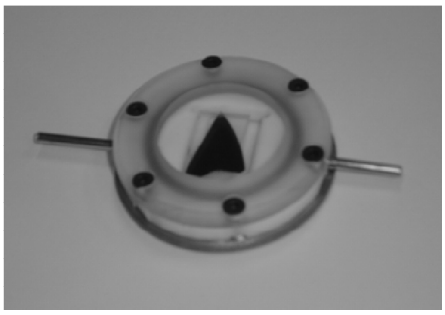

Figure 6.7: Picture of the closed home made SERS detection setup.

Before SERS measurements, the UV-Vis spectroscopy characterization of the substrates used is performed. In Figure 6.8 the UV-Vis extinction spectra of the "naked" Au NSs substrate and the same substrate cut into two different parts, which are separately covered with the diph matrix, are shown.

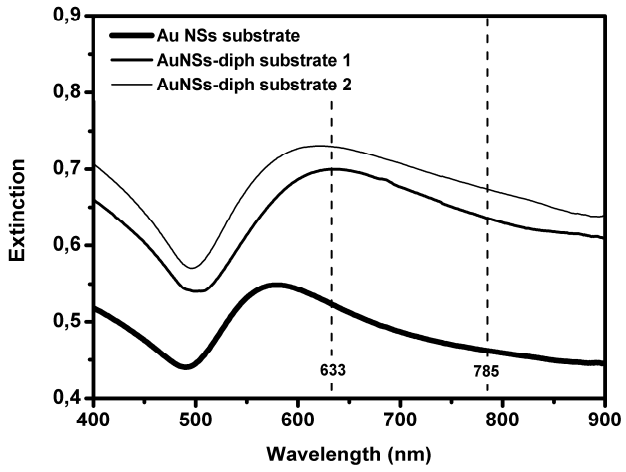

Figure 6.8: Extinction spectra of the native Au NSs substrate cut into two parts and separately covered with diph film, through spin coating.

As can be observed the extinction spectra of the diph covered Au NSs substrates are quite different with respect to the native Au NSs substrate. The extinction intensity is enhanced and the maximum band position is red shifted. This is due to the presence of the sol gel film with higher refractive index with respect to air. The two sensing substrates are demonstrated to be reproducible in terms of extinction properties.

The SERS measurements are performed putting the plasmonic substrate into the close device, directly under the microscope object, which should have a working distance corresponding at least to the thickness of the optical glass window.
With this detection setup the best signals were recorded with 785 nm excitation wavelength and a laser power of about 0.8 mW. A 100 x long working distance objective is used and the signal was collected from 20 different acquisitions, taken with 30 s accumulation time.
The best result of xilene vapor detection tests with the AuNS-diph substrate 1 is shown in the spectra of Figure 6.9.

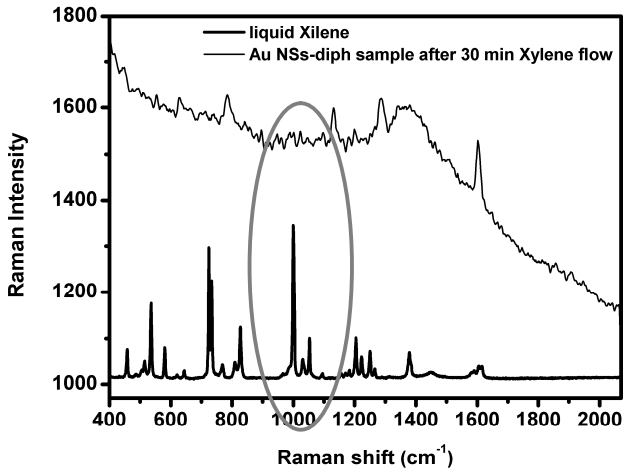

Figure 6.9: Raman spectrum of liquid Xylene and SERS spectrum of vapor Xylene in Au NSs-diph sensing system.

The signals of the diph matrix are well visible, but xylene signals could hardly be identified. This observation led to the supposition that xylene molecules in vapor phase could hardly be detectable at that low concentrations through SERS, which remains a very promising technique for selectivity detection but do not provide sufficient sensitivity for this kind of measurements.

Better results could, indeed, be obtained with the detection of liquid xylene, where the molecular concentrations are slightly higher. First tests were done incubating the Au NSs-diph substrate into pure liquid Xylene; the substrates are air dried and then put into the closed detection setup. The results with 785 nm excitation wavelength and 0.8 mW laser power (50 x objective and 20 x 30 s spectra accumulations) are shown in Figure 6.10, both for xylene on the Au NSs-diph substrate 1 and toluene on a similar substrate.

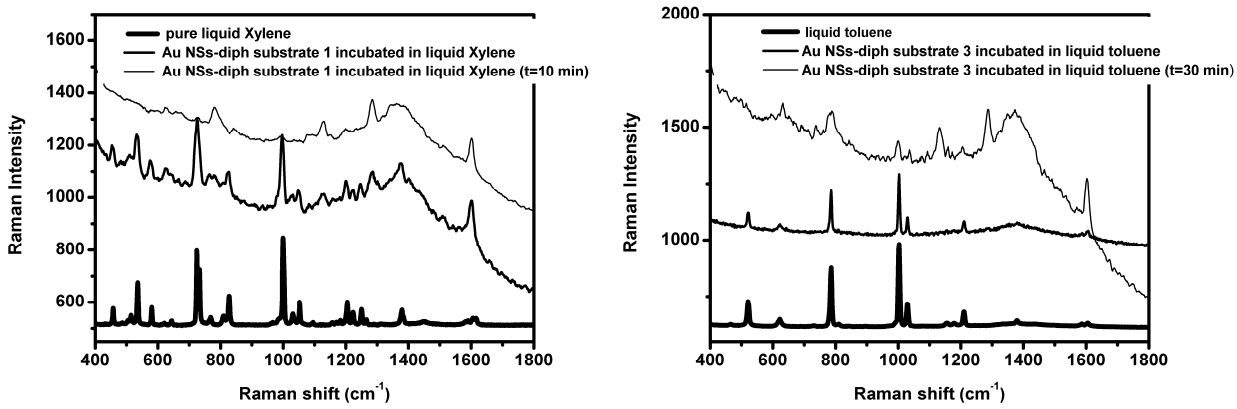

Figure 6.10: Raman/SERS spectra for AuNSs-diph substrates incubated in liquid Xylene (left) and liquid toluene (right).

The xylene and toluene signals are clearly visible right after the incubation in the pure liquid. After only ten minutes the signals are significantly lower, indicating a fast desorption of the analyte molecules from the sol gel matrix. The molecules are moving away from the plasmonic active area and could no longer be detected.

The fast desorption is the principal problem of the detection system and a solution should be found, like the use of a cooling systems or, even better, the development of a new detection system, involving much stronger interactions. For example a quinoide bridging group in the sol gel system could provide energy transfer mechanisms with aromatic molecules, increasing the interaction energy of orders of magnitude.

Nonetheless the enhancement efficiency of the realized system could be demonstrated by SERS measurements of Au NSs-diph substrate 2 immerged into a 0.5% xylene solution in organic solvent. In this experiment the closed setup was used as liquid cell: the Au NSs substrate was put in the closed device and the cell was filled with the organic solution and directly positioned under the SERS microscope. The results are shown in Figure 6.11.

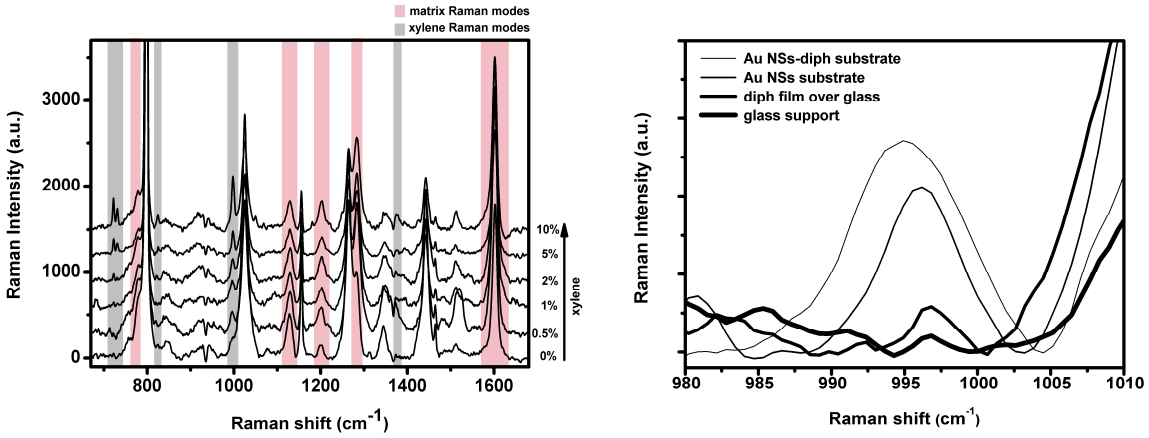

Figure 6.11: SERS spectra for AuNSs-diph substrate 2 in cyclohexane solution at different xylene concencentrations (left); spectral zoom on the 995 cm^{-1} Raman band of xylene for four different substrates immerged into a 0.5% xylene solution in cyclohexane: (right).

In the left spectra of Figure 6.11, SERS measurements at different xylene concentrations in cyclohexane solution are shown. The signals evidenced in red are the Raman bands of the sol gel matrix, the grey ones are of the xylene analyte and the others can be attributed to cyclohexane. The detection limit for this system lies around 0.5% xylene in cyclohexane. At this concentration a comparison between final sensor, naked plasmonic substrate and non plasmonic substrate is performed. The spectra of Figure 6.11 (right) evidence and enhancement of the SERS signal due to the sensor design: the naked Au NSs substrate shows a good enhancement of the xylene Raman signal, but a further enhancement is obtained through the coupling of plasmonic substrate and sol gel film.

The discussion above demonstrates that the sensor system, developed within the present work, shows interesting properties, in terms of easy and cheap realization and enhanced efficiency. The two separate components, Au NSs substrate and diph film, are easy to prepare and to assemble and their single properties work together to realize a complex system with enhanced SERS activity. The Au NSs substrate provides the enhanced local field to be exploited in SERS, while the diph film captures the analyte near the plasmonic surface.

Strong limitations are due to the weak interaction between the diphenyl bridging group and the analyte causing fast desorption, probably due to local heating of the sensor.

Future work will aim to realize a cooling system for this detection setup. Moreover, further studies on different and stronger analyte-matrix interactions should be done.

Chapter 7

SERS SUBSTRATES FOR BIOLOGICAL SENSING

7.1 Introduction

The general interest in exploiting plasmonic nanostructures for different applications has dramatically increased over the last few years, particularly in the biological area. In the past, fluorescence spectroscopy was commonly used for biological applications, but this strategy was actualized and gradually replaced by SERS, in particular for sensing applications. Some advantages of SERS over fluorescence are its higher spectral specificity and the possibility of using infrared excitation, which is very important in potential biological applications in living tissues, for example.

Many different biological applications are discussed in literature, ranging from cancer therapy[157,158], cancer imaging [137,138,159], toxicity studies [160] and biomolecular sensing. Particularly in the last application, SERS have gained high importance for biological detection, with an increasing trend of literature works [161,162].

As already explained in Chapter 3, two different approaches for the analyte detection can be used: the labelled detection and the label-free one. For biological molecules sensing the most common approach is the labelled one, where Raman dyes with high Raman cross sections (in the order of 10^{-18}-10^{-14} cm^2) are properly linked to the biological molecule and act as "indicators" for the detection of the molecule of biological interest. This is the common approach to reach the single molecule SERS (SM-SERS) sensitivity. Coupling the high Raman cross section of the probe molecule and good SERS substrates with well localized hot spots, giving EFs of about 10^{10}-10^{12}, SM-SERS can be possible [21,93,163]. In the biological

research area many different analytes are detected in literature, like proteins [71164] anti-bodies [165], DNA-strands [37,69,166], etc.

The path to SM-SERS detection was not free of controversy and problems though, and it is still the subject of active research. SM-SERS has encountered many of the same problems found in SERS in general: fluctuations in the signals, lack of reproducibility, and a lack of understanding of the origin and conditions for SM-SERS (in terms of enhancement factors and physical-chemical variables of the problem), as well as a lack of control over the magnitudes and spatial localization of hot-spots. Moreover the probe is a fixed parameter of the problem and one has to adapt all the experiment to it by choosing the appropriate SERS substrate (and possibly excitation wavelength). The indirect detection way can be misleading when not all the parameters involved with the Raman label are well known.

The idea in our work was therefore to move away from the biological sensing application with Raman label and to find solutions for label free detection of molecules of biological interest, at the cost of loss in sensitivity.

One of the most important and basic questions is therefore if any molecule can be measured with SERS. The answer to this question is most of the time `yes', but not always with the maximum level of amplification or the more convenient experimental procedures. In principle any Raman signal, produced by an analyte, can be amplified by interaction with plasmon resonances on a metallic substrate and, therefore, produce SERS. The limiting factor becomes how a molecule can be attached or brought close to the plasmonic surface and if the SERS signal of interest will be sufficiently strong to be observed and distinguished from any other unavoidable signal and noise. For the first part, chemical manipulation is usually necessary; the second part is easier with strong Raman dyes and can be more challenging with more commonly weaker molecules. In the last case a proper optimization of the various parameters should be evaluated, like the enhancement, the surface area, the number of adsorbed molecules and the optical set-up (excitation wavelength, scattering volume and incident power). A common problem in biological applications is the presence of spurious background signals: the choice of strong and narrow SERS bands can help in distinguish them from undesired ones.

Besides the principal application described in this chapter, toxicity studies and Fluorescence Correlation Spectroscopy (FCS) measurements were performed on Au NPs, in order to test their possible application as fluorescent labels in in vivo tests. Some works on Au NPs have already evidenced that Au NPs are fluorescent under two-photon excitation[167]. Although this emission is very weak, it is detectable by Two-Photon Fluorescence Correlation Spectroscopy (FCS) experiments [168]. The Au NPs can be therefore used as fluorescent tracers, without any need of surface labelling.

Particularly in the biological context it is very important to study the Au NPs toxicity. The toxicity of Au NPs in endothelial cells (HUVEC), in static and flow conditions, was measured within a collaboration with Dr. Giovanna Albertin of Anatomy Department of Padova University. The flow conditions, realized through microfluidic devices should emulate the physiological characteristics of the circulatory system. Au NPs uptake and toxicity are estimated through TEM and standard bio-analytical tests. The study shows that administration of equal concentrations of Au NPs solutions under flow condition results in lower cytotoxicity with respect to static one, which is also reinforced by ICP-AES data demonstrating a lower total amount of Au deposited in the cells under flow compared to static exposure [169].

7.2 Realization of a novel label-receptor system based on the interaction between 4-hydroxyazobenzene-2 carboxylic acid and its specific antibody

In life science the interaction processes involving two or more biological molecules could be very important for the detection, localization, quantification, and isolation of specific molecules interacting with others. The avidin-biotin (protein-vitamin) system is a well known and studied label-receptor interaction system[170]. It is commonly used in bioanalytical applications, for example, as a model of protein-protein interactions, but also as interacting system exploited for other analytical applications. In some literature works, for example, the avidin-biotin system is used as binding tool for the detection of biomolecules bound to either biotin or avidin[171]. The 4-hydroxyazobenzene-2 carboxylic acid, commonly known with his acronym HABA, is a small interesting molecule that can be used as alternative to biotin in the biotin avidin system. It provides an interesting spectroscopic opportunity and can be easily modified in order to introduce functional groups for the attachment of molecules of biological interest. In 2000 this molecule was proposed as extension of the avidin-biotin system [172] in

order to introduce a chromophore in the interaction system, which helps in following the interaction and modification reaction and in the quantification of the molecular labels.

The native HABA dye has an absorption band at 356 nm. As consequence of the binding process to the biotin-binding sites of avidin with an affinity constant in liquid of $K_d=10^{-6}$ M (relatively high compared to the affinity constant between biotin and avidin $K_d=10^{-15}$ M), the molecule undergoes a tautomeric structural change, as shown in Figure 7.1.

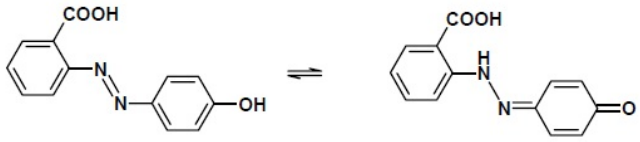

Figure 7.1: Tautomeric change of HABA dye after interaction with avidin.

This molecular change causes a red shift of the absorption band from 356 to 504 nm, which can be exploited for quantitative analysis of the molecular interaction. In fact, the modification process, probed by UV-Vis absorption spectroscopy, has been used for the quantification of avidin [173]. HABA is also commonly used for the determination of the degree of biotinylation of molecules by its displacement by the biotin moiety: the resulting back shift of the absorption maximum, from 504 to 356 nm, represents, on a molar basis, the amount of biotin that has interacted with avidin [174].

The tautomeric change is also present when HABA interacts with his specific antibody, with a more interesting affinity constant of $K_d=10^{-9}$ M.

The tautomeric structural change have already been well studied through UV-Vis and Raman spectroscopy [175–179] and also through theoretical simulations [180].

The aim of the present study is to develop a proof of concept for the realization of a label-receptor system, based on HABA and its specific antibody, using Surface Enhanced Raman Spectroscopy, instead of other indirect, much more expensive, slower and less specific analytical methods.

The idea, developed in collaboration with Dr. Morpurgo of the Department of Pharmaceutical Science of the Padova University, is to detect the structural change of the HABA dye, after interaction with its specific antibody, through SERS. The relative high Raman cross sections

of the benzene ring breathing modes and the N=N and C-N functional groups of HABA, make this system suitable for SERS investigations [177].

For SERS measurements, a thiol HABA derivative has to be synthesized in order to bind the molecule to the plasmonic nanostructured surface. The specific IgG antibody was extracted in vivo from two little rabbits, in which a proper HABA derivative was injected.

The HABA derivatives used for the experiments were properly synthesized and characterized by UV-Vis absorption and Raman spectroscopy and mass spectrometry.

7.2.1 Synthesis of HABA derivatives

Three HABA derivatives were synthesized in the present work, a HABA dye modified with a carboxyl group (named HABA-COOH), an intermediate compound with a terminal amino group (named HABA-NH_2) and a thiol derivative (named HABA-SH). The synthetic procedures are depicted in Figures 7.2 and 7.3. All the reagents are purchased from Fluka or Sigma Aldrich and used without further purification.

Synthesis of HABA-COOH (compound **IV**):

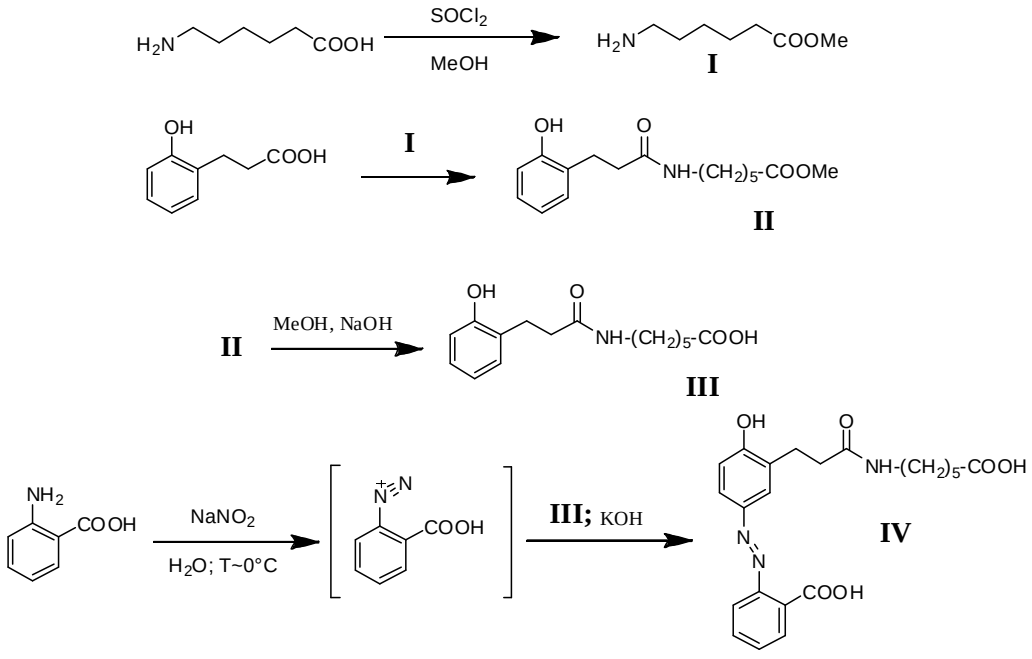

Figure 7.2: Synthesis scheme of HABA-COOH derivative.

Compound **I** is prepared by dissolving 12 g of aminocaproic acid in 50 ml of methanol. The solution is cooled in ice bucket and 20 ml of thionyl chloride are added slowly to the solution. The reaction is left overnight at room temperature. The product crystallizes after partial

methanol evaporation. The reaction is followed through thin layer chromatography (TLC). 4 mmol of 3-(2-hydoxyphenil-proprionic acid) are dissolved in 20 ml of dichloromethane and 4.2 mmol of N,N'-Dicyclohexylcarbodiimide (DCCI) are added under magnetic stirring. After approximately 30 min, 1 eq of compound **I** is added to the solution. The reaction is followed through TLC and stopped after approximately 1h stirring. The organic solution is separated by gooch filtration from the white precipitate (O-Acylisourea) and washed two times with H_2O, HCl 0.05 M, $NaHCO_3$ 1M and H_2O. After anidrification with $NaSO_4$, compound **II** is obtained by evaporation.

Compound **III** is obtained adding specific amounts of methanol and NaOH to compound **II.** The step is followed by TLC.

Compound **IV** is then obtained in the following steps: 1 mmol of sodium nitrite are dissolved in 2.5 ml of water; 1 mmol of antranilic acid are then added to the solution under magnetic stirring. The mixture is cooled into ice bucket and then few µl of concentrate HCl are added. After 5 min this solution is added dropwise to a 8 ml 0.5 M KOH cooled solution of compound **III** (2 mmol). The solution turns immediately from bright yellow to dark orange. The pH is adjusted to 8 with 0.5 M KOH and after 15 min reduced to pH 3-4 with 0.45 M citric acid. The product precipitates. The suspension is allowed to stand at RT for 1 h and then extracted with ethyl acetate. After anidrification with $NaSO_4$, compound **IV** is obtained by evaporation.

Synthesis of HABA-NH_2 (compound **III**) and HABA-SH_2 (compound **IV**):

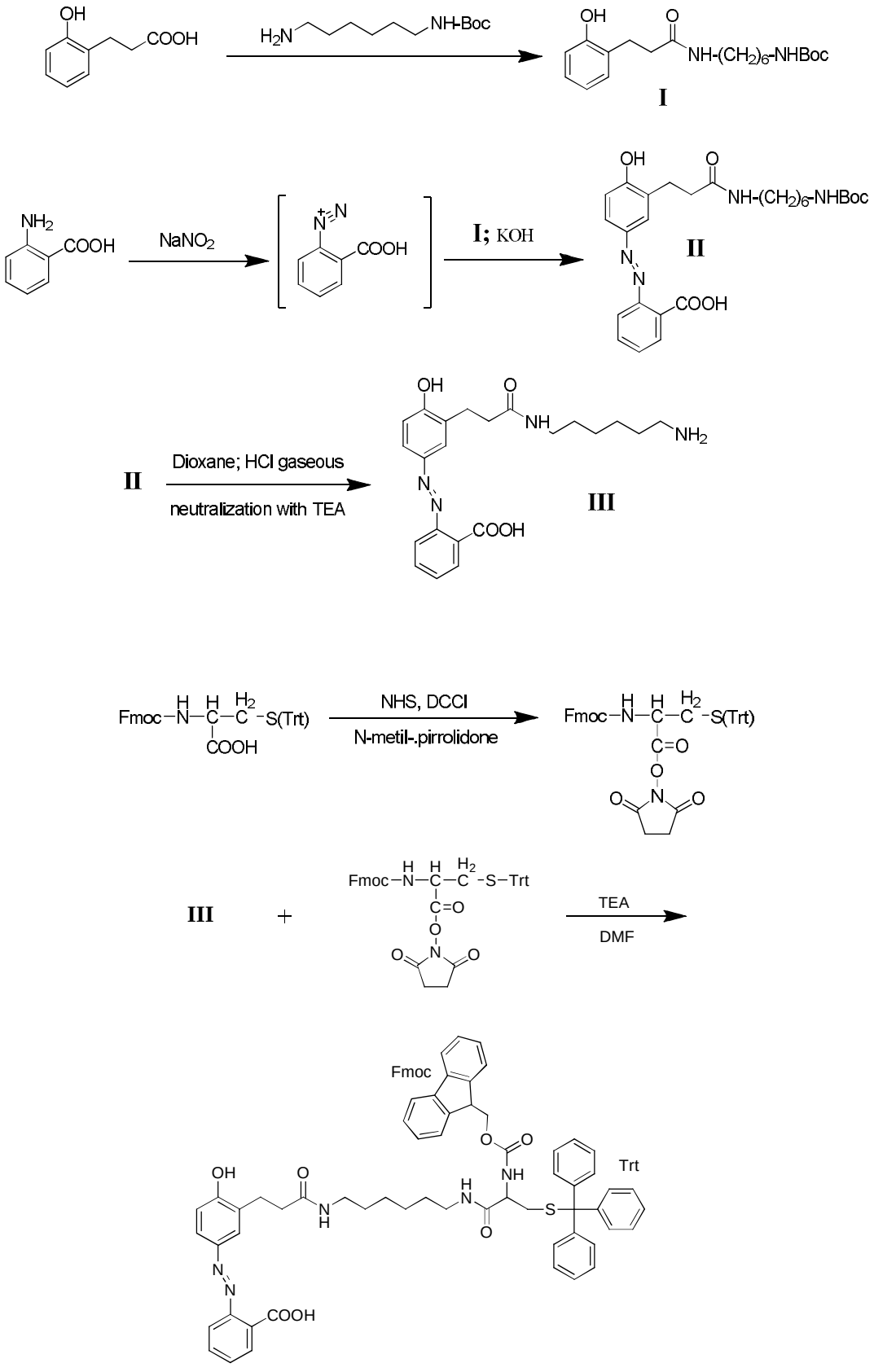

Figure 7.3: Synthesis scheme of HABA-SH derivative.

Compound **I** is prepared by dissolving 4 mmol of 3-(2-hydoxyphenil-proprionic acid) in 20 ml of dichloromethane. 4.2 mmol of N,N'-Dicyclohexylcarbodiimide (DCCI) are added to this solution under magnetic stirring. After approximately 30 min, 4 mmol of N-Boc-1,6-exanediamine are added to the solution. The reaction is followed through a thin layer chromatography (TLC) and stopped after approximately 1h stirring. The organic solution is separated by gooch filtration from the white precipitate (O-Acylisourea) and washed two times with H_2O, HCl 0.05 M, $NaHCO_3$ 1 M and H_2O. After anidrification with $NaSO_4$, compound **I** is obtained by evaporation.

Compound **II** is then obtained in the same way as compound **IV** in the last step of the previous synthesis. Compound **III** is obtained by dissolving product **II** in few ml dioxane and by bubbling gaseous HCl into the solution in anhydrous conditions. This step allows removing the protecting group (Boc). The hydrolysis is followed by TLC. The product precipitates. The supernatant is removed and compound **III** is dissolved in few ml of methanol. The pH is adjusted to 7 with trietylammine and the product is isolated by filtration after diethyl-ether precipitation. The product is a fine dark orange powder.

For the addition of the thiol group to compound **III**, L-cysteine has to be activated. 0.2 mmol of Fmoc-Cys-trt are dissolved in 1.5 ml of N-metyl-1-Pyrrolidone and 1 eq. of N-Hydroxisuccinimide (NHS) and DCCI are added to the solution. The reaction is followed by TLC and stopped after approximately 1h stirring. The undesired white precipitate (O-Acylisourea) is separated by gooch filtration. The final step is performed by dissolving 50 mg of HABA in 1.5 ml of dimetylformamide (DMF) and by adding 0.5 eq. of Fmoc-Cys-trt. The pH has to be adjusted to 7-8 with trietylamine. The reaction is followed by TLC and by controlling the pH. The product precipitates after dropwise adding of a 0.05 M HCl solution. The supernatant is separated from the red precipitate, which is then dissolved in ethyl acetate. The product is finally isolated by gooch filtration after petroleum ether precipitation.

Both the intermediate and the final compounds are characterized through mass and Raman spectroscopy.

Raman characterization is performed on native HABA (purchased from Pierce Thermo Scientific) and on the synthesized HABA-NH_2 intermediate. The final HABA-SH compound was not tested with Raman spectroscopy, because of small amount of product available.

Measurements are performed with 514.5 nm excitation laser on the native HABA (resonant Raman) and 785 nm excitation wavelength on the synthesized derivative. For the last, no spectrum could be collected at 514.5 nm excitation wavelength, because of a strong fluorescence background, probably given by synthesis impurities.

The Raman spectrum of the native HABA powder is collected with 514.5 nm laser wavelength, laser power of about 0.8 mW, 20 x objective and 1 s accumulation time. For the acquisition of the HABA-NH_2 powder Raman spectrum, instead, an excitation of 785 nm with laser power of 80 mW, 50x objective and 10 s accumulation time, is used. The chemical structure of the two molecules and their Raman spectra are reported in Figures 7.4 and 7.5, respectively. The signal assignments are listed in Table 7.1.

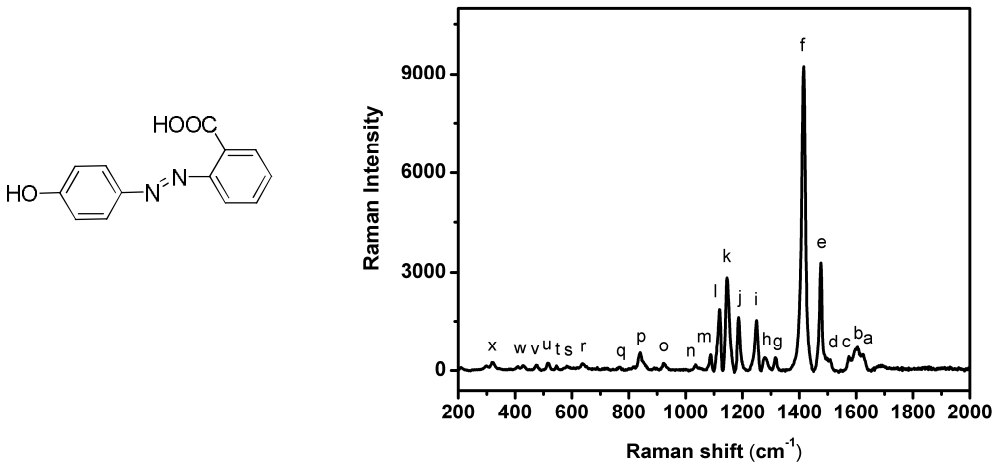

Figure 7.4: Molecular structure (left) and Raman spectrum (right) of HABA.

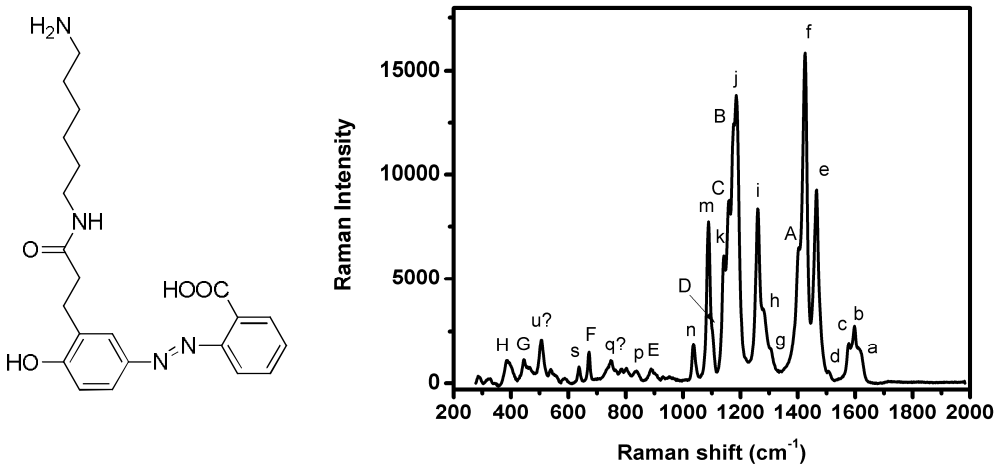

Figure 7.5: Molecular structure (left) and Raman spectrum (right) of HABA-NH_2.

Table 7.1: Raman band position and assignment of HABA and HABA-NH_2.

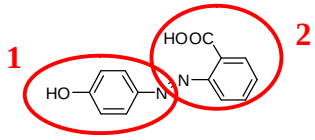

Band	**HABA** Raman shift (cm^{-1})	**HABA-NH_2** Raman shift (cm^{-1})	**Assignment** [135,176,177]
a	1625	1618	$S_{8a,8b}$
b	1603	1597	$S_{8a,8b}$
c	1575	1577	$S_{8a,8b}$
d	1506	1506	S_{19a}, $\delta_{ip}(CH)_2$, $\nu_s(CO)$
e	1476	1465	S_{19a}, $\delta_{ip}(CH)_1$; $\delta_{ip}(C_{11}H_{20})_1$
f	1416	1426	$\nu_s(N=N)$, S_{19b}
g	1315	1307	$\nu\ (CO)_2$, ν (C-COOH), $\delta(COH)_2$, $\delta(OCO)$
h	1279	1279	$\delta_{ip}(CH)_1$
i	1250	1260	$\nu(CN)_{1,2}$, $\delta_{ip}(CH)_2$
j	1186	1185	$\nu(CN)_{1,2}$, $\delta_{ip}(CH)_2$
k	1146	1142	$\delta(CN)_{1,2}$, $\delta(COH)_1$
l	1120	--	S_{19b}, $\delta_{ip}(C_{11}H_{20})_1$
m	1088	1088	S_{19a}, S_{12}, $\nu_{ip}(CH)_2$
n	1035	1035	S_{19b}, $\nu(CO)_2$, $\delta_{ip}(CH)_2$
o	923	--	$S_{1,12}$, $\delta(CNN)$
p	840	840	$S_{1,12}$, $\delta_{op}(CH)_1$
q	768	750	S_4, $\delta_{op}(CH)_2$
r	638	637	$S_{6a,6b}$, $\delta_{ip}(CH)_1$
t	545	--	$\delta_{op}(CH)_2$, $\rho(OCO)$
v	474	--	S_{16b}, $\rho(OCO)$
w	428	--	S_{16b}
A	--	1402	(C-H) sym def.
B	--	1177	$\tau\ (CH_2)$
C	--	1160	$\tau\ (NH_2)$
D	--	1102	ν (CN) (primary amine)
E	--	890	N-H def.
F	--	672	out of plane N-H def.
G	--	445	C-N def.
H	--	388	δ (NCO)

$S_{ij=}$ ring vibration modes; $\delta_{ip=}$ in plane bending; δ_{op}= out of plane bending; ν_s= symmetrical stretching.

The Raman band positions are in good agreement with literature data and a comparison between the two molecules could be easily done. Some bands (s,u), although could not be assigned. This characterization demonstrates that the synthetic procedures occurred successfully.

7.2.2 UV-Vis and Raman characterization of HABA-Avidin and HABA-IgG anti HABA

Before working on the functionalized HABA system and its specific antibody, basic UV-Vis and Raman characterization was performed, to observe the HABA interaction with avidin. In Figure 7.6 the UV-Vis spectra of HABA before and after interaction with avidin, are reported. The interaction event is studied for a 1.65 x 10^{-6} M HABA solution in the presence of an excess of avidin.

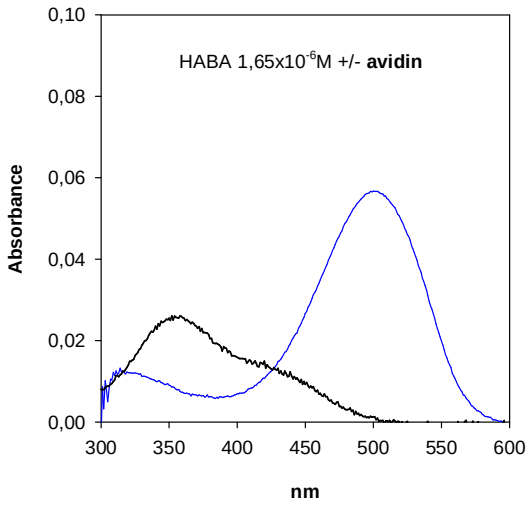

Figure 7.6: UV-Vis spectra of HABA before (black line) and after (blue line) interaction with avidin.

As can be observed, the predicted red shift of the absorption band from 350 nm to 500 nm is well visible and demonstrates the interaction event between HABA and avidin.

The interaction system was also characterized in solution through Raman spectroscopy, with 514.5 nm excitation wavelength, 80 mW laser power, 20 x objective and 10 s accumulation time. The spectra are shown in Figure 7.7. The HABA and avidin concentration in solution was 2.4 and 1.25 mg/ml, respectively. The Raman band assignments are listed in Table 7.2.

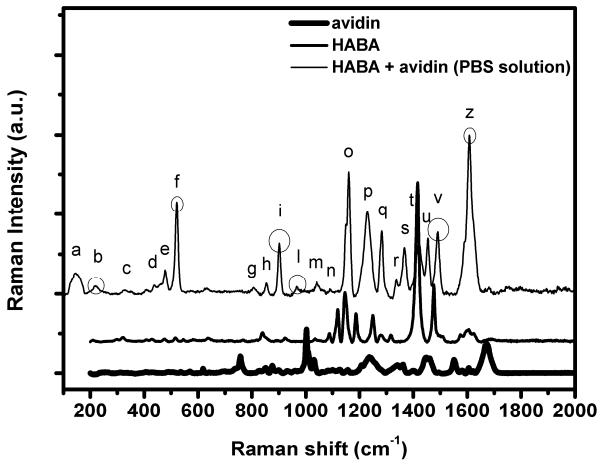

Figure 7.7: Raman spectra of HABA, avidin and HABA-Avidin solution.

Table 7.2: Raman band position and assignment of avidin and HABA-avidin complex.

Avidin (cm^{-1})	**Assignment** 135,177,181	**band**	**HABA-Avidin (cm^{-1})**	**Assignment** 135,177,181
536	ν_s S-S	a	143	vial glass
570	Trp	b	220	HABA-avidin complex
619	Phe	c	324	HABA
757	Trp	d	437	vial glass
830	Tyr	e	478	HABA S_{16b}, ρ(OCO)
852		f	522	HABA-avidin complex
877	Trp	g	805	vial glass
900	ρ CH2	h	854	avidin (Tyr)
933	ν_s C-C, Trp	i	902	HABA-avidin complex
961	Trp	l	967	HABA-avidin complex
1003	Phe, Trp	m	1041	vial glass
1032	Phe	n	1090	HABA S_{19a}, S_{12}, $\nu_{ip}(CH)_2$
1127	ν_s C-N	o	1130/1160	HABA ν_s $(CN)_{1,2}$, δ $(CN)_{1,2}$
1157		p	1229	avidin (amide III)
1236	Amide III	q	1282	HABA $\delta_{ip}(CH)_1$ ν_{as} $(CN)_{1,2}$
1340	Trp	r	1337	avidin (Trp)
1361		s	1367	HABA-avidin complex
1400	ν_s C-O-O	t	1419	HABA ν_s(N=N), S_{19b}
1447	δ CH2, δ CH3	u	1454	avidin (δ CH_2, δ CH_3)
1552	Trp	v	1490	HABA-avidin complex
1581		z	1608	ν_s C=O, S C=C; ν_s C=N (hydrazon HABA-Avidin)
1605	Trp, Phe			
1621				
1672	Amide I			

$S_{ij=}$ ring vibration modes; $\delta_{ip=}$ in plane bending; δ_{op}= out of plane bending; ν_s= symmetrical stretching; ρ_s= symmetrical rocking;

A modification of the Raman spectrum of HABA after interaction with avidin is visible in Figure 7.7. The most important signals for interaction observation are evidenced in grey in Table 7.2. The signals associated to HABA (1130/1160, 1280 and 1419 cm^{-1}) should decrease in intensity, while the 1608 cm^{-1} signal should strongly increase after HABA interaction, as shown in the Raman spectrum of the interaction solution in Figure 7.7.

In case of the more complex HABA-avidin system, UV-VIS characterization is performed, before first SERS tests. The UV-Vis spectra of HABA-COOH interacting with the two IgG anti-HABA molecules produced by two different rabbits, are shown in Figure 7.8.

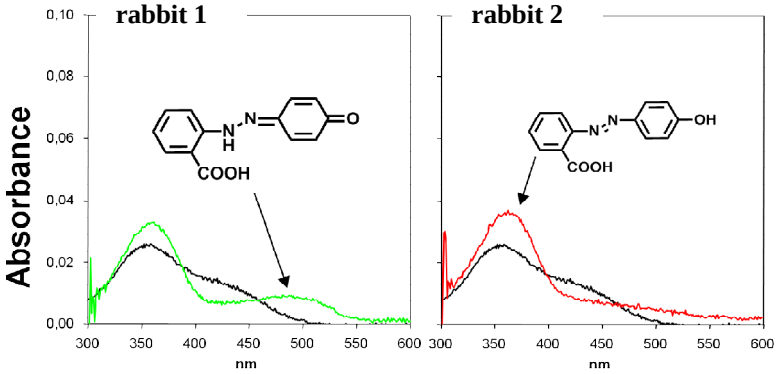

Figure 7.8: UV-Vis spectra of HABA-COOH before (black line) and after the interaction with IgG antibody developed by rabbit 1 (green line) and rabbit 2 (red line).

As depicted inside the spectra of Figure 7.8, the antibodies developed by the two rabbits cause not a complete tautomeric change of the HABA molecules. The antibody solution of rabbit 1 contains two different HABA antibodies, one specific for the azo and the other for the hydrazon form: the left spectra show the co presence of both the absorption bands at 350 nm and 500 nm. For the interaction event with the rabbit 2 antibody solution, only the azo form with the absorption band at 350 nm is visible. This antibody solution can therefore not be used for the label-receptor interaction system. The use of antibodies, produced in vivo, demonstrates that new natural systems are much more complex than expected. The behavior of the two antibody solutions makes difficult to identify the structure change due to the HABA-antibody interaction through SERS. This is also confirmed by the first SERS tests done with the antibody solution developed by rabbit 1 and described in the following paragraph.

7.2.3 SERS measurements of HABA- IgG anti HABA system

The first run of SERS measurements was done by simply functionalizing SERS solid substrates with the thiol HABA derivate described in paragraph 7.2.1, in order to test the stability of the substrate and the feasibility of the SERS experiments.

Before SERS measurements, the stability of the SERS substrates in presence of methanol and tfa traces, which are present in the functionalization HABA solution, is tested through UV-Vis absorption spectroscopy. An example of a stability test, performed on Au NSs substrate, is shown in Figure 7.9. In the spectra superposition also the two principal excitation wavelengths used, are depicted. The same tests are performed also on Au NPs substrates.

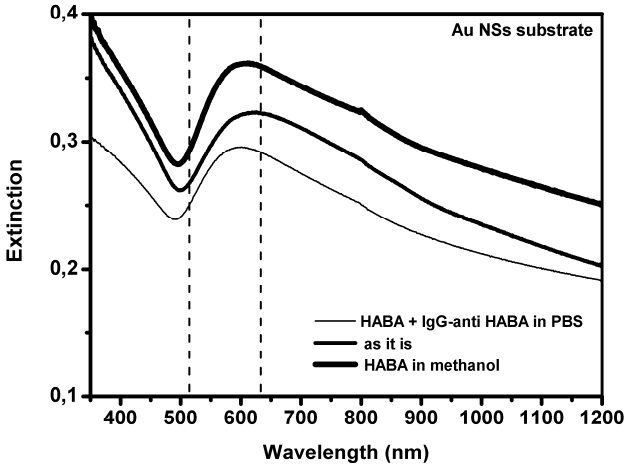

Figure 7.9: UV-Vis spectra of Au NSs substrate after HABA functionalization in methanol and after antibody incubation in PBS solution. The vertical dashed lines indicate the two excitation wavelengths used for SERS measurements.

As demonstrated in Figure 7.9, the Au NSs substrate is stable and the plasmonic band doesn't change.

The functionalization procedure is performed in a few steps. The trt thiol-protecting group of the HABA-SH molecule is removed by adding concentrated trifluoroacetic acid (tfa) to a high concentrated, protected HABA-SH solution. The reaction is left for 30 min at room temperature. The solution is then subjected to a centrifugation step, where the remaining trt molecules precipitate as white powder and can be easily separated from the unprotected HABA-SH molecule. The SERS substrates are then incubated for 24 h in a 1 mM methanol solution of HABA-SH, finally rinsed with pure methanol and dried under nitrogen flow.

As described in Chapter 5, Au NPs and Au NSs substrates have a low enhancement efficiency at 514.5 nm, but the first test where although performed at this laser excitation wavelength, in order to prove the feasibility of resonant SERS measurements with the HABA dye. Unfortunately no signal was detected probably because of high fluorescence and impurities present in the HABA sample, similar to the observations made during Raman characterization on the HABA-NH_2 powder.

Some tests at 633 nm excitation wavelength give, instead, good results. The best data are obtained using the 633 nm, 0.2 mW power on the solid sample, 50 x objective and 20 s accumulation time. The SERS spectrum of HABA on the Au NSs substrate (UV-Vis spectrum in Figure 7.8) compared to the Raman spectrum of the HABA-NH_2 powder, is shown in Figure 7.9.

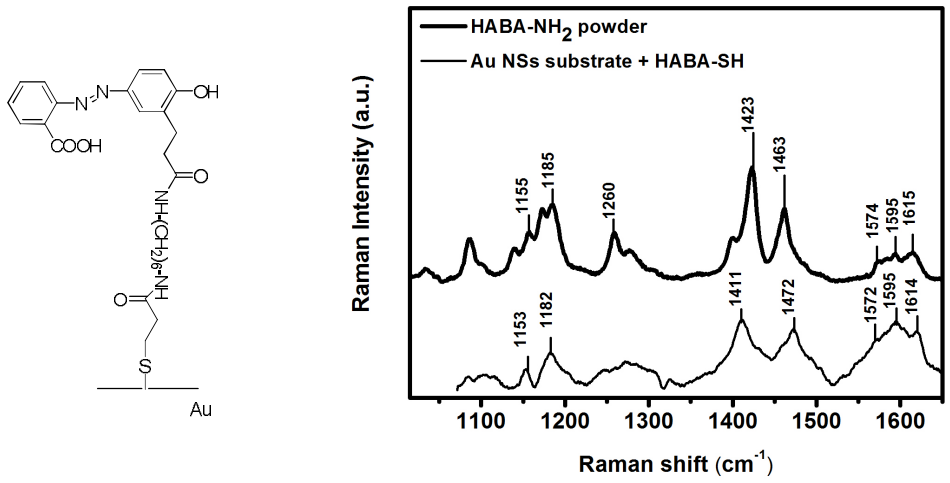

Figure 7.9: Raman spectra of HABA-NH_2 powder and SERS spectra of HABA-SH on Au NSs substrate; molecular structure of the HABA-S-Au system (left).

As observed in the spectra of Figure 7.9, the HABA molecule is well visible, even when only a monolayer over Au NSs substrate is present. The SERS spectra demonstrate that the functionalization step has been performed successfully and that the SERS substrate works well. The principal signals of the HABA molecule are well visible.

The HABA signals are also visible on Au NPs substrates, as shown in Figure 7.10, where signals of three different zones on the substrate are reported, in order to demonstrate the homogeneity of the SERS signal.

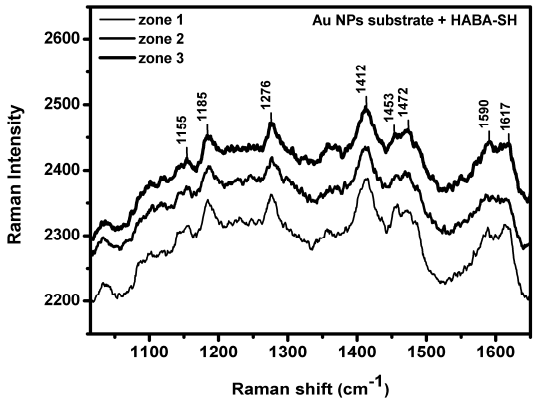

Figure 7.10: SERS spectra of HABA-SH on three different zones of the Au NPs substrate.

The high homogeneity of the Au NPs substrate and the HABA-SH monolayer on the plasmonic substrate, is demonstrated.

The next step of incubation in IgG antibody solution is performed by immersion of the SERS substrates in a 4µg/ml solution of antibody, for 24 h. All the tests are performed using the antibody solution developed by rabbit 1. In some tests the incubation was performed using specific multiplates (purchased from Grace Bio-Labs), which gives the possibility to perform the test only on a limited substrates area (5x5 mm), in order to use reduced antibody solution volumes.

Unfortunately, SERS spectra of the interacting system didn't show great spectral differences in comparison with HABA alone. SERS spectra measured on Au substrates are shown in Figure 7.11.

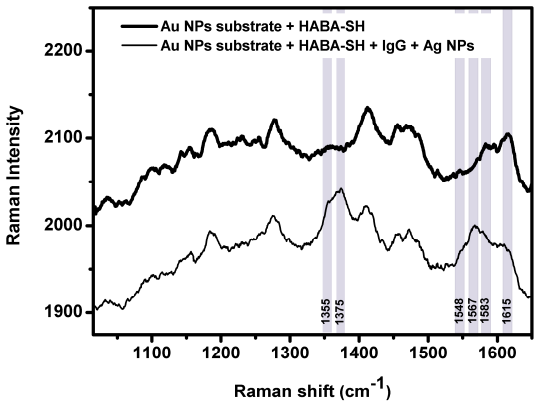

Figure 7.11: SERS spectra of HABA-IgG antibody system on Au NPs (left) and Ag NPs (right) substrates.

A little change in the 1600 cm^{-1} region is observed for the interaction system on the Au NPs substrate, and two new bands, at about 1355 and 1375 cm^{-1}, are visible on both metal nanostructure substrates. The bands are probably due to the presence of the antibody on the surface, as demonstrated in Figure 7.12, while there is no evidence of the tautomeric HABA change. In Figure 7.12 SERS spectra of only the IgG anti-HABA antibody on different substrate zones, are reported.

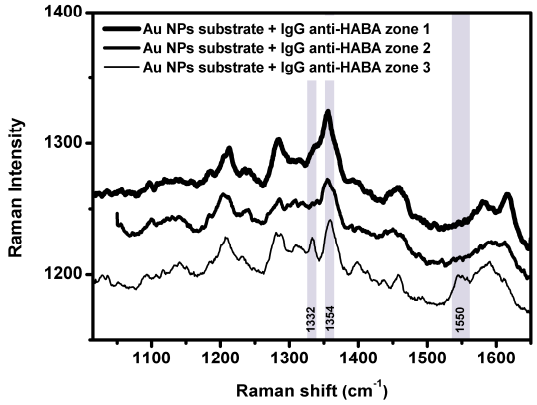

Figure 7.12: SERS spectra of IgG anti HABA on three different zones of Au NPs substrate.

The 1355, 1375 and 1550 cm^{-1} signals evidenced in grey in Figure 7.12, are demonstrated to be characteristic of the IgG anti-HABA antibody. The SERS test performed only on the antibody molecule adsorbed onto an Au NPs substrate evidences the above discussed signals at slightly lower Raman shifts. This slight shift compared to the band positions in Figure 7.11 could be due to the adsorption process onto the metal substrate.

Many other strategies have been tested, like different SERS substrates and different detection conformations. The inverted configuration was tested on a SERS substrate and also onto a glass slide. The IgG antibody molecule is adsorbed onto the substrates, which are immerged, in a second step, in the HABA solution. In both cases the staining in a Ag NPs solution is performed, in order to increase the signal to noise ration. Also Ag NPs substrates are tested, which show high enhancement factor values, but very low stability in biological environments. Unfortunately no one of these different approaches gave better results than that reported above.

With the antibody solutions, produced by the two rabbits, it is very difficult to observe a conformational change of the HABA molecule. Tests performed with the rabbit 1 antibody

solution, which contains two different antibody species, demonstrate the non-feasibility of the interaction detection.

A new strategy should be considered, for example the investigation of the intensity ratio between the doublet in the 1450 cm^{-1} region, attributable to the azo form (N=N stretch, C-H bend), with respect to the band around 1600 cm^{-1}, attributable in major part to the hydrazo form (C=O stretch, C=N stretch). Alternatively a new strategy of obtaining a monoclonal antibody should be evaluated. Both the approaches are work in progress.

Chapter 8

CONCLUSIONS

In the present work, different plasmonic nanostructures were synthesized, widely characterized and finally used for Surface Enhanced Raman Spectroscopy detection of chemical and biological molecules.

As already described in literature, it was demonstrated that different metals and nanostructure morphologies give rise to plasmonic extinction bands covering a large spectral region, from he Visible to the near IR. Ag NPs of about 45 nm diameter, present an extinction band peaked at 400 nm, while Au NPs of about 15-20 nm have its plasmonic band maximum at about 520 nm. Both Ag and Au nanosphere colloids have been synthesized in aqueous solution through Turkevich method. More complex systems, with silica core and gold outer shell, give the possibility to tune the plasmonic band from about 600 up to 1000 nm, by simply varying the core to shell dimension ratio. Three different silica cores have been synthesized within this work, with diameters of 75, 92 and 162 nm. The synthesis conditions give the possibility to vary the gold shell thickness from about 5 to 30 nm. Depending on the shell thickness, homogeneity, core coverage degree and roughness, the plasmonic band is modified in a different way. The realization of uniform and smooth nanoshells is a challenging issue: extinction spectra and TEM images show in fact that many of the Au NSs synthesized were not perfectly smooth and complete. All these nanostructures have been widely characterized, morphologically, through TEM and AFM, and optically through UV-Vis spectroscopy and Surface Enhanced Raman Spectroscopy. The Raman signal enhancement efficiency was probed, through SERS measurements, for all the structures in solution at four different excitation wavelengths (488, 514, 633, 785 nm). Thiobenzoic acid was used as Raman label.

It has been demonstrated that increasing the Raman label concentration in solution, NPs aggregation is favored with strongly increase of the enhancement factor, due to the presence of hot spots. Moreover the EF is rising from the Vis to the near IR, demonstrating the rising efficiency of hot spots in the IR region. For all Raman label concentrations and excitation wavelengths, Ag NPs demonstrate to be the most efficient plasmonic nanostructures, with EF ranging from about 10^4 in the Vis region to 10^6 in the near IR. Unfortunately Ag NPs are very less stable and coalesce in solution within a few minutes, making them suitable for microfluidic SERS devices with fast acquisition times but not for applications where longer NPs stability is required. Au NSs, although not uniformly covered, show very interesting EF values of about 10^4-10^6 in the IR region and high stability in a wide Raman label concentration range.

In order to further characterize the extinction properties of the Au NSs structures, separating the absorption and the scattering contribution to the total extinction, Photoacoustic Spectroscopy and wavelength scanned EF measurements were performed in solution. This characterization performed on Au NSs was done for the first time within the present work: no previous works are found in literature. The photoacoustic profiles, obtained for four Au NSs samples with different core (R1) and final radii (R2), show that the absorption percentage over total extinction is decreasing with increasing R2 and increasing with increasing R1/R2 ratio. These results are in agreement with theoretical predictions found in literature.

SERS EF measurements profiles were performed on the same nanoshell samples, finding very similar EF profiles with EF values increasing from about 10^3 to 10^5 in going from the Vis to the IR. Moreover, the profiles are strongly red shifted with respect to the extinction one, indicating that the systems are dominated by hot spots. Further studies should be done in order to verify if the hot spots are originating from interparticle or intraparticle interactions. In the intraparticle one, the presence of an uncompleted gold shell can give rise to hot spots on the single silica cores.

Comparing photoacoustic measurements, as probe of far field properties, and SERS measurements, describing local near field characteristics, a direct relation could hardly be found. The decreasing of the absorption contribution and increasing EF trend, from the Vis to the near IR, could indicate the importance of scattering in the local field enhancement mechanisms. The issue of comparing the extinction properties with the SERS enhancement profile remains an already opened question.

For the realization of practical sensing devices, it is necessary to realize easy and cheep small solid SERS substrates. Au NPs and Au NSs have been therefore characterized on solid substrates, easily prepared by random deposition of the nanostructures onto glass slides, prefunctionalized with APTMS. The optimization of the preparation led to stable, homogeneous and high performing SERS substrates, presenting wavelength scanned EF profiles very similar to the ones found in solution: the EF values range from 10^3 to 10^4 from the Vis to near IR for Au NPs and small Au NSs substrates. For bigger nanoshells, the EF is further rising to 10^5. The EF profiles indicate the presence of hot spots on the substrates, which are also observed through AFM and SEM characterization.

The plasmonic substrates have been exploited for two different applications: the realization of a VOC sensor, and the realization of a biological label-receptor system. The high specific and sensitive SERS technique is then used for the detection of the molecular species.

For the first application, the idea was to detect low concentrations of toxic xylene in vapor or liquid phase in a high affinity hybrid organic-inorganic sol gel matrix, enhancing the specific Raman detection sensitivity through the exploitation of Au NPs and Au NSs substrates. The xylene molecules, penetrating into the porous and functional sol-gel film, interact with the phenyl bridging groups of the organic unit through π-π interaction, and should be detected through SERS. The sol gel matrix was deposited over the SERS substrates through spin coating and the system was fully characterized and finally subjected to vapor or liquid xylene flows. The system was put in a closed home made setup and analyzed with the Raman microscope. Unfortunately the xylene presence was only observed at high concentrations in liquid phase, probably because of the fast xylene desorption from the sol gel matrix due to the strong local heating caused by the laser irradiation. Although, the enhanced SERS efficiency due to the detection design was demonstrated. Further investigations, to improve the detection systems, are work in progress.

The second application consisted in the realization of an innovative biological label-receptor system, which can be exploited for bio-analytical applications, as alternative to the well known biotin-avidin system. The 4-hydroxyazobenzene-2 carboxylic acid (HABA) molecule is very interesting for its easy functionalizability with molecules of biological interest and its absorption band at 356 nm. Due to the interaction with its specific antibody, the HABA molecule undergoes a tautomeric structural change, which causes an absorption band shift from 356 to 506 nm. This structural change could be exploited for the detection of the

interaction event, through SERS, due to the interesting Raman cross sections involved in the molecular modifications. Thiol HABA derivatives have been successfully synthetized and characterized and used for SERS substrates functionalization. Unfortunately, the HABA antibody solutions, extracted in vivo from two rabbits, did not give observations of any HABA SERS spectra modifications after interaction. The antibodies developed cause not a complete and quantitative tautomeric change of the HABA molecules, making the identification of a structural change very difficult.

REFERENCES

(1) Link, S.; El-Sayed, M. A. Shape and Size Dependence of Radiative, Non-Radiative and Photothermal Properties of Gold Nanocrystals. *Int. Rev. Phys. Chem.* **2000**, *19*, 409–453.

(2) Hartland, G. V.; Schatz, G. Virtual Issue: Plasmon Resonances - A Physical Chemistry Perspective. *J. Phys. Chem. C* **2011**, *115*, 15121–15123.

(3) Kamat, P. V. Meeting the Clean Energy Demand: Nanostructure Architectures for Solar Energy Conversion. *J. Phys. Chem. C* **2007**, *111*, 2834–2860.

(4) Oelhafen, P.; Schüler, a. Nanostructured Materials for Solar Energy Conversion. *Sol. Energy* **2005**, *79*, 110–121.

(5) Hägglund, C.; Kasemo, B. Nanoparticle Plasmonics for 2D-Photovoltaics: Mechanisms, Optimization, and Limits. *Opt. Express* **2009**, *17*, 11944–11957.

(6) Chen, F.-C.; Wu, J.-L.; Lee, C.-L.; Hong, Y.; Kuo, C.-H.; Huang, M. H. Plasmonic-Enhanced Polymer Photovoltaic Devices Incorporating Solution-Processable Metal Nanoparticles. *Appl. Phys. Lett.* **2009**, *95*, 013305.

(7) Tian, Y.; Tatsuma, T. Plasmon-Induced Photoelectrochemistry at Metal Nanoparticles Supported on Nanoporous TiO2. *Chem. Commun.* **2004**, *16*, 1810–1811.

(8) Frare, M. C.; Weber, V.; Signorini, R.; Bozio, R. Gold Nanoparticles in Polycarbonate Matrix for Optical Limiting Against Cw Laser. *J. Laser Phys.* **2014**, submitted.

(9) Qu, S.; Du, C.; Song, Y.; Wang, Y.; Gao, Y. Optical Nonlinearities and Optical Limiting Properties in Gold Nanoparticles Protected by Ligands. *Chem. Phys. Lett.* **2002**, *356*, 403–408.

(10) Ara, M. H. M.; Dehghani, Z.; Sahraei, R.; Daneshfar, A.; Javadi, Z.; Divsar, F. Diffraction Patterns and Nonlinear Optical Properties of Gold Nanoparticles. *J. Quant. Spectrosc. Radiat. Transf.* **2012**, *113*, 366–372.

(11) Homola, J.; Yee, S.; Gauglitz, G. Surface Plasmon Resonance Sensors: Review. *Sensors Actuators B* **1999**, *54*, 3–15.

(12) Hong, S.; Lee, S.; Yi, J. Sensitive and Molecular Size-Selective Detection of Proteins Using a Chip-Based and Heteroliganded Gold Nanoisland by Localized Surface Plasmon Resonance Spectroscopy. *Nanoscale Res. Lett.* **2011**, *6*, 336.

(13) Henry, A.-I.; Bingham, J. M.; Ringe, E.; Marks, L. D.; Schatz, G. C.; Van Duyne, R. P. Correlated Structure and Optical Property Studies of Plasmonic Nanoparticles. *J. Phys. Chem. C* **2011**, *115*, 9291–9305.

(14) Ghosh Chaudhuri, R.; Paria, S. Core/shell Nanoparticles: Classes, Properties, Synthesis Mechanisms, Characterization, and Applications. *Chem. Rev.* **2012**, *112*, 2373–2433.

(15) Wang, H. U. I.; Brandl, D. W. Plasmonic Nanostructures : Artificial Molecules Nanoshell Plasmons : The Sphere - Cavity. *Acc. Chem. Res.* **2007**, *40*, 53–62.

(16) Willets, K. a; Van Duyne, R. P. Localized Surface Plasmon Resonance Spectroscopy and Sensing. *Annu. Rev. Phys. Chem.* **2007**, *58*, 267–297.

(17) Le, F.; Brandl, D. W.; Urzhumov, Y. A.; Wang, H.; Kundu, J.; Halas, N. J.; Aizpurua, J.; Nordlander, P. Metallic Nanoparticle Arrays : A Common Substrate for Both Surface Enhanced Raman Scattering and Surface Enhanced Infrared Absorption. *ACS Nano* **2008**, *2*, 707–718.

(18) Fort, E.; Grésillon, S. Surface Enhanced Fluorescence. *J. Phys. D. Appl. Phys.* **2008**, *41*, 013001.

(19) Campion, A.; Kambhampati, P. Surface-Enhanced Raman Scattering. *Chem. Soc. Rev.* **1998**, *27*, 241–250.

(20) McCreery, R. L. *Raman Spectroscopy for Chemical Analysis*; John Wiley & Sons, 2005; p. 448.

(21) Nie, S. Probing Single Molecules and Single Nanoparticles by Surface-Enhanced Raman Scattering. *Science (80-.).* **1997**, *275*, 1102–1106.

(22) Ko, H.; Singamaneni, S.; Tsukruk, V. V. Nanostructured Surfaces and Assemblies as SERS Media. *Small* **2008**, *4*, 1576–1599.

(23) Freeman, R. G.; Grabar, K. C.; Allison, K. J.; Bright, R. M.; Davis, J. A.; Guthrie, A. P.; Hommer, M. B.; Jackson, M. A.; Smith, P. C.; Walter, D. G.; et al. Self-Assembled Metal Colloid Monolayers: An Approach to SERS Substrates. *Science (80-.).* **1995**, *267*, 1629–1632.

(24) Joseph, V.; Matschulat, A.; Polte, J.; Rolf, S.; Emmerling, F.; Kneipp, J. SERS Enhancement of Gold Nanospheres of Defined Size. *J. Raman Spectrosc.* **2011**, *42*, 1736–1742.

(25) Giallongo, G.; Rizzi, G. A.; Weber, V.; Ennas, G.; Signorini, R.; Granozzi, G. Green Synthesis and Electrophoretic Deposition of Ag Nanoparticles on SiO2/Si(100). *Nanotechnology* **2013**, *24*, 345501.

(26) Green, M.; Liu, F. M. SERS Substrates Fabricated by Island Lithography: The Silver/Pyridine System. *J. Phys. Chem. B* **2003**, *107*, 13015–13021.

(27) Li, M.; Cushing, S. K.; Zhang, J.; Suri, S.; Evans, R.; Petros, W. P.; Gibson, L. F.; Ma, D.; Liu, Y.; Wu, N. Three-Dimensional Hierarchical Plasmonic Nano-Architecture Enhanced Surface-Enhanced Raman Scattering Immunosensor for Cancer Biomarker Detection in Blood Plasma. *ACS Nano* **2013**, *7*, 4967–4976.

(28) Le Ru, E. C.; Blackie, E.; Meyer, M.; Etchegoin, P. G. Surface Enhanced Raman Scattering Enhancement Factors: A Comprehensive Study. *J. Phys. Chem. C* **2007**, *111*, 13794–13803.

(29) Saikin, S. K.; Olivares-Amaya, R.; Rappoport, D.; Stopa, M.; Aspuru-Guzik, A. On the Chemical Bonding Effects in the Raman Response : Benzenethiol Adsorbed on Silver Clusters. *Phys. Chem. Chem. Phys.* **2009**, *11*, 9401–9411.

(30) Zayak, A. T.; Hu, Y. S.; Choo, H.; Bokor, J.; Cabrini, S.; Schuck, P. J.; Neaton, J. B. Chemical Raman Enhancement of Organic Adsorbates on Metal Surfaces. *Phys. Rev. Lett.* **2011**, *083003*, 1–4.

(31) Wu, D.; Liu, X.; Duan, S.; Xu, X.; Ren, B.; Lin, S.-H.; Tian, Z.-Q. Chemical Enhancement Effects in SERS Spectra: A Quantum Chemical Study of Pyridine Interacting with Copper, Silver, Gold and Platinum Metals. *J. Phys. Chem. C* **2008**, *112*, 4195–4204.

(32) Le Ru, E. C.; Galloway, C.; Etchegoin, P. G. On the Connection Between Optical Absorption/extinction and SERS Enhancements. *Phys. Chem. Chem. Phys.* **2006**, *8*, 3083–3087.

(33) McFarland, A. D.; Young, M. a; Dieringer, J. a; Van Duyne, R. P. Wavelength-Scanned Surface-Enhanced Raman Excitation Spectroscopy. *J. Phys. Chem. B* **2005**, *109*, 11279–11285.

(34) Kleinman, S. L.; Sharma, B.; Blaber, M. G.; Henry, A.-I.; Valley, N.; Freeman, R. G.; Natan, M. J.; Schatz, G. C.; Van Duyne, R. P. Structure Enhancement Factor Relationships in Single Gold Nanoantennas by Surface-Enhanced Raman Excitation Spectroscopy. *J. Am. Chem. Soc.* **2013**, *135*, 301–308.

(35) Ueno, Y.; Tate, A.; Niwa, O.; Zhou, H.-S.; Yamada, T.; Honma, I. High Benzene Selectivity of Mesoporous Silicate for BTX Gas Sensing Microfluidic Devices. *Anal. Bioanal. Chem.* **2005**, *382*, 804–809.

(36) Porter, M. D.; Lipert, R. J.; Siperko, L. M.; Wang, G.; Narayanan, R. SERS as a Bioassay Platform: Fundamentals, Design, and Applications. *Chem. Soc. Rev.* **2008**, *37*, 1001–1011.

(37) Barhoumi, A.; Zhang, D.; Tam, F.; Halas, N. J. Surface-Enhanced Raman Spectroscopy of DNA. *J. Am. Chem. Soc.* **2008**, *130*, 5523–5529.

(38) Fang, C.; Agarwal, A.; Buddharaju, K. D.; Khalid, N. M.; Salim, S. M.; Widjaja, E.; Garland, M. V; Balasubramanian, N.; Kwong, D.-L. DNA Detection Using

Nanostructured SERS Substrates with Rhodamine B as Raman Label. *Biosens. Bioelectron.* **2008**, *24*, 216–221.

(39) Wood, R. W. XLII. On a Remarkable Case of Uneven Distribution of Light in a Diffraction Grating Spectrum. *Philos. Mag. Ser. 6* **1902**, *4*, 396–402.

(40) Rayleigh, L. On the Dynamical Theory of Gratings. *Proc. R. Soc. A Math. Phys. Eng. Sci.* **1907**, *79*, 399–416.

(41) Mie, G. Beiträge Zur Optik Trüber Medien Speziell Kolloidaler Metalllösungen. *Ann. Phys.* **1908**, *330*, 377–445.

(42) Pines, D. Collective Energy Losses in Solids. *Rev. Mod. Phys.* **1956**, *28*, 184–198.

(43) Ritchie, R. Plasma Losses by Fast Electrons in Thin Films. *Phys. Rev.* **1957**, *106*, 874–881.

(44) Otto, A. Excitation and Nonradiative Surface Plasma Waves in Silver Bz the Method of Frustrated Total Reflection. *Zeitschrift für Phys.* **1968**, *216*, 398–410.

(45) Kretschmann, E.; Raether, H. Radiative Decay of Non Radiative Surface Plasmons Excited by light(Surface Plasma Waves Excitation by Light and Decay into Photons Applied to Nonradiative Modes). *Zeitschrift Fuer Naturforschung, Tl. A* **1968**, *23*, 2135.

(46) Maier, S. A. *Plasmonics: Fundamentals and Applications*; Springer, 2007.

(47) Le Ru, E.; Etchegoin, P. *Principles of Surface-Enhanced Raman Spectroscopy: And Related Plasmonic Effects*; Elsevier, 2008; Vol. 2008, p. 688.

(48) Schlücker, S. *Surface Enhanced Raman Spectroscopy: Analytical, Biophysical and Life Science Applications*; John Wiley & Sons, 2011; p. 344.

(49) Raether, H. *Surface Plasmons on Smooth and Rough Surfaces and on Gratings*; Springer Berlin Heidelberg, 1988; Vol. 111.

(50) Alvarez, M. M.; Khoury, J. T.; Schaaff, T. G.; Shafigullin, M. N.; Vezmar, I.; Whetten, R. L. Optical Absorption Spectra of Nanocrystal Gold Molecules. *J. Phys. Chem. B* **1997**, *5647*, 3706–3712.

(51) Persson, B. N. J. Polarizability of Small Spherical Metal Particles: Influence of the Matrix Environment. *Surf. Sci.* **1993**, *281*, 153–162.

(52) Oldenburg, S. .; Averitt, R. .; Westcott, S. .; Halas, N. . Nanoengineering of Optical Resonances. *Chem. Phys. Lett.* **1998**, *288*, 243–247.

(53) Kreibig, U.; Vollmer, M. *Optical Properties of Metal Clusters*; Springer Verlag, B., Ed.; Berlin, 1995.

(54) Prodan, E.; Radloff, C.; Halas, N. J.; Nordlander, P. A Hybridization Model for the Plasmon Response of Complex Nanostructures. *Science* **2003**, *302*, 419–422.

(55) Lal, S.; Grady, N. K.; Kundu, J.; Levin, C. S.; Lassiter, J. B.; Halas, N. J. Tailoring Plasmonic Substrates for Surface Enhanced Spectroscopies. *Chem. Soc. Rev.* **2008**, *37*, 898–911.

(56) Miller, M. M.; Lazarides, A. a. Sensitivity of Metal Nanoparticle Surface Plasmon Resonance to the Dielectric Environment. *J. Phys. Chem. B* **2005**, *109*, 21556–21565.

(57) Moskovits, M. Surface-Enhanced Spectroscopy. *Rev. Mod. Phys.* **1985**, *57*, 783–826.

(58) Raman, C. .; Krishnan, K. S. A New Type of Secondary Radiation. *Nature* **1928**, *121*, 501–502.

(59) Kneipp, K. Surface-Enhanced Raman Scattering. *Phys. Today* **2007**, 40–46.

(60) Long, D. A. *The Raman Effect*; John Wiley & Sons, Ltd: Chichester, UK, 2002.

(61) Fleischmann, M.; Hendra, P. J.; McQuillan, A. J. Raman Spectra of Pyridine Adsorbed at a Silver Electrode. *Chem. Phys. Lett.* **1974**, *26*, 163–166.

(62) Jeanmaire, D. L.; Duyne, R. P. Van. Surface Raman Spectroelectrochemistry: Part I. Heterocyclic, Aromatic, and Aliphatic Amines Adsorbed on the Anodized Silver Electrode. *J. Electroanal. Chem. Interfacial Electrochem.* **1977**, *84*, 1–20.

(63) Moskovits, M. Surface Roughness and the Enhanced Intensity of Raman Scattering by Molecules Adsorbed on Metals. *J. Chem. Phys.* **1978**, *69*, 4159–4161.

(64) Stiles, P. L.; Dieringer, J. a; Shah, N. C.; Van Duyne, R. P. Surface-Enhanced Raman Spectroscopy. *Annu. Rev. Anal. Chem. (Palo Alto. Calif).* **2008**, *1*, 601–626.

(65) Otto, A.; Cardona, M. Light Scattering in Solids IV. In *Topics in applied physics*; 1984.

(66) Orendorff, C. J.; Gearheart, L.; Jana, N. R.; Murphy, C. J. Aspect Ratio Dependence on Surface Enhanced Raman Scattering Using Silver and Gold Nanorod Substrates. *Phys. Chem. Chem. Phys.* **2006**, *8*, 165–170.

(67) Sackmann, M.; Bom, S.; Balster, T.; Materny, A. Nanostructured Gold Surfaces as Reproducible Substrates for Surface-Enhanced Raman Spectroscopy. **2007**, *38*, 277–282.

(68) Yi, Z.; Li, X.-Y.; Liu, F.-J.; Jin, P.-Y.; Chu, X.; Yu, R.-Q. Design of Label-Free, Homogeneous Biosensing Platform Based on Plasmonic Coupling and Surface-Enhanced Raman Scattering Using Unmodified Gold Nanoparticles. *Biosens. Bioelectron.* **2013**, *43*, 308–314.

(69) Fabris, L.; Dante, M.; Braun, G.; Lee, S. J.; Reich, N. O.; Moskovits, M.; Nguyen, T.-Q.; Bazan, G. C. A Heterogeneous PNA-Based SERS Method for DNA Detection. *J. Am. Chem. Soc.* **2007**, *129*, 6086–6087.

(70) Diaz Fleming, G.; Finnerty, J. J.; Campos-Vallette, M.; Célis, F.; Aliaga, A. E.; Fredes, C.; Koch, R. Experimental and Theoretical Raman and Surface-Enhanced Raman Scattering Study of Cysteine. *J. Raman Spectrosc.* **2009**, *40*, 632–638.

(71) Han, X. X.; Zhao, B.; Ozaki, Y. Surface-Enhanced Raman Scattering for Protein Detection. *Anal. Bioanal. Chem.* **2009**, *394*, 1719–1727.

(72) Barhoumi, A.; Halas, N. J. Label-Free Detection of DNA Hybridization Using Surface Enhanced Raman Spectroscopy. *J. Am. Chem. Soc.* **2010**, *132*, 12792–12793.

(73) Yea, K.; Lee, S.; Kyong, J. B.; Choo, J.; Lee, E. K.; Joo, S.-W.; Lee, S. Ultra-Sensitive Trace Analysis of Cyanide Water Pollutant in a PDMS Microfluidic Channel Using Surface-Enhanced Raman Spectroscopy. *Analyst* **2005**, *130*, 1009–1011.

(74) Alvarez-Puebla, R. a.; dos Santos, Jr., D. S.; Aroca, R. F. SERS Detection of Environmental Pollutants in Humic Acid–gold Nanoparticle Composite Materials. *Analyst* **2007**, *132*, 1210.

(75) Guo, H.; Xu, W.; Zhou, J.; Xu, S.; Lombardi, J. R. Highly Efficient Construction of Oriented Sandwich Structures for Surface-Enhanced Raman Scattering. *Nanotechnology* **2013**, *24*, 045608.

(76) Muniz-miranda, M.; Sbrana, G. Quantitative Determination of the Surface Concentration of Phenazine Adsorbed on Silver Colloidal Particles and Relationship with the SERS Enhancement Factor. *J. Phys. Chem. B* **1999**, *103*, 10639–10643.

(77) Kato, Y.; Takuma, H. Experimental Study on the Wavelength Dependence of the Raman Scattering Cross Sections. *J. Chem. Phys.* **1971**, *54*, 5398–5402.

(78) Szafranski, C. a.; Tanner, W.; Laibinis, P. E.; Garrell, R. L. Surface-Enhanced Raman Spectroscopy of Aromatic Thiols and Disulfides on Gold Electrodes. *Langmuir* **1998**, *14*, 3570–3579.

(79) Moskovits, M. Surface Selection Rules. *J. Chem. Phys.* **1982**, *77*, 4408–4416.

(80) Moskovits, M.; Suh, J. S. Surface Selection Rules for Surface-Enhanced Raman Spectroscopy: Calculations and Application to the Surface-Enhanced Raman Spectrum of Phthalazine on Silver. *J. Phys. Chem.* **1984**, *88*, 5526–5530.

(81) Le Ru, E. C.; Meyer, S. a; Artur, C.; Etchegoin, P. G.; Grand, J.; Lang, P.; Maurel, F. Experimental Demonstration of Surface Selection Rules for SERS on Flat Metallic Surfaces. *Chem. Commun.* **2011**, *47*, 3903–3905.

(82) Ru, E. C. Le; Meyer, M.; Blackie, E.; Etchegoin, P. G. Advanced Aspects of Electromagnetic SERS Enhancement Factors at a Hot Spot. *J. Raman Spectrosc.* **2008**, *39*, 1127–1134.

(83) Porter, M. D.; Bright, T. B.; Allara, D. L.; Chidsey, C. E. . Spontaneously Organized Molecular Assemblies. 4. Structural Characterization of n-Alkyl Thiol Monolayers on Gold by Optical Ellipsometry, Infrared Spectroscopy and Electrochemistry. *J. Am. Chem. Soc.* **1987**, *109*, 3559–3568.

(84) Lacy, W. B.; Olson, L. G.; Harris, J. M. Quantitative SERS Measurements on Dielectric-Overcoated Silver-Island Films by Solution-Deposition Control of Surface Concentrations. *Anal. Chem.* **1999**, *71*, 2564–2570.

(85) Sackmann, M.; Materny, a. Surface Enhanced Raman Scattering (SERS)—a Quantitative Analytical Tool? *J. Raman Spectrosc.* **2006**, *37*, 305–310.

(86) Le Ru, E. C.; Dalley, M.; Etchegoin, P. G. Plasmon Resonances of Silver Colloids Studied by Surface Enhanced Raman Spectroscopy. *Curr. Appl. Phys.* **2006**, *6*, 411–414.

(87) Wang, C.; Ruan, W.; Ji, N.; Ji, W.; Lv, S.; Zhao, C.; Zhao, B. Preparation of Nanoscale Ag Semishell Array with Tunable Interparticle Distance and Its Application in Surface-Enhanced Raman Scattering. *J. Phys. Chem. C* **2010**, *114*, 2886–2890.

(88) Li, X.; Hu, H.; Li, D.; Shen, Z.; Xiong, Q.; Li, S.; Fan, H. J. Ordered Array of Gold Semishells on TiO2 Spheres: An Ultrasensitive and Recyclable SERS Substrate. *ACS Appl. Mater. Interfaces* **2012**, *4*, 2180–2185.

(89) Litz, J. P.; Camden, J. P.; Masiello, D. J. Active Hot Spots via the Discrete-Dipole Approximation. *J. Phys. Chem. Lett.* **2011**, *2*, 1695–1700.

(90) Zuloaga, J.; Nordlander, P. On the Energy Shift Between Near-Field and Far-Field Peak Intensities in Localized Plasmon Systems. *Nano Lett.* **2011**, *11*, 1280–1283.

(91) Baker, G. a; Moore, D. S. Progress in Plasmonic Engineering of Surface-Enhanced Raman-Scattering Substrates Toward Ultra-Trace Analysis. *Anal. Bioanal. Chem.* **2005**, *382*, 1751–1770.

(92) Fan, M.; Andrade, G. F. S.; Brolo, A. G. A Review on the Fabrication of Substrates for Surface Enhanced Raman Spectroscopy and Their Applications in Analytical Chemistry. *Anal. Chim. Acta* **2011**, *693*, 7–25.

(93) Fan, M.; Brolo, A. G. Silver Nanoparticles Self Assembly as SERS Substrates with Near Single Molecule Detection Limit. *Phys. Chem. Chem. Phys.* **2009**, *11*, 7348–7389.

(94) López, I.; Vázquez, A.; Hernández-Padrón, G. H.; Gómez, I. Electrophoretic Deposition (EPD) of Silver Nanoparticles and Their Application as Surface-Enhanced Raman Scattering (SERS) Substrates. *Appl. Surf. Sci.* **2013**, *280*, 715–719.

(95) Haynes, C. L.; Duyne, R. P. Van. Nanosphere Lithography: A Versatile Nanofabrication Tool for Studies of Size-Dependent Nanoparticle Optics. *J. Phys. Chem. B* **2001**, *105*, 5599–5611.

(96) Yu, Q.; Guan, P.; Qin, D.; Golden, G.; Wallace, P. M. Inverted Size-Dependence of Surface-Enhanced Raman Scattering on Gold Nanohole and Nanodisk Arrays. *Nano Lett.* **2008**, *8*, 1923–1928.

(97) Gunnarsson, L.; Bjerneld, E. J.; Xu, H.; Petronis, S.; Kasemo, B.; Käll, M. Interparticle Coupling Effects in Nanofabricated Substrates for Surface-Enhanced Raman Scattering. *Appl. Phys. Lett.* **2001**, *78*, 802.

(98) Cao, G. *Nanostructures & Nanomaterials: Synthesis, Properties & Applications*; Imperial College Press, 2004.

(99) Israelachvili, J. *Intermolecular and Surface Forces*; Academic, Ed.; London, 1992.

(100) Mironov, V. *Fundamentals of Scanning Probe Microscopy*; Technosfera, Ed.; Moscow, 2004.

(101) Mayer; Feldman. *Fundamentals of Surface and Thin Film Analysis*; Holland, N., Ed.; 1986.

(102) Putnis, A. *An Introduction to Mineral Sciences*; Cambridge University Press, 1992.

(103) Turkevich, J.; Stevenson, P. C.; Hillier, J. A Study of the Nucleation and Growth Processes in the Synthesis of Colloidal Gold. *Discuss. Faraday Soc.* **1951**, *11*, 55.

(104) Lee, C.; Meisel, D. Adsorption and Surface-Enhanced Raman of Dyes on Silver and Gold Sols'. *J. Phys. Chem.* **1982**, *86*, 3391–3395.

(105) Li, T.; Albee, B.; Alemayehu, M.; Diaz, R.; Ingham, L.; Kamal, S.; Rodriguez, M.; Bishnoi, S. W. Comparative Toxicity Study of Ag, Au, and Ag-Au Bimetallic Nanoparticles on Daphnia Magna. *Anal. Bioanal. Chem.* **2010**, *398*, 689–700.

(106) Raveendran, P.; Fu, J.; Wallen, S. L. Completely "Green" Synthesis and Stabilization of Metal Nanoparticles. *J. Am. Chem. Soc.* **2003**, *125*, 13940–13941.

(107) Amendola, V.; Meneghetti, M. Size Evaluation of Gold Nanoparticles by UV - Vis Spectroscopy. *J. Phys Chem C* **2009**, *113*, 4277–4285.

(108) Brust, M.; Walker, M.; Bethell, D.; Schiffrin, D. J.; Whyman, R. Synthesis of Thiol-Derivatised Gold Nanoparticles in a Two-Phase Liquid–liquid System. *J. Chem. Soc., Chem. Commun.* **1994**, *7*, 801–802.

(109) Leff, D. V; Ohara, P. C.; Heath, J. R.; Gelbart, W. M. Thermodynamic Control of Gold Nanocrystal Size: Experiment and Theory. *J. Phys. Chem.* **1995**, *99*, 7036–7041.

(110) Hostetler, M. J.; Wingate, J. E.; Zhong, C.; Harris, J. E.; Vachet, R. W.; Clark, M. R.; Londono, J. D.; Green, S. J.; Stokes, J. J.; Wignall, G. D.; et al. Alkanethiolate Gold Cluster Molecules with Core Diameters from 1 . 5 to 5 . 2 Nm : Core and Monolayer Properties as a Function of Core Size. *Langmuir* **1998**, *14*, 17–30.

(111) Thomas, K. G.; Zajicek, J.; Kamat, P. V. Surface Binding Properties of Tetraoctylammonium Bromide-Capped Gold Nanoparticles. *Langmuir* **2002**, *18*, 3722–3727.

(112) Maye, M. M.; Zheng, W.; Leibowitz, F. L.; Ly, N. K.; Zhong, C. Heating-Induced Evolution of Thiolate-Encapsulated Gold Nanoparticles : A Strategy for Size and Shape Manipulations. *Langmuir* **2000**, *16*, 490–497.

(113) Skrabalak, S. E.; Chen, J.; Sun, Y.; Lu, X.; Au, L.; Cobley, C. M.; Xia, Y. Gold Nanocages: Synthesis, Properties and Applications. *Acc. Chem. Res.* **2008**, *41*, 1587–1595.

(114) Shi, W.; Sahoo, Y.; Swihart, M. T.; Prasad, P. N. Gold Nanoshells on Polystyrene Cores for Control of Surface Plasmon Resonance. *Langmuir* **2005**, *21*, 1610–1617.

(115) Pham, T.; Jackson, J. B.; Halas, N. J.; Lee, T. R. Preparation and Characterization of Gold Nanoshells Coated with Self-Assembled Monolayers. *Langmuir* **2002**, *18*, 4915–4920.

(116) Stöber, W.; Fink, A.; Bohn, E. Controlled Growth of Monodisperse Silica Spheres in the Micron Size Range. *J. Colloid Interface Sci.* **1968**, *26*, 62–69.

(117) Preston, T. C.; Signorell, R. Growth and Optical Properties of Gold Nanoshells Prior to the Formation of a Continuous Metallic Layer. *ACS Nano* **2009**, *3*, 3696–3706.

(118) Brinson, B. E.; Lassiter, J. B.; Levin, C. S.; Bardhan, R.; Mirin, N.; Halas, N. J. Nanoshells Made Easy : Improving Au Layer Growth on Nanoparticle Surfaces. *Langmuir* **2008**, *24*, 14166–14171.

(119) Kalele, S.; Gosavi, S. W.; Urban, J.; Kulkarni, S. K. Nanoshell Particles : Synthesis , Properties and Applications. *Curr. Sci.* **2006**, *91*, 1038–1052.

(120) Sylvestre, J.; Poulin, S.; Kabashin, A. V; Sacher, E.; Meunier, M.; Luong, J. H. T. Surface Chemistry of Gold Nanoparticles Produced by Laser Ablation in Aqueous Media. *J. Phys. Chem. B* **2004**, *18*, 16864–16869.

(121) Khoury, C. G.; Vo-Dinh, T. Gold Nanostars For Surface-Enhanced Raman Scattering: Synthesis, Characterization and Optimization. *J. Phys. Chem. C* **2008**, *112*, 18849–18859.

(122) Wei, G.-T.; Yang, Z.; Lee, C.-Y.; Yang, H.-Y.; Wang, C. R. C. Aqueous-Organic Phase Transfer of Gold Nanoparticles and Gold Nanorods Using an Ionic Liquid. *J. Am. Chem. Soc.* **2004**, *126*, 5036–5037.

(123) Lala, N.; Lalbegi, S. P.; Adyanthaya, S. D.; Sastry, M. Phase Transfer of Aqueous Gold Colloidal Particles Capped with Inclusion Complexes of Cyclodextrin and Alkanethiol Molecules into Chloroform. *Langmuir* **2001**, *17*, 3766–3768.

(124) Ghosh, P.; Han, G.; De, M.; Kim, C. K.; Rotello, V. M. Gold Nanoparticles in Delivery Applications. *Adv. Drug Deliv. Rev.* **2008**, *60*, 1307–1315.

(125) Liu, Y.; Shipton, M. K.; Ryan, J.; Kaufman, E. D.; Franzen, S.; Feldheim, D. L. Synthesis, Stability, and Cellular Internalization of Gold Nanoparticles Containing Mixed Peptide-Poly(ethylene Glycol) Monolayers. *Anal. Chem.* **2007**, *79*, 2221–2229.

(126) Jain, P. K.; Lee, K. S.; El-Sayed, I. H.; El-Sayed, M. a. Calculated Absorption and Scattering Properties of Gold Nanoparticles of Different Size, Shape, and Composition: Applications in Biological Imaging and Biomedicine. *J. Phys. Chem. B* **2006**, *110*, 7238–7248.

(127) Braslavsky, S. E.; Heibel, G. E. Time-Resolved Photothermal and Photoacoustic Methods Applied to Photoinduced Processes in Solution. *Chem. Rev.* **1992**, *92*, 1381–1410.

(128) Patel, C. K. N.; TAM, A. C. Pulsed Optoacoustic Spectroscopy of Condensed Matter. *Rev. Mod. Phys.* **1981**, *53*, 517–553.

(129) Tam, A. C. Applications of Photoacoustic Sensing Techniques. *Rev. Mod. Phys.* **1981**, *58*, 381–434.

(130) Cunningham, V.; Lamela, H. Laser Optoacoustic Spectroscopy of Gold Nanorods Within a Highly Scattering Medium. *Opt. Lett.* **2010**, *35*, 3387–3389.

(131) Evanoff, D. D.; Chumanov, G. Size-Controlled Synthesis of Nanoparticles. 2. Measurement of Extinction, Scattering, and Absorption Cross Sections. *J. Phys. Chem. B* **2004**, *108*, 13957–13962.

(132) Lim, C.; Hong, J.; Chung, B. G.; deMello, A. J.; Choo, J. Optofluidic Platforms Based on Surface-Enhanced Raman Scattering. *Analyst* **2010**, *135*, 837–844.

(133) Cecchini, M. P.; Hong, J.; Lim, C.; Choo, J.; Albrecht, T.; Andrew, J.; Edel, J. B. Ultrafast Surface Enhanced Resonance Raman Scattering Detection in Droplet-Based Microfluidic Systems. *Anal. Chem.* **2011**, *83*, 3076–3081.

(134) Casadevall i Solvas, X.; DeMello, A. Droplet Microfluidics: Recent Developments and Future Applications. *Chem. Commun.* **2011**, *47*, 1936–1942.

(135) Socrates, G. *Infrared & Raman Characteristic Group Frequencies : Tables & Charts*; Wilthshire, 1994.

(136) Varsanyi, G. *Vibrational Spectra of Benzene Derivatives*; Akademiai Kiado-Budapest, 1969.

(137) Loo, C.; Lin, A.; Hirsch, L.; Lee, M.-H.; Barton, J.; Halas, N.; West, J.; Drezek, R. Nanoshell-Enabled Photonics-Based Imaging and Therapy of Cancer. *Technol. Cancer Res. Treat.* **2004**, *3*, 33–40.

(138) Loo, C.; Hirsch, L.; Lee, M.-H.; Chang, E.; West, J.; Halas, N.; Drezek, R. Gold Nanoshell Bioconjugates for Molecular Imaging in Living Cells. *Opt. Lett.* **2005**, *30*, 1012–1014.

(139) Feis, A.; Gellini, C.; Salvi, P. R.; Becucci, M. Photoacoustic Excitation Profiles of Gold Nanoparticles. *Photoacoustics* **2014**, *accepted*.

(140) Von Raben, U.; Chang, R. K.; Laube, B. L.; Barber, P. W. Wavelength Dependence of Surface-Enhanced Raman Scattering from Ag Colloids with Adsorbed CN-Complexes, SO32-, and Pyridine. *J. Phys. Chem.* **1984**, *88*, 5290–5296.

(141) Dr. Roberto Pilot. Self-Absorption Simulations of Plasmonic Nanostructures in Solution at Different Excitation Wavelengths. *Pers. Comun.*

(142) Ru, E. C. Le; Blackie, E.; Meyer, M.; Etchegoin, P. G. Supporting Information for " SERS Enhancement Factors : a Comprehensive Study ". 1–19.

(143) Natan, M. J. Concluding Remarks : Surface Enhanced Raman Scattering. *Faraday Discuss.* **2006**, *132*, 321.

(144) Haynes, C. L.; Van Duyne, R. P. Plasmon-Sampled Surface-Enhanced Raman Excitation Spectroscopy. *J. Phys. Chem. B* **2003**, *107*, 7426–7433.

(145) Cheng, C.-S.; Chen, Y.-Q.; Lu, C.-J. Organic Vapour Sensing Using Localized Surface Plasmon Resonance Spectrum of Metallic Nanoparticles Self Assemble Monolayer. *Talanta* **2007**, *73*, 358–365.

(146) Chen, Y.-Q.; Lu, C.-J. Surface Modification on Silver Nanoparticles for Enhancing Vapor Selectivity of Localized Surface Plasmon Resonance Sensors. *Sensors Actuators B Chem.* **2009**, *135*, 492–498.

(147) Chen, K.-J.; Lu, C.-J. A Vapor Sensor Array Using Multiple Localized Surface Plasmon Resonance Bands in a Single UV-Vis Spectrum. *Talanta* **2010**, *81*, 1670–1675.

(148) Carron, K.; Peltersen, L.; Lewis, M. Octadecylthiol-Modified Surface-Enhanced Raman Spectroscopy Substrates: A New Method for the Detection of Aromatic Compounds. *Environ. Sci. Technol.* **1992**, *26*, 1950–1954.

(149) Mosier-Boss, P. .; Lieberman, S. . Detection of Volatile Organic Compounds Using Surface Enhanced Raman Spectroscopy Substrates Mounted on a Thermoelectric Cooler. *Anal. Chim. Acta* **2003**, *488*, 15–23.

(150) Guizard, C.; Bac, A.; Barboiu, M.; Hovnanian, N. Hybrid Organic-Inorganic Membranes with Specific Transport Applications in Separation and Sensors Technologies. **2001**, *25*, 167–180.

(151) Shea, K. J.; Loy, D. A. Bridged Polysilsesquioxanes . Molecular-Engineered Hybrid Organic - Inorganic Materials. *Chem. Mater* **2001**, *13*, 3306–3319.

(152) Dąbrowski, a.; Barczak, M.; Robens, E.; Stolyarchuk, N. V.; Yurchenko, G. R.; Matkovskii, O. K.; Zub, Y. L. Ethylene and Phenylene Bridged Polysilsesquioxanes Functionalized by Amine and Thiol Groups as Adsorbents of Volatile Organic Compounds. *Appl. Surf. Sci.* **2007**, *253*, 5747–5751.

(153) Brigo, L.; Cittadini, M.; Artiglia, L.; Rizzi, G. A.; Granozzi, G.; Guglielmi, M.; Martucci, A.; Brusatin, G. Xylene Sensing Properties of Aryl-Bridged Polysilsesquioxane Thin Films Coupled to Gold Nanoparticles. *J. Mater. Chem. C* **2013**, *1*, 4252–4260.

(154) Brigo, L.; Gazzola, E.; Cittadini, M.; Zilio, P.; Zacco, G.; Romanato, F.; Martucci, a; Guglielmi, M.; Brusatin, G. Short and Long Range Surface Plasmon Polariton Waveguides for Xylene Sensing. *Nanotechnology* **2013**, *24*, 155502.

(155) Burleigh, M. C.; Markowitz, M. A.; Spector, M. S.; Gaber, B. P. Porous Polysilsesquioxanes for the Adsorption of Phenols. *Environ. Sci. Technol.* **2002**, *36*, 2515–2518.

(156) Wilmshurst, J. K.; Bernstein, H. J. The Infrared and Raman Spectra of Toluene, Toluene-a-D3, m-Xylene, and m-Xylene-Aa'-D6. *Can. J. Chem.* **1957**, *35*, 911–925.

(157) Huang, X.; Jain, P. K.; El-Sayed, I. H.; El-Sayed, M. a. Plasmonic Photothermal Therapy (PPTT) Using Gold Nanoparticles. *Lasers Med. Sci.* **2008**, *23*, 217–228.

(158) Jain, S.; Hirst, D. G.; O'Sullivan, J. M. Gold Nanoparticles as Novel Agents for Cancer Therapy. *Br. J. Radiol.* **2012**, *85*, 101–113.

(159) Durr, N. J.; Larson, T.; Smith, D. K.; Korgel, B. a.; Sokolov, K.; Ben-Yakar, A. Two-Photon Luminescence Imaging of Cancer Cells Using Molecularly Targeted Gold Nanorods. *Nano Lett.* **2007**, *7*, 941–945.

(160) Chithrani, B. D.; Chan, W. C. W. Elucidating the Mechanism of Cellular Uptake and Removal of Protein-Coated Gold Nanoparticles of Different Sizes and Shapes. *Nano Lett.* **2007**, *7*, 1542–1550.

(161) Huh, Y. S.; Chung, A. J.; Erickson, D. Surface Enhanced Raman Spectroscopy and Its Application to Molecular and Cellular Analysis. *Microfluid. Nanofluidics* **2009**, *6*, 285–297.

(162) Smith, W. E. Practical Understanding and Use of Surface Enhanced Raman Scattering/surface Enhanced Resonance Raman Scattering in Chemical and Biological Analysis. *Chem. Soc. Rev.* **2008**, *37*, 955–964.

(163) Michaels, A. M.; Brus, L. Ag Nanocrystal Junctions as the Site for Surface-Enhanced Raman Scattering of Single Rhodamine 6G Molecules. *J. Phys. Chem. B* **2000**, *104*, 11965–11971.

(164) Xu, S.; Ji, X.; Xu, W.; Li, X.; Wang, L.; Bai, Y.; Zhao, B.; Ozaki, Y. Immunoassay Using Probe-Labelling Immunogold Nanoparticles with Silver Staining Enhancement via Surface-Enhanced Raman Scattering. *Analyst* **2004**, *129*, 63–68.

(165) Han, X. X.; Cai, L. J.; Guo, J.; Wang, C. X.; Ruan, W. D.; Han, W. Y.; Xu, W. Q.; Zhao, B.; Ozaki, Y. Immunoabsorbent Assay Based on Surface-Enhanced Resonance Raman Scattering. **2008**, *80*, 3020–3024.

(166) Cao, Y. C.; Jin, R.; Mirkin, C. a. Nanoparticles with Raman Spectroscopic Fingerprints for DNA and RNA Detection. *Science* **2002**, *297*, 1536–1540.

(167) He, H.; Xie, C.; Ren, J. Nonbleaching Fluorescence of Gold Nanoparticles and Its Applications in Cancer Cell Imaging. *Anal. Chem.* **2008**, *80*, 5951–5957.

(168) Fortunati, I.; Weber, V.; Ferrante, C. Two Photon Fluorescence Correlation Spectroscopy for Characterization of Static and Dynamic Features of Gold Nanoparticles. *Prep.*

(169) Fede, C.; Fortunati, I.; Weber, V.; Rossetto, N.; Bertasi, F.; Petrelli, L.; Guidolin, D.; Signorini, R.; Albertin, G. Comparison Between Static And Flow Conditions In The In Vitro Evaluation Of Gold Nanoparticles Toxicity Towards Human Endothelial Cells. *Prep.*

(170) Wilchek, M.; Bayer, E. a; Livnah, O. Essentials of Biorecognition: The (strept)avidin-Biotin System as a Model for Protein-Protein and Protein-Ligand Interaction. *Immunol. Lett.* **2006**, *103*, 27–32.

(171) Dupont-Filliard, a; Billon, M.; Livache, T.; Guillerez, S. Biotin/avidin System for the Generation of Fully Renewable DNA Sensor Based on Biotinylated Polypyrrole Film. *Anal. Chim. Acta* **2004**, *515*, 271–277.

(172) Hofstetter, H.; Morpurgo, M.; Hofstetter, O.; Bayer, E. a; Wilchek, M. A Labeling, Detection, and Purification System Based on 4-Hydroxyazobenzene-2-Carboxylic Acid: An Extension of the Avidin-Biotin System. *Anal. Biochem.* **2000**, *284*, 354–366.

(173) Green, N. M. A Spectrophotometric Assay for Avidin and Biotin Based on Binding of Dyes by Avidin. *Biochem. J.* **1965**, *94*, 23C–24C.

(174) Rutstein, D.; Ingenito, E. F.; Reynolds, W. E.; M., B. J. The Determination Of Albumin In Human Blood Plasma And Serum . A Method Based On The Interaction Of Albumin with an Anionic Dye-2-(4-Hydroscybenzeneazo) Benzoic Acid. *J. Clin. Invest.* **1954**, *33*, 211–221.

(175) Farrera, J.-A.; Canal, I.; Hidalgo-Fernández, P.; Pérez-García, M. L.; Huertas, O.; Luque, F. J. Towards a Tunable Tautomeric Switch in Azobenzene Biomimetics: Implications for the Binding Affinity of 2-(4'-Hydroxyphenylazo)benzoic Acid to Streptavidin. *Chemistry* **2008**, *14*, 2277–2285.

(176) Trotter, P. J. Azo Dye Tautomeric Structures Determined by Laser-Raman Spectroscopy. *Appl. Spectrosc.* **1977**, *31*, 30–35.

(177) Dines, T. J.; MacGregor, L. D.; Rochester, C. H. A Resonance Raman Spectroscopic Study of the Protonation of 2-(4′-Hydroxyazo)-Benzoic Acid Adsorbed on Oxide Surfaces. *Vib. Spectrosc.* **2003**, *32*, 225–240.

(178) Thomas, E. W.; Merlin, J. C. Resonance Raman Spectroscopic Studies of 2-(4′-Hydroxyphenylazo)-Benzoic Acid and Some Substituted analogs—II. Binding to Avidin and Bovine Serum Albumin. *Spectrochim. Acta Part A Mol. Spectrosc.* **1979**, *35*, 1251–1255.

(179) Merlin, J. C.; Thomas, E. W. Resonance Raman Spectroscopic Studies of 2-(4′-Hydroxyphenylazo)-Benzoic Acid and Some Substituted analogs—I. pH Effect on Spectra. *Spectrochim. Acta Part A Mol. Spectrosc.* **1979**, *35*, 1243–1249.

(180) Biswas, N.; Umapathy, S. Structures, Vibrational Frequencies, and Normal Modes of Substituted Azo Dyes: Infrared, Raman, and Density Functional Calculations. *J. Phys. Chem. A* **2000**, *104*, 2734–2745.

(181) Fagnano, C.; Fini, G.; Torreggiani, A. Raman Spectroscopic Study of the Avidin-Biotin Complex. *J. Raman Spectrosc.* **1995**, *26*, 991–995.

SCIENTIFIC CONTRIBUTIONS

Papers:

- Giallongo, G.; Rizzi, G. A.; Weber, V.; Ennas, G.; Signorini, R.; Granozzi, G. Green Synthesis and Electrophoretic Deposition of Ag Nanoparticles on SiO2/Si(100). *Nanotechnology* **2013**, *24*, 345501.

- Frare, M. C.; Weber, V.; Signorini, R.; Bozio, R. Gold Nanoparticles in Polycarbonate Matrix for Optical Limiting Against Cw Laser. *J. Laser Phys.* **2014**, submitted.

- Fede, C.; Fortunati, I.; Weber, V.; Rossetto, N.; Bertasi, F.; Petrelli, L.; Guidolin, D.; Signorini, R.; Albertin, G. Comparison Between Static And Flow Conditions In The In Vitro Evaluation Of Gold Nanoparticles Toxicity Towards Human Endothelial Cells. *In preparation.*

- Fortunati, I.; Weber, V.; Ferrante, C. Two Photon Fluorescence Correlation Spectroscopy for Characterization of Static and Dynamic Features of Gold Nanoparticles. *In preparation.*

Conferences:

- Oral presentation titled "**Absorption and Scattering Properties of Gold Nanoshells Studied by Photoacoustic and Surface Enhanced Raman Spectroscopy**" at the 10th International Conference on Nanosciences & Nanotechnologies, 9-12 July 2013, Thessaloniki, Greece.
  V. Weber, R. Bozio, A. Feis, C. Gellini, D. Pedron, P.R. Salvi, R. Signorini

- Poster titled **"Plasmonic substrates for SERS detection of aromatic molecules in high affinity sol-gel matrix"** at the Workshop nazionale Plasmonica 2013, 1-3 July 2013, Milan.
  Verena Weber, Laura Brigo, Giovanna Brusatin, Raffaella Signorini, Danilo Pedron, Renato Bozio

- Poster titled **"Plasmonic substrates for ultrasensitive SERS detection of biological molecules",** at 1st International Conference On Enhanced Spectroscopy, ICES 2012**,** 2-6 October 2012 IGESA, Porquerolles Island (F).
  Verena Weber, Davide Silvestri, Margherita Morpurgo, Danilo Pedron, Renato Bozio, Raffaella Signorini

- Poster titled **"Plasmonic substrates for ultrasensitive SERS detection of biological molecules"**, at Congresso nazionale di Spettroscopie Raman e ottica non lineare (GISR 2012), 6-8 June 2012 CNR Bologna.
  Verena Weber, Davide Silvestri, Raffaella Signorini, Margherita Morpurgo, Danilo Pedron, Renato Bozio

- Poster titled **"Plasmonic nanoparticles as SERS ultrasensitive sensors"**, at 2nd Conference on Laser Ablation and Nanoparticle Generation in Liquids (ANGEL 2012), 22-24 May 2012, Hotel Caparena, Taormina.
  V. Weber, R. Signorini, D. Pedron, E. Giorgetti, P. Marsili, R. Bozio

- Oral presentation titled **"Plasmonic nanoparticles for SERS ultrasensitive detection"**, at Trento Innovation Conferences on Materials Engineering (TICME 2012), 12-14 Dicember 2011, Castello del Buonconsiglio, Trento.
  Verena Weber, Laura Brigo, Giovanna Brusatin, Raffaella Signorini

- Poster titled **"Plasmonic nanostructures for ultrasensitive detection of biological molecole"** at VIII INSTM Conference, 26-29 June 2011, Catania.
  Verena Weber, Ida Ros, Raffaella Signorini, Renato Bozio, Margherita Morpurgo, Danilo Pedron

Ringraziamenti

Per il lungo lavoro di questi tre anni di Dottorato, vorrei ringraziare in primo luogo il mio supervisore Raffaella Signorini, per il sostegno scientifico e personale e, con lei anche il Prof. Renato Bozio per i confronti scientifici sempre chiarificatori.
Per l'aiuto e i consigli riguardanti la spettroscopia Raman/SERS ringrazio Roberto Pilot (soprattutto per le ultime misure in cui ci siamo confrontati molto) e il Prof. Danilo Pedron per la grande disponibilità ad ascoltare ogni mio dubbio e per l'aiuto ad imparare ad usare la strumentazione in autonomia.
Ringrazio poi Giovanna Brusatin e Laura Brigo del Dipartimento di Ingegneria Industriale per il lavoro sul sensore di Xilene, Margherita Morpurgo e Davide Silvestri del Dipartimento di Farmacia per la collaborazione bio e Alessandro Feis e Cristina Gellini del Dipartimento di Chimica dell'Università di Firenze per le misure di foto acustica e per gli interessanti confronti. Ringrazio anche Emilia Giorgetti del CNR di Firenze per averci fornito nanoparticelle per laser ablation e nanostelle d'oro. Inoltre ringrazio il Prof. Giovanni Mattei e con lui Valentina Bello e Valentina Russo per la disponibilità per immagini TEM, SEM e AFM e il Dott. Piero Schiavuta per l'aiuto con le misure AFM al Civen-NanoFab.
Per i confronti scientifici e per le simpatiche chiacchierate in ufficio ringrazio la Camilla Ferrante, Tode, Betta, Nicola, Cate, Ale, Luca e Lucio: nonostante la convivenza in un grande open space potesse sembrare difficile, abbiamo mantenuto l'equilibrio e le pause sono sempre state momento di divertimento. Ringrazio in particolare le mie colleghe, ma soprattutto amiche Ilaria, Maria Chiara e Alessia per l'affetto il sostegno e le coccole.

Ringrazio ovviamente la mia famiglia, soprattutto mamma e papà, e tutte le persone che hanno condiviso questi tre anni, non sempre facili, insieme a me: il Vis per le belle distrazioni e i miei amici extra-universitari, in particolare Rick e Anna. Un grazie particolare va alla mia amica Vale, sempre presente.
Infine ringrazio Federico per avere condiviso tanto in questi anni. Grazie per esserci sempre stato, nei momenti di difficoltà come nei momenti di gioia.